Technische Universität München

Fakultät für Physik

Lehrstuhl für Experimentelle Astroteilchenphysik

Improving Particle Discrimination and Achieving a 4π-Veto Detector Concept for the CRESST Experiment

Marc Wüstrich

Vollständiger Abdruck der von der Fakultät für Physik der Technischen Universität München zur Erlangung des akademischen Grades eines

Doktors der Naturwissenschaften (Dr. rer. nat.)

genehmigten Dissertation.

Vorsitzender: Prof. Dr. Alejandro Ibarra
Prüfer der Dissertation: 1. Prof. Dr. Stefan Schönert
2. apl. Prof. Dr. habil. Hubert Kroha

Die Dissertation wurde am 12.06.2019 bei der Technischen Universität München eingereicht und durch die Fakultät für Physik am 29.01.2020 angenommen.

Abstract

Most experiments aiming at the direct detection of dark matter rely on a detector technology, which allows them to collect large exposure within small time scales. This is achieved by combining large targets with a low background rate as it is possible with liquid noble gas experiments. The CRESST-II experiment, however, uses detector modules based on the ″phonon-light‟-technique. By instrumenting scintillating $CaWO_4$ crystals with superconducting temperature sensors, the world's lowest detection thresholds are achieved with these detectors. Background discrimination is achieved using a spatially separated light detector which simultaneously quantifies the amount of scintillation light that created is case of an interaction in the target.

The discovery potential of the CRESST-II detector modules is currently limited by the poor discrimination power in the low energy range. In order to improve the particle discrimination in this energy range, the performance of the light channel has to be improved. To achieve this goal, two approaches are investigated in this work. First, by improving the performance of the superconducting thermometer used for reading out the light detector and, second, by improving the light collection efficiency in the detector modules.

For the first aspect, the efficiency of phonon collectors connected the thermometer is investigated. This efficiency is directly related to the diffusion properties of the quasiparticles that created inside phonon collectors. Using a dedicated setup, the diffusion length of the generated quasiparticles is measured to be $\mathcal{O}(2\,\mathrm{mm})$, opening the way to equip the existing thermometer structures with larger and thicker phonon collectors to improve their sensitivity by up to 30 %.

The second aspect is assessed by developing two new detector concepts, in which the losses occurring during the propagation of the scintillation light in the detector module are reduced. Based on a ray tracing simulation, the losses in the CRESST-II detector module are analyzed, revealing that 75 % of the created light is lost. In the *slice detector concept*, the measured light signal is enhanced by $\approx 50\,\%$ compared to a conventional CRESST-II detector, while in the *beaker detector concept*, the measured light signal is increased by 250 %. These improvements are translated in a significantly improved rejection power which allows to extend the energy range for particle identification to lower values. In comparison, the average limit can be lowered from 11.2 keV (avg. CRESST-II) to 6.4 keV (slice) and 4.4 keV(beaker).

In addition, the *beaker detector concept* is first ″phonon-light‟detector providing, on itself, an active and true 4π-veto system for external backgrounds. In this work, the veto system is investigated in detail, confirming a powerfull rejection efficiency which allows to implement this system in future CRESST detector modules and other application in which external background sources limit the sensitivity of the experiment.

Zusammenfassung

Bei der direkten Suche nach Dunkler Materie ist das Sammeln von großen Datensätzen innerhalb von kurzer Zeit der dominierende Aspekt bei der Entwicklung der Experimente. Deswegen verlassen sich viele Experimente auf Detektoren die flüssige Edelgase mit szintillierenden Eigenschaften als Target verwenden. Diese erlauben große Targetmassen mit sehr niedrigen Untergrundraten zu kombinieren. Das CRESST-II Experiment verwendet dagegen Detektoren, die auf der "Phonon-Licht"-Technologie basieren. Dabei werden szintillierende $CaWO_4$ mit hochempfindlichen Temperatursensoren instrumentiert, wodurch die weltweit niedrigsten Energieschwellen erreicht werden.

Momentan ist die Sensitvität der CRESST-II Detektoren durch die schwache Untergrundindentifikation bei niedrigen Energien eingeschränkt. Grund dafür ist die schwache Leistung des Lichtdetektors in diesem Energiebereich. Um diese Einschränkung bei zukünftigen Messkampagnen zu vermeiden, wird im Rahmen dieser Arbeit auf zweierlei Art und Weise versucht die Leistung des Lichtkanals zu steigern. Zum einen, in dem die Leistungs des Temperatursensors verbessert wird und, zum anderen, in dem die Lichtsammeleffizienz innerhalb des Detektormodule gesteigert wird.

Um die Leistung der verwendeten Thermometer zu steigern, wird mittels eines speziellen experimentellen Aufbaus die Effizienz der Phononkollektoren untersucht. Phononkollektoren sind supraleitende Aluminiumfilme, in denen generierte Quasiteilchen positive zum Temperatursignal beitragen können, falls die Dimensionierung passend zu den Diffusionseigenschaften gewählt werden. Die experimentell bestimmten Werte der Diffusionslänge bewegen sich im Bereich von $\mathcal{O}(2\,\mathrm{mm})$, wodurch eine Neudimensionierung der Phononkollektoren auf quantitative Wiese möglich wird und somit die Leistung der Thermometer um bis zu 30 % gesteigert werden kann.

Der zweite Ansatz zielt darauf ab durch die Neuanordnung der einzelnen Detektorkomponenten die Lichtverluste innerhalb der Detektormodule zu reduzieren. Im Rahmen dieser Arbeit werden daher zwei neue Detektorkonzepte mit gesteigerter Lichtsammeleffizienz vorgestellte: Das *Slice Detektorkonzept* und das *Beaker Detektorkonzept*. In beiden Detektorkonzepten kann die Lichtsammeleffizienz gegenüber dem konventionellen CRESST-II Detektormodul gesteigerter werden (um 50 % bzw. 250 %). Dadurch sind deutlich Verbesserung in der Untergrundsindentifikation erreichbar, die es erlauben die untere Schwelle der Akzeptanzregion von einem Durchschnittswert von 11.2 keV (CRESST-II (Phase 1&2)) auf 6.4 keV (Slice) bzw. 4.4 keV (Beaker) zu senken.

Zusätzlich ist das Beaker Detektorkonzept das erste "Phonon-Licht"-Detektormodul, das ein aktives und vollständiges 4π-Veto System für externe Untergründe anbietet. Die Leistungsfähigkeit des Systems wird durch die Untergrundanalyse einer Langzeitmessung bestätigt und erlaubt die Anwendung des System in zukünftigen CRESST Detektoren und anderen astrophysikalischen Experimenten.

Inhaltsverzeichnis

1 Dark Matter in the Universe

The existence of dark matter was proposed for the first time in 1933 by the Swiss physicist F. Zwicky. During his investigation of the kinematic behavior of the galaxies in the Coma cluster [1], he noticed that the luminous matter being present in the cluster does not provide sufficient gravitational potential to bind the individual galaxies in the cluster. Therefore, he suggested the presence of additional "dark matterto solve the conflict in his findings.

Though, it took about 40 years until his concept became widely accepted in cosmology. In the 1970's, the accurate measurement of the rotation velocity of the stars in the Andromeda galaxy (M31) revealed a mismatch between visible matter and observed gravitation. After this observation, the existence of dark matter was not longer doubted [2]. Since then, the gravitational influence of dark matter has been observed on all cosmic scales. The nature of dark matter, though, has remained an unsolved problem of cosmology and astroparticle physics until today.

This first chapter gives a brief overview on the different cosmological observations supporting the existence of dark matter. Additionally, some candidates intended to provide a stringent explanation of the dark matter phenomenon are introduced. Finally, at the end of this chapter, an introduction to the basic concepts for the direct detection of dark matter is given.

1.1 Cosmological Observations

There are numerous observations in the Universe, which indicate the presence of dark matter. The gravitational influence of dark matter on baryonic matter is observed on different cosmic scales. Although alternative theories are able to explain the individual phenomena, only the concept of dark matter is able to provide a generally valid and stringent explanation. In the following, the most important cosmological observations are listed.

1.1.1 Rotation Velocity of Spiral Galaxies

The motion of stars within a spiral galaxy can be described by using classical mechanics. When applying Newton's law, one can derive equation 1.1 to describe the rotation velocity v_r of a star circiling around the galactic center as a function of the radius r.

$$v_r(r) = \sqrt{\frac{M(r) \cdot G}{r}} \propto \frac{1}{\sqrt{r}} \tag{1.1}$$

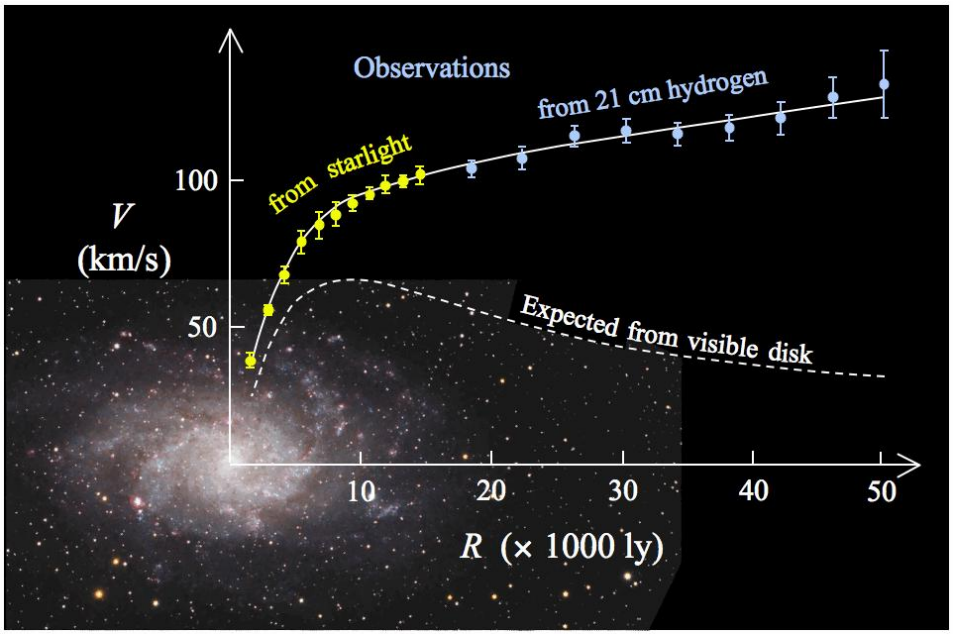

Abbildung 1.1: Comparison of the expected distribution of the rotation speed (dashed blue line) and the observed (yellow data points and blue interpolation) of the spiral galaxy M33. The observed rotation velocity of spiral galaxies is not consistent with Newton's laws considering only luminous matter. The shape of the velocity distribution implies that most of the mass is located in the outer regions of the galaxies and hence not visible [5].

In equation 1.1, G is the gravitational constant ($G = 6.6738 \cdot 10^{-11} m^3/kg \cdot s^2$) [3] while *M(r)* denotes the galactic mass which is enclosed within the corresponding sphere of radius r given the observed luminous mass distribution. Equation 1.1 implies that the rotation speed of stars in the spiral arms of a galaxy is expected to decrease with increasing distance from the rotation center.

This assumption is not in agreement with the observations made for spiral galaxies (i.e. the spiral galaxy M33 [4]). If the measured and expected rotatation velocity $v_r(r)$ are compared , a large discrepancy between them is revealed (see figure 1.1). While in the galatic center the observed discrepancy is relatively small, it increases towards larger radii. This observation indicates that the mass distribution observed from the luminous matter does not correspond to the total mass distribution. One possible explanation for the observation is the presence of a dark matter halo which contributes significant amount of mass to the total mass in the outer regions of the galaxy [6].

Alternative theories are able to explain the observations made for spiral galaxies, too. For example, the presence of Massive Compact Halo Objects (MACHOs) is able to give an explanation for the observed behavior. MACHOs are defined as non-luminous, baryonic astrophysical objects (i.e. brown dwarfs, white dwarfs, black holes, ...). By assuming a significant presence of MACHOs in the outer parts of a galaxy, the observed rotation curve can be explained without the need to introduce additional mass in the

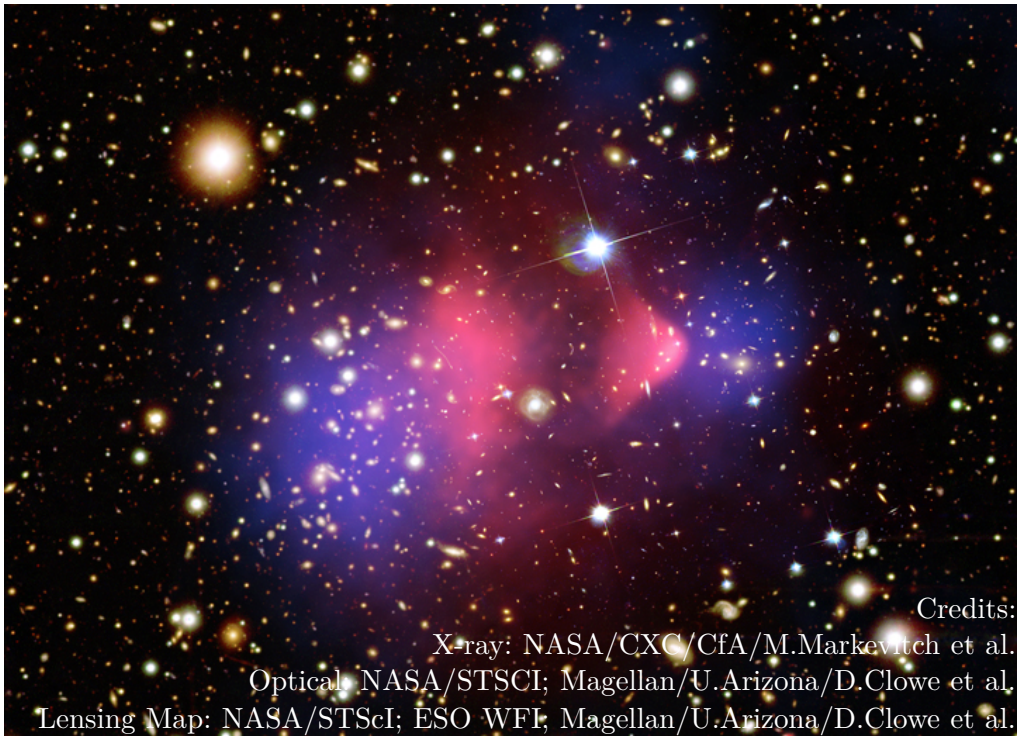

Abbildung 1.2: Composite picture of the "Bullet Cluster"(1E 0657-558) containing the visible spectrum, the X-ray emission (red) and the mass distribution (blue) obtained by gravitational lensing [8].

form of dark matter. Though, last measurements indicate that the observed number of MACHOs in our galaxy is by far not sufficient to explain the rotation velocity in the outer regions [7].

1.1.2 Bullet Cluster

The term "bullet clusterrefers to the observed behavior of the collusion of two galaxy clusters (1E 0657-558 [8]) and is another cosmological phenomenon which is related to the existence of dark matter. By analyzing the mass distribution of two colliding galaxy clusters, discrepancies are observed between the visible matter and the actual mass distribution. In figure 1.2, a composite picture of 1E 0657-558 is shown.

The picture of the bullet cluster reveals that the different mass contributions in the clusters interact differently with each other during the collision. From the visible spectrum, one can derive that the baryonic matter contained in stars remains dominantly unaffected from the collision and is able to continue its propagation without any major interaction. Using gravitational lensing to determine the total mass distribution in the galaxy clusters (i.e. baryonic matter and dark matter) is determined (indicated in blue). The X-ray component of the picture reveals that the interstellar gas, contributing a major fraction to the total baryonic matter contained in galaxies, is decelerated

and heated up because of the collision (marked in red). The picture indicates that the heated interstellar gas lags behind the respective centers of mass of the galaxy clusters. The gravitational lensing also reveals that most of the mass remains unaffected from the collision and shows no sign of any major interaction process. Since the mass contained in stars is insufficient to explain the observed strength of gravitational lensing, it can be assumed that a large fraction of this mass is made of dark matter. Since no interaction with normal, baryonic matter (i.e. the interstellar gas) nor with itself is observed, the strength of dark matter interactions can be expected to be very small [9].

The "bullet clusterchallenges most explanation attempts which intend to explain other cosmological observations without the presence of dark matter. Theories like the MM-odified Newtonian Dynamics"(MOND) fail to describe the observed behavior of the bullet cluster which supports the presence of dark matter in our Universe even more [10].

So far a second example for a "Bullet Cluster"has been discovered [11]. Also here, the amount of directly observed matter and the total amount of matter disagrees confirming the observations made for 1E 0657-558.

1.1.3 Cosmic Microwave Background

The cosmic microwave background radiation (CMB) is an electromagnetic radiation which was produced in the early Universe. In the time shortly after the Big Bang, the temperature of the Universe was high enough to allow thermal equilibrium between matter and radiation. With the expansion of the Universe, the temperature fell below the necessary level to maintain this equilibrium. Approximately 380000 y after the big bang, the temperature level dropped sufficiently that electrons and protons were able to form electrically neutral hydrogen which, consequently, yielded to the Universe becoming transparent for photons. These photons were able to propagate freely since this time, therefore, the measurement of the CMB photons allows to take a snapshot of the early Universe at the time of the decoupling.

Since its discovery in 1965 by Wilson and Penzias [12], numerous experiments were performed to measure and characterize the CMB accurately. Today, the measured temperature spectrum of the CMB is determined to correspond to a blackbody spectrum with a temperature of $2.725 \pm 0.002\,\mathrm{K}$ [13]. After the COBE satellite discovered in the early 90's anisotropies in the CMB in the $10\,\mu\mathrm{K}$ range [14], more precise satellite based experiments were deployed to measure these anisotropies precisely. The latest measurements of the WMAP satellite [15] or the PLANCK satellite map the CMB over the full sky with a precision of up to $10^{-6}\,\mathrm{K}$ [16] (see figure 1.3).

The sky map recorded for the CMB can be analyzed on position dependencies by plotting the the CMB power spectrum as function of the angle scales. Using Λ-CDM model (introduced in the following section) the amount of dark matter being present in the Universe can be extracted from the information contained in the CMB power spectrum. The analysis reveals that a significant part of the existing mass is contributed by dark matter while the fraction baryonic matter contributes to the total matter in the Universe is five times smaller.

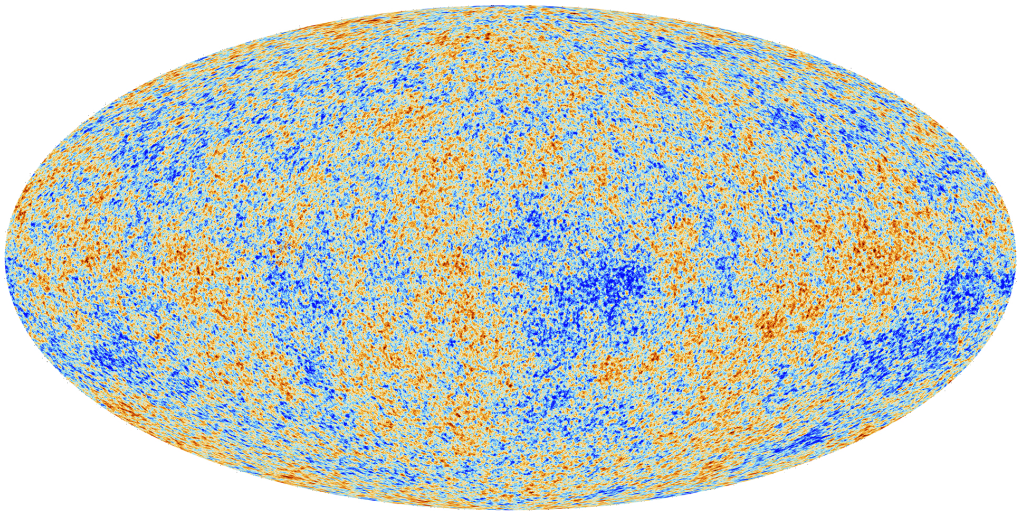

Credits: ESA and the Planck Collaboration

Abbildung 1.3: CMB temperature map recorded by the PLANCK satellite. The color coding indicates the local temperature difference to the average temperature of the CMB which is determined to be 2.725 K [16].

1.2 Cosmological Framework

Next to the explanation of astrophysical phenomena indicating a significant lack of visible mass in the current Universe, dark matter is assumed to play also a major role in the evolution of the Universe.

The Λ-CDM model is an established cosmological model to describe the evolution of the Universe over time. It considers the curvature of space as well as the contribution of the Universe's constituents to the total energy density and complies with the concept of an expanding Universe (i.e. "Big Bang Theory").

The Friedman-Lemaitre equation is the solution of the Einstein field equations with Friedman-Lemaitre-Robertson-Walker metric.

$$\underbrace{H(t)^2}_{\text{expansion}} + \underbrace{\frac{c^2\kappa}{a(t)^2}}_{\text{curvature}} = \underbrace{\frac{8\pi}{3}G\rho}_{\text{matter}} + \underbrace{\frac{c^2\Lambda}{3}}_{\text{vacuum energy}} \quad . \tag{1.2}$$

In equation 1.2, $a(t)$ is the scale factor at the time t while $H(t)$ is the Hubble constant. Based on the observations of E. Hubble in 1929 [17] and the theory of an expanding Universe introduced by G. Lemaitre two years before [18], a relation between the Hubble parameter $H(t)$ and the scale factor $a(t)$ is established.

$$H(t) = \frac{\dot{a}(t)}{a(t)} \tag{1.3}$$

The notation H_0 is used for the currently measured Hubble parameter ($H_0 = H(t = t_0) = 67.8 \pm 0.9\,\mathrm{km/(s \cdot Mpc)}$ [19]).

Λ denotes the cosmological constant which accounts for the acceleration the of the Universe's expansion caused by presence of vacuum/dark energy [20]. Initially introduced by A. Einstein to allow the description of a steady Universe, the present value of Λ is controversially discussed since the discovery of an expanding Universe in 1998 [20].

The parameter κ describes the curvature of the Universe. Three cases are distinguished for this parameter: An open Universe ($\kappa = -1$), a closed Universe ($\kappa = +1$) or a flat Universe ($\kappa = 0$).

Under the assumption of a flat Universe and a vacuum energy $\Lambda = 0$, a critical density ρ_c can be defined for finding a solution for equation 1.2 at present time:

$$\rho_c = \frac{3H_0^2}{8\pi G} \tag{1.4}$$

ρ_c allows to rewrite equation 1.2 to achieve a clear separation of the different constituents.

$$1 = \underbrace{\frac{\rho_M}{\rho_c}}_{\text{matter}} \underbrace{- \frac{c^2\kappa}{a^2(t)H_0^2}}_{\text{curvature}} + \underbrace{\frac{c^2\Lambda}{3H_0^2}}_{\text{vacuum energy}} \tag{1.5}$$

By defining the respective terms of equation 1.5 as ratio of the density of the respective consistent and the critical density (i.e. $\Omega_x = \rho_x/\rho_c$) the total energy density of the Universe at present time can be written as

$$1 = \Omega = \Omega_m + \Omega_\kappa + \Omega_\Lambda. \tag{1.6}$$

Based on the analysis of the angular power spectrum of the CMB (see section 1.1.3), the PLANCK collaboration published values for the respective energy densities fulfilling the Λ-CDM model [19]. The density parameter for matter is measured with $\Omega_m = 0.3156 \pm 0.0091$ being composed of $\Omega_{DM} = 0.2642 \pm 0.0049$ (non-baryonic, cold dark matter) and $\Omega_b = 0.0490 \pm 0.0005$ (baryonic matter). In addition, the vacuum density parameter is derived to be $\Omega_\Lambda = 0.6825 \pm 0.020$. In a combination with a negligibly small curvature term of Ω_κ, the results are compatible with a flat Universe $\Omega = 1.0023 \pm 0.0055$.

This measurement complies also with the value obtained for the baryonic energy density by analyzing Big Bang Nucleosynthesis. Using a complete independent approach, a similar value for the baryonic matter contribution is determined ($\approx 5\,\%$) [21].

These findings imply that the majority of the matter being present in our Universe at the moment is made of non-baryonic and, therefore, non-visible dark matter.

1.3 Particle Candidates for Dark Matter

1.3.1 Observed Properties of Dark Matter

Based on the observations and phenomena described before, the following properties of dark matter are derived (adapted from [22] [23]).

- Since no absorption and emission of electromagnetic radiation is observed, dark matter is expected to be **electrically neutral**.
- Since no interaction based on the strong nuclear force is observed, dark matter has to be **color neutral**. Combining both points mentioned before, dark matter is of **non-baryonic** character.
- Since the gravitational influence of dark matter on baryonic matter is observed on all cosmic scales, dark matter has to be **massive**.
- Since the influence dark matter is observed from the beginning of the early Universe, dark matter has to be **stable** on the cosmological time scale.
- Based on simulations for modeling the structure formation in the Universe (e.g. the Millennium Run" [24]) and observations made for the genesis of large scale structures, dark matter has to be **non-relativistic**, thus, **cold**.

Since these properties are well established, new models and theories providing possible candidates for dark matter have to comply with the accepted models and observations for stellar formation and the big bang nucleosynthesis.

Another important consideration is, that the experimental proof of a dark matter candidate is only possible if an interaction channel with baryonic matter exists. In order to comply with the elusive character of dark matter, it has to be assumed that the strength of the assumed interaction channel is on the scale of the weak nuclear interaction.

The SStandard Model of Particle Physicsïs unable to provide a suitable candidate for dark matter. Therefore, the experimental proof of dark matter would also imply the existence of physics beyond the SStandard Model of Particle Physics".

1.3.2 WIMP Dark Matter

The term "Weakly Interacting Massive Particle"(WIMP, χ) describes a hypothetical group of particles with the properties listed in section 1.3.1.

WIMPs are assumed to be in thermal equilibrium in the early Universe. This means, the production and annihilation of dark matter is in equilibrium as long $m_\chi \ll k_b T$ and the particle number density is sufficiently high. Since the particle number density as well as the temperature of the Universe decreases according to its expansion, at some point in time the thermal freeze out of the WIMPs take place which results in stable relic density for this particle. If no additional decay possibilities are assumed, a relic dark

matter density $\Omega_{DM} \approx 0.3$ can be obtained for WIMPs with a mass of $m_\chi \approx 100\,\mathrm{GeV/c^2}$ and an average annihilation rate in the range of the electroweak interaction scale [25].

$$\langle v \cdot \sigma \rangle \approx 10^{-25}\,\mathrm{cm^3/s} \tag{1.7}$$

This coincidence of matching quantities to achieve the correct dark matter abundance is known under the name "WIMP Miracle".

A candidate for a WIMP is provided in the minimal supersymmetric extension of the standard model (MSSM) [26]. Therein, to each standard model particle is assigned a supersymmetric partner. Main difference between a standard model particle and its supersymmetric partner is that fermions are converted to bosons and vice versa. Furthermore, an additional quantum number is introduced: The R-parity. This quantum number is conserved and prevents/suppresses the decay of the lightest supersymmetric particle (LSP) into standard model particles. Therefore, the LSP is considered as a suitable stable candidate for dark matter [26].

For the WIMP, a theoretical lower limit of exists (i.e. Lee-Weinberg bound") which rules out a WIMP mass below $\approx 3\,\mathrm{GeV/c^2}$. Since the annihilation cross-section decreases towards smaller WIMP masses, the relic abundance increases accordingly to the rules of the thermal freeze out process. Consequently, a lighter WIMP causes an increased relic abundance of dark matter which would lead to a closed Universe [26].

1.3.3 Other Candidates

Since the first postulation of dark matter, numerous theories and candidates have been proposed to explain the phenomena of dark matter. While the WIMP is the particle candidate used to motivate most direct dark matter searches, also other theories provide convincing arguments to pursue their experimental verification. A review on this topic can be found in [26]. In addition, two of the most attractive theories/candidates are shortly mentioned in the following.

One of the favored dark matter candidates of the last years is the axion. Initially postulated to answer the question why CP violation only occur for weak interactions, it is the natural dark matter candidate as it only interacts with baryonic matter via the weak force [27]. Axions with a mass between $10^{-6} - 10^{-3}\,\mathrm{eV}$ would be able to contribute significantly to the observed dark matter presence in our Universe [26]. For experimentalists, this dark matter candidate is interesting because the axion is accessible via its coupling to photons via the Primakoff effect [28].

Dark matter searches below the Lee-Weinberg boundcan be motivated by asymmetric dark matter models (reviews on this topic can be found in [29] [30]), by postulating an asymmetry between dark matter and its antimatter. The models assume that this asymmetry is closely linked to the baryon asymmetry observed in the early Universe and that separate freeze-out mechanism exists for the two sectors. Using the observed asymmetry between dark matter and baryonic matter, a dark matter mass of $5\,\mathrm{GeV/c^2}$ (i.e. 5 times m_p) is predicted. Further assumptions allow to motivate dark matter masses in the range between $0.1\,\mathrm{GeV/c^2}$ and $10\,\mathrm{GeV/c^2}$ [30]. For the experiments aiming at the

direct detection of dark matter, these particles are expected to induce an event signature which is indistinguishable from WIMP dark matter because the interaction is assumed to take place via the exchange of heavy dark mediators (i.e. point-like interaction).

1.4 Direct Detection of WIMP Dark Matter

In the following, it is assumed that the dark matter searches mentioned aim for the detection of WIMPs or dark matter candidates interacting in a similar way. Therefore, the terms "dark matteränd "WIMPäre assumed to have the same meaning.

The existence for dark matter can be probed using three different experimental approaches:

- Production of dark matter at colliders able to reach very high energies (e.g. LHC).
- Indirect detection of dark matter via the measurement of secondary particles created during the annihilation of dark matter.
- Direct detection of dark matter via the measurement of its interaction with baryonic matter.

For the production as well as for the indirect detection of dark matter a set of model-dependent assumptions have to be made to set constrains the on nature of dark matter. Therefore, the direct detection of dark matter is considered as more straight forward approach, because only a reduced set of assumptions is necessary to explain a positive signal. In the following, these basic assumptions and concepts for direct detection experiments are explained.

1.4.1 Dark Matter in our Galaxy

The Earth is positioned in a spiral galaxy for which the existence of a dark matter halo is expected (see section 1.1.1). For the direct detection of dark matter, the knowledge of the local dark matter density and the velocity distribution of dark matter is of importance as it affects the expected interaction rate in the detectors.

Over the last years, the dark matter density profile of our galaxy has been investigated using different methods [31]. The published results show a large variance reporting values for the local dark matter density ρ_χ between $0.20 - 0.56\,\mathrm{GeV/c^2cm^{-3}}$. To allow a comparison, all experiments aiming for the direct detection of dark matter agreed on using a common local dark matter density of $\rho_\chi = 0.3\,\mathrm{GeV/c^2cm^{-3}}$.

A common approach is also chosen for the velocity distribution of dark matter. Under the assumption that dark matter was thermally produced, a Maxwell-Boltzmann distribution is used to describe the velocity distribution of dark matter in the galactic rest frame. Using the average velocity of the Sun around the galactic center, the peak of the Maxwell-Boltzmann distribution is set to be 220 km/s [32]. Due to the movement of the earth around the Sun, an additional annual modulation of $\pm 30\,\mathrm{km/s}$ is expected for the

peak of the velocity distribution. Therefore, the measurement of an annual modulation of the dark matter interaction rate is widely considered as the ßmoking gunßignature.

In addition, the rotation of the earth around itself is expected to induce a daily modulation to the dark matter signal. The effect of this modulation is expected to affect the expected dark matter rate on a permille level, i.e. beyond the current experimental reach [33].

1.4.2 Expected Signal Properties

Based on the properties defined for WIMP dark matter (see section 1.3.1), certain characteristics can be assumed for events which are caused by a WIMP interacting in a detector [23].

Direct detection through elastic scattering on nuclei is considered the most relevant for the direct detection of dark matter. This allows to reject certain backgrounds if discrimination for different interaction types is achieved (i.e. nuclear recoils vs. electron recoils).

Compared to neutron interactions, which interact with the atomic nucleus the same way as it is expected for dark matter, the assumed cross section of dark matter interactions is small. Therefore, only events with signal multiplicity of 1 (i.e. single scatters) are accepted as valid candidates for dark matter interactions.

In case of a positive signal caused by dark matter interactions, additional signal features can be expected. As mentioned before, an annual modulation of a dark matter signal is expected due to the movement of the Earth in our solar system. In addition, a target dependent interaction rate is expected because of the material dependence of the dark matter-nucleus cross section and the kinematics. Thus, for multi-element targets, the analysis of the observed signal rate for the individual nuclei allows to isolate and confirm a possible dark matter signal.

In experiments providing a directional sensitivity, the information of the direction can be additionally used to identify the daily and annual modulation of the signal. Though, a relative large interaction rate is necessary to perform a rate analysis with a good precision. Currently, no experiment is able to provide a directional sensitivity.

1.4.3 Differential Interaction Rate

The interaction rate R in a certain target volume is calculated for dark matter as the product of the cross section σ_χ, the particle flux Φ_χ through the target and the number of available scattering partners n_N in the target:

$$R = \Phi_\chi \sigma_\chi n_N = \frac{\Phi_\chi \sigma_\chi m_d}{m_N}. \tag{1.8}$$

Writing the mass of the detector as $m_d = n_N \cdot m_N$, one can normalize the interaction rate for different target nuclei (with a mass m_N). In order to normalize the rate for different detector sizes, equation 1.8 is multiplied in the following with $1/m_d$. The flux of dark

matter Φ_χ in the detector can be written as:

$$\Phi_\chi = \frac{\rho_\chi}{m_\chi} \cdot v \tag{1.9}$$

when v is the relative velocity of the dark matter particles, ρ_χ is the local dark matter density and m_χ is the mass of the dark matter particle.

Equation 1.8 allows to give a rough estimate of the observed rate. However, since the energy dependence of flux and cross section are not reflected in equation 1.8, the differential interaction rate dR/dE_R is used to estimate the spectral shape signal caused by the dark matter interactions.

Staying in the non-relativistic regime, the energy transfered to the recoiling target nuclei E_R can be written as function of the scattering angle θ and the reduced mass $\mu_{N\chi}$ without relativistic corrections:

$$E_R = \frac{\mu_{N\chi}^2 v^2 (1 - \cos\theta)}{m_N}. \tag{1.10}$$

Under the assumption that a dark matter particle is able to transfer the maximal energy to the target nucleus (i.e. $\cos\theta = -1$ and $m_\chi = m_N \approx \mathcal{O}(10\,\mathrm{GeV/c^2})$), the detected recoil energy is expected to have maximum of 10 keV.

The differential interaction rate dR/dE_R for dark matter is calculated with:

$$\frac{dR}{dE_R} = \frac{d}{dE_R}\frac{\Phi_\chi \sigma_\chi}{m_N} = \frac{1}{m_N}\Phi_\chi \frac{d\sigma_\chi}{dE_R} = \frac{1}{m_N}\underbrace{\frac{\rho_\chi}{m_\chi}\int_{v_{min}}^{\infty} d^3v f(\overrightarrow{v}) v}_{\Phi_\chi} \frac{d\sigma_\chi(\overrightarrow{v}, E_R)}{dE_R}. \tag{1.11}$$

v_{min} is the minimal velocity a dark matter particle is allowed to have to induce a recoil energy E_R:

$$v_{min} = \sqrt{\frac{E_R m_N}{2\mu_{N\chi}^2}}. \tag{1.12}$$

The upper limit of the integral is can be infinity on a theoretical level. However, an upper limit for the velocity for a dark matter particle exists to assure that the particle is gravitationally bound in our galaxy. This escape velocity is derived to be $v_{esc} = 544\,\mathrm{km/s}$ for our galaxy [32].

For the differential cross section $d\sigma/dE_R$ the spin dependent and the spin dependent case have to be considered ($\sigma = \sigma_{SD} + \sigma_{SI}$). Depending on the target nuclei, the spin dependent contribution to the total differential cross section can be small and therefore neglected[1]. The spin independent contribution to the differential cross section can be written for the coherent scattering of dark matter off protons or neutrons [34] as:

$$\frac{d\sigma_{SI}}{dE_R} = \frac{2 m_N A^2 f^2}{\pi v^2} F^2(E_R). \tag{1.13}$$

[1]For the CRESST experiment, $CaWO_4$ is used as target. Thus, all involved nuclei carry a total spin of zero rendering the spin dependent case irrelevant.

In equation 1.13 f is introduced to quantify the coupling strength of dark matter to protons and neutrons individually while the term A^2 represents the influence of the nucleus as a whole on the coherent scattering process (i.e. linear addition of all scattering amplitudes). Due to the A^2 term, the use of heavy nuclei is favorable for dark matter searches. The nuclear form factor $F(E_R)$ describes the energy dependent coherence loss for heavy nuclei which reduces the energy transfer at higher recoil energies (more information can be found in [35]). While for light nuclei a precise description for the form factor is available, the form factors for heavy nuclei are only estimated. The most common parametrization used in the field of dark matter searches is is the one introduced by Helm [36].

By using $E_{R,max}(v) = 2v^2\mu_{N\chi}^2/m_N$ to estimate the maximum energy a particle can transfer to a nucleus, equation 1.13 can be rewritten to:

$$\frac{d\sigma_{SI}}{dE_R} = \frac{\sigma_0}{E_{R,max}(v)}F^2(E_R) = \sigma_0 \cdot \frac{m_N}{2v^2\mu_{N\chi}^2}F^2(E_R). \tag{1.14}$$

to describe the spin independent and point-like cross section for WIMP-nucleon scattering. The introduced cross section σ_0 is strongly dependent on the target nucleus. Therefore, a normalization for different target nuclei is required to compare different experiments. The normalized, target independent WIMP nucleon cross section σ_{WN} is defined according to [37] with (m_p is the mass of a proton):

$$\sigma_{WN} = \left(\frac{1 + m_\chi/m_N}{1 + m_\chi/m_p}\right)^2 \frac{\sigma_0}{A^2}. \tag{1.15}$$

Rewriting equation 1.11 using the derived parameters results in:

$$\frac{dR}{dE_R} = \frac{\rho_\chi}{2m_\chi\mu_{N\chi}^2}\sigma_0 F^2(E_R)\int_{v_{min}}^{\infty} d^3v \frac{f(\overrightarrow{v})}{v}. \tag{1.16}$$

The evaluation of the integral requires the knowledge of the velocity distribution $f(\overrightarrow{v})$. As mentioned before, a Maxwell-Boltzmann distribution is used for describing this quantity:

$$f(\overrightarrow{v}) = C\left(\frac{3}{2\pi w^2}\right)^{3/2} \exp\left(-\frac{3v^2}{2w^2}\right). \tag{1.17}$$

By analyzing $f(\overrightarrow{v})$ with the correct astrophysical input parameters, the root mean square w of the distribution is derived to be 270 km/s while the escape velocity is currently defined to be $v_{esc} = 544$ km/s [32].

1.4.4 Differential Count Rate of current Dark Matter Experiments

In figure 1.4, the expected recoil spectra are shown for the currently used target materials in direct detection experiments for different dark matter masses ($m_\chi = 60\,\mathrm{GeV/c^2}$ and $m_\chi = 10\,\mathrm{GeV/c^2}$), assuming of a dark matter cross section of $\sigma_0 = 1 \cdot 10^{-46}\,\mathrm{cm}^{-2}$.

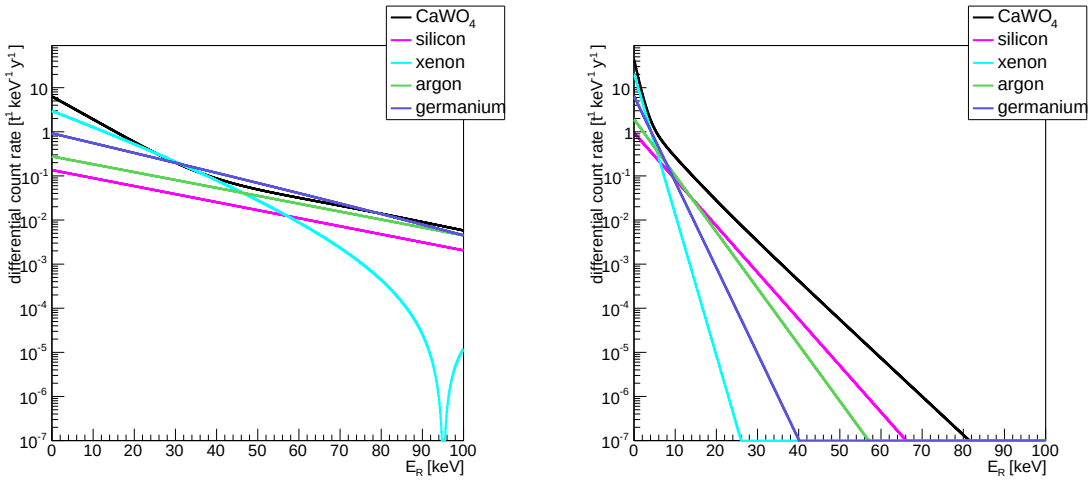

(a) Recoil spectra for $m_\chi = 60\,\mathrm{GeV/c^2}$ (b) Recoil spectra for $m_\chi = 10\,\mathrm{GeV/c^2}$

Abbildung 1.4: Calculated differential count rate for currently used target materials in direct detection experiments.

In figure 1.4 the influence of the different input parameters on the differential count rate is illustrated. The differential rate for heavy target nuclei exceeds the one for lighter nuclei because of $dR/dE_R \propto A^2$. Furthermore, the influence of the dark matter mass on the kinematics of the scattering process is shown. For light dark matter particles the energy transfer on heavy nuclei is smaller, which shifts the induced recoil spectrum to lower values. In comparison, light nuclei experience a larger energy transfer which results in larger differential count rate at higher recoil energies. Therefore, light target nuclei are able to contribute significantly to the total count rate although heavy nuclei have a larger cross section. Towards larger recoil energies, the influence of the nuclear form factor becomes visible in the depicted spectra since for heavy nuclei, the differential count rate is generally suppressed. In addition, local minima arise because of the presence of diffraction maxima in the Helm form factors as it is visible for xenon. The position of the first minimum depends on the mass of the target nucleus and is shifted towards smaller energies for heavy nuclei.

The influence of the detection threshold on the total rate (i.e. the integral over the accessible spectrum) observed in an experiment can be motivated from figure 1.4, too. Experiments with small detection thresholds are able to probe the low energy region of the spectrum in which the differential count rate rises exponentially. The effect is enhanced for light dark matter searches since only experiments providing a sufficiently low detection threshold are able to probe a region of the spectrum in which a significant signal rate is expected.

Since this thesis is written in the scope of the CRESST experiment which uses $CaWO_4$ as target, the differential interaction rate for this material is shown in figure 1.5 including the respective contributions of the individual nuclei. The black solid lines showing the total differential count rate of $CaWO_4$ are identical in the figures 1.4 and 1.5 for the respective dark matter masses m_χ.

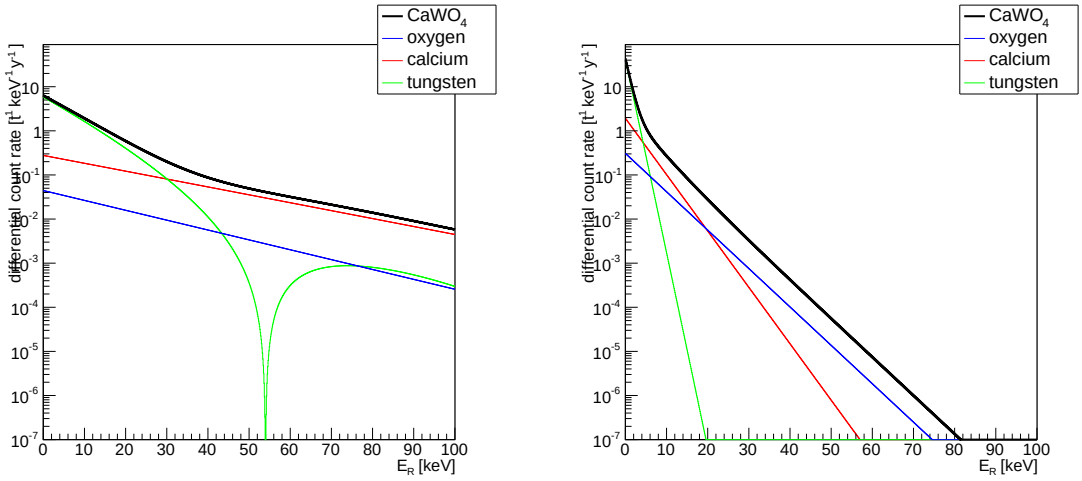

(a) Recoil spectra for $m_\chi = 60\,\mathrm{GeV/c^2}$ (b) Recoil spectra for $m_\chi = 10\,\mathrm{GeV/c^2}$

Abbildung 1.5: Calculated differential count rate for $CaWO_4$. See text below for more information.

In a multi-element target like $CaWO_4$, each nucleus contributes according to its abundance in the target to the total differential count rate. Each of the nuclei show the expected features in the calculated spectrum (i.e. A^2 dependence, kinematics, form factor). Tungsten is a heavy nucleus which provides a higher counter rate, however, the kinematics of the interaction process shifts the expected events to smaller recoil energies. Additionally, the influence of the form factor on the cross section of tungsten reduces the signal contribution further at larger recoil energies. Because of this, the light nuclei oxygen and calcium are able to contribute significantly to the total differential rate for larger recoil energies. These effects are enhanced for dark matter particles with smaller mass. Since light as well as medium and heavy nuclei are present, $CaWO_4$ is able to provide a relative large differential count rate over the full recoil energy range independent of the assumed dark matter mass. Therefore, the use of this material as target can be considered as advantageous for the CRESST experiment if compared to other experiments which rely on a single target nucleus.

2 CRESST Experimental Setup

The elusive character of dark matter has two gernal implications for a direct dark matter searches: The expected interaction rate with baryonic matter and the energy transfer in case of an interaction is very small (see chapter 1). These two constrains imply that all experiments aiming at the direct detection of dark matter face the same experimental requirements:

- The elastic scattering process of dark matter with a target nucleus is expected to cause an energy transfer of $\mathcal{O}(10\,\mathrm{keV})$. To be able to detect energies in this range, highly sensitive particle detectors are needed. In the case of CRESST, the detectors are cryogenic calorimeters which are operated in low temperature environment to reach the required sensitivity.

- Because of the small interaction rate of dark matter with baryonic matter, the establishment of a low background environment is necessary. Otherwise, the small number of dark matter interactions in the target is overwhelmed and covered by background interactions. Therefore, the detectors are operated in a massively shielded setup and are equipped with an active, particle sensitive veto mechanism for background rejection. In addition, the detectors have to be large in size and/or in number to achieve large exposures within a reasonable time scale (i.e. $\mathcal{O}(1\,\mathrm{y})$).

The CRESST experiment addresses these requirements by using the setup depicted in figure 2.1. The considerations leading to this setup are explained in the following sections.

2.1 Low Temperature Detectors

The CRESST experiment uses cryogenic calorimeters to measure the energy transfer occurring during a particle interaction in an absorber volume. Energy depositions are measured as temperature change of the absorber using an appropriate, highly sensitive thermometer.

A simplified model of cryogenic calorimeter consist of three components [38]. First, an absorber with a given heat capacity C in which the particle interaction takes place, i.e. in which the energy ΔE is deposited. Second, a thermometer connected thermally to the absorber which measures the temperature change $\Delta T = \Delta E/C$ and, third, the thermal link G to the heat bath with temperature T_{eq} that enables the system to return to thermal equilibrium with the temperature T_{eq} with the time constant $\tau = C/G$. A scheme of a cryogenic detector is shown in figure 2.2.

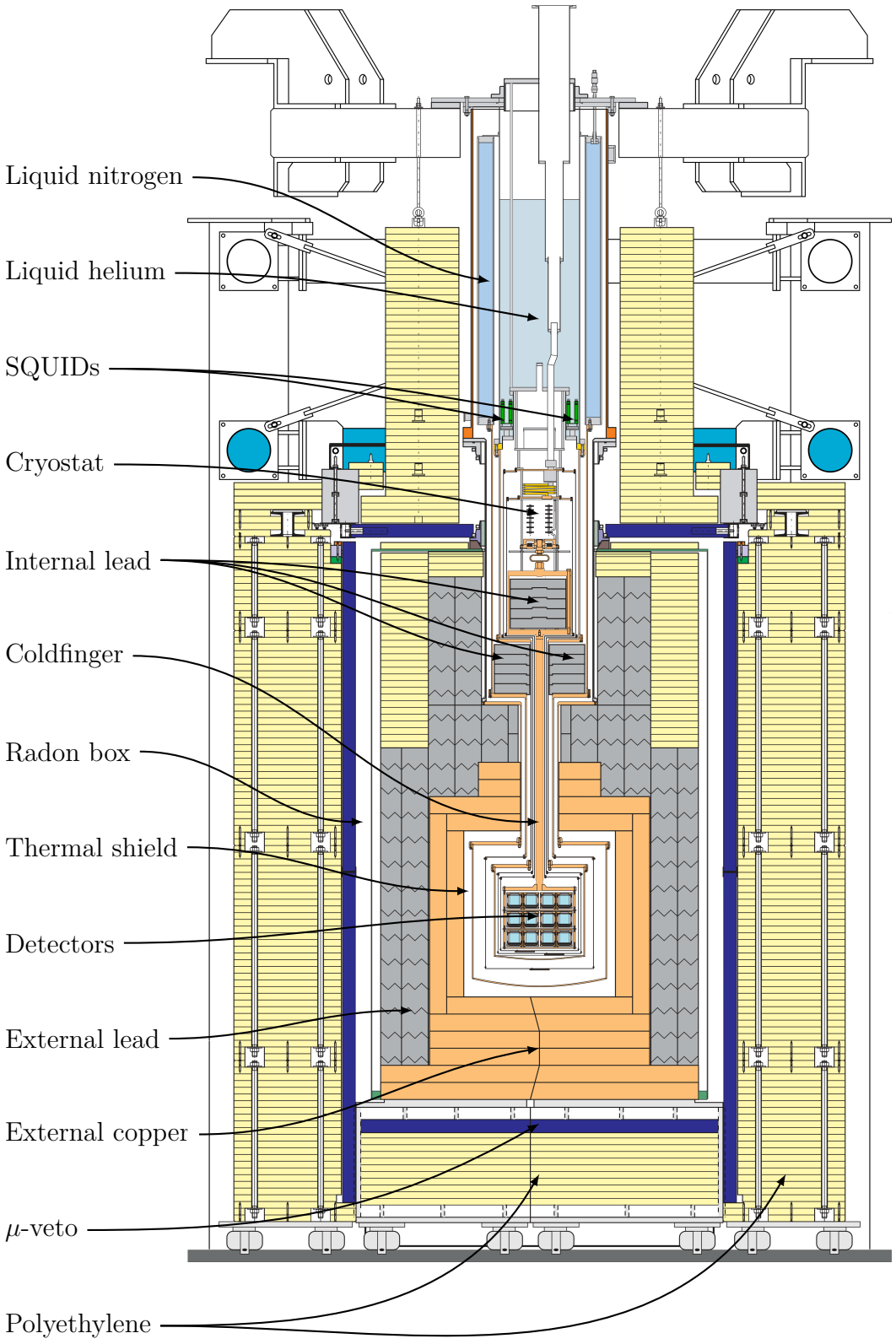

Abbildung 2.1: Technical drawing of the CRESST setup with labeling for the individual components (adapted from [22]).

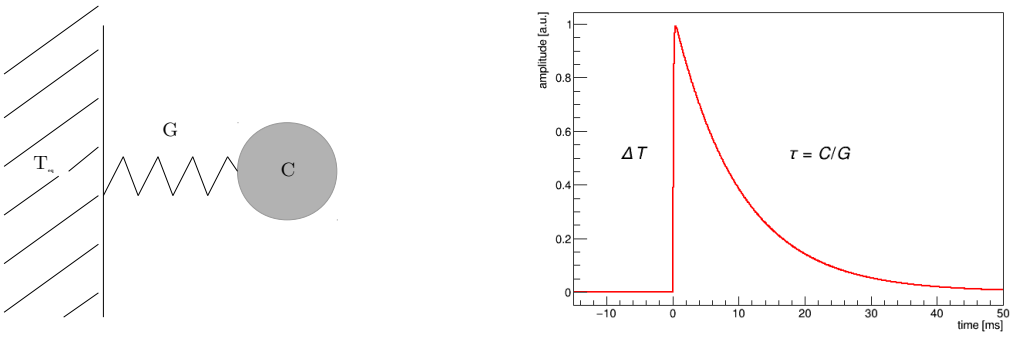

Abbildung 2.2: Scheme of a calorimetric temperature measurement is given on the left. The expected temperature change as a function of the time is given on the right. The temperature rise $\Delta T = \Delta E/C$ decays with a time constant of $\tau = C/G$ via thermal link with a thermal conductance of G. Picture adapted from reference [38].

The three parameters C, G and T_{eq} describe a very simplified version of a cryogenic calorimeter. Nevertheless, the model allows to motivate the operation of such a device at the lowest possible temperature since the following physical properties can be exploited:

- **Small heat capacity:** The heat capacity C of dielectric materials, the usual choice for targets, scales cubic with the temperature $C \rightarrow T^3$. Thus, the temperature change for a given energy deposition is increased towards lower temperatures.
- **Low thermal noise:** Cryogenic detectors are in thermal equilibrium with the heat bath unless a particle interaction disturbs the system. Still, random energy flow between the thermal bath and the absorber introduce a change of the energy content of the calorimeter (i.e. thermal noise ΔE). For low temperatures, though, the thermal noise is $\langle \Delta E^2 \rangle = k_B T^2 C$ which implies that the thermal noise is reduced towards lower temperatures. In addition to the thermal fluctuation noise, the current induced Johnson noise of resistors adds with $\sqrt{4k_b T R}$ (spectral density$[1/\sqrt{f}]$) to the total noise. Also this noise contribution is reduced towards lower temperatures.

In summary, the performance of cryogenic calorimeters is improved by lowering the operation temperature of the devices since the temperature signal induced by an energy deposition is increased while the thermal noise is simultaneously reduced.

In order to exploit the advantages of a low operation temperature, the CRESST experiment aims for an operation temperature of the detectors which is smaller than 20 mK. To reach these temperatures, the detectors are operated inside a ^{3}He-^{4}He dilution cryostat which defines the depicted setup structure shown in figure 2.1. Using different cooling stages, the coldest temperature is reached at mixing chamber of the cryostat which is directly linked to the detector carousel. At the mixing chamber, temperatures of < 6 mK can be reached which allows to operate the detectors in the desired temperature window.

2.2 Low Background Environment

Direct dark matter searches are usually limited by the presence of backgrounds. These can be introduced by environmental radioactivity, by particle interactions induced by cosmic rays and by the intrinsic contamination of the setup. To avoid these backgrounds to cause a signal in the detectors, the establishment of a low background environment is crucial. The techniques to achieve such a condition for the CRESST experiment are explained in the following section.

2.2.1 Muon Background

The primary cosmic radiation reaching the Earth's atmosphere consists mainly of protons ($\approx 87\,\%$). These protons interact with the nuclei being present in the upper atmosphere creating dominantly pions. The ensuing decay of the short living pions creates dominantly muons which are able to penetrate the Earth's surface. At sea level the integrated muon flux above an energy of 1 GeV is $70\,m^{-2}s^{-1}sr^{-1}$, while the flux of other components of the cosmic radiation is reduced to negligible level by the presence of the atmosphere [39]. To shield the detectors against muons created by the cosmic radiation, the CRESST experiment is located in the underground laboratory of *Laboratori Nazionali del Gran Sasso* (LNGS) in the Italian Abruzzi. Protected by 1400 m of rock (3800 m.w.e), the cosmic muon flux is reduced by 5 to 6 magnitudes compared to a shallow experimental site [40].

Muons do not only contribute to the backgrounds observed in the detectors by directly depositing energy therein. By interacting with surrounding materials, they are able to produce secondary particles which can reach the detectors and cause a signal. Particularly dangerous for dark matter experiments are neutron emissions and spallation processes in the vicinity of the detectors because neutron interactions are able to cause a detector response which is indistinguishable from a dark matter signal.

In order to tag events which are correlated with the penetration of the setup by muons, the cryostat is almost completely surrounded by a muon veto system. 26 plastic scintillator plates read out with photomultipliers surround the cryostat and cover 98.6% of the solid angle seen by the detectors [41]. A full coverage of the experimental space cannot be achieved due to the presence of an opening trough which the cryostat is fed into the shielding (see figure 2.1).

In case the muon veto system is triggered by an interaction, a predefined time window is vetoed. Hence, events occurring in this time window are not accepted.

More detailed information on the muon veto system of the CRESST experiment is found in reference [41].

2.2.2 Gamma Background

The products of the muon interactions in the surrounding rock walls of the lab as well as the contamination of the experimental setup with radioactive isotopes requires to shield the detector carousel against β/γ-backgrounds. For the experimental hall A of the LNGS (where the CRESST experiment is located), a total γ-flux of $0.25\,\mathrm{cm}^{-2}\mathrm{s}^{-1}$ is reported in the energy range between 7 and 2734.2 keV [42]. The dominant fraction of this background rate is related to the natural decay chains of ^{238}U and ^{232}Th in the surrounding rock of the underground laboratory.

To reduce the background rate introduced by external β/γ-radiation, the detectors are surrounded in all directions by at least 20 cm of low background lead (total mass $\approx 24\,\mathrm{t}$, see figure 2.1). Lead is chosen for shielding purposes because it provides a high stopping power for γ radiation. However, the usage of standard lead introduces a large contamination with ^{210}Pb to the setup which requires an inner copper shielding structure to reduce the influence of this background source (see figure 2.1). Copper can be produced in high quality and with low internal radioactive contamination. Thus, in each direction at least 14 cm of copper are mounted around the detector carousel. Additionally, all support structures in the vicinity of the detector carousel are produced of copper. This avoids the introduction of further radioactive contaminations close to the detectors.

2.2.3 Neutron Background

Neutrons can be generated by muon induced spallation in the surrounding rock and in the shielding as well as by spontaneous fission and (α,n)-reactions due to the natural radioactivity of the rock and shielding. Since their experimental signature in a dark matter experiment is expected to be similar to dark matter interactions (i.e. a nuclear recoil in the target), neutrons are a particularly dangerous source of background.

In order to prevent neutron interactions in the target, the CRESST cryostat is surrounded with 10 t of polyethylene which provides at least 40 cm of shielding in any direction (see figure 2.1) [43] . Polyethylene consists primarily of hydrogen which effectively moderates neutrons.Neutrons entering the experimental setup are intended to be stopped before reaching the detectors. If a complete moderation is not achieved, the shielding is expected to moderate the neutrons to an energy below the threshold of the detectors.

Most of the polyethylene is located around the lead and copper structures. Thus, neutrons created in the inner shielding are not prevented from reaching the detectors if no additional neutron shielding close to the detector carousel is provided. Therefore, the detector carousel itself is equipped with an additional polyethylene shield which reduces the expected neutron background reaching the detectors by one order of magnitude [43].

2.3 CRESST-II Detectors

The passive shielding efforts are able to reduce the total background rate seen by the detectors significantly. The remaining background sources originate dominantly from the intrinsic contaminations of the detectors. To suppress this source of background, the detectors have to provide an active particle identification system which is able to distinguish between different interaction types. In CRESST-II detectors, this is achieved by using detectors based on the phonon-lighttechnique. In the following section, the standard version of a CRESST-II detector module is introduced and explained.

2.3.1 General Working Principle

As the name suggests, detectors of this type consist of a phonon and light detector which are, in the case of CRESST-II, both cryogenic particle detectors. As target, scintillating crystals are used. In case of an energy deposition in this target crystal, a temperature rise is induced which is measured using an appropriate low temperature thermometer (*phonon channel*"[1]). In addition, part of the energy deposition is simultaneously emitted by the target crystal as scintillation light. Using a dedicated light detector which is mounted in close proximity and in direct line of sight to the target crystal, the scintillation light is measured (*light channel*"). The light detector is operated as individual cryogenic calorimeter in which the created scintillation light is detected as temperature rise of the light absorber.

The combination of both detectors (phonon and light channel) form a detector module. Both absorbers are located in a highly reflective detector housing to enhance the collection of emitted photons.

The thermometers coupled to the respective absorbers are transition edge sensors (TES). The TES are thermally linked to the heat bath while the absorbers are dominantly linked to the respective TES. Figure 2.3a shows schematically the components of a CRESST-II detector module. In addition, a photograph of a opened CRESST-II detector module is shown in figure 2.3b.

Most inorganic scintillators show an interaction dependent scintillation efficiency. Therefore, the ratio of the signals measured in light and phonon channel can be used to determine the nature of the interaction. In particular, electron recoils, induced by β/γ-radiation and nuclear recoils, induced by neutron interactions or dark matter, show a characteristic detector response which is exploited to achieve an active background discrimination on an event-by-event basis.

[1] The designation as phonon channelïs motivated by the fact that the temperature rise of the attached thermometer is caused by an excited phonon population in the target crystal.

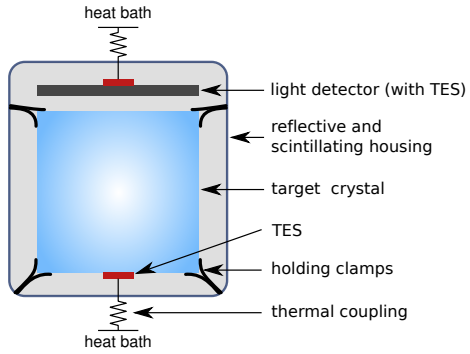

(a) CRESST-II detector module (scheme)

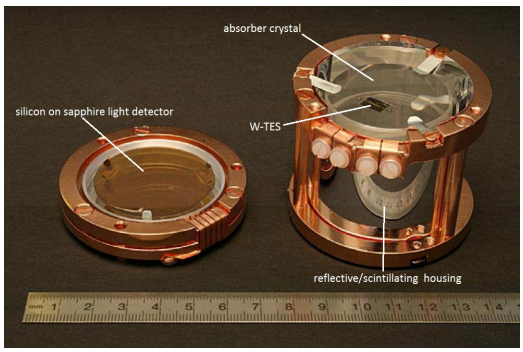

(b) CRESST-II detector module (photograph)

Abbildung 2.3: The CRESST-II detector module. The combination of a scintillating $CaWO_4$ target crystal and a spatially separated light detector establish a two channel readout system. Energy depositions in the absorbers are measured as temperature using a dedicated thermometer. The detectors are surrounded by scintillating and reflective foil (VM2002©).

2.3.2 Target Crystal ($CaWO_4$)

The CRESST-II experiment uses scintillating $CaWO_4$ single crystals as target material. $CaWO_4$ is a multi element target since three different types of nuclei are present (O, Ca, W) in the crystals.

Using the Czochralski-method, high quality single crystals are grown at temperatures of ≈1600 °C from the melt of ultra pure material [44]. Because of the inherent cleaning mechanism of the crystal growth process, intrinsic backgrounds can be significantly reduced by this production procedure. A segregation coefficient of up to 0.12 is achieved for certain radioactive isotopes (^{226}Ra) [45]. Still, intrinsic radioactive contaminations of the target crystals remain the dominant background source for CRESST-II detectors when operated in the main setup at Gran Sasso [45].

For CRESST-II, the grown crystals are machined to cylindrically shaped absorbers having the dimensions 40 mm x 40 mm (diameter x height). This results to a total absorber mass of ≈ 300 g. All surfaces, except the surface facing the light detector, are polished to optical quality to allow large phonon life times and a good light collection efficiency in the detector module.

$CaWO_4$ is an inorganic, excitonic scintillator in which the WO_4^{2-} complex serves as scintillation center [46] [47]. The scintillation spectrum peaks usually at a wavelength of (420±40) nm/(2.9±0.29) eV which is within the visible spectrum of a human eye [44]. Thus, the scintillation feature of the target crystals can be observed as blue emission if the crystal is excited with UV light (see figure 2.4).

The scintillation efficiency of a scintillator is defined as the fraction of energy which is transformed for a given energy into scintillation light. The scintillation efficiency of $CaWO_4$ at mK temperatures is reported to be 8.3% [47]. Measurements confirm that the $CaWO_4$ crystals used for CRESST-II detectors have a scintillation efficiency of 8.3±0.8 %

Abbildung 2.4: Photograph of scintillating $CaWO_4$ crystals under UV light excitation. The blue emission of the scintillation spectrum peaks at $(420 \pm 30)\,\mathrm{nm}/(2.9 \pm 0.2)\,\mathrm{eV}$.

[48]. A reduced scintillation efficiency is observed for crystals with an increased number of crystal defects [44] [46] [47].

The production process of a tungsten TES requires the heating of the absorber to high temperatures (up to 600 °C) in high vacuum in order to achieve the desired transition temperature T_c and steepness (i.e. $\Delta R/\Delta T$). Unfortunately, this creates oxygen deficiencies on the surface of $CaWO_4$ which results in a reduction of the scintillation efficiency. The difference of the scintillation efficiency before and after the heating process is up to 20 % [49]. In order to avoid the exposure of the main absorber to these high temperatures, the so called composite detector design can be used. The TES is not deposited directly on the main absorber, but on a significantly smaller carrier crystal which is exposed to the production process instead [22] [50]. The carrier has the dimensions $(20\text{x}10\text{x}1)\,\mathrm{mm}^3$ and carries, as the name suggests, the thermometer for reading out the target crystal. To connected the target crystal with the carrier crystal an EPOTEK© glue spot is used.

The fact that the scintillation efficiency of $CaWO_4$ depends on the nature of an interaction allows for particle identification based on the ratio between light and phonon channel. For electron recoils induced by β/γ-radiation, the scintillation efficiency achieves the reported value of $\approx 8.3\,\%$ [47]. For α-decays as well as for nuclear recoils the scintillation efficiency is reduced according to their respective quenching factor QF_X. The quenching factor QF_X is defined as the ratio between the light signal created by a interaction caused by a particle X and an electron recoil event with the same energy [51]:

$$QF_X = \frac{E_{L,X}}{E_{L,\text{electron recoil}}} \tag{2.1}$$

Table 2.1 summarizes the quenching factors relevant for $CaWO_4$ absorbers.

interaction	QF_X
electron	100% (definition)
α-particle	0.2
oxygen	0.112±0.005
calcium	0.059±0.007
tungsten	0.017±0.005

Tabelle 2.1: Quenching factors for different particle interactions in $CaWO_4$ [51].

It is important to note that the quenching factors are generally not energy independent. Therefore, a dedicated measurement campaign was carried out by the CRESST collaboration to determine the quenching factors and their energy dependence in the energy range relevant for the experiment. More information on this topic can be found in reference [51].

2.3.3 Light Detector

The amount of created scintillation light is measured using a cryogenic calorimeter as light detector. Mounted in close proximity to the main absorber, the light collection efficiency is expected to be optimized. As light absorber, a circular shaped silicon-on-sapphire (SOS) wafer with a diameter of 40 mm and a thickness of 400 μm is used. The thermometer is directly evaporated on to the surface of the SOS wafer. Providing a better absorption probability than pure silicon, SOS wafers are the best choice as light absorber if a flat light detector geometry is chosen (measured absorption probability $\approx 85\,\%$ [52]). The standard light detector of CRESST-II detector is depicted in figure 2.3b on the left hand side.

2.3.4 Detector Housing

The housing of a detector module provides the necessary structures to keep the target crystal and the light absorber in position. The mechanical integrity of a detector module is assured by a copper structure. To establish a connection between this structure and the absorbers, bronze clamps are used. Bronze provides the needed material elasticity at low temperature to avoid events caused by stress relaxation [53]. Additionally, bronze is available as clean material. [43]

The dominant fraction of the detector housing is lined by scintillating and reflective foil (VM2002) [54]. The main goals of such a detector housing are:

1. **Enhancement of the light collection:** After an energy deposition in the target crystal, the generated scintillation light is emitted with isotropically. In order to collect photons which initially have a direction not pointing to the light detector, the remaining surfaces of the detector housing are designed highly reflective. The foil used for lining the detector housing provides a reflectivity of more than 99% for the relevant wavelengths around 420 nm [44].

2. **Tagging of events that deposit energy in the detector surrounding:** The ratio between light and phonon signal allows an unambiguous particle identification as long the full energy of a particle interaction is deposited in the target crystal. This condition is not fulfilled for events with external origin (i.e. surface α-decays, external β-radiation) for which part of the energy can be deposited in the detector surrounding. In order to identify events of this type, a scintillating detector housing is needed since the energy deposited therein is translated to an additional light signal. Using the sum of scintillation signal created in the detector housing and in the target crystal an identification of these events becomes possible.

2.3.5 Transition Edge Sensors

The CRESST experiment uses transition edge sensors (TES) as thermometers. A TES is a superconducting metal (thin) film which is deposited on to the surface of the absorber (i.e. carrier crystal, SOS light absorber). Operated in the steep phase transition between the normal conducting and superconducting state, small temperature changes($\mathcal{O}(1\,\mu\mathrm{K})$) are converted in a relatively large resistance changes ($\mathcal{O}(1\,\mathrm{m}\Omega)$) (see figure 2.5).

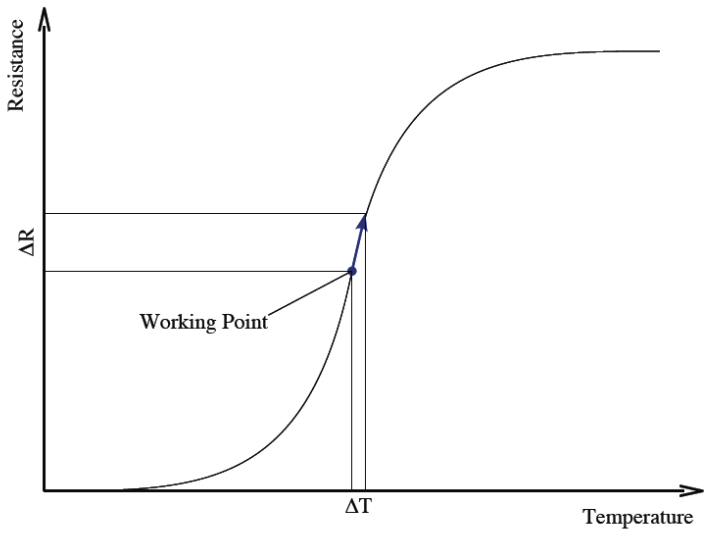

Abbildung 2.5: Schematic view of the TES resistance as a function of the temperature. In the steep transition between the normal conducting and superconducting phase small temperature changes lead to large resistance changes.

The TES used in CRESST are based on tungsten thin films. TES made of this material show a transition temperature which is usually $< 20\,\mathrm{mK}$. The transition width is $\approx 1 - 2\,\mathrm{mK}$. To achieve TES with these properties, a well defined production procedure is necessary. Although large efforts are carried out to achieve reproducible conditions during the production process, small variations between different thermometers require an independent optimization of the operation temperature for each TES. Therefore, each

TES is equipped with an individual heater, which allows to adjust the temperature of the TES according to its transition to achieve the best sensitivity.

The heaters are also used to inject heat pulses which are intended to measure and control the operating point of the TES. By controlling the control pulse height using a feedback loop to the heater, the long term stabilization of the operation point is achieved. In addition, low energetic test pulses with defined amplitudes are injected to the TESs via the heater. These are used to extrapolate the energy calibration obtained with radioactive sources energetic enough to penetrate the detectors to the energy range relevant for dark matter searches.

2.4 Electronics

Cryogenic calorimeters using transition edge sensors as thermometer convert energy depositions of the absorber to a measurable resistance change of the TES. Although the steepness of the transition allows to translate even small temperature changes ($\mathcal{O}(1\,\mu\mathrm{K})$) into a relatively large resistance change ($\mathcal{O}(1\,\mathrm{m}\Omega)$), further signal amplification is necessary. The CRESST experiment uses SQUID based amplifier to translate the resistance changes of the TES in an amplified voltage signal.

In the following, a short introduction to the readout circuit of the TES and the data acquisition system is given. Detailed information on this topic is found in the references [22], [43] and [55].

In figure 2.6, the schematic illustration of the electronics is shown. The differently colored areas indicate the different components of the system. Three major sub components can be identified in the scheme. The first part of the electronics controls the heaters of the TES allowing their stabilization (marked in blue, see section 2.4.2). The second part of the electronics allows to apply a constant bias current to the TES in order to allow the measurement of the TES's resistance (purple). The third part converts resistance changes of the TES in an amplified voltage signal using a SQUID amplified readout system (red). Since the second and third part of the electronics are strongly connected, a combined explanation of these is found in section 2.4.1

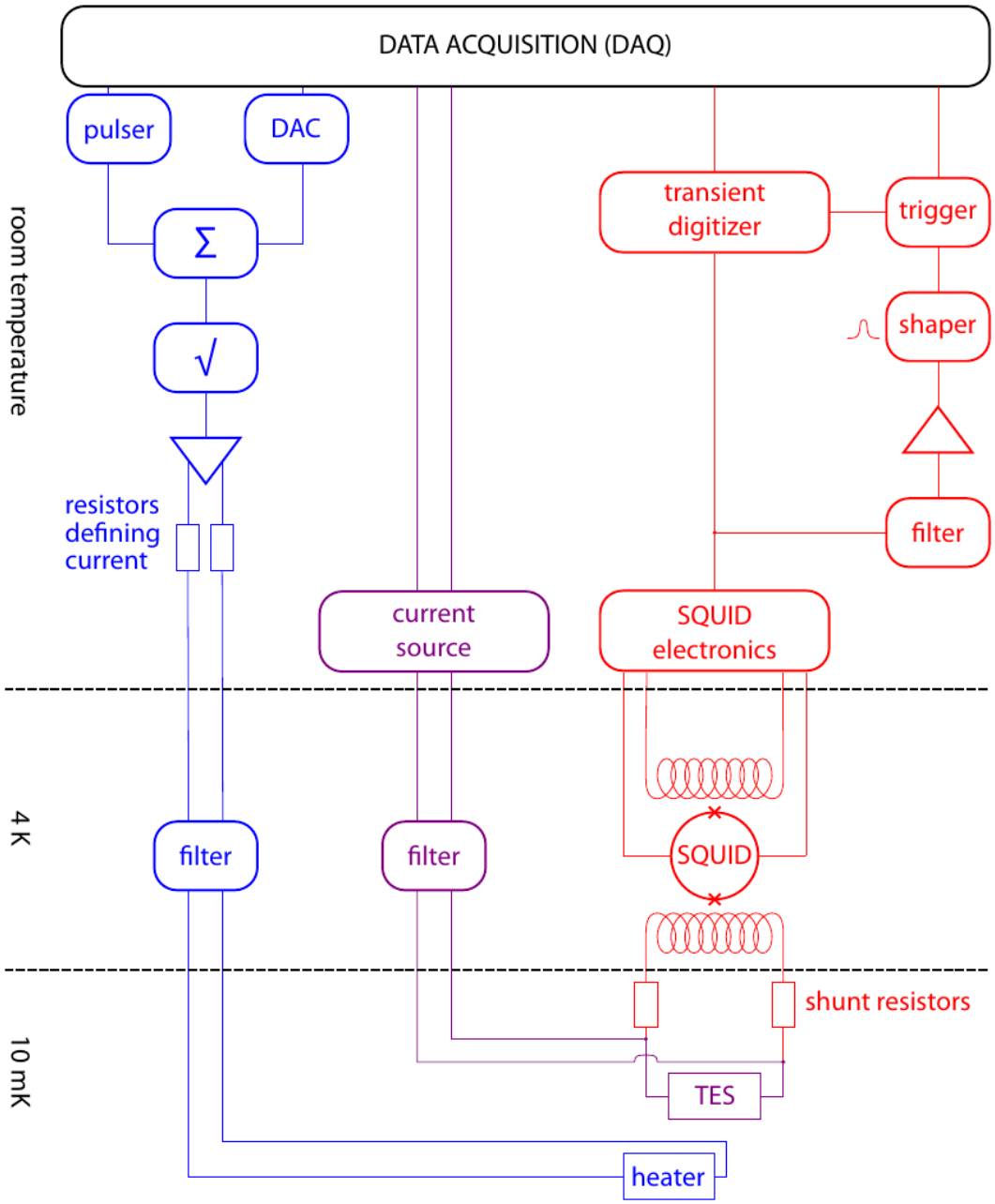

Abbildung 2.6: Schematic illustration of the CRESST electronics. Electronics related to the detector stabilization (test and control pulse system) is given in blue, electronics related to the SQUID readout system is given in red and electronics responsible for the TES biasing is indicated in purple.

2.4.1 SQUID Readout Electronics and TES Bias

Given the low resistance of the TES and the low temperature the detectors are operated at, the use of a SQUID (superconducting quantum interference device) based signal amplification is the natural choice for reading out the detectors of the CRESST experiment [56] [57]. Additionally, the low inductance of the readout circuit as well as the low input noise of SQUID amplifiers can be exploited for achieving the lowest detection thresholds.

SQUIDs are highly sensitive magnetometers which can be used to measure current changes of a circuit via the inductive/magnetic influence of an input coil on to the SQUID loop [56]. A scheme of the electronic readout circuit used for CRESST is shown in figure 2.7.

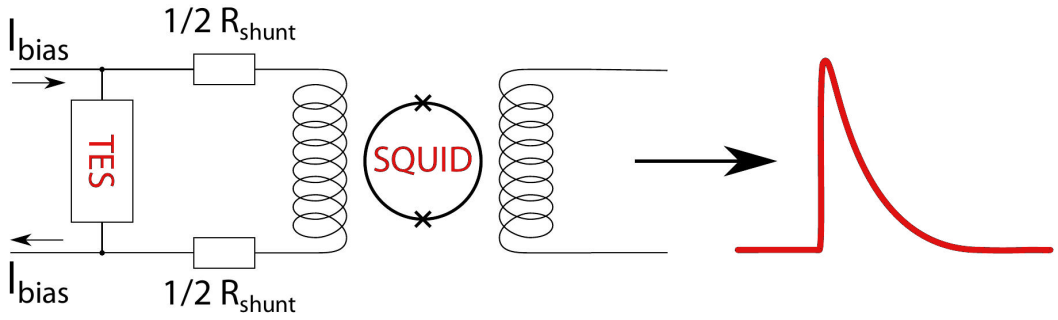

Abbildung 2.7: Scheme of the electronic readout circuit used for measuring the resistance of TES in the CRESST experiment. The TES is biased in parallel with a shunt resistance and a input coil. A SQUID translates current changes on the left side of the scheme to amplified voltage signal which is fed to the DAQ system (adapted from [43]).

To convert the resistance change of a TES into an amplified voltage signal, the TES is connected in parallel to a shunt resistance (R_S) (divided into two resistances for symmetry reasons) and the input coil of a SQUID. The TES's resistance defines the current splitting between the two arms of the circuit if a constant bias current I_{bias} is applied with an appropriate, low noise current source. Changes of the TES's resistance result in a current change in the input coil of the SQUID. Consequently, the magnetic field of the input coil changes which is detected by the SQUID loop. The SQUID system amplifies the signal and outputs a voltage signal which is fed into the DAQ system for triggering and digitalization.

2.4.2 Test and Control Pulse System

The usage of TESs as temperature sensors requires that the thermometers are operated in the narrow temperature window of the phase transition between the normal conducting state and the superconducting state of the film. Since each TES features a unique transition (e.g. T_C, steepness of the transition, normal conducting resistance), it is necessary to adjust the operating temperature individually and according to the bias current I_{bias} for each TES[2]. For this reason each TES is equipped with a independent heater which is used to change the temperature of the thermometer in respect to the heat bath provided by the cryostat. By applying a constant current to the heater, a temperature difference between the heat bath and the TES is established.

In order to operate the TESs in the same operating point over long time periods, a system to measure and control the current position in the transition is necessary. This is achieved by sending test and control pulses to the each TES on a regular time basis (see section 2.3.5). The electronic system is equipped with pulse generators which add to the constant heating power for changing the temperature of the TES particle like heater pulses.

For a detailed discussion on the test and control pulse system used for the operation and stabilization of TES, see references [23] and [55].

[2]The TES itself is heated according to the current flowing through the metal film. This effect is called ßelf-heatingänd reduces the amount of heating power which has to be provided by the electrical heater of the TES.

3 Signal Evolution in Cryogenic Calorimeters with TES Readout

The sensitivity of a cryogenic calorimeter is defined by its capability to translate an energy deposition in a temperature signal. To achieve the best performance of the readout channels, a thorough understanding of the detectors and a careful design of the absorber/thermometer system is a crucial part of the detector development process.

The calorimeters used for CRESST are devices operated in thermal equilibrium. When energy is deposited in the absorber, the steady state between the absorber and the heat bath is disturbed. An excited phonon population is created in the absorber which propagates and evolves over time. The temperature signal induced in the thermometer as a consequence of an energy deposition in the absorber is described by a semi-empirical model developed by F. Pröbst et. al. in 1995 [58]. In this chapter, an introduction to this model is given. In addition, the implications of the model on the TES design are discussed using the CRESST-II phonon and light channels as reference.

3.1 Pulse Formation in CRESST-II Detectors

3.1.1 Initial Phonon Evolution in the Absorber

In case of an energy deposition in a crystal absorber of a CRESST-II detector, high-frequency, non-thermal phonons are created. This first generation of optical phonons decays within a few ns into acoustical phonons of about half the Debye frequency ν_D of the absorber material.

$$\frac{\nu_D}{2} = \frac{k_B \Theta_D}{2h} \tag{3.1}$$

The Debye frequency of a material is defined as 3.1, where k_b and h are the Boltzmann and Planck constants respectively and Θ_D is the Debye temperature of the material[1]. This phonon population is not in equilibrium and continues to decay towards a thermalized phonon population. The decay rate of the phonons is $\propto \nu^5$ which causes that spontaneous decay of phonons is reduced at smaller phonon frequencies ν. Therefore, the scattering processes on crystal surfaces and lattice defects becomes the dominant reason for the thermalization and decay of the phonons being present in the absorber volume. In case single crystals are used as main absorbers, the density of crystal defects can be assumed to be negligible. Thus, the thermalization speed of a phonon population in an absorber is mainly defined by the number of surface scatters taking place

[1] $\Theta_{D,CaWO_4} \approx 350\,\mathrm{K}$ [59]

within a certain time. Therefore, the life time of this phonon population is related to the surface-to-volume ratio of the absorber [60].

In summary, one can state that after a fast decay of the initially phonon population, a much slower decay rate is observed. This results in a phonon population having frequency distribution which stays almost constant for $\mathcal{O}(10\,\mathrm{ms})$. During this time scale, the phonons propagate ballistically in the absorber filling the volume homogeneously. Nevertheless, the frequency of the phonons is still high enough to justify the designation non-thermalfor this population.

3.1.2 Phonon Absorption in the TES

For the next considerations, the initially created phonon population has decayed in such a way that the non-thermal phonon population being present in the absorber crystal can be assumed to be homogeneously distributed in the volume. In addition, the spectral shape of the phonon population can be considered as stable.

For the description of the absorber/TES system of CRESST-II the basic picture of a cryogenic calorimeter introduced in section 2.1 is too simplified. In reality, a model has to consider the individual subsystems of such a device. To account for these, the $CaWO_4$ crystal and the TES are included in the following considerations as individual weakly coupled thermal systems. In addition, in order to describe the thermalization processes in the TES correctly, the TES itself is divided in two subsystems i.e. the phonon and electron systems of the metal film. For a better understanding, the extended system is schematically shown in figure 3.1.

The heat bath is an heat reservoir with temperature T_b and an infinite heat capacity (not shown). The main absorber is described with the temperature T_a and the heat capacity C_a and the TES is described as two thermal subsystems which are characterized by the temperatures T_{ph} and T_e and heat capacities C_{ph} and C_e.

The initial phonon population in the main absorber has two possibilities to thermalize: By surface scattering in the absorber or by absorption in the thermometer. Longitudinal non-thermal phonons interact very efficiently with the electron system of the TES (because of the space charge associated with the density variation) and are absorbed in the metal film[2] causing a temperature rise of the latter. The resistance change of the TES reflects the temperature change of its electron system before thermal equilibrium is reestablished. The temperature level of the TES can be brought back to thermal equilibrium via its direct thermal link to the heat bath G_{eb} or by transferring the energy back to the main absorber. For the second path, an effective thermal coupling G_{ea} ($1/G_{ae} = 1/G_{ep} + 1/G_{ap}$) between the phonon system of the main absorber and the electron system of the TES is defined. Since the heat capacity of the TES's phonon system C_{ph} is negligible , the definition of an effective thermal coupling G_{ea} is justified. As a consequence of this definition, the TES can be described by the temperature T_e and the

[2]Transverse phonons involve no density changes and hence no space charge effects, therefore the interaction with electrons arises only from the magnetic field associated with the moving ions and is consequently much weaker.

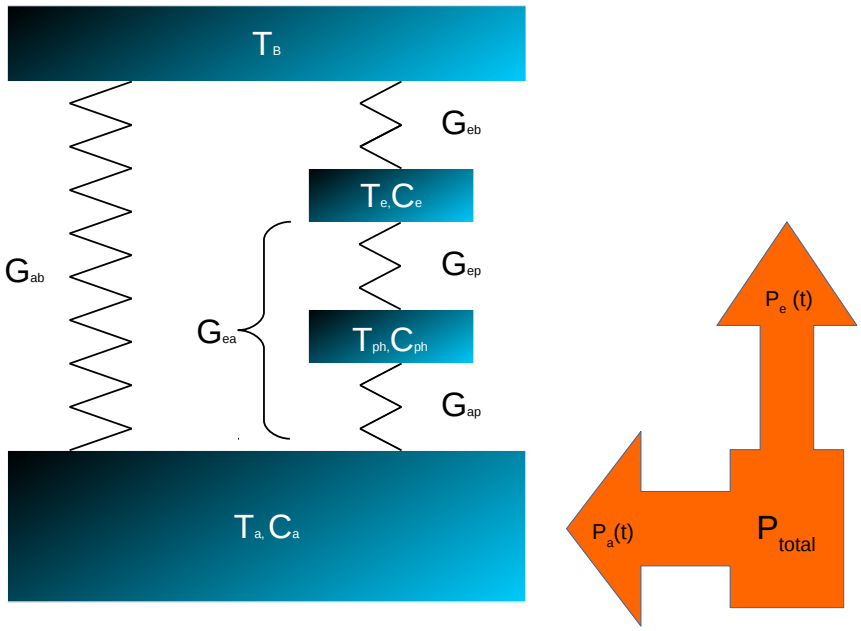

Abbildung 3.1: Schematic depiction of the TES absorber system with the respective thermal couplings and temperatures.

heat capacity C_e of its electron system. The electron-phonon coupling G_{ep} scales with $\propto T^5$ which impedes the heat transfer from the thermometer to the absorber and leads to dominant removal of the heat being present in thermometer via the direct thermal link to the heat bath using a normal conducting metal connection.

To describe quantitatively the detected signal in the TES, the power of the initial, non-thermal phonon population P_{total} is separated into a fraction that provides a power input $P_e(t)$ causing a temperature change of the electron system of the TES and a fraction that provides a power input $P_a(t)$ causing the temperature change of the absorber volume:

$$P_e(t) = \Theta(t) \cdot P_0 \cdot e^{-t/\tau_n}, \tag{3.2}$$

$$P_a(t) = \Theta(t) \cdot \frac{(1-\epsilon)}{\epsilon} \cdot P_0 \cdot e^{-t/\tau_n} \tag{3.3}$$

with:

$$P_0 = \frac{\epsilon \Delta E}{\tau_n}. \tag{3.4}$$

being the initial power input into the TES. The step function $\Theta(t)$ describes the instantaneous start of the power input, ϵ represents the fraction of non-thermal phonons thermalized in the thermometer. The life time of the non-thermal phonon population τ_n is defined by the competing decay processes in the crystal and in TES:

$$\tau_n = \left(\frac{1}{\tau_{cr}} + \frac{1}{\tau_{film}} \right)^{-1}. \tag{3.5}$$

where τ_{cr} and τ_{film} are the time constants for the thermalization in the absorber crystal and in the thermometer film respectively. The fraction ϵ that is calculated with:

$$\epsilon = \frac{\tau_{cr}}{\tau_{cr} + \tau_{film}}. \tag{3.6}$$

Using the equations 3.2-3.6 the ratio of $P_e(t)/P_a(t)$ is defined with:

$$\frac{P_e(t)}{P_a(t)} = \frac{\epsilon}{1-\epsilon} = \frac{\tau_{cr}}{\tau_{film}}. \tag{3.7}$$

From equation 3.7, one derive that $P_e(t)$ is maximized if $\tau_{film} << \tau_{cr}$ meaning that the thermalization in the TES happens much faster than in the absorber crystal. While τ_{cr} only depends on the absorber dimensions (is expected to scale as the ratio between the volume and the surface area of the absorber [60]), τ_{film} is described by equation 3.8:

$$\tau_{film} \propto \frac{2 \cdot V_A}{A_{TES}\langle v_\perp \cdot \alpha \rangle}. \tag{3.8}$$

τ_{film} is a function of the area of the TES A_{TES}, the volume of the absorber V_A, the phonon group velocity normal to the interface $v_\perp$, and the transmission probability α. Since $\langle v_\perp \cdot \alpha \rangle$ is defined by the materials involved at the interface, the only parameter influenced by the geometry of the detector is the ratio of absorber volume V_A and the area the TES covers A_{TES}.

The thermal model is described by a system coupled differential equations for the temperatures of the electrons in the TES T_e and the phonons in the absorber crystal T_c:

$$C_e \cdot \frac{T_e}{dt} + (T_e - T_c) \cdot G_{ec} + (T_e - T_b) \cdot G_{eb} = P_e(t), \tag{3.9}$$

$$C_c \cdot \frac{T_c}{dt} + (T_c - T_e) \cdot G_{ec} + (T_c - T_b) \cdot G_{cb} = P_c(t). \tag{3.10}$$

. The solution of this system with the initial conditions $T_c(0) = T_e(0) = T_b$ gives the following solution for the measured signal in the thermometer $\Delta T_e(t)$:

$$\Delta T_e(t) = \Theta(t) \cdot \left[A_n(e^{-t/\tau_n} - e^{-t/\tau_{in}}) + A_t(e^{-t/\tau_t} - e^{-t/\tau_n}) \right]. \tag{3.11}$$

Equation 3.11 is divided in two parts. A non-thermal component with the amplitude A_n which is caused by the non-thermal phonons interacting with the electron system of the TES and a thermal component with the amplitude A_t which reflects the heating of the thermal phonon population in the main absorber. τ_{in} describes the intrinsic time the thermometer needs for the thermal relaxation after an energy deposition while τ_t reflects the time scale the absorber needs to return to thermal equilibrium and τ_n still describes the life time non-thermal phonon population in the absorber.

In the following, the mentioned parameters are discussed according to reference [58] under the assumption that the heat capacity of the electron system of the TES is much

smaller than the heat capacity of the absorber ($C_e << C_A$). In this case, the amplitude of the non-thermal component A_n can be written as:

$$A_n = \frac{-\epsilon \cdot \Delta E}{C_e(1-\tau_n/\tau_{in})(1-\tau_{in}/\tau_t)}. \qquad (C_e << C_a) \tag{3.12}$$

τ_t which, as already mentioned, characterizes the thermal relaxation time of absorber, is dependent on the direct thermal coupling of the absorber to the thermal bath and by the thermal coupling which is provided via the TES and can be written as:

$$\tau_t = \frac{C_A}{G_{eb}G_{ea}/(G_{eb}+G_{ea})+G_{ab}}. \qquad (C_e << C_a) \tag{3.13}$$

and τ_{in} can be written as:

$$\tau_{in} = \frac{C_e}{G_{ea}+G_{eb}}. \qquad (C_e << C_a) \tag{3.14}$$

Both time constants can be adjusted by applying changes to the thermal link of the thermometer G_{eb} and the thermometer size which is related to G_{ea} (see reference [38] and [58] for more information).

The detectors used in the CRESST-II framework are calorimeters. Energy depositions are contained in an isolated volume and a thermometer evaluates the total energy deposit. Nevertheless, the TES can be designed to work in two different operation modes which are defined by the ratio of τ_{in}/τ_n [58].

- $\tau_{in}/\tau_n << 1 \rightarrow$ **Bolometric mode:**
  In this mode, the relaxation of the thermometer back to thermal equilibrium happens faster than the collection of the non-thermal phonons in the TES. The measured signal amplitude A_n is estimated to be $A_n \approx P_0/(G_{ae}+G_{eb})$. Hence, the measured amplitude A_n is proportional to the power absorbed and to the thermal link between the absorber and the thermometer. τ_{in} describes the rise time of the non-thermal signal while the decay time of the non-thermal component corresponds to τ_n.
  The measured signal is proportional to the power input $P_0(t)$ to the thermometer meaning the thermometer behaves like a bolometer measuring the flux of non-thermal phonons entering the thermometer. A typical pulse, including the two components of the pulse model, is shown in figure 3.2a.

- $\tau_{in}/\tau_n >> 1 \rightarrow$ **Calorimetric mode:**
  In this mode, the collection of the non-thermal phonons is faster than the thermometer is able to relax back to thermal equilibrium. The non-thermal amplitude can be approximated with $A_n < 0 \approx -\epsilon\Delta E/C_e$. τ_n defines the rise time of both signal components, while the respective decay time constants are τ_{in} and τ_t.
  The measured signal corresponds to the integrated/total energy of the non-thermal phonons entering the thermometer. Thus, the thermometer is operated like a calorimeter, measuring the full energy deposition. Figure 3.2b shows a typical pulse of thermometer operated in the calorimetric mode.

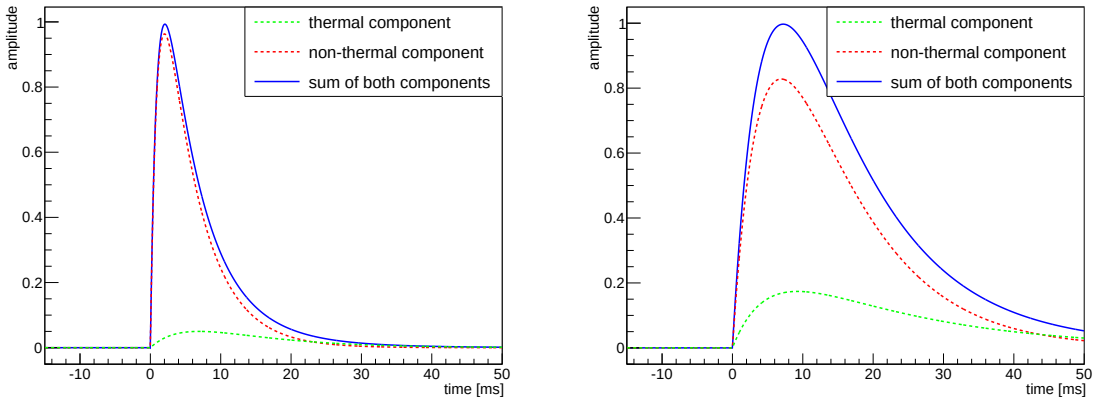

(a) Observed pulse shape of an event from a detector operated in bolometric mode.

(b) Observed pulse shape of an event from a detector operated in calorimetric mode.

Abbildung 3.2: Comparison between the measured pulse shapes of thermometers operated in bolometric or calorimetric mode.

The two operation modes differ mainly in their capability to translate a given phonon population being present in the absorber into a measurable signal within a given time scale. Generally, the calorimetric mode provides a larger measured amplitude for a certain energy and, therefore, grants access to lower recoil energies. On the other hand, the bolometric mode allows to measure larger energy depositions while reestablishing the thermal equilibrium faster than it is possible for thermometers operated in the calorimetric mode. Thus, depending on the experimental demands both operation modes can be justified.

3.2 Adjustment of Absorber-Thermometer System

The use of a certain operation mode is defined by the experimental requirements and affects the design of the absorber/TES system. In the case of CRESST-II, the experimental demands to the phonon channel and the light channel differ strongly. For example, the size of the energy depositions in the phonon channel exceed the simultaneous energy deposition in the light channel by a factor of 50. Likewise, the time constants of the measured pulse shapes are desired to have the same order of magnitude. How this task is achieved for the CRESST-II experiment is explained in the following.

3.2.1 Overview of the Detector Parameters

The characteristics of an absorber/TES system depends on the design of the individual components and their layout. Based on the model presented in section 3.1, an overview how the detector properties influence the individual pulse model parameters is given in figure 3.3.

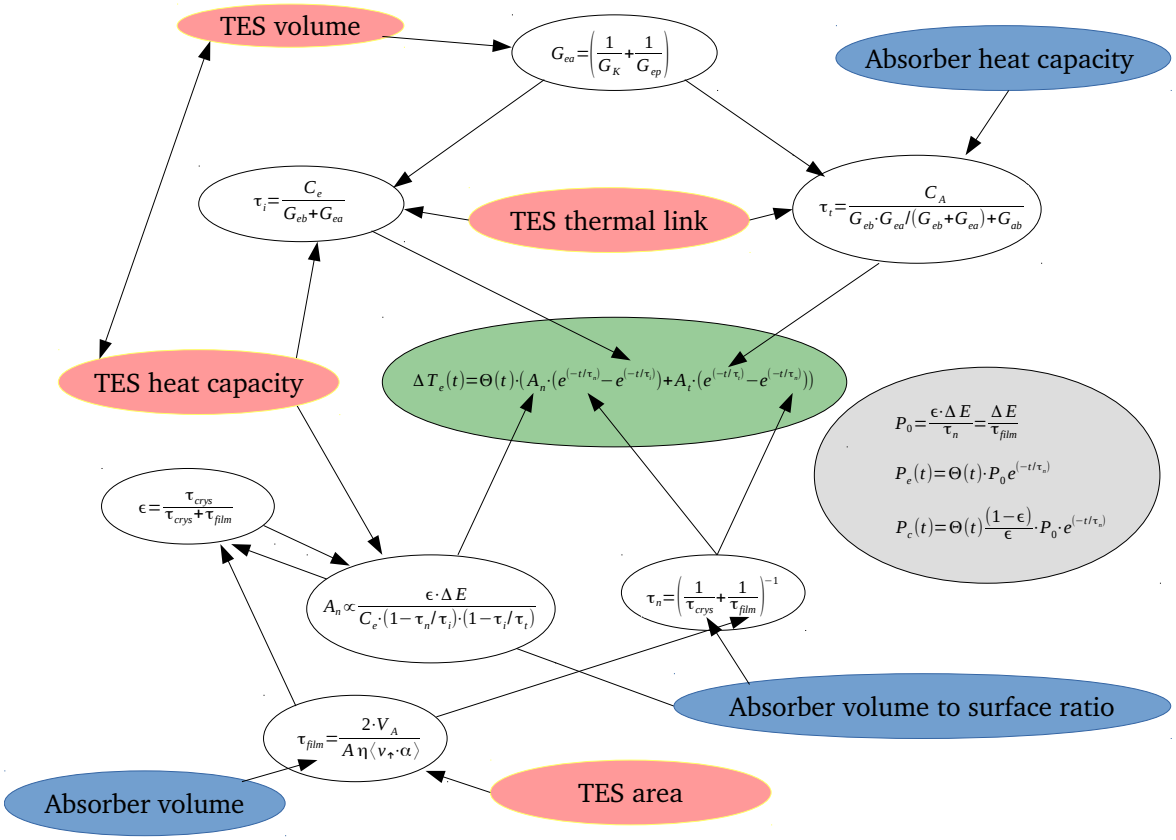

Abbildung 3.3: Overview on the parameters describing the absorber/TES system of an cryogenic particle detector according to the thermal model introduced in section 3.1. Additionally, the relations between these parameters are shown.

Figure 3.3 indicates that the behavior and sensitivity of a absorber/thermometer system can be strongly influenced the design. The pulse parameters can be influenced by the absorber properties (blue: i.e. size and geometry) and the thermometer design (red: i.e. geometry, total area, volume, thermal link). The figure also shows that many detector parameters affect more than a single pulse shape parameter. Therefore, careful adjustment of the individual input parameters is required to find the optimal setup for a certain absorber/thermometer system. This is also reflected in the current detector designs of phonon and light channel of CRESST-II which are discussed in the following subsections.

3.2.2 TES Design of the CRESST-II Phonon Channel

The phonon channel of a CRESST-II detector module is based on 300 g $CaWO_4$ target crystal in which energy depositions > 1 keV are intended to be detected. The chosen target crystal size allows to achieve the desired detection threshold without compromising on the exposure achievable within reasonable timescales (i.e. $\approx 100\,\mathrm{kg} \cdot \mathrm{d}/(\text{module and year})$).

The size of the absorber as well as its geometry (i.e. cylindrical) allow a long life time of the non-thermal phonon population in the crystal (i.e. τ_{crys}). The mean free path of the phonons in the absorber is large which allows a long natural life time of the non-thermal phonons in the $CaWO_4$ crystal [58] [60]. Therefore, the time constant τ_{crys} is long compared to the desired length of a pulse ($\mathcal{O}(10\,\mathrm{ms})$). To achieve a time constant for the non-thermal phonons in the system (τ_n) with the desired length, the TES has to cover a relative large area to reduce τ_{film} (see equation 3.5). The TES used for the CRESST-II phonon channel is equipped with a TES which covers an area of $(8\text{x}6)\,\mathrm{mm}^2$ (see figure 3.4).

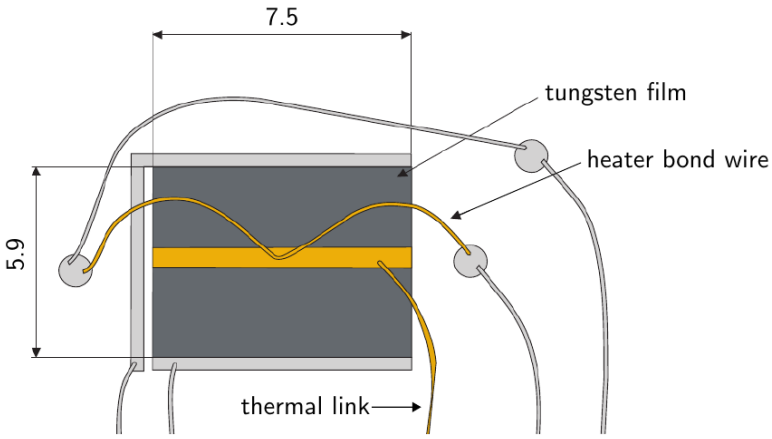

Abbildung 3.4: TES structure phonon channel of the CRESST-II detector modules [61].

Due to the thermometer design, the collection efficiency of non-thermal phonons in the TES is increased (equation 3.6). Though, an increase in signal height is not achieved because the larger collection efficiency in the TES is counterbalanced by the increased heat capacity of the thermometer film.

Because of the large collection efficiency of the thermometer and the general size of the energy depositions, the energy entry to the thermometer is relatively large which has to be considered in the design of the thermal link to the heat bath. According to the ideal model of a cryogenic calorimeter (see section 2.1) the time scale for returning to thermal equilibrium is $\tau = G/C$. Thus, in order to reestablish a thermal equilibrium within the desired time scale, the thermal link from the thermometer to the heat bath G_{eb} has to be designed sufficiently strong. Therefore, the TES of the phonon channel is connected to the heat bath using a bond wire (see figure 3.4).

As a consequence of the TES design, the detected pulse height is not maximal for the phonon channel because of the following reasons:

- Operation of the thermometer in the bolometric mode (see section 3.1.2).
- According to equation 3.12, the amplitude A_n is maximized in case ϵ is maximized. This is achieved because by reducing τ_{film}, ϵ is maximized (equation 3.6). Though, the heat capacity of the electron system of the TES C_e is scales linearly with the area the TES covers, too. Thus, the increase of the area the phonon channel's TES covers leads to:

$$\lim_{\tau_{film}\to 0} \epsilon = 1 \text{ but } A_n \propto \frac{\epsilon}{C_e}. \tag{3.15}$$

Nevertheless, both reductions of the detector performance are accepted since the detector performance is considered as sufficient for the experiment demands and since they allow to achieve the desired time constants.

3.2.3 TES Design of the CRESST-II Light Channel

The CRESST-II light detector is intended to be sensitive to the smallest amounts of scintillation light. To achieve this task, the absorber is chosen to provide a large collection area for photons while minimizing the volume. In addition, the thermometer design is adapted to the requirements.

Since the absorber is significantly smaller and the geometry is flat, the life time of the non-thermal phonon population τ_n is naturally shorter than in the large $CaWO_4$ crystal i.e. τ_{crys} is smaller. Therefore, τ_n is generally shorter in this system and has not to be fasten artificially by a large area thermometer (see argumentation for phonon channel). Hence, the use of a smaller thermometer structure to enhance the detected signal amplitude becomes possible. The used thermometer structure is shown in figure 3.5.

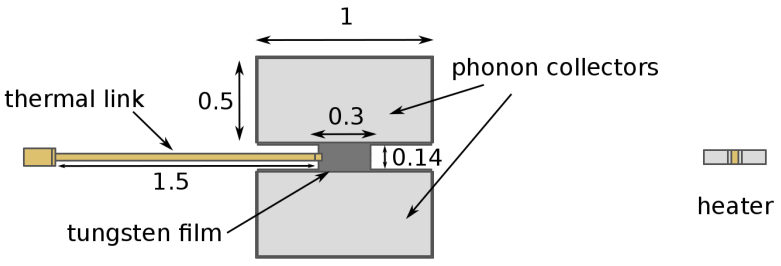

Abbildung 3.5: TES structure used for CRESST-TT light detector [61].

The area the thermometer of the light channel covers is reduced to$\approx 2\,\mathrm{mm}^2$ which results in a smaller collection efficiency of thermometer and a increased τ_{film}. This leads to a reduced ϵ (equation 3.6). On the other hand, the heat capacity of the thermometer C_e is reduced due to the smaller size of the TES. Following a similar argumentation as before for the phonon channel, the detected amplitude is enhanced with this approach.

Although the collection efficiency in the TES ϵ is reduced by a larger τ_{film}, the increase in A_n due to the reduced heat capacity C_e counterbalances this effect and leads to an larger detected amplitude.

Because of the reduced collection efficiency of the TES and the smaller power input into the TES in combination with the small capacity C_e, the thermal link of the TES G can be designed weaker than the thermal link used for the TES of the phonon channel. Also here, this design choice is motivated by $\tau = G/C$ (see section 2.1) and the fact that the total power input to the TES is smaller. By adjusting G according to the heat capacity C_e to achieve a reestablishment of the thermal equilibrium within desired time scale ($\mathcal{O}(10\,\mathrm{ms})$) the thermal link can be provided via a thin gold strip (see figure 3.5). Like this, the thermal coupling G is matched to the TES in order to achieve the operation in the calorimetric mode, meaning the heat flux into the TES is larger than the heat removal via the thermal link of the TES.

The thermometer structure of the CRESST-II light detector also includes large areas covered by superconducting aluminum films. These films are intended to serve as phonon collectors which are explained in the following section.

3.3 Phonon Collectors

According to the model introduced in section 3.1, the sensitivity of a TES for a phonon population in the main absorber is mainly defined by τ_{film} and the heat capacity of the electron system of the TES C_e. Though, a small τ_{film} in combination with a small heat capacity C_e are competing detector properties.

To achieve a better sensitivity of a TES, a reduction of its heat capacity of a TES has to be obtained while keeping the area for phonon collection constant. Two approaches can be chosen for achieving this goal.

On one hand, this can be obtained by a reduction of the thermometer thickness. By doing so the heat capacity of the TES is reduced while the area for phonon absorption can be kept constant. However, the normal conducting resistance of the thermometer is changed by the reduction of the film thickness.

The second approach to decrease the heat capacity of a thermometer without compromising the area the TES covers is the use of superconducting metal films as phonon collectors". At temperatures well below the transition temperature, the heat capacity C of the electron system of a superconducting material becomes negligible because

$$C(T) \propto e^{-1/T}. \tag{3.16}$$

Thus, the total heat heat capacity of a thermometer can be lowered by replacing parts of the tungsten TES with superconducting phonon collectors made of aluminum. Under the assumption, that the collection efficiency and the heat capacity of a TES are linearly connected, a partial replacement of the tungsten film does not change the sensitivity of the thermometer. However, any signal contribution achieved by the phonon collectors contributes to the detected signal in addition enhancing the detected signal. Thus, by

the implementation of phonon detectors the sensitivity of the TES cannot be affected negatively as long the collection efficiency in the TES ϵ is defined by τ_{crys}

In case non-thermal phonons reach and enter a phonon collector, they can contribute to the measured temperature signal via their interaction with the Cooper pairs being present in the superconducting material. High energy phonons are able to break Cooper pairs to quasiparticles (i.e. free electrons) as long their energy is twice the energy of the band gap Δ of the material [62]. The initially generated, highly excited quasiparticles propagate in the superconducting material, loosing energy under the spontaneous emission of additional phonons. As long the energy of the generated phonons is $> 2\Delta$, more Cooper pairs are broken. The process of Cooper pair breaking continues until the energy of generated quasiparticles is $< 2\Delta$. Afterwards, the emitted phonons do not carry sufficient energy for further Cooper pair breaking. Phonons carrying an energy $< 2\Delta$ are not able contribute to quasiparticle signal and diffuse dominantly back in to the main absorber. Due to this characteristics (i.e. the emission of sub-gap phonons back into the main absorber) of the propagation and creation of quasiparticles, the phonon collector has a theoretical efficiency of $E/1.68$ [63] to convert the energy E to a quasiparticle population with the described characteristics. Figure 3.6 illustrates the processes involved in the creation and propagation of quasiparticles in a superconducting film.

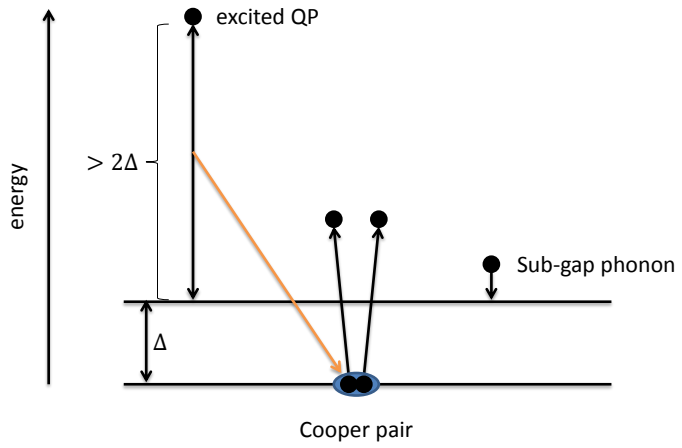

Abbildung 3.6: Illustration for quasiparticle creation and propagation in a superconductor/phonon collector.

Measurements of the recombination rate of quasiparticles in aluminum reveal a strong energy dependence. Quasiparticles carrying an energy much larger than the band gap Δ recombine within a short time scale (1 ns). In contrast to this, for quasiparticles with an

energy close to the band gap (i.e. $\Delta + 10\%$) the recombination rate is strongly reduced. Quasiparticles in this energy range were measured lifetimes of $\mathcal{O}(100\,\mu\text{s})$ [64]. Thus, the generated quasiparticle populations can be assumed to be mostly low energetic and relatively stable after short period of time the initial phonon has entered the phonon collector [62].

However, the recombination to Cooper pairs via the emission of sub-gap phonons remains the relevant loss process. As elaborated before, the majority of these phonons diffuse back to the main absorber and, therefore, do not directly contribute to the signal. Thus, the recombination of quasiparticles before their interaction with the electron system of the TES represent a loss to the non-thermal signal component generated by the phonon collectors [62].

In areas of the phonon collector where the band gap is reduced (i.e. due to impurities), quasiparticles are collected and trapped. In this regions of the phonon collector, an increased recombination rate of quasiparticles to Cooper pairs is observed (i.e. loss of signal). A similar situation is also present in the connecting part between phonon collector and tungsten TES. Operated in the transition between the normal conducting and superconducting phase, the band gap in the tungsten TES is negligible. Therefore, the local band gap in the overlapping region between TES and phonon collector is reduced via the proximity effect. Quasiparticles trapped in this region of the phonon collector interact highly efficient with the electron system of the TES via electron-electron interactions causing an additional temperature rise therein [62].

In order to contribute to the measured temperature signal in the TES, the generated quasiparticles have to diffuse and stay to/in those regions of the phonon collector where they can interact with the electron system of the TES. Losses of the phonon collector signal are generated by quasiparticles recombining to Cooper pairs before reaching the TES (i.e. impurities). Therefore, the efficiency of the phonon collector system is closely related to the diffusion properties of the quasiparticles in the used phonon collector material and their life time therein. Thus, the thickness as well as the quality (i.e. the number of impurities) of the material used as phonon collector are crucial detector parameters as they define the efficiency of the system to collect phonons in the given thermometer structure.

The determination of diffusion properties in the current layout of the phonon collectors in CRESST was performed for this thesis in order to investigate the efficiency of this system. The results are presented in chapter 5.

4 Analysis of CRESST-II Detectors

During CRESST-II (Phase 1 & Phase 2), most of the deployed detectors modules were of the conventional"design (see section 2.3). These detector modules feature a 300 g $CaWO_4$ target crystal and a wafer based light detector with a diameter of 40 mm. Both detector components are placed in a scintillating and highly reflective detector housing. Each detection channel is operated as cryogenic calorimeter with TES readout.

In this chapter, the methods to determine the performance of a CRESST-II detector module are summarized. The main focus is to establish criteria for the evaluation of their capability to identify background interactions and of the performance of the individual calorimeters. The average performance of the detectors operated during CRESST-II (Phase 1 & 2) and the latest dark matter results are given.

At the end of this chapter, the performance limitations and design related flaws of these CRESST-II detectors are discussed to motivate the R&D efforts carried out during this work.

4.1 Raw Data Treatment

The signal traces recorded by the DAQ for the individual detector channels are stored having a fixed structure. This structure is defined by the trigger setup and the way the data is recorded. Since the data structure is relevant for the analysis of the data, it is explained in the following section.

For signal processing and digitalization, the analog readout voltage signal from the SQUIDs is split to be fed simultaneously into the transient digitizer and to the hardware trigger. The digitizer stores 16-bit signal samples with a given timebase in a ring buffer (i.e. FILO buffer: First in, last out). The trigger system filters, shapes and amplifies the SQUID output to achieve the best performance, i.e. to be able to trigger on pulses with an amplitude which is only slightly larger than the baseline noise.

After triggering, a predefined time is waited before the ring buffer is read out and signal is stored on disk. The time after triggering, the post trigger region, corresponds in CRESST-II to 3/4 of the total record window. The first quarter of the record window, called pre-trigger region, carries information about the baseline conditions before the triggered signal occurred. Figure 4.1 illustrates the time distribution of a record window in CRESST-II.

The ratio of the pre-trigger and post trigger is chosen in a way that the record window contains the relevant information for a correct interpretation of a signal. The record window has to be sufficiently long to allow the detector after the signal to return to stable conditions (i.e. baseline). The length of the record window also determines how

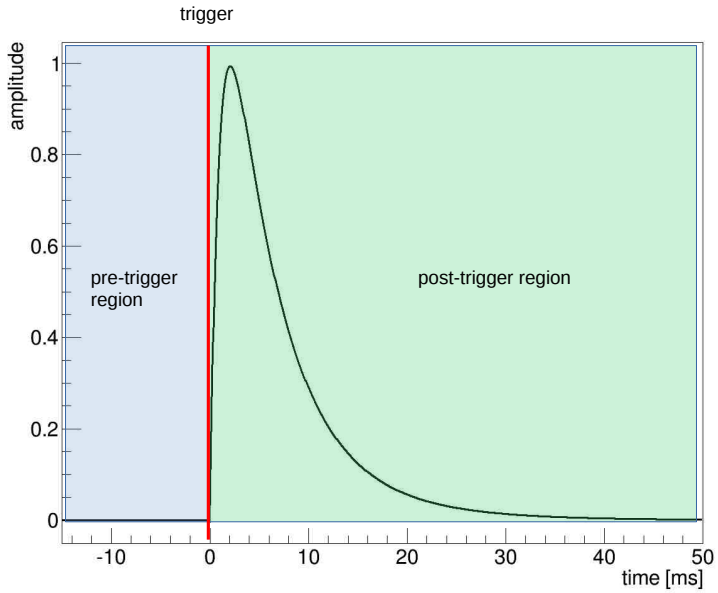

Abbildung 4.1: Time distribution of pre- and post-trigger region in a record window.

precise certain signal parameters can be determined (i.e. decay time of the signal). The data samples stored in the pre-trigger region is crucial for determining the quality of a recorded signal in regard of detector conditions. Events, for which the properties of the signal trace cannot be determined correctly because of non-stable measurement conditions can be identified based on the information contained in the pre-trigger region. For example, pulses which are located on the decaying baseline caused by a previous pulse can identified reliably based on the features of the baseline in the pre-trigger region.

Triggered pulses are recorded for off-line analysis assuming the outlined structure. Before performing any analysis, the stored data is processed in the following way. For each record basic pulse parameters like amplitude onset position, peak position, rise and decay time are determined using a dedicated, in-house developed, software. The software also detemines baseline parameters like baseline tilt, baseline RMS, and left-right baseline are determined. To evaluate the amplitude of a pulse, thus, the energy of an event in fast and precise way and to reveal pulse shape differences, all records of a detector are fitted with a template/standard event. A template/standard event reflects the average pulse shape for a certain class of events (i.e. phonon signal for events occurring in the target crystal, light signal of scintillation light produced in the target crystal). Usually, the standard event can be parametrized analytically with the pulse model introduced in chapter 3. Averaging of a small amount of pulses ($\mathcal{O}$(100events)) with known character and good quality, a noise free pulse template can be generated for a certain event class. By scaling the amplitude, shifting the onset position and changing the baseline level and slope, the standard event fit allows to precisely determine the amplitude of an event. Additionally, the goodness of the fit, thus, the RMS of the fit is determined. This allows to identify events which differ from the assumed pulse shape

and to reject background events effectively. After performing these tasks, each signal has a catalog of pulse parameters which allow the characterization of an event.

More information in the standard event fit and the general approach for data analysis is found in the references [23], [43] and [65].

4.2 Performance of a Cryogenic Calorimeter

The sensitivity of a detector module for dark matter strongly depends on the performance of the phonon and light channels as cryogenic calorimeters. Since the dimensions of the absorber and the TES structure used for quantifying the temperature signals have a large influence on the sensitivity of cryogenic device, significant performance differences between phonon and light channel are observed. However, the evaluation of both channels is performed using the same methods.

4.2.1 Baseline Noise & Detector Threshold

To evaluate the size and time dependence of the baseline noise of a detector σ_b, empty signal traces are recorded on a regular time basis. These data samples allow to track the noise conditions of a detector over time. By fitting the baseline samples with the standard event built for the respective detector, the baseline noise can be quantified. In contrast of using the baseline RMS to determine the noise of the detectors, this method considers the spectral shape of a signal. Therefore, the value derived for σ_b with the template fit is generally smaller than the RMS of the baseline. The fitted pulse amplitude of empty baselines are normal distributed around zero. This allows to derive the baseline resolution σ_b as fitted 1σ width of the distribution. In case the energy scale of the detector is calibrated, the baseline resolution can be translated into an energy equivalent value.

The real detector threshold depends on the hardware trigger settings. Based on the good long term stability of the CRESST setup at Gran Sasso, the trigger level of the electronic readout system can be usually set to a value which corresponds to $\approx 5\sigma_b$ without triggering in the noise.

The detector threshold E_{thres} can be determined by a direct measurement. By injecting heater pulses in the relevant energy range, the trigger efficiency is measured as a function of energy as the fraction of triggered heater pulses. The detector threshold E_{thres} is defined as the energy for which a trigger efficiency of >50% is achieved. The trigger efficiency as a function of the energy is fitted using a error function [66].

$$f(E) = \frac{1}{2}\left(1 + \mathrm{erf}\left(\frac{E - E_{thres}}{\sqrt{2}\sigma_{thres}}\right)\right) \tag{4.1}$$

For detectors for which the hardware trigger is optimized correctly, the width of the error function σ_{thres} is comparable to the baseline resolution σ_b. A complete explanation of this method is given in reference [43].

For CRESST-II phonon detectors, baseline noise level of 0.1-1 keV have been observed. The variations in baseline noise of one order of magnitude are caused by the individual properties of the TES and the performance of the readout electronics connected to respective detector channel. In case the trigger level is optimized according to the baseline noise, a detector threshold of $E_{thres} \approx 5\sigma_b$ can be set which corresponds to $E_{thres} \approx 0.5 - 5\,\text{keV}$. CRESST-II light detectors achieve an average baseline noise of $5 - 10\,\text{eV}$ based on the empty baseline samples. Since the trigger system is set to be activated by the phonon channel while the light channel is read out in coincidence, the trigger threshold of the light detector is usually not determined.

4.2.2 Detector Resolution

The energy scale of a detector is derived by illuminating the absorber with a radioactive source with known characteristics. In CRESST-II, the 122.08 keV and 136.46 keV γ-rays from a ^{57}Co-source are used for the calibration of the phonon channel [67]. For the light detector, the 5.89 keV and 6.45 keV X-rays of an an ^{55}Fe source are used [67]. After identifying the characteristic emission lines of these radioactive sources in the calibration data, the energy range of the detectors is set.

The resolution of the detectors at the energy of the peaks is quantified by fitting the peak with a Gaussian using the 1σ width as the resolution of the detector.

The resolution of a detector is usually energy dependent. In sapphire absorbers, the degradation of the relative energy resolution for events with an energy larger zero has been reported since 2000 [68]. Several reasons can be named for a worsening of this detector parameter at higher energies. One of them is the influence of the transition curve of the TES on the resolution. Inhomogeneities in the steepness as well as the saturation of signals for events which exceed the dynamic range of the TES are one obvious explanation for particle detectors with TES readout. Additionally, the phonon propagation/light propagation in the absorber/the detector housing are able to cause a degradation of the relative detector resolution at higher energies.

Until now, the aspects of the energy dependent detector resolution can not explained by a theoretical model. However, using an empirical approach, the energy dependence can be modeled with a linear, first order approximation.

$$\sigma(E) = \sigma_b + E \cdot a_{cal} \tag{4.2}$$

Next to the baseline noise of the detector σ_b, an energy dependent term is added which includes the linear scaling factor a_{cal} that can be derived by fitting the experimentally derived detector resolution at different energies. Different event classes can be investigated in regard of their detector resolution (i.e. test pulses, direct energy depositions, scintillation signals). The behaviour of different event classes is not required to be identical meaning different event classes can have different scaling factors a_{cal}.

It is important to note, the the linear approximation of the energy dependent detector resolution with this simple method is influenced by the corrections which are applied to derive a linear energy scale. These corrections are introduced to account for inhomogeneities in the TES's transitions and are used to interpolate a linear detector response

over the complete energy range. This approach also allows to describe the detector resolution $\sigma(E)$ using equation 4.2 since all other inhomogeneities are already considered in the linearization of the energy scale. More information on the linearization of the energy scale is found, for example, in reference [23].

To illustrate the behavior, the test pulse amplitudes are used which were injected to the detector module Lise [43] [69]. Test pulses do reflect the detector response for a specific event type which is well defined in the position. Hence, this event class is able to probe the thermometer response without the influence of position dependencies and physical signal production processes (e.g. scintillation process). Therefore, the derived detector resolution for test pulses is usually better than for scattering events taking place in the detectors. The resolution of the test pulse amplitudes of the phonon channel of detector module Lise is shown in figure 4.2 as a function of the energy E. The fit of the data is done using equation 4.2.

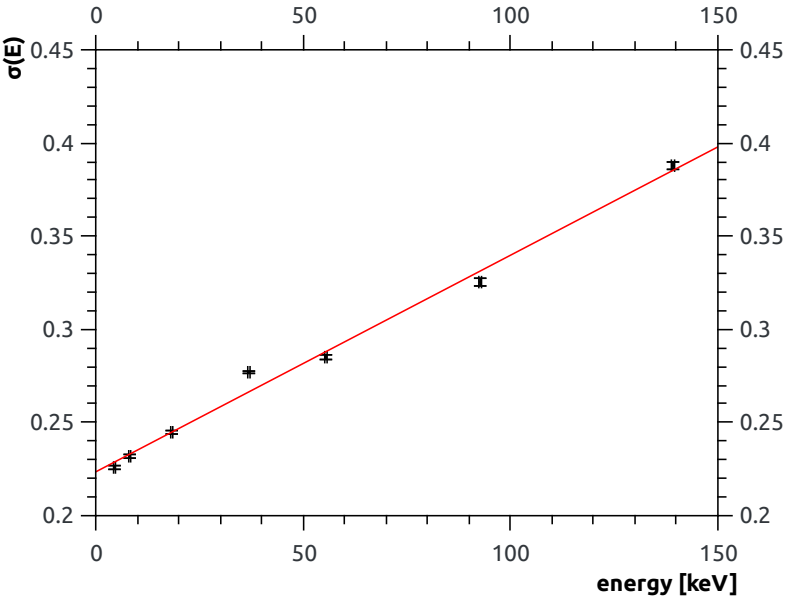

Abbildung 4.2: Test pulse resolution of the detector Lise [69] as function of the energy. The values are fitted with linear slope of $a_{cal} = 0.0012\,1/\text{keV}$ (equation 4.2).

In case of the phonon channel of CRESST-II detectors, the energy resolution is usually derived for the γ lines produced by a ^{57}Co source (122.06 keV and 136.49 keV). For those, an energy resolution of $\approx 1-2\,\%$ is common depending on the individual performance of the channel. Assuming an average baseline noise of $\sigma_b = 0.5\,\text{keV}$, a_{cal} can be estimated with $\approx 0.015\,\text{keV}^{-1}$.

The light detectors are usually calibrated with an ^{55}Fe source which emits X-rays with energies 5.89 keV and 6.49 keV. For these, a detector resolution of $1-2\,\%$ is common which corresponds to $a_{cal} \approx 0.015\,\text{keV}^{-1}$ as well. The similarity of the two values is a

coincidence.

In case of a scintillation signal, the resolution of the light detector differs compared to the resolution obtained for direct energy depositions and test pulses. The observed light detector resolution for the scintillation light created by a ^{57}Co source illuminating the $CaWO_4$ crystal is usually 4-6 %, depending on the individual detector module. The reason for this is, as mentioned before, the additionally uncertainties introduced by the position dependent light collection efficiency in the detector modules and the characteristic width of the scintillation response of $CaWO_4$ (420 ± 40 nm [44] [70]).

4.3 Parametric Band Description

The cryogenic particle detectors based on the simultaneous readout of phonon and light signals take advantage of the the particle dependent scintillation efficiency of the target material to establish a particle identification system on event-by-event basis. Consisting of a scintillating target crystal (i.e. main absorber) and a light detector, a two channel readout system is established in each detector module that is able to measure the phonon and scintillation signal of an interaction in coincidence.

Therefore, the light yield parameter is introduced for phonon-light detectors. The light yield is defined as the ratio of light signal and phonon signal.

$$\text{light yield (LY)} = \frac{E_{L,ee}}{E_P} \tag{4.3}$$

Since the scintillation efficiency of most target materials depends on the nature of an event, the light yield allows particle discrimination on event-by-event basis. The energy scale of the light detector (keV_{ee}) is set using the scintillation light of 122 keV γ-rays from a ^{57}Co source and is indicated by the subscript ee. As a consequence of this calibration choice, the light yield of γ-events with an energy of 122 keV is equal to one.

The particle dependent scintillation efficiency of $CaWO_4$ is quantified by the respective quenching factor of an interaction type QF_X (see table 2.1.). The light yield LY_X for a particle interaction of type X is defined to be

$$LY_X = QF_X \cdot LY_\gamma. \tag{4.4}$$

β/γ-backgrounds and α-decays can be well discriminated from nuclear recoils (i.e. potential dark matter interactions) because the light yield of the event types differ according to the respective quenching factors.

By plotting the data in the light yield vs. energy plane, the events form bands which reflect the particle dependent characteristics of the respective interaction. Figure 4.3 shows the expected event distribution for different interactions types and illustrates the mechanism used for particle discrimination. The electron recoil band is centered around a light yield of one. The nuclear recoil bands arise according to their quenching factors QF_X at lower light yields.

Because of its relative nature, the light yield is highly sensitive to the performance of the light detector. Especially towards small energies, this effect is observed with

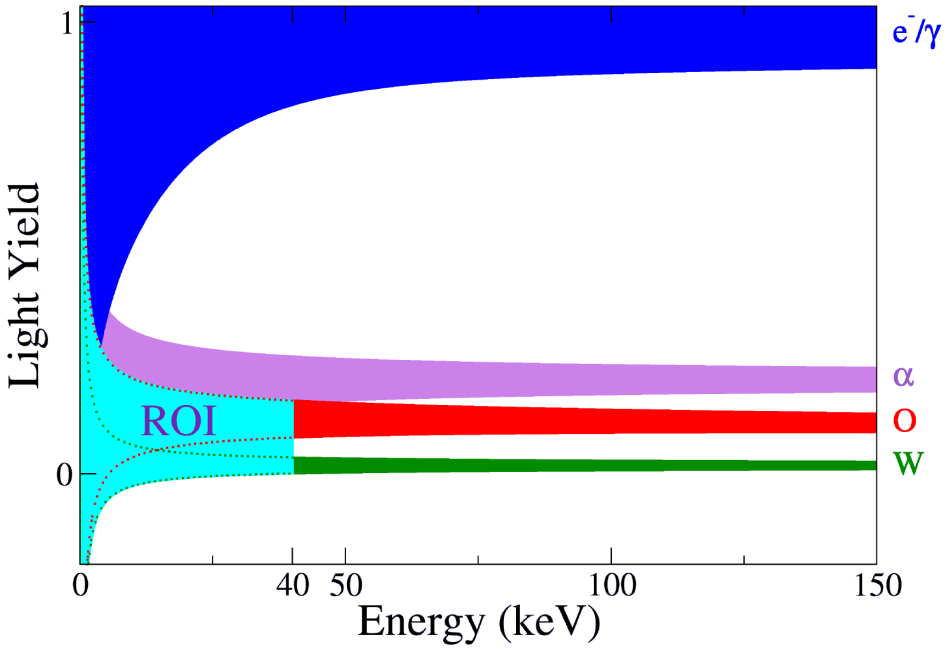

Abbildung 4.3: Schematic view of the event distribution plotted in the light yield vs. energy plane. Depending on the light yield, an event can be identified as electron/γ-interaction, α-interaction or nuclear recoil (oxygen, calcium, tungsten). The electron recoil band centers around a light yield of 1 because of the choice of calibration. Towards smaller energy depositions, the degraded resolution of the light detector is reflected in the broadening of the light yield bands.

increasing strength because the detected light signal becomes small. Due to a decreasing signal-to-noise ratio of the light channel, the (relative) detector resolution (i.e. $\sigma(E)/E$) becomes reduced which results in degraded capability to determine the light yield of an event precisely. In figure 4.3, this effect is illustrated in the low energy region by the broadening of the bands which finally results in an overlapping of the different event populations and the failure of the unambiguous particle identification.

For CRESST-II detectors using a $CaWO_4$ target crystal, the acceptance region for dark matter searches is defined to be below energies of $E < 40\,\text{keV}$ and below the center of the oxygen recoil band which corresponds to a $LY < 0.112$. For the energy the upper limit is chosen based on the expected event rate for dark matter which drops at this energy due to the nuclear form factor of tungsten (see chapter 1). In terms of light yield, the use center of the oxygen band as the upper limit of the acceptance region was found to be the best compromise between background leakage and the possibility to probe all nulcei in the absorber [43].

The light yield of certain interaction type (i.e. electron recoil, nuclear recoil) for a fixed energy deposition is, in most cases, normal distributed around a value close to the quenching factor of the event type QF_X at this energy. This allows to extract the center LY_c and the width σ_{LY} of a recoil band for given energy by fitting the data with

a Gaussian (see figure 4.4).

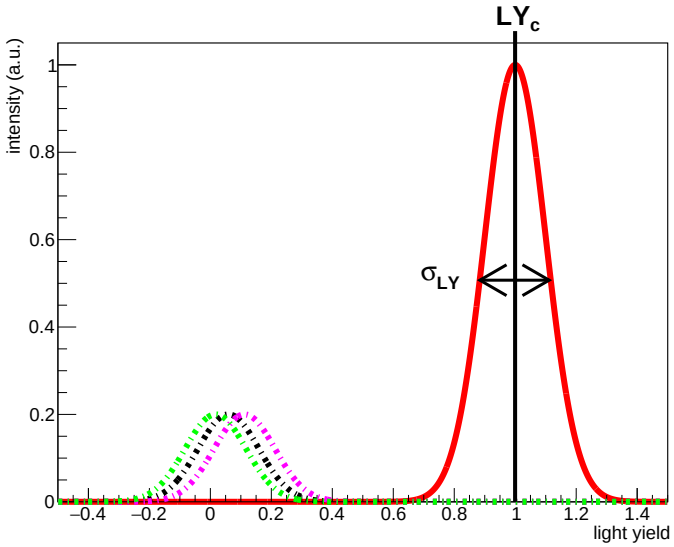

Abbildung 4.4: Scheme of the light yield distribution in a given energy interval. The light yield of an event class can be approximated by a single Gaussian distribution which allows to extract the center LY_c and the width σ_{LY}. Here, the electron recoil band is given (centered ≈ 1, red solid line). Additionally, the nuclear recoil bands of $CaWO_4$ are shown using the corresponding quenching factors as center values of the respective scattering partners.

The behavior of the fitted quantities LY_c and σ_{LY} can be described as function of the energy E using phenomenological models. Hence, the data shown in the light yield vs. energy presentation can be described with a 2-D likelihood function.

Equation 4.5 parametrizes the center of the light yield distribution $LY_{c,e}$ of the electron recoil band:

$$LY_{c,e}(E) = (p_0 + p_1 \cdot E) \cdot (1 - p_2 \cdot \exp(-E/p_3)). \tag{4.5}$$

The parametrization uses 4 parameters (p_0, p_1, p_2, p_3) to describe the observed experimental behavior of the light yield band observed for electron recoils. p_0 gives an energy independent value for the center of the light yield band. Since p_0 reflects the average light yield of the band, it has a value close to unity due to the calibration. For large energies, the light yield band usually bends towards smaller values because the light output is reduced for large energies [46]. Therefore, the fit value of p_1 is usually negative. For small energies, the light yield of electron recoils is smaller, too, which is expressed by the fact the electron recoil band is bent downwards to smaller light yields. This effect, called non-proportionality effect", is characterized by the parameters p_2 and p_3 (more information is found in reference [46]).

The width $\sigma_{LY,e}(E)$ of the electron recoil band is described with equation 4.6:

$$\sigma_{LY,e}(E) = \frac{1}{E}\sqrt{S_0 + S_1 \cdot E \cdot LY_{c,e}(E) + S_2 \cdot E^2 \cdot LY_{c,e}(E)^2}. \tag{4.6}$$

where $LY_{c,e}(E)$ is given in equation 4.5. The term $E \cdot LY_{c,e}(E)$ corresponds to the energy detected in the light channel E_L for a certain energy deposition E. Here, three parameters are necessary to describe $\sigma_{LY,e}$ phenomenologically over the full energy range. S_0 accounts for the individual baseline noise of phonon and light channel[1].

$$S_0 = \sigma_{b,PD}^2 + \sigma_{b,LD}^2. \tag{4.7}$$

The parameter S_0 is independent of the deposited energy E and dominates the resolution $\sigma_{LY,e}$ of a typical CRESST-II detector module in the energy range below 1 keV. For energies between $E \approx 1\,\text{keV}$ and $\mathcal{O}(500\,\text{keV})$, the S_1 term is the dominant one of $\sigma_{LY,e}$. This parameter accounts for the quantization of the scintillation photons and, therefore, reflects the uncertainty which is introduced per detected photon in the light channel. Hence, the statistical fluctuations in the number of detected photons (n) scales according to a Possion distribution, i.e. $S_1 \propto \sqrt{n}$. S_1 is not influenced by the performance of the phonon channel, and , therefore, allows to compare the performance of the light channel in different detector modules independently from the performance of the phonon channel. S_2 accounts for position dependences in the scintillation and light collection efficiency.

For the quenched nuclear recoil bands, the equations 4.5 and 4.6 are adapted. Since the non-proportionality effect is only observed for the electron recoil band, equation 4.5 is reduced for nuclear recoils to:

$$LY_{c,X} = QF_X \cdot (p_0 + p_1 \cdot E). \tag{4.8}$$

The width of a nuclear recoil band $\sigma_{LY,X}$ corresponds to the energy of the quenched light signal $E_L = E \cdot LY_{c,X}$ and is, therefore, described with:

$$\sigma_{LY,X} = \frac{1}{E}\sqrt{S_0 + S_1 \cdot E \cdot LY_{c,X}(E) \cdot QF_X + S_2 \cdot E^2 \cdot LY_{c,X}(E)^2 \cdot QF_X^2}. \tag{4.9}$$

Also here, the value diverges if the energy deposition becomes small leading to an overlapping of the nuclear recoil bands.

To analyze the recorded data, the band model is usually fitted as a 2-D maximum-likelihood function to the recorded event distribution in the light yield vs. energy plane. Equation 4.10 shows the 2-D maximum-likelihood function for the electron recoil band:

$$L(E_i, LY_i)) = \frac{1}{\sqrt{2\pi}\sigma_{LY}(E_i)} \cdot \exp\left(-\frac{(LY_i - LY_L Y_{c,e}(E_i))^2}{2\sigma_{LY}^2(E_i)}\right). \tag{4.10}$$

The use of equation 4.10 to fit data without detector specific adaptations is only possible for ideal detectors. In reality, the parametrization of the function describing center of a recoil band $LY_{c,e}(E)$ has to be modified in most cases. This is necessary to account for inhomogeneities in the detector responses (i.e. inhomogeneities in the TES's transition) or to respect the particle dependent scintillation efficiency for β and γ interactions in $CaWO_4$ in the low energy range (i.e. $E_r < 50\,\text{keV}$) [46]. Modifications are

[1]The baseline noise of the light detector is translated in energy equivalent units using $\sigma_{b,LD,ee} = \sigma_{b,LD}/(\text{energy share detected as light (EDL)})$

usually not necessary for the light yield distribution for a certain energy interval or the energy dependent description of σ_{LY} (equation 4.6). The assumption, that the light yield for events witht the same energy are normal distrubuted holds for the large majority of detectors. Therefore, the parameters S_0, S_1 and S_2 can be used to evaluate and compare the experimental performance of detectors on a fair level because no further adjustments are necessary to describe the data correctly.

4.4 Discrimination Power for Internal Backgrounds

The discrimination power of a detector module is defined by its capability to identify the nature of the particle interaction taking place in the main absorber. While for large energy depositions the amount of created scintillation light is sufficiently large to determine the interaction type unambiguously, this ability degrades towards smaller energy depositions.

The quality of the light signal and, thus, the discrimination power of a detector module depends on numerous factors like the crystal properties (e.g. scintillation efficiency, optical properties,...), the detector geometry (i.e. size of main absorber and light detector, light collection efficiency) and on the individual performance of the cryogenic detectors. These properties are included in the parametric band description which was introduced in section 4.3. Additionally, the sensitivity of a detector for dark matter also depends on the level of radioactive contaminations in the target. The amount of β/γ-backgrounds leaking into the region of interest for dark matter searches also depends on total background rate. Therefore, a low intrinsic contamination of the target is a crucial detector parameter.

To disentangle the parameters responsible for the definition of the detector properties and the overall detector performance, a data driven simulation is used to model the the expected event distribution for a normalized background rate and detector exposure. The light yield distribution is modeled for given detector geometry using equation 4.10. The output of the simulation can be understood as probability distribution for a given crystal operated within different detector designs for the same amount of time.

Based on the simulated detector response, two approaches can be chosen to define the rejection capabilities of a detector:

1. *Expected number of background events in the region of interest:*
   The first method is to count the expected number of events being present in the region of interest (see figure 4.3). In a detector with average performance, this acceptance region is expected to be free of events for energies above 10 keV [71]. Towards small energies, leakage of electron recoil events into the region of interest becomes more likely as the discrimination power is reduced. The number of events present in the region of interest depends dominantly on the performance of the light channel, the number of events in the electron recoil band (i.e. the amount of β/γ-background present in the main absorber) and the strength of the non-proportionality effect.

Major drawback of this method is the influence of the performance of the phonon detector on the result. Two aspects have to be considered.

First, the acceptance region is partially defined by the performance of the phonon channel. Usually, the acceptance extends to lowest energy the detector module is able to probe, i.e. to E_{thres} of the phonon channel. Since this detector property is different for each detector module, the respective acceptance region is different, too. Consequently, the number of events expected to be observed in the acceptance region is strongly influenced by the individual detector performance. This effect is additionally enhanced by the reduced discrimination power towards smaller energies which causes more events to be located in the acceptance region. To avoid a biased analysis, a common acceptance region has to be defined for all detectors which are intended to be compared.

Secondly, events with an energy close to the detection threshold can be shifted from lower energies above the threshold and vice versa due to finite detector resolution of the phonon channel. In case a flat spectrum is assumed, the effect should equalize (i.e. the number of events shifted above the detector threshold is equal to the number shifted below). Though, this assumption is not correct because the probability that an events has a light yield which places the event in the acceptance region rises towards smaller energies. To avoid a biased statement using this method, a common detector resolution of the phonon is necessary, too.

2. *Definition of an analysis threshold:*
   The second method is to set an analysis threshold above which a defined number of leakage is expected. This also allows to derive the energy above which energy, for a given confidence level, a background free acceptance region is expected. The method was used to analyze the data of CRESST-II(Phase 1) [71]. There, the acceptance region for dark matter was set to expect not more than 1 electron recoil event in the acceptance region in the whole data set recorded by a single detector.

   This method is also influenced by the performance of the phonon channel. Like in method 1, the shifting of events across the analysis threshold is able to affect the result. Therefore, the definition of a common detector resolution is necessary for this approach, too. However, the influence of this simulation parameter on the result is usually insignificant because the influence of the light channel's performance is dominates the result.

In figure 4.5, the different approaches to estimate the capability of a detector to reject backgrounds are illustrated.

In figure 4.5 the electron (red) and nuclear (blue) recoil bands are shown schematically. The region, in which the event bands overlap, hence, an unambiguous particle identification is not granted, is indicated in pink. The acceptance region for dark matter is indicated in yellow. Method 1 counts the events being present in the ROI. Since usually only events from the electron recoil band contribute to this number, the relevant

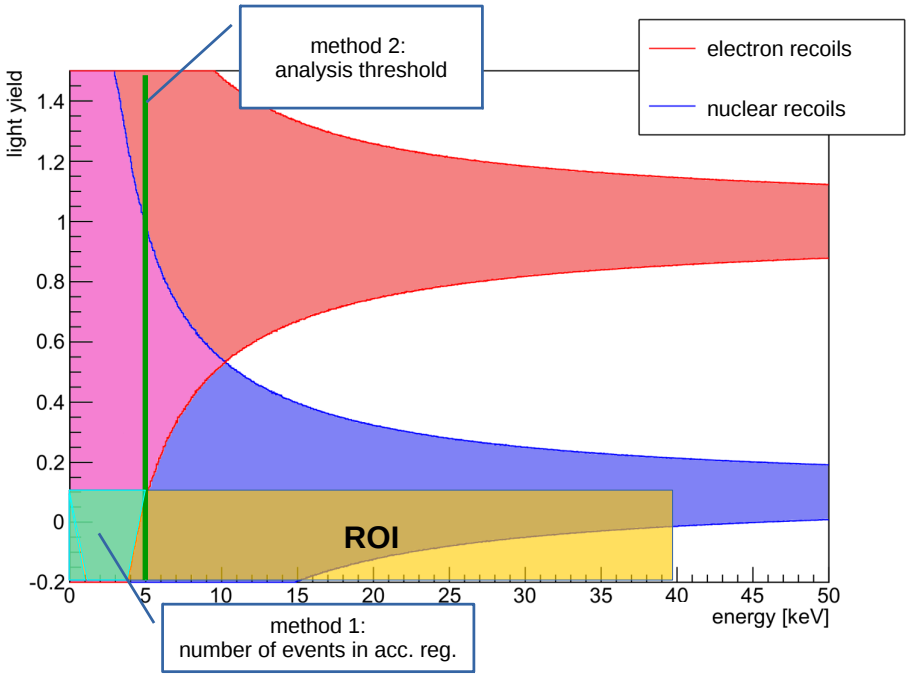

Abbildung 4.5: Illustration of the different criteria for determining the particle discrimination capabilities of a detector.

region contributing dominantly to the total number is indicated in cyan. Method 2 sets a discrimination threshold (green line) above which a defined number of events is expect in the ROI. This discrimination threshold is dominantly defined by the performance of the light channel while the influence of the phonon channel's performance can be considered as negligible.

Both methods are give reliable results on the performance of different detector designs in terms of the discrimination power and allow a fair comparison between different detector designs. Method 2 is expected to give less biased results than method 1 as the result is mainly defined by the performance of the light channel. Nevertheless, the comparison of the discrimination power of different detectors in the low energy region and the investigation of the light detector's performance on the discrimination power in this energy range is only possible by using method 1. Since both aspects are of special importance for the investigations carried out during this thesis, both methods are used in the following chapters.

4.5 Energy Detected as Light

The fraction of energy which is detected in the form of light (EDL) is defined as the ratio of energy detected in the light channel and the total amount of deposited energy

in the target crystal.

$$EDL = \frac{\text{energy detected in the light detector}}{\text{total amount of deposited energy}} \tag{4.11}$$

The EDL has a definition which is very similar to the definition of light yield. The main difference between light yield and EDL is the fact that for the EDL, the light detector's energy scale corresponds to the actually detected energy while for the light yield the energy scale of the light detector is set by the scintillation signal of electron recoil events taking place in the $CaWO_4$ target crystal. Thus, the EDL can be understood as scaling factor which allows to translate between these two energy scales.

In the following sections, the energy sharing between the two existing readout channels in phonon-light detectors is explained. Based on these explanation, the method to determine the EDL is introduced.

4.5.1 Energy Sharing in Phonon-Light Detectors

The performance of the light detector as cryogenic device exceeds the performance of the phonon detector (see section 4.2). The main reason for this is that the mass of the light absorber is much smaller than that of the target crystal. Therefore, the light channel is, proportional to its smaller volume, a factor 100 more sensitive than the phonon detector. However, the better performance is counterbalanced by the small amount of energy which is detected by the light detector. The reason for the small amount of detected energy in the light detector are the intermediate processes between an initial energy deposition in the $CaWO_4$ target crystal and the final detection of a photon in the light detector. Figure 4.6 illustrates the energy sharing in a phonon-light detector and illustrates the losses which reduce the energy detected in the light channel.

After an energy deposition in a $CaWO_4$ target crystal, scintillation light is produced according to the scintillation efficiency f which is reported for $CaWO_4$ with $(8.3 \pm 0.8)\,\%$ [47] [48]. The remaining part of the initial energy deposition is directed to the phonon channel readout and is detected there or is lost in the non-active detector parts.

After the scintillation process, the created photons propagate in the detector module where they are subject to different loss processes. In case a photon is reabsorbed in the target crystal, the energy it carries is redirected to the phonon channel. The probability for this process (η) depends on the crystal quality, thus, on how fast a photon is reabsorbed in the crystal due to impurities, and on the probability for a photon to be trapped within the crystal without any possibility of ever reaching the light detector. In case a photon is able to leave the target crystal before being re-absorbed, it can be either lost in the detector housing (i.e. absorption/transmission in the reflective foil or in the holding structures) or detected in the light detector. The combination of all loss processes finally defines the probability of a generated photon to reach the light detector. This probability is called light collection efficiency (ϵ). It is mainly defined by the average distance a photon travels inside the detector module before being absorbed in the light detector since loss due to (re-)absorption in crystal and foil scale with the traveled distance.

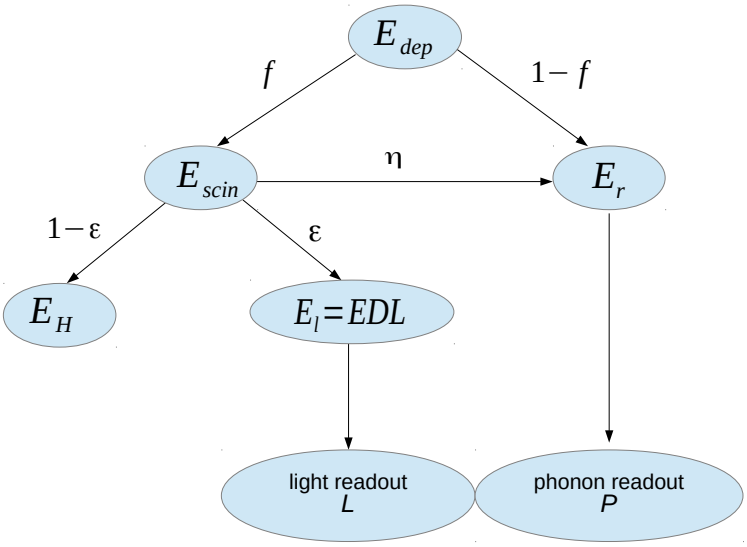

Abbildung 4.6: Energy sharing in a scintillating bolometer. Figure is adapted from [48].

In conclusion, the amount of energy detected as light depends on the scintillation efficiency and on the optical properties of the target crystal as well as on the detector design which defines its light collection efficiency. The EDL is therefore defined as the product of the scintillation efficiency f and the light collection efficiency ϵ and disentangles the intrinsic scintillation efficiency from the other loss processes.

$$EDL = E_{dep} \cdot f \cdot \epsilon \tag{4.12}$$

The average value of the EDL derived for the conventional detector module varies between 1.7-2.54 %. This value is composed of a scintillation efficiency of 7.9-8.4 % and a light collection efficiency 17-28 % [48]. Since in most cases the scintillation efficiency of the target crystal is not precisely known, an average, constant value is assumed for all $CaWO_4$ crystals while the variations in the EDL are dominantly related to the detector design and the light collection efficiency therein.

4.5.2 Determination of the EDL

To determine the EDL, the method described in the following is used.

The scintillation signal of an event occurring in the main absorber can be determined precisely for events with an energy ($E > 10\,\mathrm{keV}$). Using a calibration source hitting the target crystal (e.g. ^{57}Co), the scintillation signal of γ-ray interactions in the crystal with known energy is determined. With a second calibration source, which illuminates the light detector (e.g. ^{55}Fe source), the energy scale of the latter is determined for direct energy depositions. By relating the fraction of energy detected for scintillation events to the energy which is actually seen by the light detector, the EDL can be determined.

The energy E of a recorded event corresponds, in case of a calorimetric measurement, to the integrated area of a pulse which is described by the function $P(t)$.

$$E = \int_{-\infty}^{\infty} P(t)dt \tag{4.13}$$

As long the pulse shape reflected in $P(t)$ is constant for all events, the maximum value of the pulse amplitude A_P is directly proportional to E. In this case, the pulse amplitude can be used as energy equivalent quantity.

$$E \propto A_P \tag{4.14}$$

This relation is used during the data analysis of CRESST-II to determine the energy of an event by determining the amplitude with the standard event fit.

To determine the exact energy of an event, a linear calibration factor ζ_{cal} is used to directly relate the energy of an event E to the measured pulse height of an event A_P.

$$E = \zeta_{cal} \cdot A_P = \frac{E_{cal}}{A_{cal}} \cdot A_P \tag{4.15}$$

The calibration factor ζ_{cal} is determined using a calibration source for which the deposited energy E_{cal} and the corresponding maximal amplitude A_{cal} of $P(t)$ are known. This approach is valid as long all events fitted by the standard event feature the same pulse shape and can be applied to the phonon and light channel.

To derive the EDL, though, the energy input into the light channel has to be determined for different event signatures: For direct hits of X-rays and for scintillation light. Their way to interact with the light detector is different and causes a pulse shape difference between the two event signatures. D irect energy depositions (i.e. X-rays) interact with the light absorber at a single location where they deposit their full energy at once. Scintillation signals are created by a large number of photons which are absorbed at distributed locations of the absorber surface. Furthermore, the time structure of the signal is different since the emission of the photons during the scintillation process happens over a time of $\mathcal{O}(100\,\mu\text{s})$ [44].

Since pulse shape differences between the two event classes are observed, the use of the pulse height of an event to determine its energy is not appropriate. Therefore, the following calibration is used to allow the comparison of signals with different pulse shapes.

Signals detected by the light detector, thus $P(t)$, can be seen as a convolution of energy deposition $L(t)$ and detector response $D(t)$.

$$P(t) = L(t) \otimes D(t) \tag{4.16}$$

The pulse shape of $P(t)$ is generally defined by the shape of the light signal $L(t)$ and by the detector response to an energy deposition $D(t)$. $D(t)$ can be assumed to be constant for all energy depositions[2]. For direct energy deposition and fast scintillators, the energy

[2]This assumption is not correct for very large energy depositions because of the limited dynamic range of TES.

deposition $L(t)$ can be expressed by a δ-function. In this case, the observed pulse shape is defined by the detector response $D(t)$. For slower scintillators, the description of the light signal $L(t)$ using δ-function is not correct and the observed pulse shape of $P(t)$ is defined by both sub components. Hence, if pulse shape differences between direct detector hits and scintillation events are observed, these are caused by a pulse shape difference in $L(t)$ while the pulse shape of the detector response $D(t)$ is expected to be constant.

According to equation 4.13, the energy measured in the light detector E_L is equal to the area under the pulse $P(t)$. Thus, the energy of an events with different pulse shape, but with the same pulse height/amplitude are not identical. The disentanglement of light signal $L(t)$, reason for the pulse shape differences, and detector response $D(t)$ is not possible, since $P(t)$ is the observable. Though, for the energy of an event E_L, the disentanglement is possible. Using Fubini's theorem [72], one can write E_L as

$$E_L = \int_{-\infty}^{\infty} P(t)dt = \int_{-\infty}^{\infty} L(\tau) \cdot D(t-\tau)d\tau = \int_{-\infty}^{\infty} L(\tau)d\tau \cdot \int_{-\infty}^{\infty} D(t-\tau)d\tau. \quad (4.17)$$

Equation 4.17 allows to show that the origin for pulse shape differences can be disentangled without affecting the result of E_L. Hence, the ratio of the energy detected for events with different pulse shape but the same pulse height is the ratio of the integrals of light signals.

$$\frac{E_{L,1}}{E_{L,2}} = \frac{\int_{-\infty}^{\infty} L_1(\tau)d\tau}{\int_{-\infty}^{\infty} L_2(\tau)d\tau} \quad (4.18)$$

For the determination of the EDL, this method can be used to relate the energy calibration, which is based on direct light detector hits, to the energy of scintillation events. By determining the integral of the standard events build for direct energy depositions I_{direct} and scintillation events I_{scin} with the same maximal amplitude, equation 4.15 can be corrected to

$$E_L = \frac{E_{cal}}{A_{cal}} \cdot A_P \cdot \frac{I_{scin}}{I_{direct}}. \quad (4.19)$$

The integral ratio introduced in equation 4.19 allows to use the detected amplitude of an event as energy equivalent unit although pulse shape differences between the respective event classes exist. Equation 4.19 is used to determine the energy detected in the light detector for a given amount of energy deposited in the target crystal using equation 4.11.

The error of the determined EDL is derived by standard error propagation. For the uncertainty of the amplitude values the detector energy dependent resolution is used. On average the scintillation signal of an isolated peak form a calibration source shows a resolution in the range 4-5 %, while the resolution of direct hits is usually 1 %. The uncertainty introduced by the numerical integration is expected to be small and is estimated to be < 0.1 %, respectively. Thus, the total uncertainty of this method is expected to be dominated by the resolution of the light detector for scintillation signals. Further systematic uncertainties, which are introduced, for example, by the energy calibration, are discussed for the respective measurements presented later in this work.

4.6 Background Identification using the Detector Surrounding

For all interactions depositing energy in the main absorber, the light yield mechanism allows to determine the nature of an interaction unambiguously over a wide range of energies. Nevertheless, the light yield veto mechanism is not able to distinguish between events that interact solely in the target crystal and events that loose part of their energy in the detector surrounding before they interact with the target crystal. The signals detected in phonon and light channel are characteristic to the energy an event deposits in the target crystal while the energy deposited in other detector parts remains undetected.

Due to this flaw, the external β-backgrounds, as well as, α-decays taking place on surfaces in direct line of sight to the main absorber are able to contribute to the total background rate observed in the target. Therefore, the detector surrounding has to provide an additional signal input which allows to identify events depositing part of their energy in the detector housing.

The use of the light channel to veto external backgrounds is the natural choice for detector based on the phonon-lighttechnique. In case an additional input to the light channel is generated by external events, these events can be indentified as such. A indirect veto signature is provided if the main absorber is surrounded by a scintillating materials in which external backgrounds deposit part of their energy before interacting within the target crystal. These events are identified by the additional scintillation light created by the detector housing which adds to the scintillation light created by the energy deposition in the $CaWO_4$ crystal. This veto mechanism also works for surface α-decays in which the daughter nucleus reaches the target crystals as they are identified by the additional scintillation light created by the escaping α-particle absorbed in the foil. Alternatively, a direct veto signal can be generated in the light channel. In this case, instead of using the scintillation mechanism of the detector housing, all surface facing the main absorber are instrumented and actively read out becoming effectively an additional detector. Here, the energy which remains undetected by the phonon channel, is detected as direct energy entry in the veto detector. The observed signal characteristics allow an unambiguous tagging of these events as external background. Advantageous of this method is that the intermediate scintillation process of the foil is avoided and the signal which allows to identify backgrounds as such is larger. Thus, an active veto system is expected to achieve a better discrimination power at smallest energies.

Both systems require that any surface which is direct line of sight with the main absorber provides a veto mechanisms. In case a complete 4π coverage is not achieved, events with external origin can be misinterpreted as events only interacting with the main target crystal. For the conventional CRESST-II module, this condition is not achieved. To keep the main absorber and the light detector in position, non-scintillating bronze clamps are used. The surface of the clamps in direct line of sight to the target crystal is small compared to the total surface of the detector housing, but a small probability for non-vetoed surface background events remains. More information is found in section 4.8.

4.7 Detector Performance in CRESST-II

4.7.1 Average Performance of Conventional Detector Modules

During CRESST-II (Phase 1 & Phase 2) more than 20 detectors of the conventional detector design were operated (see references [23], [43], [65], [71]). All detectors were analyzed using the parametric band model described in section 4.3. This implies that these detectors are presented and analyzed in light yield vs. energy plane. Based on these results, the average performance of a CRESST-II detector with the standard detector design is derived.

Since the position of the electron recoil band $LY_c(E)$ is generally not defined by the detector design or the performance of the readout channels but by the properties of the $CaWO_4$ target crystal as scintillator, no average values are given for the parameters p_0, p_1, p_2 and p_3 (see equation 4.5) since these parameters are not useful to describe the average performance of a set of detector modules in meaningful way.

For the width $\sigma_{LY}(E)$ (see equation 4.6), the average values for the parameters S_0, S_1 and S_2 can be used to determine the average performance of the readout channels and the discrimination power of a set of detector modules. This is possible, since $\sigma_{LY}(E)$ mainly relies on the performance of the phonon and the light channel and the design of the detector module. The average values for S_0, S_1 and S_2 of all conventional detector modules analyzed in [23], [43] and [65] are summarised in table 4.1

parameter	*CRESST-II detector modules average value*
S_0 [eV^2]	0.612±0.210
S_1 [eV]	0.580±0.025
S_2	0.0003±0.0002

Tabelle 4.1: Average parameter values for describing the light yield band of electron recoils in a conventional CRESST-II detector module. The given uncertainty corresponds to the standard deviation of the values.

The parameters S_0 and S_1 are influenced by the amount of energy which is detected as light (EDL). Hence, these parameters are not only influenced by the detector design but also, to some extend, by the scintillation efficiency of the target crystal (see section 4.5.1).

The parameter S_0 describes the noise of the baseline obtained for the light and phonon channel (see equation 4.7). Therefore, S_0 is dominantly defined by the individual performance of the phonon and light channel of a detector module (TES & SQUID system). This parameter is most influenced by the large variations in the performance observed between different cryogenic detectors. Therefore, the statistical uncertainty of this parameter is larger than the statistical uncertainty of S_1 and S_2. In an average

detector module the phonon and light channel contribute to same degree to S_0.[3] Thus, both channels of a detector module have to perform convincingly in order to achieve a small value for S_0 and to provide good particle discrimination capabilities in the low energy range.

S_1 term contributes dominantly to σ_{LY} in a large energy range (i.e. $\approx 1-500\,\mathrm{keV}$). The parameter reflects the uncertainty which is introduced per detected photon in the light detector. Fluctuations in the number of photons produced (n) are described using the Poisson statistics. Accordingly, S_1 scales with $\propto \sqrt{n}$. As a consequence, this parameter is mainly defined by the detector design and the scintillation properties of the $CaWO_4$ target crystal and not by the performance of the respective phonon and light detector. Therefore, the parameter S_1 given in table 4.1 is determined with a small uncertainty since neither the design nor the scintillation efficiency changes to large extend for the analyzed detectors.

The parameter S_2 is usually small $\leq 10^{-3}$, though, large fluctuations of this value are observed which is reflected in the large uncertainty of this value. The influence of this parameter becomes only dominant for very high energies ($E > \mathcal{O}(500-700\mathrm{keV})$). In the relevant energy range for dark matter searches this parameter has almost no influence on the capability to reject backgrounds.

In summary, one can state that the parameter S_1 is the most suitable detector parameter for comparing the performance of different detector modules. S_1 is not influenced by the performance of the phonon detector like the parameter S_0. Therefore, it allows to evaluate the influence of the of the light channel's performance on the overall performance of the detector module in regard of discrimination power in a independent way.

In regard to the capability of being a sensitive detector for dark matter, the different detector modules are compared in this work using the methods introduced in section 4.4. For the analysis of the data acquired during CRESST-II (Phase 1 & 2), the lower boundary of the acceptance region was defined as the energy above which less than one electron recoil is expected to be present in the acceptance region. This boundary varied between 12.1 keV and 19.0 keV. These analysis thresholds are significantly higher than the thresholds which are provided by the phonon channel. This implies that the performance of the light channel is limiting the sensitivity of the CRESST-II detectors.

[3] Using the average values for $\sigma^{PD}_{b,ee} = 0.55\,\mathrm{keV}$ and $\sigma^{LD}_{b,ee} = 0.01\,\mathrm{keV}$ [71], S_0 is calculated, according to equation 4.7, to be $S_0 = (\sigma^{PD}_{b,ee})^2 + (\sigma^{LD}_{b,ee})^2 = (\sigma^{PD}_{b,ee})^2 + (\sigma^{LD}_{b}/EDL)^2 \approx (0.55\,\mathrm{eV})^2 + (0.01\,\mathrm{eV}/0.02)^2$.

4.7.2 CRESST-II (Phase 1)

During CRESST-II (Phase 1), 18 detector modules were operated over a time period of approximately 2 years (2010-2012). Eight fully operational detector modules were used for a combined dark matter analysis based on a final exposure of 730 kg days. The results achieved with this data is published in reference [71]. Additional information on the analysis is also found in [23] and [43].

The likelihood analysis of the data yielded in an excess of events in the ROI which is not in agreement with the assumed background model. The high overall rate of background at the time implied nevertheless large uncertainties in its modeling, therefore a significant reduction of the background level was the goal for the subsequent data taking campaign.

Several detector improvements were implemented which all focused at a reduction of the overall background level. The most important measure addressed the reduction of surface α-decays and the related lead recoil backgrounds. These events are caused by the surface contamination of the detector module with ^{222}Rn. In the decay chain of ^{222}Rn, the first long-living isotope is ^{210}Pb ($\tau_{1/2} = 22.3$ y [67]) which decays to ^{210}Po via the emission of a β. The ensuing α-decay of ^{210}Po to ^{206}Pb ($\tau_{1/2} = 138.37$ d)has a Q-value of 5407 keV which is divided between the Pb nucleus (103 keV) and the α-particle (5304 keV [67]). If the α emitted in the decay remains undetected, i.e. deposits its energy in a non-scintillating part of the detector housing, the observed event is due to the recoiling daughter nucleus absorbed in the target crystal. In general, the energy of the nucleus is too large to be relevant for dark matter searches with $CaWO_4$, but the energy deposited into the phonon channel can be reduced in case the mother nucleus is implanted on a nearby surface [73]. In such a case the detected Pb-recoil can be shifted in energy to the ROI causing a signal which is indistinguishable from a possible dark matter interaction.

Avoiding this source of background is of extreme importance for direct dark matter searches. Therefore both passive and active measures were taken in the following measurement campaign of CRESST-II. One of these measures was the development of the so called beaker detector design which is presented in chapter 7.

4.7.3 CRESST-II (Phase 2)

The measurement campaign of CRESST-II (Phase 2) started in 2013 and lasted approximately 2 years.

In CRESST-II (Phase 2), 12 out of 18 detector modules were constructed based on the conventional detector design (see section 2.3). To avoid the contamination of the detectors with ^{222}Rn during the production and mounting, large efforts were carried out to prevent the exposure of the detectors to ordinary air. By storing the detectors in nitrogen and assembling them in radon-free air, the time of exposure was reduced compared to the detectors operated during CRESST-II (Phase 1). Still, a complete radon prevention over the full production cycle was not achievable because most of the production processes cannot be performed in a confined environment.

All operated detector modules of the conventional design observed events that are

correlated to the α-decay of ^{210}Po. Despite the efforts to prevent this background source, the reduction in rate can be considered negligible since the contamination of the ROI with the degraded Pb-recoils is observed with similar intensity. Therefore, the passive efforts to avoid this background source were found to be not sufficient [43] [65].

Next to the conventional detector modules, new detector designs were test during CRESST-II (Phase 2), featuring a fully vetoed detector housing against external backgrounds.

The so called stick design uses a fully scintillating detector housing to achieve a veto of surface related events. By replacing the bronze clamps by $CaWO_4$ sticks, non-scintillating surfaces are completely avoided in direct line of sight of the target crystal from the detector housing. In this detector configuration, the escaping α particle is guaranteed to create sufficient scintillation light to be vetoed as background. The discrimination power of the detector concept proved to be highly efficient, preventing all surface related α-decays to contribute to the backgrounds observed the ROI. For more information on this detector design and its performance, see reference [74]).

The second prototype design operated during CRESST-II (Phase 2) establishes a complete active 4π-veto system for identifying external backgrounds actively. The so called beaker design surrounds the main absorber with a large scale, beaker shaped light detector. In combination with a large carrier crystal, all surfaces surrounding the main absorber are actively readout. Detailed information on the beaker design is presented in chapter 7).

The dark matter results of this measurement campaign are based on the data sets obtained with two detector modules.

The first module used for a dark matter analysis belongs to the stick prototype (TUM40 [66]). Featuring a detector threshold of 603 eV (phonon channel) and a fully scintillating housing with a highly effective veto system for external backgrounds, the detector module was able to explore new parameter space for dark matter masses < 3 GeV. The exclusion limit based on this data of TUM40 is given in figure 4.7 as dashed red line [66].

The second module (Lise [69]) used for a dark matter analysis is a conventional detector module. This means that non-scintillating surfaces are present in direct line of sight of the main absorber and that surface related α-backgrounds are expected to be present in the ROI for dark matter searches. The unique feature of this detector module is the excellent detector threshold of the phonon channel (306 eV) and the extremely flat background down to threshold which allow to probe new parameter space in the low-mass dark matter region. The exclusion limit achieved with this detector module is also shown in figure 4.7 as solid red line, illustrating the influence of the detector threshold on the sensitivity of a module for probing the low mass dark matter space.

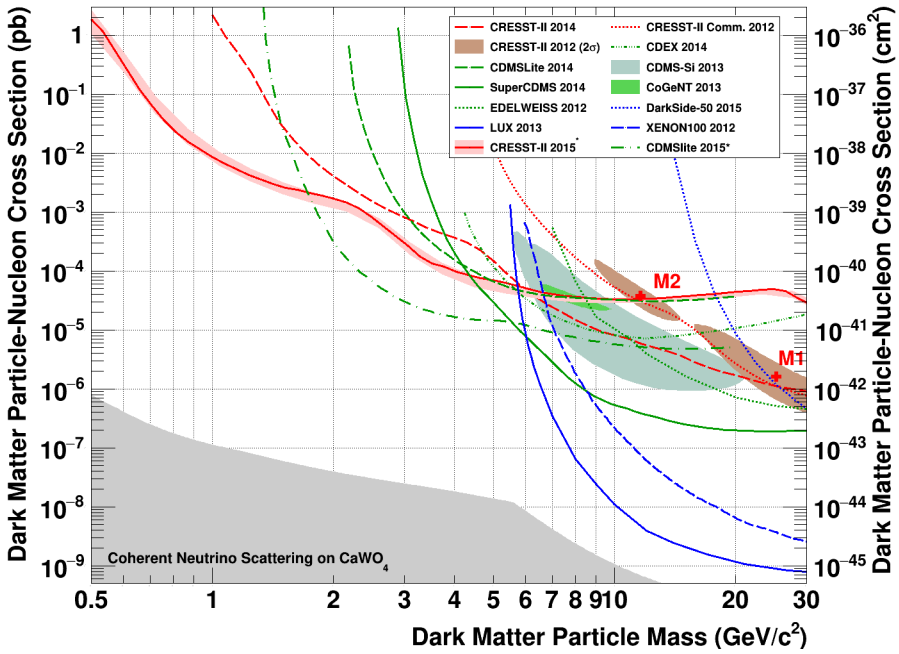

Abbildung 4.7: Dark Matter parameter space at the time the CRESST-II (Phase 2) data was released [69]. Next to the TUM40 result, the exclusion limit achieved by Lise is shown. Since the detection threshold achieved by these two detector modules is better than the detection thresholds of other experiments, new parameter space is excluded in the low mass dark matter region.

4.8 Limitations of the Conventional Detector Design

The conventional detector design provides a very good performance over a large energy range. Designed to achieve large exposures within reasonable time scales, the size of the main absorber was found to be to be a good compromise between detector performance and exposure. Still, three aspects limiting the sensitivity for dark matter searches can be identified for the conventional detector design.

4.8.1 Excess Light Events

As mentioned in section 2.3.4, the surrounding foil provides a veto mechanism which allows to tag β-backgrounds which enter the detector housing from the outside. These β-backgrounds loose a fixed amount of their energy in the detector housing before being absorbed in the target crystal. Thus, an additional and constant light signal is created in the scintillating foil surrounding the target crystal which adds to the ordinary scintillation signal produced because of the absorption of the particle in the target crystal. The amount of additionally created scintillation light is relatively small since the foil has a low scintillation efficiency (i.e. 0.8 % [74]). Accordingly, the size of the additional light signal, which is related to the interaction of external β-backgrounds with the scintillating

foil, is small. For events having an energy >150 keV, no discrimination between ordinary β/γ-interactions solely taking place in the main absorber and events with excess light character is possible. Towards smaller energies, though, the foil related scintillation signal contributes a relevant fraction to the detected light signal, which causes that events belonging to background source have light yields well above 1.

As long the discussed background source has an additional light contribution, it does not impact the sensitivity of a detector module for dark matter searches because, in this case, the light yield of this event class is well above the expected light yield of dark matter interactions Though, the analysis of the data has to be adapted to its presence because an asymmetric tail towards higher light yields is observed in the event distribution. Therefore, the light yield distribution is not well described by a Gaussian in the low energy range. To account for the presence of excess light events, a phenomenologically motivated modification is added to the band description [43]. The excess light event population can be described using equation 4.20:

$$f(x) = \frac{\lambda}{2} \cdot e^{\frac{\sigma_{LY}^2 \lambda^2}{2}} e^{-\lambda(x-LY_c)} \left(1 - erf\left(\frac{-((x-LY_c)-\sigma^2\lambda)}{\sigma_{LY}\sqrt{2}}\right)\right). \tag{4.20}$$

$f(x)$ is a convolution of an exponential decay and an error function which serves to cut off the exponential decay for small light yields. The error function is described with the parameters LY_c and σ_{LY}, respecting the light detector's resolution and the center of the electron recoil band. The exponential decay is parametrized with the decay constant λ.

By adding equation 4.20 to the 2-D likelihood (equation 4.10), the low energy range can be described phenomenologically. This model allows to disentangle events with internal origin from external background, which is necessary to estimate the amount of expected background in the ROI. However, the limited amount of statistics in the low energy region impedes the disentanglement of the backgrounds.

In case no veto system is provided for the β-backgrounds with external origin, these background events remain indistinguishable from ordinary β/γ-interactions in the target. This means, background interactions with external and internal origin are located in the electron recoil band showing no difference in their event signature. Generally, this does not affect the sensitivity of a detector module. However, the energy of these events is shifted to smaller energies because of the energy loss in the detector surrounding. Due to the decreasing discrimination power of a detector module in the low energy range, the sensitivity for dark matter interactions can be affected by this external background contribution because they can add to the backgrounds observed in the ROI for dark matter searches.

Therefore, an alternative method to identify this background class unambiguously and to remove events of this kind from the final data set is desirable. One possibility to achieve this task is the use of an actively read out detector housing. In this case, the identification of an event of this kind is achieved by its direct interaction in the surrounding detector parts. By skipping the intermediate lossy scintillation process as well as the ensuing light collection process, the detected veto signal is assumed to be large and to allow an effective rejection of external β backgrounds.

4.8.2 Performance of the Light Channel

To determine the nature of a particle interaction taking place in the target crystal, the amount of created scintillation light has to be determined precisely. Thus, the performance of the light channel has to provide a good performance to allow an unambiguous particle identification in the low energy range.

As mentioned before, the fraction of energy which is finally detected in the light detector is small compared to the energy deposit into the phonon detector (see section 4.5). Due to the decreasing signal-to-noise ratio for small energy depositions, the relative resolution of the light channel is degraded for small energy deposition in the target crystal. As a result of that and because of the relative nature of the light yield parameter, the light yield bands start to broaden towards smaller energy depositions which prevents the unambiguous particle identification at small energies. Therefore, the light channel is considered the weaker part of a detector module although the performance of the light detector as cryogenic device exceeds the performance achieved by the phonon channel (see section 4.2).

Figure 4.8 illustrates the influence of the light detector's performance on the particle discrimination. The light detector resolution changes by a factor of 3 between the left and the right panel showing the impact on the discrimination power of a detector module.

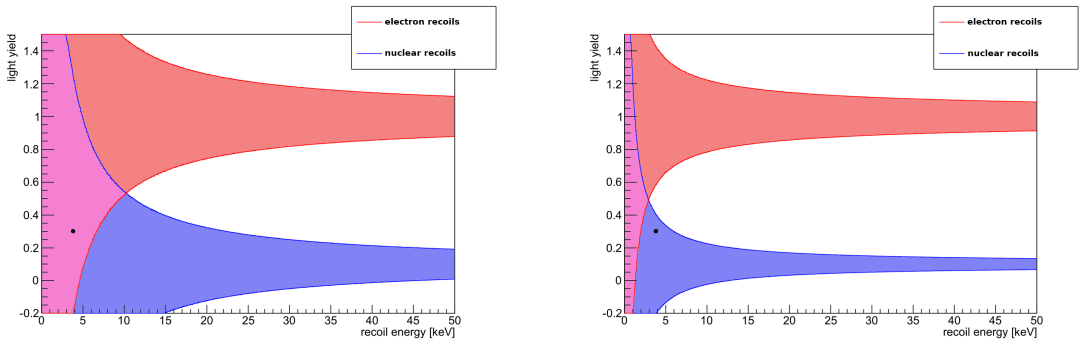

Abbildung 4.8: Scheme to illustrate the dependence of the discrimination power on the performance of the light detector. On the left side, the event (black dot) is located in the purple shade area in which an unambiguous particle identification is not possible. On the right side, the resolution of the light channel is improved by a factor 3. Here, the discrimination power of the detector module is sufficient to identified the same event as nuclear recoil.

The relative resolution of the light channel for a given energy deposition in the target crystal can be influenced positively by improving the performance of the light detector as cryogenic device or by increasing the amount of detected light. Both approaches are investigated during this thesis.

By investigating the influence of the phonon collectors on the performance of thermometers used for the light detectors, an optimization of the light detectors as cryogenic devices is made (chapter 5). To increase the light signal, either the scintillation efficiency

of the target crystal or the light collection efficiency can be improved (see section 4.5.1). Since the scintillation efficiency of the target crystal can be considered as an invariant material property, the influence of the detector design on the performance of the light channel is investigated in the scope of the conventional CRESST-II detector design in the following paragraphs.

Featuring a large target crystal, the conventional CRESST-II detector module is not optimized for the best light collection efficiency. As already discussed, the EDL is defined by the scintillation efficiency of the $CaWO_4$ target crystal and by the light collection efficiency of the detector module. The scintillation efficiency of $CaWO_4$ is 8.3 % [47], the light collection efficiency is measured to vary between 17 and 28 % for the conventional CRESST-II detector modules [48]. Hence, the fraction of energy detected as light (EDL) is $\approx 2.0\%$ in the conventional detector modules.

The light collection efficiency of a detector module mainly depends on the average distance photons travel inside the target crystal before the absorption in the light detector. In addition, the average number of reflections on the surrounding surfaces plays a major role for the probability that a photon reaches the light detector. Hence, during the propagation process of a photon in the detector module, losses because of (re-)absorption in the crystal and the housing reduce the detected light signal.

For a photon propagating in a crystal, the probability p_x for having an absorption or scattering process scales with the traveled distance l according to equation 4.21.

$$p_x = \int_0^l \frac{1}{l_x} \cdot exp(-x/l_x)dl = 1 - exp(-l/l_x) \tag{4.21}$$

The quantity l_x represents scattering length or absorption length of a photon in the medium the photon is propagating. Thus, equation 4.21 can be used to calculate the probability for a photon to travel a certain distance in the target crystal unaffected, using the experimentally derived values of the scattering and absorption length. While the absorption of a photon reduces the amount of detected light signal, the scattering of photons affects the average length a photon travels before absorption. Important to note is that the scattering of photons helps to wash out position dependencies in the scintillation efficiency as well as in the light collection efficiency. On the other hand, the scattering of light in the target crystal enhances the average distance a photon travels before absorption which increases the probability that a photons is lost.

The crystals used as target material are of cylindrical shape. In combination with the high refractive index of $CaWO_4$ (1.92@420 nm) [75], the probability is enhanced that light is trapped within the crystal following infinite paths without the possibility to leave the crystal. This probability of light trapping is further increased by the polishing of the CRESST-II target crystals to optical quality.

Next to the loss processes inside the target crystal, an additional reduction of the light signal is caused by the detector surrounding. The reflective foil used for lining the inner parts of the detector modules is reported to have a high reflectivity ($R > 99\,\%$) [76]. The probability for a photon to be lost during a reflection process is independent of the number of previous reflections and dependents only on the reflectivity R of the surface. Hence, the probability that a photon is lost after a given number of reflections n is

calculated with

$$p_{foil}(n) = R^n. \tag{4.22}$$

In case a large number of reflections is needed to guide a photon to the light absorber, the probability increases that a photon is lost during the propagation. In addition, the presence of non-reflective parts in the direct line of sight to the crystal (i.e. the bronze clamps, TES) causes a further reduction of the light collection efficiency.

To investigate the parameters influencing the light collection efficiency, a dedicated simulation for tracking the photon paths within a detector module has been written in C++ to be run in the ROOT framework. Goal of the simulation is to investigate the different loss processes occurring during the propagation of the photons and to estimate the influence of the detector layout on the detected light signal.

The simulation uses the following approach for each simulated event:

1. Creation of photons: The energy of an event is determined randomly according to the assumed energy spectrum. In this case a flat spectrum is used which allows to apply the parametric band model to the simulation to estimate the performance of a detector design without further adaptations. The location of an event is at a random position in the target crystal. This location serves as starting point for all photons generated during this event. The number of created photons scales according to the scintillation efficiency of $CaWO_4$ (i.e. 8.3 % [47]).. The actual number of created photons is Poisson distributed around the expected average of photons. Each photon has a set of properties: The photon energy (i.e. normal distributed around 420 nm using a FWHM of 40 nm [44]) and the initial direction which is set randomly.

2. Propagation of the simulated photons: The path of each photon is calculated in small discrete steps (0.1 mm) considering the following physical processes:
   - Absorption of the photon in the crystal: The distance to the absorption is determined by dicing a probability between 0 and 1 and calculating the distance the photon is able to propagate in the crystal unaffected using equation 4.21. Once reaching this distance the photon is considered as lost.
   - Scattering of the photon in the crystal: The distance to the next scattering is determined by dicing a probability between 0 and 1 and calculating the distance the photon is able to propagate in the crystal unaffected using equation 4.21. After this distance the photon is equipped with a new random direction and the distance to the next scattering process is recalculated.
   - Transmission/reflection of a photon on a crystal surface: If a photon reaches a crystal surface, the probability for the transmission or reflection of the photon is determined according to the Fresnel laws and the refractive index of the target crystal [77]. Which process is chosen is determined by randomly dicing a probability between 0 and 1 and comparing this value with the probability for reflection/transmission of the photon for the given boundary conditions. Depending on which process is determined, the trajectory of the photon is recalculated according to Snells' law [77].

- Absorption/reflection of a photon on a surface in the detector housing: In case a photon hits a surface of the detector housing, the photon is either reflected or absorbed therein. In case, the photon is transmitted trough the foil, the photon is considered as absorbed. The probability for the reflection of the photon on this surface is implemented in the simulation according to its literature values. For the foil, a reflectivity of 99 % [76] is reported. The other detector parts (i.e. the bronze clamps holding the $CaWO_4$ crystal and the light detector, TES) are considered in the simulation with their respective reflectivities mentioned in reference [77]. By dicing a random probability between 0 and 1, the occurring process is determined by comparing the randomly sampled probability to the actual probability for reflection/absorption. If the reflection of the photon is the process which occurs, the trajectory of the photon is recalculated according to Snells' law. If the photon is absorbed, it is considered as lost.

3. Detection/absorption of a photon in the light detector: In case a photon is able to propagate in the detector housing and the target crystal until it hits the surface of the light absorber, the photon is either reflected or absorbed therein. The transmission of photons through the light absorber is not considered because the probability for this process is less than 1 % in SOS wafers [78]. Which process is taking place is selected randomly based on the reported values for absorption and reflectivity for the light absorber [76]. By dicing a random probability between 0 and 1 and comparing this probability with the reported probability for reflection, the nature of the process is determined (i.e. absorption or reflection). In case, the photon is absorbed in the light detector, its energy is added to the detected light signal. If the photon is reflected, the propagation of the photon is continued in the detector housing using the methods described in point 2.

To achieve results close to reality, the detector geometry inside the detector housing is implemented in full detail. Hence, the clamps holding the absorbers and the TES structures are implemented in the simulation as highly absorbing detector parts. The remaining surfaces of the detector housing are simulated to be covered with foil.

Since the performance of the conventional detector design is well characterized, the simulation is calibrated based on the experimental findings for this detector design (see section 4.7.1). This is necessary since the precise numbers for absorption length l_{abs} and scattering length l_{scat} are only indirectly accessible via the measurement of the attenuation length l_{att} ($1/l_{att} = 1/l_{scat} + 1/l_{abs}$). The attenuation length l_{att} of $CaWO_4$ crystals used within the CRESST-II experiment is reported to vary between 5 and 75 cm with an average value of approx. 12.5 cm [44]. Though, the ratio between scattering and absorption is not precisely known, which is problematic since the impact of these parameters on the result of the simulation is significant. In order to overcome this lack of information, the simulation is run using different values for absorption and scattering length while the attenuation length is kept constant using the average value for this parameter. Intention of the optimization procedure is that the parametric band fit, once

applied to the simulation data, returns the average values of the parameters describing the electron recoil band within an uncertainty of $< 10\,\%$.

The adjustment of the input parameters (i.e.: attenuation length, reflectivity of the foil, absorption probability in the light detector) to match the recorded data turns out to be challenging. If experimentally derived parameters are used for the simulation, the light collection efficiency of the conventional CRESST-II detector module is overestimated by up to a factor of two in respect to the measured light collection efficiency. The shape of the light yield distribution for a given energy interval is well described by the model assumption (i.e. normal distributed), indicating that position dependencies are small. In order to achieve the measured light collection efficiency of 17 and 28 % [48], though, the optical properties of the main absorber and/or the reflectivity of the foil have to reduced. These changes result in a increased amount of position dependencies which cause that the light yield distribution in a certain energy range is usually not well described by a Gaussian. This stands in contrast with the observation made with the conventional detector modules.

Three possible explanations are given in following under the assumption that the simulation code includes all other processes correctly:

1. The absorption probability of the light detector is lower than expected. Measurements of the absorption probability at room temperature report a absorption probability of $\approx 85\,\%$ [78]. In case the absorption efficiency of the light detector is smaller than expected, the average distance a photon travels in the detector housing is increased. This results in a washing out of position dependencies since the average distance traveled by photons becomes large compared to the possible position differences of the starting point. In addition, the overall light collection efficiency is reduced by the longer distance a photon travels before its detection in the light detector.

2. The scintillation efficiency of the target crystal is smaller than expected at low temperatures. In this case, the number of photons created during a particle interaction in the crystal is reduced. Since the number of photons is assumed to be Poisson distributed, the relative uncertainty on the number of created photons is increased. This effect does not solve the problem of the overestimation of light collection efficiency in general but it allows to achieve a Gaussian shape light yield distribution while the losses during the photon propagation in the detector module are increased. In addition, it allows to match the experimental EDL with the EDL derived by the simulation without the need to reduce the light collection efficiency in the detector by increasing the losses in the target crystal and the detector housing.

3. At room temperature the emission spectrum of $CaWO_4$ is centered around a peak with a wavelength of 420 nm and shows a width of ± 40 nm [44]. Therefore, a fraction of $\approx 30\,\%$ of the emitted light is generally lost since the reflectivity of the foil decreases below photon energies of 400 nm rapidly [76]. The reduction is enhanced by a wavelength shift of the scintillation spectrum to higher energies

or by a shift of the foil's absorption edge to larger wavelengths. Both effects can be induced by the low operation temperature of the detectors and have not been investigated in detail up to now.

Despite the fact that is not possible with the present knowledge to explain which of the proposed explanations is the main cause for the discrepancy, the reproducibility of the measured data using a simulation can be considered as satisfying result. The simulation allows to understand the involved loss processes and to investigate the their influence on the light collection efficiency in a given detector geometry.

The results of the simulation of the light propagation in a conventional CRESST-II module are discussed in the following. In order to confirm that the simulation code is able to reflect the detector geometry and the physical processes during the photon propagation in a realistic way, figure 4.9 is given. Figure 4.9 illustrates the simulation output for two cases: A large number of events (1000) and a single event. The color coding allows to illustrate the simulated geometry and to trace the path of a simulated photon.

As mentioned before, the simulation is calibrated to match the performance of an average CRESST-II detector module. After the optimization procedure, the band parameters determined for the simulation vary by $\pm 10\,\%$ to the average values of a conventional detector module (see table 4.1). However, the light collection efficiency determined by the simulation differs from the observed one by a factor of two reaching $\approx (38.9 \pm 10.3)\,\%$ depending on the distance the location of the event has to the light detector (i.e. z direction). The average distance a photon travels inside the detector housing is $\approx (12.3 \pm 2.4)\,\mathrm{cm}$ depending on the assumed crystal quality. On average, 11.2 ± 1.5 reflections on the foil are necessary to guide a photon to the light detector. This number indicates that a large number of reflections on the surrounding foil is necessary to guide a photon to the light absorber. During the propagation, the light signal is reduced due to reflections on the foil ($\approx 43.6\,\%$), re-absorption in the crystals ($\approx 11.5\,\%$) and losses in absorbing materials (i.e. clamps, TES: $\approx 5.9\,\%$).

In figure 4.10, the event distribution of the simulated data is shown in the light yield vs. energy plane. The black line indicate the fit of the simulated data with parametric band fit (equation 4.10).

The following conclusions can be drawn based on the insights gained with the simulation:

- The amount of losses during the photon propagation in the detector housing are large and are able to reduce the number of detected photons by more than a factor of two. Although the used materials were carefully chosen to increase the probability for a photon to be detected, the majority of the created photons is lost during propagation. This finding is confirmed experimentally by measurements.

- Compared to the dimensions of the detector module, the simulation reveals that the average distance a photon travels before absorption is long. Due to the high refractive index and the high symmetry of the target crystal, the probability is large that a photon is trapped inside the target crystal and lost because of reabsorbtion.

- On average, a large number of reflections are necessary to guide a photon to the light detector. Reason for this is that the solid angle the light detector covers when the photon is created strongly depends on the location the event takes place. For locations, which are close to the light detector (i.e. upper part of the target crystal) the solid angle the light detector covers is large. With increasing distance to the light detector, the solid angle the light detector covers becomes smaller which increases the influence of the foil. The reflection and redirection of photons to the light detector is crucial for the light collection and requires a highly reflective detector housing. In addition, a high reflective detector housing is mandatory to avoid large position dependencies in the light collection efficiency.

Most of the named reasons reducing of the amount of detected light signal are related to the design of the CRESST-II detector modules and the components used for building them. Especially, the position of the light detector can be identified as limiting factor for the light collection efficiency. Consequently, a rearrangement of the detector components to achieve a better coverage and to reduce the distance a photon has to travel before detection promises a better performance of the light detector and, thus, a better particle discrimination.

Important to note is that the influence of the scintillation efficiency on the EDL, and consequently on the resolution achieved with the light detector, depends on the energy scale. For intermediate and large energy depositions, the light detector's resolution is dominated by inherent width of the scintillation process in $CaWO_4$, the Poisson statistics (i.e. photon counting) and the position dependence of the light collection efficiency. Thus, in this energy range, the influence of the EDL on the capability to identify the nature of interaction is negligible. In the low energy range, though, in which the light detector's resolution is most important for assuring an unambiguous particle identification in phonon-light detectors, the impact of the EDL is able influence the sensitivity of a detector module significantly.

4.8.3 Non-Scintillating Surfaces

In the conventional CRESST-II detector module, the identification of backgrounds, depositing part of their energy in the detector surrounding, relies on the scintillation mechanism of foil which lines the inner surfaces of the detector housing. Though, there are non-scintillating surfaces in direct line of sight to the target crystal (i.e. bronze clamps). Therefore, the possibility exists that surface related α-decays create a degraded nuclear recoil which can be misinterpreted as possible dark matter interaction (see section 4.7.2).

Since these background events cause an event signature identical to the one expected for dark matter, the veto of this event class is of crucial importance. In case of the conventional detector module, this is not achieved for all circumstances since non-scintillating surfaces are present in direct line of sight to the target crystal. The passive prevention efforts to protect the detectors from the exposure to Rn-contaminated air has proven to be insufficient [43]. Therefore, a fully scintillating detector housing was considered as mandatory for future detector modules to veto this background class. Alternatively, the

surrounding surfaces can be read out actively. In both cases, the detected event signature differs sufficiently to allow a reliable discrimination of this background source.

4.9 Motivation for the R&D work presented in this Work

Based on the results obtained with CRESST-II (Phase 1 & 2), the strategy for CRESST-III was tuned. To achieve the best sensitivity for low mass dark matter, the lowering of the detector threshold was considered the most important R&D goal. This is achieved by reducing the mass of the target crystal increasing the phonon energy density after an energy deposition. Consequently, the detected temperature signal in the TES is enlarged proportionally. Additionally, a fully scintillating detector housing is implemented in the detector design which allows to reject all external backgrounds. More information on this topic is found in reference [79].

In the scope of this thesis, the development of detector modules for larger dark matter masses is in focus. For the detector concept used to probe this region of the dark matter parameter space, several limitation have been identified.

First, the performance of the light detector as cryogenic particle detector can be improved by optimizing the dimensions of the phonon collectors. Therefore, the efficiency of the phonon collectors used for improving the performance of the light detector is investigated in order to optimize the used thermometers. The main intention of the measurements is to characterize the diffusion properties of quasiparticles in the currently used phonon collectors made of aluminum. Therefore, a dedicated setup for measuring the diffusion properties of quasiparticles in the superconducting phonon collectors was operated. The results of these measurements are presented in chapter 5.

Second, the detector design of the standard CRESST-II detector was found to have conceptual flaws (see section 4.8). These are the poor light collection efficiency, which is related to the disadvantageous arrangement of the detector components, and the presence of non-scintillating surface in direct sight to the target crystal. Based on the identified weaknesses, two new detector concepts were developed, tested and analyzed for this work. For both detector concepts, the amount of background events leaking in the ROI for dark matter searches is expected to be reduced by improvements made by the design changes. In addition, both detector designs feature new detector design concepts which can be used to improve the performance of the current generation of CRESST detector modules (i.e. CRESST-III [80]). The characterization and evaluation of these newly developed detector concepts are presented in the chapters 6 and 7.

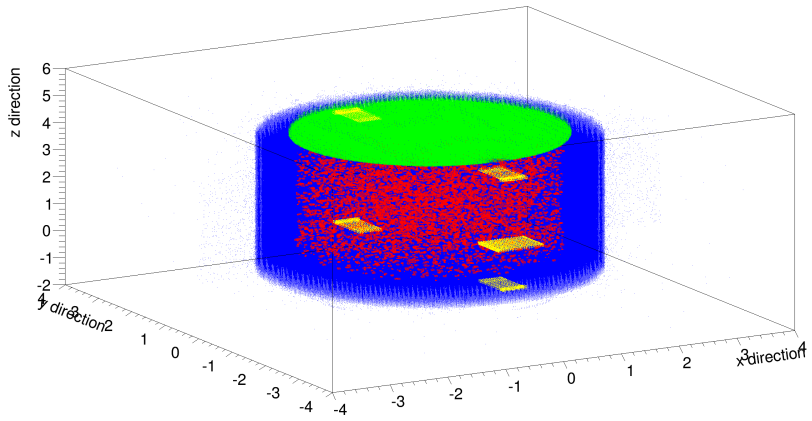

(a) Simulation of multiple events, each creating a large number of photons.

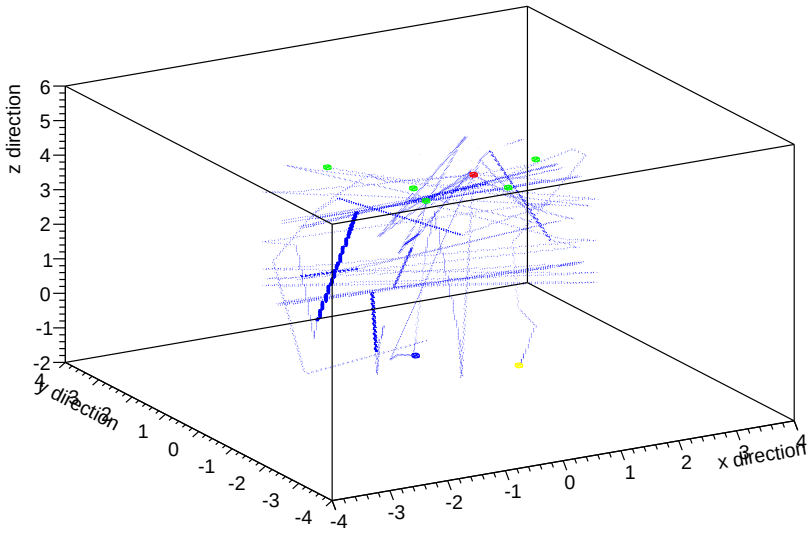

(b) Simulation of a single event, creating 20 photons.

Abbildung 4.9: Simulation output to confirm the simulated detector geometry and the processes occurring during the photon propagation. The colors respect different event types to illustrate the effects. In red the starting positions of the photons in the crystal are shown. In yellow, non-reflective detector parts are shown (i.e. clamps, TES). In green the location is shown where a photon is absorber in the light detector. In blue the traces of the photons are indicated. Reflections on the foil are not shown for clarity reasons. In case, a large number of events in simulated, the color coding allows to confirm the implemented detector geometry (left side). If a single event is simulated, the trajectories of the simulated photons can be illustrated (right side).

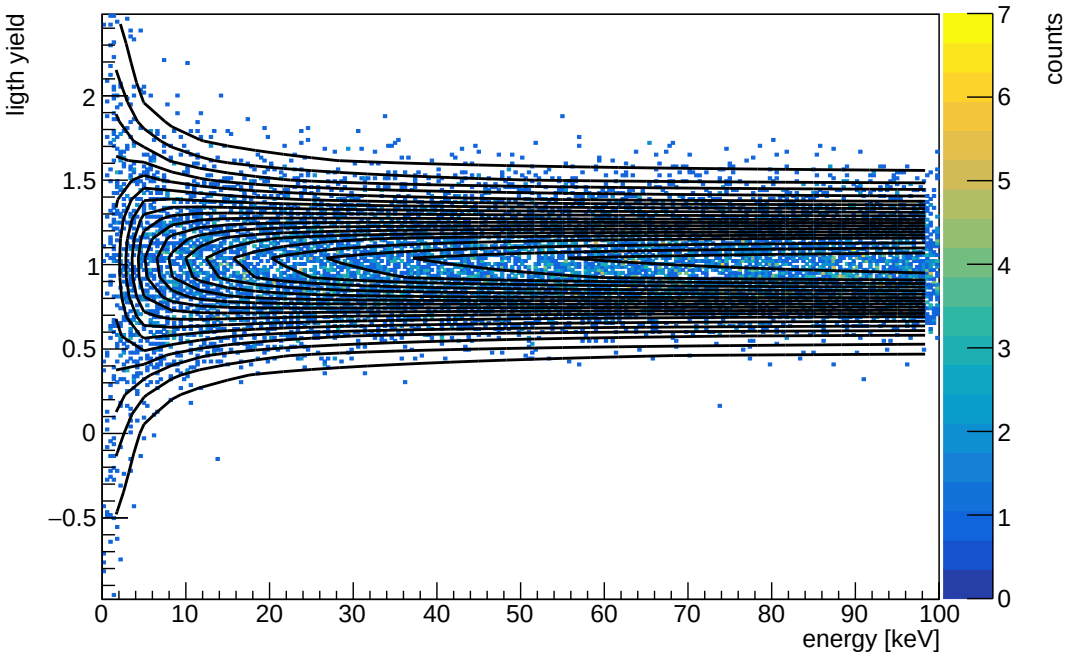

Abbildung 4.10: Event distribution of the simulated data in the light yield vs. energy plane for the conventional CRESST-II detector module. 10000 events with an energy between 0 and 300 keV are simulated. The black lines indicate the 2-D likelihood fit using equation 4.10.

5 Quasiparticle Diffusion in Superconducting Phonon Collectors

Phonon collectors are superconducting films meantd to improve the sensitivity of a TES by increasing the collection area of the thermometer without increasing its heat capacity. By doing so the sensitivity of a TES is increased by an additional signal contribution generated in the phonon collectors (see section 3.3).

The additional signal contribution is generated by non-thermal phonons which enter the superconducting film serving as phonon collector in which they break Cooper-pairs to quasiparticles (i.e. free electrons[1]). The generated quasiparticles propagate within the superconducting material until they recombine or eventually interact with the electron system of the TES contributing to the temperature rise of the latter.

Crucial for the operation of phonon collectors are the diffusion parameters of the quasiparticles in the superconducting film. To contribute to the detected temperature signal, generated quasiparticles have to achieve diffusion lengths sufficiently long to cover the distance necessary for reaching the TES. In case a generated quasiparticle is lost by recombination, the energy contribution to the signal from the phonon collectors is reduced. The recombination process is promoted by lattice defects and surface scattering. Therefore, the quality of material used as phonon collectors is crucial for assuring a good performance of the system.

To determine the diffusion properties of the quasiparticles in the phonon collectors used by CRESST-II, a dedicated setup is developed. By measuring the quasiparticles contribution to two individually operated TESs connected by a single phonon collector, the diffusion parameters are determined for the current generation of the CRESST-II thermometers.

5.1 Setup for Determining the Diffusion Properties of Quasiparticles

To measure the diffusion length of quasiparticles in the phonon collectors used for the CRESST-II light detectors a dedicated detector layout is used (see figure 5.1). A first version of this setup was developed within the CRESST experiment about a decade ago [62] [81].

A new characterization campaign has been become necessary because the aluminum films, which are used in CRESST-II as phonon collectors, improved in quality during

[1] The electrons are still bound in the lattice of the superconducting material.

the last years due to an optimized production process. Therefore, the setup used for this measurement is equipped with a phonon collector which is identical to the current generation phonon collectors used within CRESST-II. The goal of this measurement is the determination of the diffusion parameters of quasiparticles in the superconducting aluminum films in order to find the optimal dimensions for the phonon collectors.

In figure 5.1, the setup used for the measurement is shown.

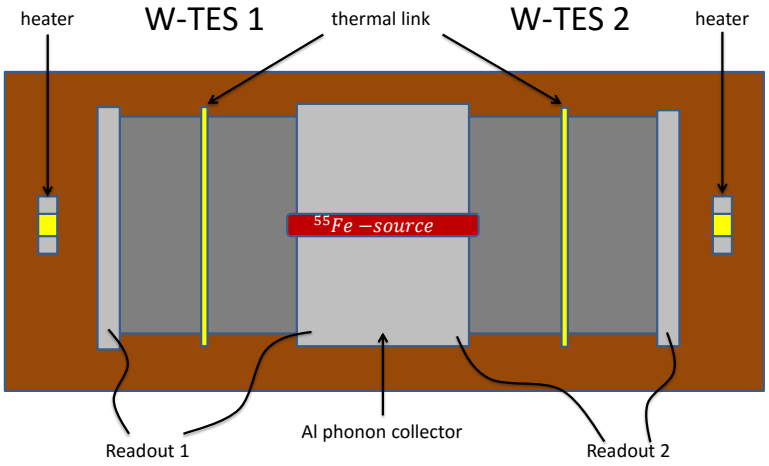

(a) Scheme of the setup.

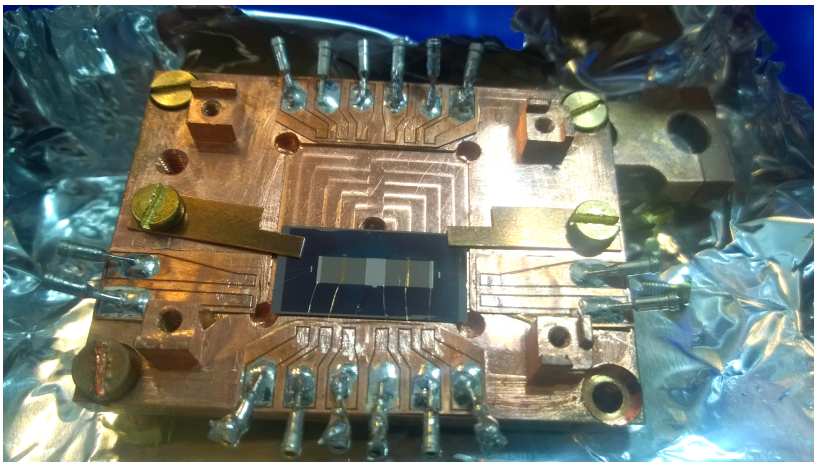

(b) Photograph of the setup. The cover with the slit is removed to allow a view on the setup.

Abbildung 5.1: Experimental setup for the measurement of the diffusion length in CRESST light detectors. A silicon carrier is equipped with two tungsten TESs (dark grey) that are connected with a single superconducting aluminum phonon collector (light gray).

The setup is produced on a silicon substrate on which two tungsten TESs are evaporated. Each covers an area of (8x6) mm^2 having a thickness of 200 nm. The two thermometers are connected with a single phonon collector made of aluminum. Below the aluminum, the tungsten film is continued to reproduce the same configuration used for the CRESST-II light detectors. There, the tungsten underneath the phonon collector is placed to increase the film quality of the aluminum (i.e. a higher rest resistivity ratio is measured). The aluminum film has the same film properties as the phonon collectors used for CRESST-II thermometers. Hence, it is produced using an high vacuum, electron beam evaporation system to achieve the best film quality possible. The phonon collector has the dimensions (4x6) mm^2 and a thickness of 1 μm. Due to the low thermal conductance of the superconducting aluminum phonon collector at the typical operation temperature of the TES, the TES can be operated individually, even if their transition temperature T_C is different. The tungsten film below the phonon collector becomes superconducting due to the proximity effect and can be considered as part of the phonon collector. A strong thermal link is provided for each TES via a gold stripe and a gold bond located in the middle of each TES. With this configuration, a fast relaxation to thermal equilibrium after a energy deposition is guaranteed and allows a high event rate (>10 Hz). To allow the stabilization in the correct operating point each TES is equipped with an electrically and spatially separated heater. The phonon collector is illuminated with a X-ray source (i.e. ^{55}Fe) through a slit with a width of 0.5 mm and a length of 5 mm.

By using only a thin slit for the illumination of the phonon collector, the diffusion and decay of a given quasiparticle population can be modeled using a 1-D diffusion equation (more information on the model and the solution of the diffusion equation is found in the references [62] and [82]):

$$\frac{\delta n(x,t)}{\delta t} = \frac{n(x,t)}{\tau_{qp}} - D \cdot \frac{\delta^2 n(x,t)}{\delta x^2}. \tag{5.1}$$

In equation 5.1, the quasiparticle density $n(x,t)$ is described at the position x and for the time t using two terms (right side of equation 5.1). The first term describes the time evolution of the quasiparticle density using the inverse of quasiparticle lifetime τ_{qp} as the decay constant. The second term describes the position dependence of the quasiparticle density using the diffusion constant D. The diffusion constant D allows to calculate the distance l a quasiparticle travels within a time t:

$$l(t) = \sqrt{D \cdot t}. \tag{5.2}$$

The maximal distance a quasiparticle is able to diffuse before it recombines and is lost is defined as the diffusion length l_{diff}: It is calculated with

$$l_{diff} = \sqrt{D \cdot \tau_{qp}}. \tag{5.3}$$

.

A solution of $n(x,t)$ is derived using the approach presented in [62] [82]. The following boundary conditions are needed to find an explicit solution for $n(x,t)$:

1. Before an energy deposition in the film, the quasiparticle density at the locations of the TES 1 ($x = 0$) and TES 2 ($x = L$) is zero:

$$n(x, t = 0)|_{x=0,L} = 0. \tag{5.4}$$

2. In case of an energy deposition in the film, the created number quasiparticles N_0 at the location of the absorption $x_a \in [0, L]$ is point like:

$$n(x, t = 0) = N_0 \cdot \delta(x - x_a). \tag{5.5}$$

By separating $n(x, t)$ into the components describing the position $X(x)$ and the time $T(t)$ independently, the following ansatz can be used:

$$n(x, t) = T(t) \cdot X(x). \tag{5.6}$$

The solution for $n(x, t)$ is derived in references [62] and [82], including detailed information on the respective terms. Here, only the final solution is given:

$$n(x,t) = \frac{2N_0}{L} \sum_{k=1}^{\infty} \underbrace{e^{-\left(D\cdot(2k+1)^2\cdot\frac{\pi^2}{2L^2}+\frac{1}{\tau_{qp}}\right)\cdot t}}_{T(t)} \cdot \underbrace{\sin\left((2k+1)\cdot\frac{\pi}{2L}\cdot x_a\right)\cdot\sin\left((2k+1)\cdot\frac{\pi}{2L}\cdot x\right)}_{X(x)}. \tag{5.7}$$

The sum over k is introduced to consider all possible solutions and can be considered as the available modes in the system.
The energy detected in the TES located at the position $x = 0$ of the setup after a energy deposition at the position x_a corresponds to the sum of all quasiparticles detected therein. This number is calculated by integrating the flux of quasiparticles at the location of the TES (i.e. $D \cdot \delta n/\delta x|_{x=0}$) over time.

$$N = D \int_0^{\infty} \frac{\delta n(x = 0, t)}{\delta t} dt. \tag{5.8}$$

To solve equation 5.8, $\delta n/\delta t$ is calculated from equation 5.7:

$$\frac{\delta n(x = 0, t)}{\delta t} = \frac{N_0\pi}{L^2} \sum_{k=1}^{\infty} (2k + 1) e^{-\left(D\cdot(2k+1)^2\cdot\frac{\pi^2}{(2L)^2}+\frac{1}{\tau_{qp}}\right)\cdot t} \cdot \sin((2k + 1) \cdot \frac{\pi}{2L} \cdot x_a) \tag{5.9}$$

This allows to derive the final result for the number of detected phonons in the TES located at $x = 0$.

$$N = D \cdot \frac{N_0\pi}{L^2} \cdot \sum_{k=1}^{\infty} \frac{(2k + 1) \cdot \pi/(2L)}{D \cdot (2k + 1)^2 \cdot \pi^2/(2L)^2 + 1/\tau_{qp}} \cdot \sin((2k + 1) \cdot \frac{\pi}{2L} \cdot x_a) \tag{5.10}$$

This expression can be found in reference [72] as series expansion of

$$N = N_0 \frac{\cosh(\alpha(1 - \frac{x_a}{L}))}{\cosh(\alpha)}. \tag{5.11}$$

In equation 5.11, the parameter $\alpha = L/\sqrt{D \cdot \tau_{qp}}$ is able to describe the quasiparticle diffusion properties as well as the signal losses in a phonon collector with the dimension L. In a more visual approach, the parameter α can be interpreted as the ratio between the length of the setup L and the diffusion length $l_{diff} = \sqrt{D \cdot \tau_{qp}}$.

The energy detected in TES 2 (i.e. $x = L$) is calculated using same approach which results in a change of sign. Additionally, one can perform a coordinate transformation to derive a symmetrical solution for the setup coordinates which extend from $x \in [-L/2, L/2]$. The final result for the number of quasiparticle detected in TES 1 or TES 2 is

$$N_{1,2}(x_a, \alpha) = N_0 \frac{\sinh\left(\alpha(\frac{1}{2} \mp \frac{x_a}{L})\right)}{\sinh\alpha}. \tag{5.12}$$

The solution of $n(x,t)$ (equation 5.7) assumes that the interaction of the quasiparticles at the location of the TES is highly effective. This means, that a quasiparticle, once reaching the location of a TES, is in any case absorbed therein and that the possibility of back diffusion into the phonon collector does not exist. To account for the possibility of back diffusion of quasiparticles into the phonon collector, $n(x,t)$ would have to be adapted. The process for deriving the solution of $n(x,t)$ for this special case is based on the same methods used to find equation 5.7. In references [83] and [62], a detailed discussion is found on finding the solution for this case. The final solution for the expected signals in the TES 1 and 2 is, in case the back diffusion of quasiparticles is considered,

$$N_{1,2}(x_a, \alpha, \beta) = N_0 \frac{\sinh(\alpha(\frac{1}{2} \pm \frac{x_a}{L})) + \beta\cosh(\alpha(\frac{1}{2} \pm \frac{x_a}{L}))}{(1+\beta^2)\sinh(\alpha) + 2\beta\cosh(\alpha)}. \tag{5.13}$$

In equation 5.13, the parameter $\beta = \tau_{tr}/\tau_{qp}$ is introduced to account for the possibility for back diffusion. It is defined as the ratio of time constants τ_{tr} , i.e. the time scale a quasiparticle needs to interact with/to be trapped by the electron system of the TES, and τ_{qp}. In case no back diffusion is observed, i.e. $\tau_{tr} \to 0$, β converges to zero and equation 5.13 is reduced to equation 5.12.

Based on the signals detected in the two TES $N_{1,2}$, the position x_a is calculated using equation 5.14.

$$x_a = \frac{L}{2\alpha}\ln\left(\frac{N_1 \cdot (1-\beta) \cdot e^{-\alpha/2} + N_2 \cdot (1+\beta) \cdot e^{+\alpha/2}}{N_1 \cdot (1-\beta) \cdot e^{+\alpha/2} + N_2 \cdot (1+\beta) \cdot e^{-\alpha/2}}\right) \tag{5.14}$$

Hence, the position of the initial energy deposition can be reconstructed based on the detected signals.

To test the influence of the individual parameters on the diffusion, one can calculate the detector response of the setup for a given set of parameters. In case the phonon collector is illuminated with a mono energetic source, a signal distribution is expected as depicted in figure 5.2. Due to the loss of quasiparticles during the diffusion process in the phonon collector, the sum of the signals is not constant for all absorption locations x_a ($N_1 + N_2 \neq N_0$). Therefore, the total signal is smaller for events which are equally distant to the two TES readout channel. This is reflected in figure 5.2 by the curved

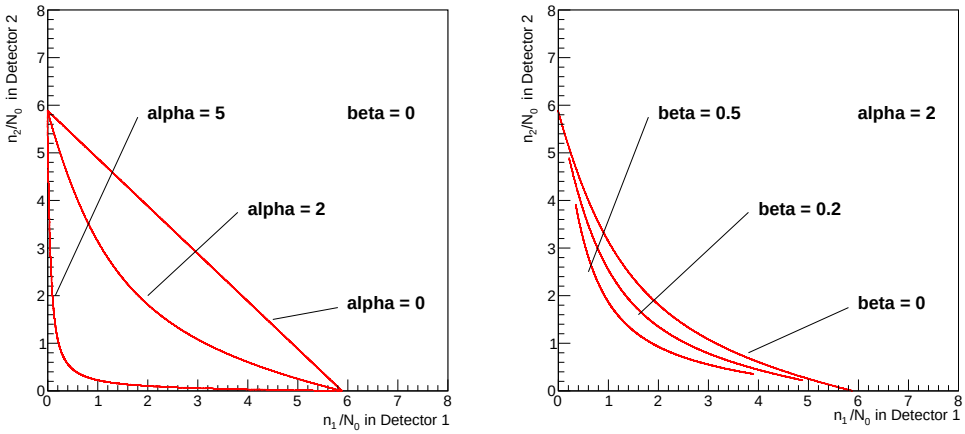

Abbildung 5.2: Calculation of the distribution of mono-energetic events randomly distributed through the slit of the diffuision setup for different values of α (*left*) and β (*right*). The shape of the event distribution strongly depends on the two diffusion parameters and allows the extraction of each parameter with high precision.

event distribution when $\alpha > 0$. The shape of the event distribution of mono-energetic events strongly depends on the parameters α and β and allows to extract these two parameters by fitting the data with equation 5.15.

$$N_2(\alpha, \beta, x_a) = -N1 \cdot \frac{N_2 \cdot (1+\beta) \cdot e^{+\alpha/2} - N_1 \cdot (1-\beta) \cdot e^{-\alpha/2} \cdot e^{\frac{2\alpha x_a}{L}}}{N_1 \cdot (1-\beta) \cdot e^{-\alpha/2} - N_2 \cdot (1+\beta) \cdot e^{+\alpha/2} \cdot e^{\frac{2\alpha x_a}{L}}} \tag{5.15}$$

Systematic errors introduced by the fit routine are negligible compared to the uncertainties introduced by the experimental setup during the determination of the absorption point x_a and the uncertainty introduced by the intrinsic detector resolutions (see results presented in section 5.2).

With the determination of the parameter α, the diffusion length l_{diff} is determined unambiguously since $\alpha = L/l_{diff}$. However, the diffusion constant D and the quasiparticle lifetime τ_{qp} are not unambiguously defined with α. To derive these parameters, it is required to derive either D or τ_{qp} with an independent method.

The diffusion constant can be derived independently using the following approach [62]. The time the first quasiparticles need to reach a TES is defined solely by the speed of the diffusion process of a quasiparticle population in the film and not by the losses occurring during the diffusion. Hence, the group velocity and the mean free path of the quasiparticles in the phonon collector define the time the first quasiparticles require to arrive in the TES while the other parameters describing the diffusion process are irrelevant. Therefore, the measured onset difference between the signals in the two TES of the setup (Δt_{on}) can be used to determine the diffusion constant D in a independent way. To relate Δt_{on} with the diffusion constant D, equation 5.7 is solved with $1/\tau_{qp} = 0$ using the same approach as outlined before. This simplification is possible because the

quasiparticles which cause the first signal in the respective TES are not influenced by the quasiparticle lifetime τ_{qp} or a reduced probability to interact with the TES.

By deriving the steepest point of $N_{1,2}(x_a, t)$ (equation 5.13) numerically, the onset difference Δt_{on} can be written as function of the position of absorption x_a. By fitting this function to the experimentally derived onset difference Δt_{on}, one can derive the diffusion constant $D = L^2/\Delta t_{on}$ without any further dependencies (see figure 5.3). If the experimental independent time parameter $\tau = D/L^2 \cdot t$ is introduced for the fit routine, the determination of the diffusion constant D can be achieved independently from the available diffusion length L the respective setup provides.

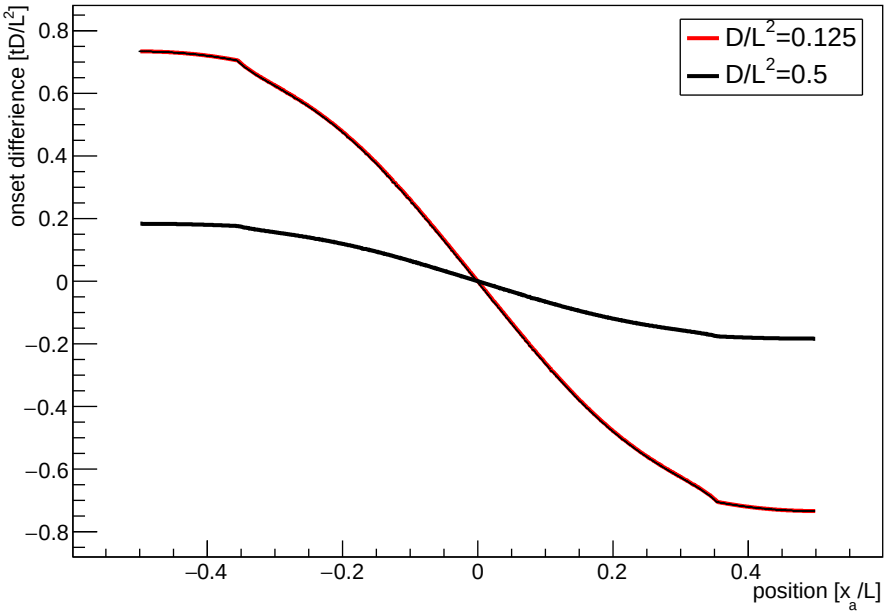

Abbildung 5.3: Numerically derived onset difference for $D/L^2 = 0.5$ (black) and $D/L^2 = 0.125$ (red). Due to the uncertainties introduced by the numerical determination of this parameter, the smoothness of the curve is not fully given at boundary regions of the curve. On the y-axis the values are given in $\tau = D/L^2 t$ while on the x-axis the values are given in x_A/L

5.2 Results

During this thesis, four independent measurements were performed with the same detector layout described in section 5.1. This was done to determine the diffusion properties of the currently used phonon collectors in independent measurements and to confirm the results.

In the following, the analysis sequence for the first measurement is shown in detail. The other measurements performed during this investigation are analyzed using the same methods.

For the analysis, several, energy independent quality cuts are applied to the raw data. These cuts are intended to select only events with a valid signature for the following analysis. Since the statistics is not a limiting factor during the analysis, the accidental removal of valid events does not limit the capability to determine the diffusion properties of the quasiparticles in the phonon collector. This allows to apply a rigorous data selection policy.

Figure 5.4 shows the data set after applying the quality cuts.

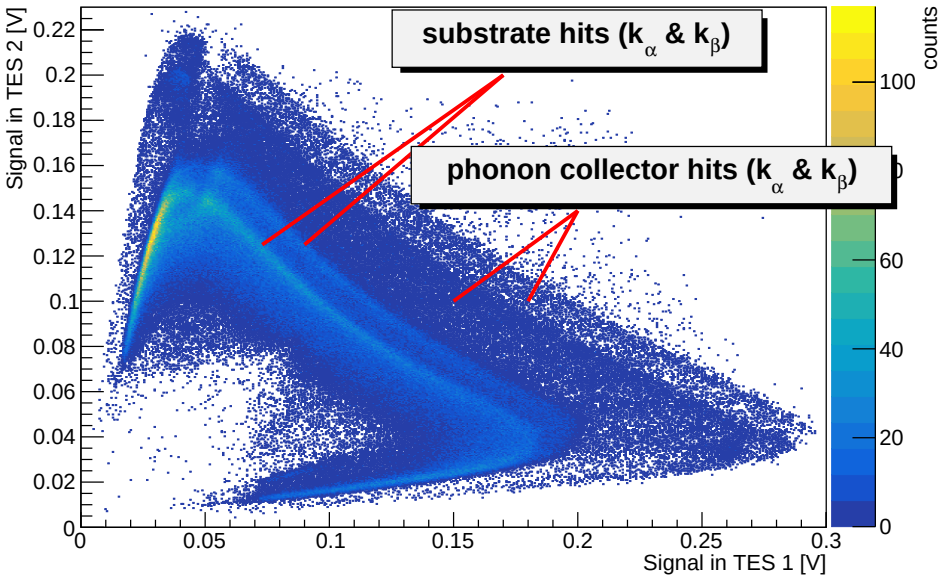

Abbildung 5.4: Data set of the measurement #1 after the application of all quality cuts. Different event population are identified for the respective interaction processes.

In the scatter plot, the characteristic X-ray energies of a ^{55}Fe-source (5.89 keV & 6.49 keV [67]) can be identified for two cases: Either the energy of the X-ray is absorbed in the phonon collector or in the silicon substrate underneath. All four event populations show the expected shape (see section 5.1). The size of the detected signal scales inversely to the distance between the location of the energy deposition and the thermometer. Due

to the losses during the signal propagation in the setup, the events are not located on a straight line but on bended curve (see also figure 5.2).

A position dependent detector response is observed for phonon collector hits as well as for substrate hits. This indicates, that due to the small absorber volume and the large area the thermometer covers, the initial phonon evolution is affected (see section 3.1.1). While for large absorbers the non-thermal phonon population fills the volume homogeneously before a significant part of them is absorbed in the thermometer, this is not the case for this setup. Here, the collection of the phonons in the thermometer structure is fast which prevents that the energy flow from the substrate to the thermometer is homogeneously distributed over the full collection area. Therefore, a position dependent detector response is observed for phonon collector and substrate hits.

For the following analysis, only phonon collector hits are used since these contain the information necessary to extract the parameters describing the diffusion of quasiparticles therein. Substrate hits and phonon collector hits can be separated from each other by using pulse shape analysis because significant pulse shape differences are observed between these two event classes.

The ratio of the observed events in phonon collector and substrate corresponds to the absorption probability of the emitted X-rays in the phonon collector film (i.e. aluminum) with this thickness. For an aluminum film with a thickness of $10\,\mu$m, a transmission probability of 0.946 is calculated for X-rays with an energy 6 keV. The probability for a direct interaction in the tungsten TES is negligible for the film thickness of 200 nm (< 0.0005).

For the extraction of the parameters α and β from the recorded data, only the shape of the event distribution is relevant. Variations in the local intensity, as they are observed in figure 5.4, are not relevant for this analysis, meaning, the inhomogeneous illumination of the phonon collector by the ^{55}Fe source is not affecting the determination of the diffusion properties.

Each event population shows an abrupt decrease of pulse height when the outer regions of the setup are hit. Especially, direct TES hits in the outer regions of the illumination area are observed with a reduced pulse height. The reduction of the detected signal height is caused by the local vicinity of the thermal link which removes the energy fast from the thermal system via the gold bonds. Hence the energy leaves the thermometer system before a signal is developed which causes that a reduced signal height is detected in both thermometers.

In figure 5.4, one can observe that both event populations do not reach the respective axis. Although an event occurs at a large distance from a TES, it is still able to induce a significant signal in therein. A relation of this effect to a reduced collection efficiency of the TES and the observation of back diffusion (i.e. $\beta > 0$) is ruled out because both event populations (i.e. substrate hits and phonon collector hits) show this behavior. By comparing events depositing energy in close and far distance from the TES in regard of their pulse shape, a possible explanation can be given [62]. Both event types are shown in figure 5.5.

Based on the pulse model introduced in section 3.1.2, the signal components of the recorded pulses are separated and analyzed. Events which occur in close distance to a

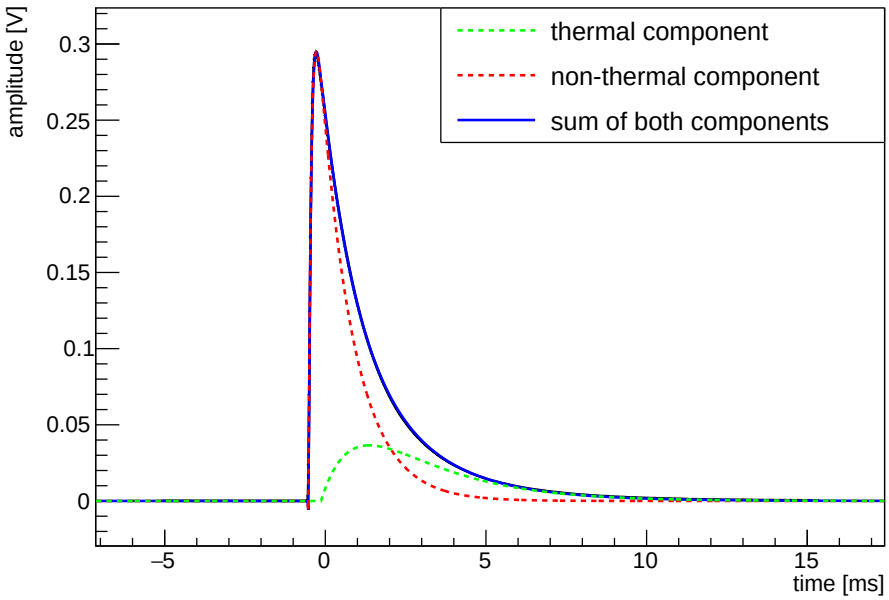

(a) Signal in close distance.

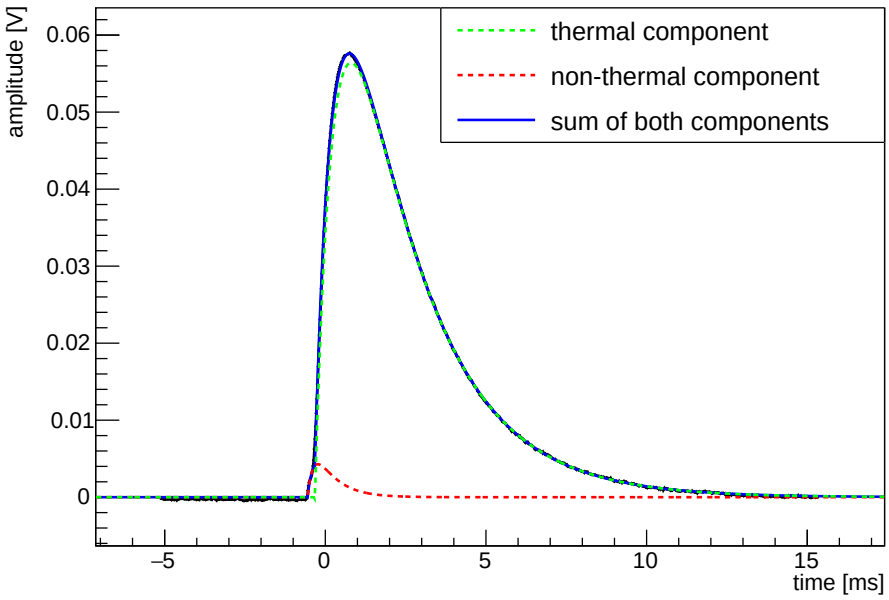

(b) Signal in large distance

Abbildung 5.5: Standard events created for events detected in close and large distance to a TES. In addition, the non-thermal and thermal signal components are shown.

TES feature a large, fast non-thermal component in the recorded signals. On the other hand, events which occur at a large distance show only small non-thermal component while the slower, thermal component dominates the observed signals.

The observation that phonon collector hits occurring at a large distance to the detecting TES feature a dominating thermal signal component indicates that the detected signal is mainly caused by the transmission of energy via the substrate while the signal contributed via the direct absorption of quasiparticles in the TES is small. This observation is in agreement with the general concept of the phonon collectors and the experimental setup used in this scope. The signal contributed by the phonon collectors to the complete detected signal scales according to the distance the quasiparticles have to diffuse on the phonon collectors. Hence, events occurring at a large distance to the detecting TES experience only a small signal contribution via the phonon collector while the dominant signal fraction is detected via the energy flow through the substrate. Since for these events a very small non-thermal signal component is confirmed, one can state that the available length in the setup provides for the diffusion of quasiparticle is longer than the actual diffusion length of the quasiparticles in the aluminum film.

Based on the considerations mentioned in the passage above, the non-thermal signal component reflects the diffusion of quasiparticles in the phonon collector, while the thermal component is dominantly caused by the energy flow via the substrate. For the determination of the diffusion properties, only the non-thermal signal component of direct phonon collector hits is used (see figure 5.5). This signal contribution is determined by fitting the events with the pulse model introduced in section 3.1.2.

In figure 5.6, the final data set for deriving the diffusion length is shown. The plot shows the amplitude of the non-thermal signal component in the two readout channels of the ^{55}Mn k_α (black) and k_β (red) event populations interacting phonon collector. In addition to the data points, the best fit lines with equation 5.15 to extract fit parameters α and β are shown. To account for the sensitivity variations between the two TESs, an experimental scaling factor is introduced. This linear scaling factor is used to normalize the pulse height for events that have the same distance to the detecting TES. It does not affect the determination of parameters α and β.

As expected, the signal detected for events happening far from a TES is close to zero. Hence, the diffusion length of the quasiparticles is too short to create a significant additional signal contribution in the distant thermometer. For the parameter α, an average value of 1.720 ± 0.095 is extracted from the two isolated event populations. Based on this value the diffusion length l_{diff} is calculate to be $(2.23 \pm 0.05)\,\mathrm{mm}$. The values derived for β are smaller than 10^{-5} for both event populations. Thus, the collection of quasiparticles, once reaching the TES, is efficient while the back diffusion into the phonon collector is negligible.

For both values, the uncertainty introduced by the fit is in the permille range for each event population. Since two event populations are available, the determined values for α and β reflect the average of both. Though, there are additional systematic uncertainties. These are introduced, for example, by the assumption that the absorption of quasiparticles in the thermometer is the only reason for the detected non-thermal signal amplitude and no significant non-thermal signal is contributed via the substrate. Furthermore, the

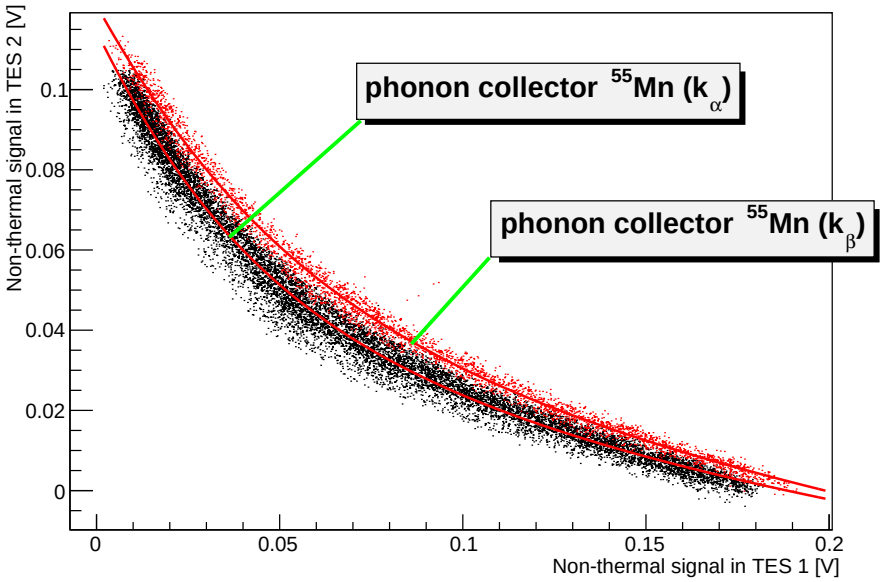

Abbildung 5.6: Scatter plot of the non-thermal signal amplitude of phonon collector hits in diffusion setup 1. Events that are assigned to the X-ray emission of ^{55}Mn k_α emission are marked in black, events assigned to the X-ray emission of ^{55}Mn k_β emission are marked in red. The best fit, using equation 5.15, is shown as red line.

detector resolution as well as the uncertainty introduced to determine the position of an event x_a accurately have to be considered. The position of the energy deposition x_a is determined from the data shown in figure 5.4 using equation 5.14. The uncertainty for this quantity is defined by the energy resolution of the TES. This is determined using the limited range of $x_a = 0 \pm 0.025L$ (i.e. the central part of the illuminated phonon collector) to be 4.8% (TES 1) and 5.1% (TES 2) for an energy of 5.89 keV.

The reconstructed location where the events take place x_a is used to determine the diffusion constant D. To extract the diffusion constant D with the observed onset difference of correlated signals, Δt_{on} is plotted as a function of the position where the energy deposition took place x_a. An onset difference for correlated signals is only observed for phonon collector hits, while for substrate hits no onset difference is observed. Figure 5.7 shows the onset difference Δt_{on} of all phonon collector hits in the first measurement. An onset difference Δt_{on} of 0.363 ms is derived by fitting for this measurement. The uncertainty of the fit procedure is 1.2 %. The determination is limited by the sampling rate of 20 μs which prevents a better precision in the measurement of Δt_{on} due to the quantization of data in the onset difference values.

By using the numerically derived onset difference (see figure 5.3) and by comparing this value with the experimentally derived Δt_{on} , the diffusion constant is derived with $D = 8.45 \cdot 10^{-3}\,\mathrm{m^2/s}$. With the diffusion length l_{diff}, extracted from the data shown in figure 5.6 using the parameter α, a quasiparticle lifetime of 0.692 ms is calculated.

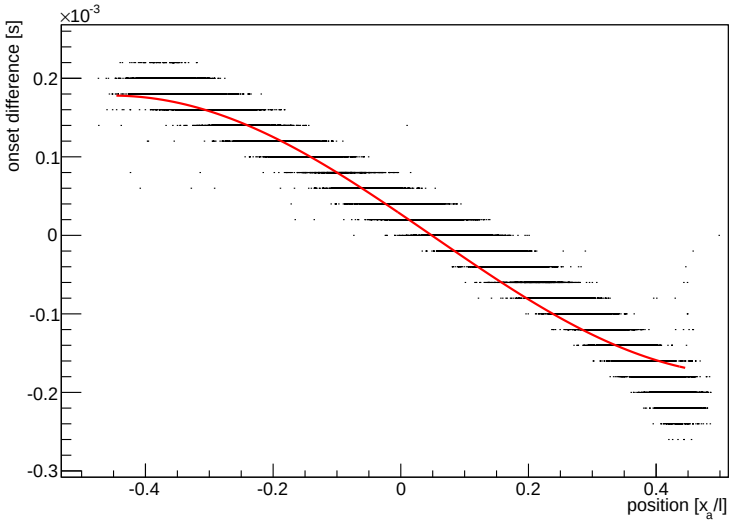

Abbildung 5.7: Onset difference of the events shown in figure 5.6 plotted in respect of their initial position x_a. The best fit of the data is shown in red.

As mentioned before, the measurement was carried out four times using four different detectors with the same layout. Using the same approach as for the first measurements, the results of the all measurements are summarized in table 5.1.

#	α	Δt_{on} [ms]	D [m^2/s]	τ_{qp} [ms]	l_{diff} [mm]
1	1.72 ± 0.095	0.363 ± 0.004	$(8.45 \pm 0.23) \cdot 10^{-3}$	0.692 ± 0.023	2.23 ± 0.05
2	2.33 ± 0.12	-	-	-	1.72 ± 0.03
3	1.610 ± 0.083	0.129 ± 0.003	$(2.28 \pm 0.13) \cdot 10^{-2}$	0.272 ± 0.017	2.48 ± 0.06
4	3.42 ± 0.14	0.821 ± 0.012	$(3.78 \pm 0.21) \cdot 10^{-3}$	0.361 ± 0.019	1.16 ± 0.5

Tabelle 5.1: Summary of the results of four individually performed measurements of the diffusion properties of quasiparticles in CRESST-II like phonon collectors. An explanation for the missing values for measurement 2 is found in the text.

The diffusion lengths determined with the measurements are $\mathcal{O}(> 2\,\text{mm})$ and exceed previous expectations. Large variations are observed for the diffusion constant D and the quasiparticle lifetime τ_{qp}. This indicates that these parameters are highly sensitive to the individual film quality of the phonon collectors.

In three out of four measurements, the diffusion constant D can be extracted from the experimentally derived onset difference Δt_{on} while in the remaining measurement no onset difference is observed. Since the parameter α can be extracted from the data, the diffusion length l_{diff} is unambiguously defined. Though, the diffusion constant D and the quasiparticle lifetime τ_{qp} cannot be determined because no onset difference Δt_{on} is observed. Two possible explanations can be proposed for the outlier. Either the

diffusion is extremely fast in this measurement and generated quasiparticles diffuse and thermalize in TES within a time scale that an onset difference cannot be resolved by the data acquisition. In this case one can assume that τ_{qp} is significant larger than the time the quasiparticles need to interact with and thermalize in the TES. Alternatively, the diffusion of quasiparticles in the phonon collector is extremely impeded. Generated quasiparticles recombine fast and transmit their energy dominantly to the substrate. In this case an onset difference cannot be measured because the signal caused in the TES is dominated by the energy flow to the thermometers via the substrate. Consequently, no signal contribution is created by the absorption of quasiparticles in the TES. Since in all other measurements no onset difference is observed for substrate hits, this explanation is favored.

The results in all four measurements show that the process of the quasiparticle diffusion in the investigated aluminum films is slower than theory predicts. Since the diffusion length is long, the lifetime of the quasiparticles τ_{qp} has to be long, too (see equation 5.3). These findings stand in contrast with the theory. The diffusion length of quasiparticles can be estimated using the residual resistivity ratio (RRR) of the aluminum films using the band theory. The free mean path is calculated based on the known diffusion length of electrons in aluminum at room temperature and in bulk material ($l_{RT} = 411\,\text{Å}$) [62]. At low temperatures, the upper limit for the diffusion length is $l_{diff} = RRR \cdot l_{RT}$. Since for the aluminum films used for these measurements a RRR between 50-90 is measured, the theoretical l_{diff} can be estimated with $2.1 - 3.7\,\mu$m. By using this theoretical approach to calculate the diffusion constant $D = l_{diff} \cdot v_g/3$ [62][2], diffusion constants of $D = 0.14 - 0.24\,\text{m}^2/\text{s}$ are predicted. Thus, diffusion constant is expected be at least $\mathcal{O}(10)$ larger in the measurements carried out in this thesis.

The mean scattering lengths of quasiparticles in a superconductor is defined by the number of impurities in the material and the number of surface scatters which limit the free mean path. In thin film systems, the the diffusion length exceeds the thickness of the phonon collector by several orders of magnitude implying that surface scatting is the dominant process limiting the quasiparticle diffusion. The influence of the film thickness d on the the diffusion length l can be estimated using the Fuchs theory [85]. The result of this approximation can be considered as effective diffusion length l_{eff} valid in thin metal films (see equation 5.16).

$$l_{eff} = \frac{3d}{4} \cdot \left(ln\frac{l}{d} + 0.442 \right) \tag{5.16}$$

Using equation 5.16, the measured diffusion length ($l_{diff} = l_{eff}$) can be translated to the theoretical diffusion length in the bulk. Values of $l = \mathcal{O}(10\,\text{m})$ are necessary to explain the measured diffusion lengths with the Fuchs model. Hence, the Fuchs model is not able to explain the results of the measurements. However, one can assume that the film thickness is limiting the quasiparticle diffusion in the current layout of the phonon collectors. Unfortunately, all efforts to confirm this assumption using the same detector layout with a larger film thickness failed because of technical difficulties.

[2]The group velocity v_g of quasiparticles in aluminum is $v_g = 2 \cdot 10^5\,\text{m/s}$ [84]

The obtained results agree with other experimental measurements of diffusion properties in superconducting films, Loidl et. al. [81] derive diffusion lengths in superconducting aluminum films of the same size ($\mathcal{O}(2\,\mathrm{mm})$) while the investigated films had a even smaller diffusion constant and a longer quasiparticle life times. In the scope of the CDMS experiment, superconducting aluminum films are used as phonon collectors, too. Yen et. al. [86] [87] reported for these phonon collectors a diffusion length of quasiparticles of $\mathcal{O}(500\,\mu\mathrm{m})$. These authors also state that the the quasiparticle diffusion in their films is limited by the film thickness.

5.3 Conclusions and Implications

The diffusion length of quasiparticles in superconducting aluminum thin films like the ones used for the phonon collectors of CRESST-II detectors was derived in four independent measurements to be $l_{diff} = 1.16 - 2.42\,\mathrm{mm}$. These diffusion lengths are combined with a slow diffusion process ($D = 3.78 \cdot 10^{-3} - 2.28 \cdot 10^{-2}\,\mathrm{m^2/s}$) in the films and long quasiparticle lifetimes ($\tau_{qp} = 0.272 - 0.692\,\mathrm{ms}$). These values indicate that the quasiparticle diffusion in the superconducting aluminum films is efficient and experiences only small amounts of losses.

In order to scale the dimensions of a phonon collector according to the diffusion length of the quasiparticles therein, the following considerations are made. The setup described in the previous sections is used to determine the quasiparticle diffusion for point like energy depositions. In case of an energy deposition in the absorber volume of a detector, hence, the common case for the phonon collectors used for CRESST-II detectors, the energy entering the phonon collector is homogeneously distributed. This changes the second boundary condition for finding a solution of quasiparticle density $n(x,t)$ (see section 5.1) to:

$$n(x, t = 0) = N/L \cdot \Theta(x)\Theta(x - L). \tag{5.17}$$

$\Theta(x)$ is the heavyside function which is expanded into a series for finding a solution of $n(x,t)$ with the same approach as used in section 5.1. As final result, one obtains that the collection efficiency of a phonon collector stripe with the length L in a TES located at the position $x = 0$ [82]

$$\frac{N}{N_0} = \frac{l_{diff}}{L}\tanh\left(\frac{L}{l_{diff}}\right) \tag{5.18}$$

Figure 5.8 depicts equation 5.18 using the ratio of l_{diff}/L as input parameter.

This model allows to estimate that a phonon collector with the dimensions identical to the diffusion length have a collection efficiency of $\approx 60\,\%$. In case the diffusion length is smaller than the dimensions of the phonon collector, the collection efficiency scales linearly while the collection efficiency starts to saturate if the diffusion length is significant larger than the dimensions of the phonon collector.

Based on these findings, an increase of the current size of the phonon collectors can be recommended. In the scope of this thesis, different adaptations to the standard geometry of the CRESST-II light detectors were tested in direct comparison with the standard

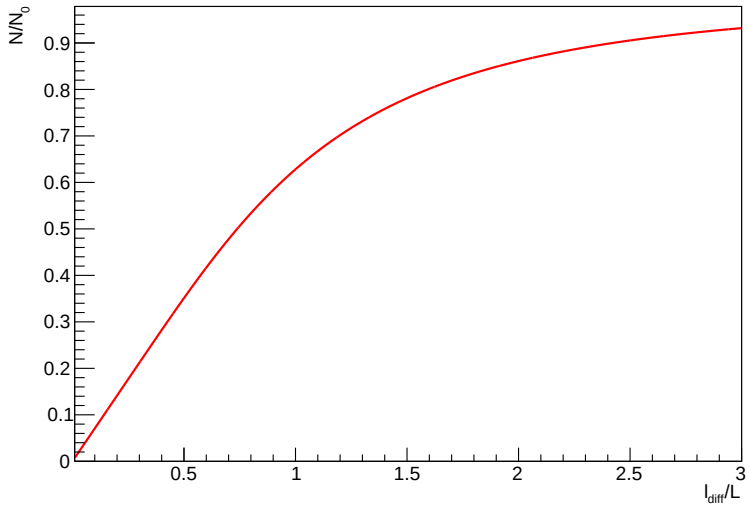

Abbildung 5.8: Plot of equation 5.18, using the ratio of l_{diff}/L as input parameter.

geometry (i.e. two thermometers on a single absorber). In the standard version of these thermometer structures, the longest necessary diffusion of quasiparticles is ≈ 0.2 mm). With a diffusion length of $\mathcal{O}(2\,\mathrm{mm})$, the dimensions of the phonon collectors can be increased to this size to enhance the sensitivity of the TESs. A test with doubled phonon collector size achieved an improvement in signal height by 30% compared to a standard geometry. This enhancement is in good agreement with the findings and scale according to the model depicted in figure 5.8.

Likewise, the increase of the phonon collector thickness was investigated using the same method. By increasing the thickness of the phonon collector by a factor 5, the detected pulse height was measured to be 30 % higher than with standard configuration. An increase of the phonon collector thickness to improve the quasiparticle diffusion is also supported by the findings of Yen et. al. [87]. Using a similar setup for measuring the diffusion of quasiparticles in superconducting aluminum films, a linear relation between the diffusion length and the thickness of the phonon collectors was confirmed. Since for film thicknesses up to 1 μm no saturation of this relation is observed, an increase of the current phonon collector thickness of CRESST-II from 1 μm to larger film thicknesses is advisable.

6 Slice Detector Concept

For the conventional CRESST-II detector design, two major design related limitations have been identified (see section 4.8). These are the presence of non-scintillating surfaces in direct line of sight to the target crystal and the poor performance of the light detector for low energetic events. This chapter covers the development and testing of a new detector design which is dominantly designed to overcome the poor performance of the light detector in the relevant energy range of dark matter searches (i.e.$<$ 40 keV): The ßlice detectormodule.

The main intention of this design to improve the light collection efficiency inside the detector module by shortening the average distance the scintillation light has to travel before it is absorbed in the light detector. This goal is achieved by positioning the light detector ″inside‟the target crystal. Therefore, the main design component of this detector concept is a cylindrically shaped target crystal which is cut in such a way that a narrow opening from the mantel to the center is created (a slice/slit). Therein, the light detector is positioned. Like in other CRESST-II dertectors, the crystal and the light detector are lined with scintillating and reflective foil to enhance the light signal. Figure 6.1 shows a scheme of the slice detector including the dimensions used in this work for testing the layout.

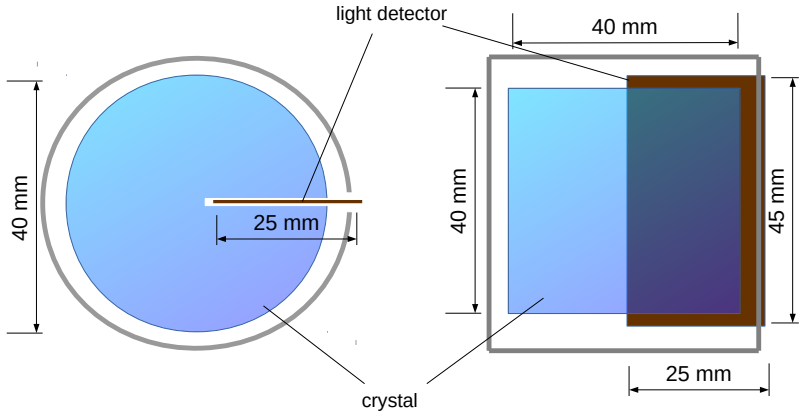

Abbildung 6.1: Scheme of the slice module from different angles. The light detector is positioned in a narrow cut indent which creates an opening from mantel to the geometric center of the main crystal. Crystal and light detector are lined with scintillating and reflective foil.

The slice detector module is a R&D prototype which is not intended to probe dark matter in the CRESST setup at Gran Sasso. The detector concept is developed to determine the influence of the light detector's position on the light collection and to draw conclusions for future detector designs.

6.1 Design Goals

The slice detector concept is introduced to investigate the influence of the light detector's position in the detector housing on the light collection efficiency in direct comparison to the standard detector design of CRESST-II. Therefore, the changes to the general detector layout of slice detector are intended to be kept as small as possible to allow a fair comparison between the two concepts. As a consequence of this intention, the changes applied to the detector geometry are limited to the light detector, its position and the cut created in the target crystal to generate the opening in which the the light detector is placed in. The dimensions and geometry of the target crystal used in the slice detector design are identical to the target crystal used in the standard CRESST-II detector design.

The chosem geometry of the slice detector design is expected to improve the light collection efficiency inside the detector housing because of the following considerations.

In the conventional detector design, the use of cylindrically shaped target crystal introduces a high probability that a photon is trapped within the crystal without the possibility to reach the light detector (see discussion in section 4.8). For $CaWO_4$ crystals, the probability for such a propagation path is enhanced due the high refractive index of this material (1.94@420 nm [88]). Therefore, the incident angle above which total reflection happens is smaller than in other materials ($\gtrapprox 31°$). In the slice detector design, the effect of light trapping in the target crystal is exploited for a better light collection. By placing the light detector ïnsidethe crystal, the signal fraction trapped inside the main crystal is guided to the light detector.

Additionally, the slice detector design aims to reduce the average distance a photon travels inside the detector housing before being absorbed in the light detector. Starting from a naive perspective, the solid angle a light detector covers at a certain position in the target crystal defines the probability for a photon to be absorbed therein without any previous reflection processes. In a conventional CRESST-II detector module, most positions within the target crystal provide a larger solid angle for these first generationpphotons than it is the case in the slice detector design. Though, the situation changes if the reflection and redirection of photons becomes necessary to guide the photons to the light detector since, in the slice detector design, the ëffectiveärea the light detector provides after the first or second reflection process is larger than in the conventional detector design. Therefore, the number of reflections necessary to guide a photon to the light detector as well as the average distance a photon has to travel inside the crystal is shortened which, consequently, reduces the probability that a photon is lost during propagation.

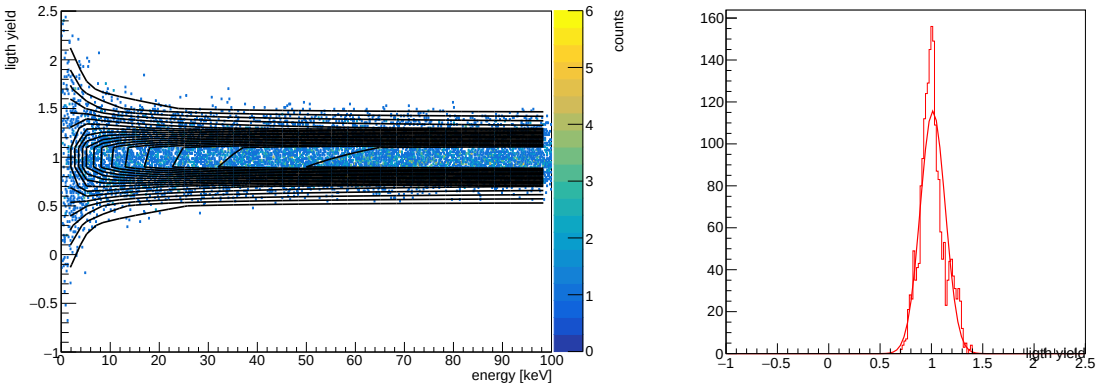

(a) Event distribution in the light yield vs. recoil energy plane.

(b) Projection of figure 6.2a in the light yield plane (E =80 and 100 keV).

Abbildung 6.2: Simulation output for estimating the light collection properties of slice detector design. Figure 6.2a shows the light yield vs. energy scatter plot including the fit of the data using equation 4.10. Due to the asymmetric detector layout, the expected light yield distribution shows an increased position dependency which is expressed in the form of non-gaussian light yield distribution (see figure 6.2b).

Using the simulation code described in section 4.8, the light collection efficiency of the slice module is investigated. The simulation predicts a reduction of the average distance a detected photon travels inside the detector housing from (12.3 ± 2.4) cm (conventional) to (4.9 ± 1.5) cm (slice). In addition, the average number of reflection processes a photon is required to make on foil surfaces to reach the light detector is reduced from 11.2 ± 1.5 to 4.6 ± 0.8. The combination of reduced distance and reduced number of reflections yields in a predicted improvement of the light collection efficiency from (38.9 ± 10.3) % (conventional) to (53.9 ± 13.4) % (slice). Based on the results of the simulation, the losses are caused to 33.6 % by the foil, to 7.1 % by reabsorption in the target crystal and to 5.3 % by non-reflective detector parts.

The output of the simulation reveals that, due to the detector layout, the influence of position dependencies is increased. Figure 6.2a shows the result of the simulation in the light yield vs. energy plane. The plot reveals that the asymmetry of the detector layout results in a variation of the light collection efficiency which is expressed in leakage of events to lower light yields. To illustrate this behavior, the projection of the light yield in the energy range between 80 and 100 keV is shown in figure 6.2b. The figure shows that the assumption of Gaussian distributed light yield cannot be applied to the slice detector design.

The asymmetry of the light yield distribution (figure 6.2b) can be related to the position where the energy deposition takes place. Figure 6.3 depicts the light collection efficiency as a function of the position the photon is created (x-y plane).

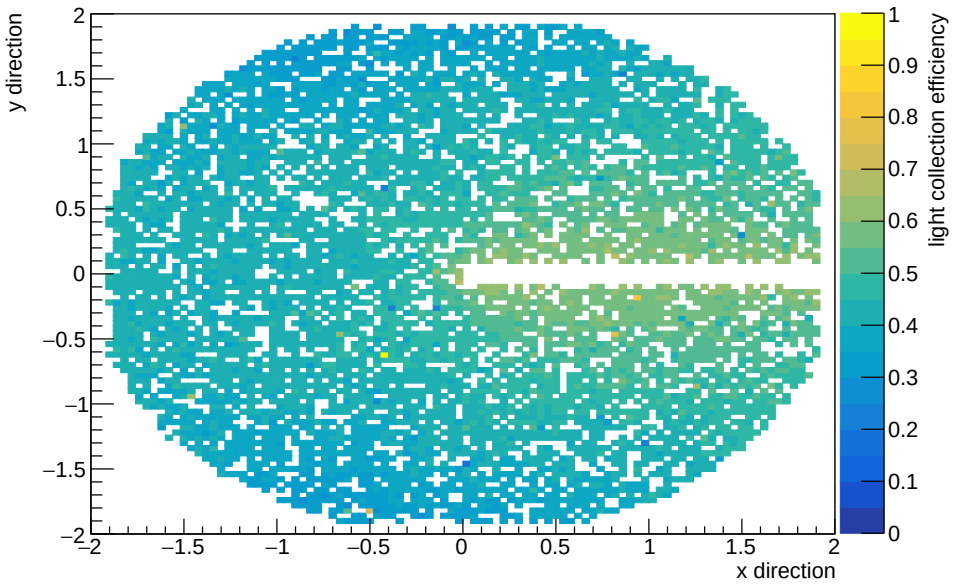

Abbildung 6.3: Simulated light collection efficiency as a function of the position where the photons are started in the crystal (x-y plane). The color coding indicates the local variance of light collection efficiency. "Darker"(blue) and "brighter"(yellow) spots are caused by the asymmetric layout of the detector design.

Figure 6.3 indicates the presence of "darkeränd "brighterßpots in the target crystal. These variations in the light collection efficiency can be explained with the average distance a photon travels inside the detector housing before being detected. While some regions in the crystal generally require a longer propagation path before being absorbed in the light detector, other regions have a shorter propagation path. The simulation also reveals that the average distance a photon travels before detection is not directly related to the geometric distance between the position the photon is created and the light detector. This observation can be related with an enhanced probability for light trapping for certain locations within the crystal. This effect is, for example, observed for the "brighterßpot located at the opposite site of the light detector (x≈-1.5, y≈ 0). In case photons are created in this region of the crystal, the probability is enhanced that the photon is emitted with a trajectory for which total reflection on the crystal surfaces is causing a positive focus towards the light detector. The opposite effect is observed for a region which is located in close distance to the light detector (x≈-0.5, y≈ ±1.5). Here, the average distance a photon travels before absorption is prolonged by the fact that the solid angle the light detector covers initially is small and a significant number of reflections on the surrounding foil is necessary to finally reach the light detector. Therefore, the light collection efficiency at this position is smaller than the average.

For dark matter searches, an asymmetric deformation of the light yield population requires an adaptation of the standard analysis methods. Hence, the parameterization

described in section 4.3 has to be modified accordingly. Nevertheless, based on the understanding acquired by the simulation, the adjustment of the band fit can be achieved in so that the event distribution of certain event classes (i.e. electron recoils) is correctly described.

Depending on the strength of the observed asymmetry in the recoil bands and the improvement achieved for light collection efficiency, the total improvement in discrimination power varies. More precisely, since the leakage of events with small light yield is expected to increase due to the asymmetric detector design, the improvements in discrimination power achieved in by the better performing light channel is partially counterbalanced. In the low energy region, though, the influence of position dependencies is expected to be negligible as other detector effects dominate the light channel's resolution. Hence, the discrimination power in the ROI for dark matter searches is expected to be significantly improved due to the better light collection efficiency.

Regardless of the asymmetric light yield distribution, the slice design provides a good response to the problem of the small light collection efficiency in the conventional detector design. The potential to improve the light collection efficiency by 50% by rearranging the detector components in the suggest way is a promising way to improve the discrimination power for background interactions in the target crystal and to increase the sensitivity for dark matter searches.

6.2 Technical Description of the Detector Design

As mentioned before, the detector design of the slice detector is intended to investigate the effect of the position of the light detector on the light collection efficiency. Therefore, the detector layout is very similar to the detector layout of the standard CRESST-II detector design. In the following, the major design features of the slice detector are discussed.

The geometry of the target crystal is kept cylindrically and the dimensions are unchanged remaining at 40 mm diameter and 40 mm height. The only change applied to the geometry of the main absorber is the slit in which the light detector is positioned. The slit has a width of 1.0 mm and extends over the full height of the target crystal from the mantel to the center. The amount of material removed because of the cut is ≈ 10 g in case $CaWO_4$ is the target material. The thermometer structure used for reading out the phonon channel is identical to the one used conventional CRESST-II detector design. The TES is located on a small carrier crystal which is connected to the main absorber using an EPOTEK glue spot [89].

The changes applied to the light detector are more substantial. The geometry is changed from round to a rectangular shape while the thickness of the absorber is identical. The new dimensions are $(50\text{x}30\text{x}0.4)\,\text{mm}^3$, resulting in an enlargement of the area for light absorption by 25 %. The SOS wafers used as light absorbers in the conventional detector modules show a difference in the absorption efficiency depending on which side the wafer is irradiated [44]. In the conventional detector design, the position of the light detector allows to neglect this material property because the light absorber is dominant-

ly irradiated from one side (see figure 2.3). In the slice detector design, the light detector is irradiated from both sides equally. Therefore, an absorber material is needed for the light detector that shows no difference in the absorption efficiency for both surfaces. Mono-crystalline silicon shows a generally slightly smaller absorber for the scintillation light of $CaWO_4$ [44], but avoids the the introduction of this additional, design related position dependency. Therefore, the light absorber is made of this material.

The TES structure used for the light channel of the slice detector module is changed compared to the TES used standard CRESST-II light detector which was presented in section 3.2.3. The tungsten part of the thermometer remains unchanged, but significant changes are applied to the design of the phonon collectors. Based on the knowledge gained with the setup for measuring the quasiparticle diffusion (see chapter 5), the size of the phonon collectors is increased by a factor of five compared to the thermometer design used for the standard CRESST-II light detector. This change enhances the collection efficiency of non-thermal phonons in the thermometer without changing the time constants since the area the TES covers is still sufficiently small to not influence the life time of the non-thermal phonons in the absorber crystal (see section 3.2). No changes are applied to the thermal link of the light detector system which keeps the combination of absorber and TES in the calorimetric operation mode.

The light detector is mounted on a dedicated copper structure. This allows to establish the necessary electrical and thermal connections using bond wires in individual mounting steps for phonon and light detector. The pairing of phonon and light detector is performed after all connections are established.

The detector housing is almost completely lined by scintillating and reflective VM2002 foil. An opening in the mantel, extending over the full height of the detector module, exists to allow the merging of phonon and light detector. This opening in the reflective foil is designed to be as small as possible to avoid light losses and reduce the area not covered by scintillating material. For the realized prototype detector, the opening in the mantel surface is smaller than $(55\text{x}5)\,\text{mm}^2$ which corresponds to less than 3% of the total area of the foil. As a consequence, the light collection efficiency is slightly reduced in this prototype.

The opening for the light detector as well as the use of bronze and copper parts for holding phonon and light detector prevents the establishment of a fully scintillating housing. Therefore, the slice design is not able to provide a full veto for surface backgrounds. Though, for investigating the performance this detector geometry in regard of the EDL a fully scintillating detector housing is not necessary.

Figure 6.4 shows a photograph of the prototype before the detector module is closed for operation.

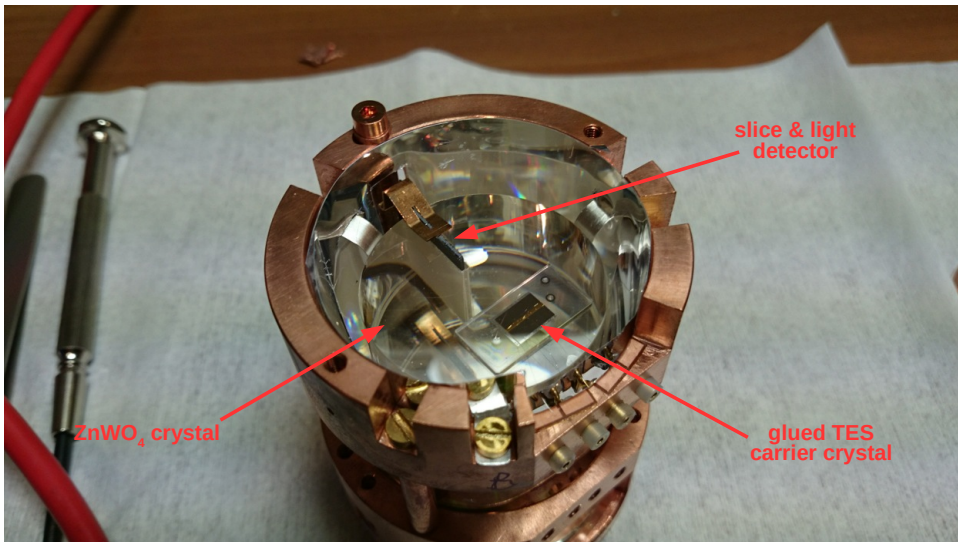

Abbildung 6.4: Photograph pf the prototype of the slice detector design. The light detector is placed in a slit created in the target crystal. The TES for reading out the phonon channel is evaporated on a carrier crystal, which is connected to the main absorber using a EPOTEK glue spot. The detector housing is completely lined by reflective and scintillation VM2002 foil except the opening necessary for mounting the light detector.

6.3 Testing and Results

Since the slice detector design features a large target crystal ($\approx 300\,\mathrm{g}$), a stable operation of the detector above ground is not possible. The high rate induced by the direct interaction of cosmic radiation in the target in combination with the generally slow response of large cryogenic detectors demands that a reliable test of such a detector is performed in an underground laboratory. For this purpose, the CRESST collaboration operates such a test setup in the Gran Sasso Underground Laboratory (LNGS) which allows the testing of new detector concepts in a low background environment (for more information on the setup, see reference [53]).

This setup is used to operate a prototype module of the slice concept. The main goal of the measurement is the determination of the EDL. Since the acquired statistics during this measurement is small compared to data sets recorded in the main setup of CRESST, no dark matter analysis is performed. Nevertheless, the influence of the EDL on the discrimination power for background interactions and, thus, on the sensitivity of such a detector for dark matter is investigated. Additionally, a direct comparison to a conventional detector module with average performance is made.

6.3.1 Prototype Module and Data Sets

The first experimental test of the slice design was performed with a detector module having a geometry as described in section 6.2. A significant change was applied to the target crystal. Since a $CaWO_4$ crystal was not available for this test measurement, a 280 g $ZnWO_4$ single crystal was used as main absorber instead. This material has very similar material and scintillation properties as $CaWO_4$. However, the scintillation efficiency is reported to be $\approx 10\,\%$ larger than in $CaWO_4$ [90] [91] which has to be considered during the evaluation the prototype and during the comparison of this detector module with other detector modules equipped with a $CaWO_4$ target crystals.

A direct calibration of the light detector was performed using ^{55}Fe source mounted in close proximity to the light detector. The characteristic X-ray emissions are used as reference to determine the energy scale of the light detector for direct energy depositions. For the determination of the EDL of the detector design the knowledge of this energy scale is mandatory (see section 4.5). The same source also illuminates the surface of the main absorber and is used for calibrating the phonon detector in the low energy range.

For higher energies, the detector module is calibrated by using a ^{57}Co-source emitting 122.06 keV and 136.46 keV γ-rays [67]. Radiation with this energy is able to penetrate the dewar, to reach the experimental chamber and to deposit its energy in the target crystal. Hence, the source can be placed outside the cryostat which allows to put and remove the calibration source if necessary.

The scatter plots of the recorded data sets are shown as light vs. phonon energy plots in figure 6.5a (^{57}Co calibration data set, $\approx$ 15 h measurement time) and figure 6.5b (background data set, $\approx$ 19 h measurement time). The energy scale of the light detector is given in electron equivalent units, i.e. in the scale for electron recoil events in the target crystal. Thus, a slope of ≈ 1 is expected for the electron recoil band in the chosen presentation of the data.

In both data sets, the electron recoil band is strongly populated over the full energy range. These events originate from internal contaminations (i.e. contamination of the target crystal) and from external backgrounds introduces by the experimental setup. The distinct, mono-energetic peaks in the recorded energy spectra can be attributed to certain background processes. The prominent peak with an energy 238.63 keV is related to the β^--decay of ^{212}Pb which correlates with the emission of a γ-ray with this energy [67]. In the low energy range, the ^{55}Fe source is identified in the phonon channel by its characteristic X-ray lines at 5.89 keV and 6.49 keV in both data sets [67]. By comparing the calibration and the background data, the 122.06 keV and 136.46 keV γ-ray lines of the ^{57}Co-source [67] are identified which allows to set the energy range for events taking place in the main absorber unambiguously.

As predicted by the simulation, a position dependent light signal is observed in the data. Over the full energy range, an asymmetric event distribution is observed for events having the same phonon energy.

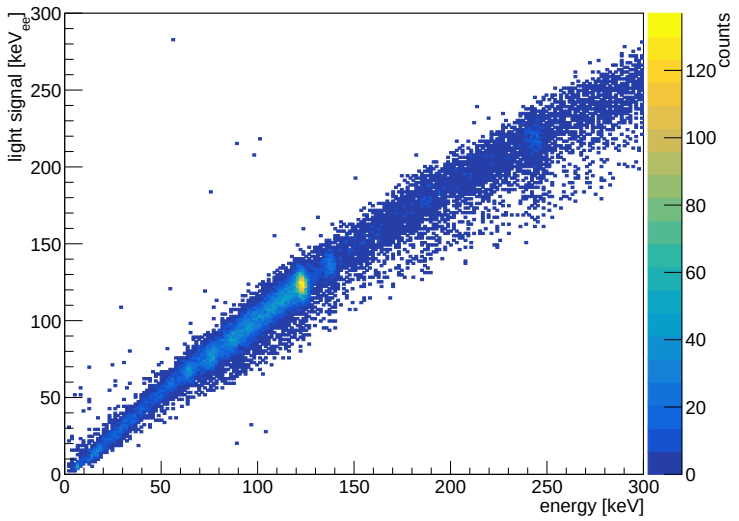

(a) Calibration data set (^{57}Co source).

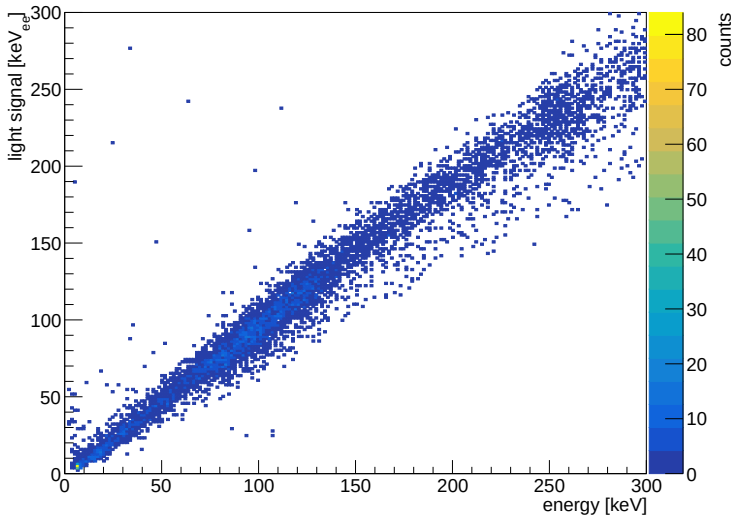

(b) Background data set.

Abbildung 6.5: Scatter plots showing the light vs. phonon energy plane of the calibration data set 6.5a and background data set 6.5b). Over full energy range, the presence internal and external background sources is observed. A prominent peak is visible in the spectrum at an energy 238.63 keV. It is related to the β^--decay of ^{212}Pb which is related to a γ emission of this energy [67]. In the calibration set, the ^{57}Co-source can be identified as additional peaks with energies of 122.06 keV and 136.46 keV. Because of geometric effects of the detector design, a leakage of events to smaller light signals is observed over the full energy range in both data sets.

6.3.2 Intrinsic Performance of the Phonon Detector

Although the dimensions and the global geometry of the target crystal are not changed, the layout of the target crystal is changed significantly by the slit created for the light detector. Therefore, an analysis of the phonon channel's pulse shape is performed to investigate if the phonon propagation in the absorber is influenced by the slit.

Two aspects are investigated:

First, the presence of a cut in the crystal could affect the phonon propagation in the target crystal. As a consequence, the position where an event takes place might be reflected in the pulse shape which yields to a position dependency in the phonon channel. For the recorded data, this effect is not observed. The pulse shape of all events taking place in the target crystal is homogeneous indicating no position dependency.

Second, the surface-to-volume ratio is increased to 126% in comparison to cylindrical crystal without the slit. Thus, the observed pulse shape can differ from the pulse shape normally observed in the phonon channel of a CRESST-II detector module because the thermalization speed of the non-thermal phonon signal component is accelerated (see section 3.1.2). However, the comparison of the standard event obtained for the phonon channel of the slice module prototype with a typical standard event obtained for the phonon channel of a conventional detector module reveals no significant difference between them. The pulse shape parameters which are derived by fitting the pulse model (equation 3.11) to the standard events indicate no variance above the normally observed level of $10 - 20\,\%$ which is normally observed between cryogenic detectors of the same kind.

Next to the influence of the detector design on the observed pulse shapes in the phonon channel, the performance as cryogenic detector is investigated using the methods introduced in section 4.2. Due to the fact that empty baseline samples are not available, the baseline resolution σ_b and the trigger threshold E_{thres} of the phonon channel are determined using the smallest triggered test pulse. The energy of this test pulse amplitude is 3.41 keV. The detector resolution at this energy is $\sigma_{PD} = 241\,\text{eV}$. For this test pulse amplitude, the trigger efficiency shows no degradation in comparison to test pulses with higher energy. This indicates that this pulse amplitude is well above the hardware trigger threshold.

The energy resolution $\sigma(E)$ of a cryogenic detector is expected to scale with energy according to equation 4.2. Based on this model, the energy dependent resolution $\sigma_{PD}(E)$ (e.g. for the smallest triggered test pulse) is expected to be larger than the baseline resolution $\sigma_{PD,b}$ of the respective detector. Therefore, $\sigma_{PD,b} = 0.241\,\text{keV}$ can be considered as upper limit for the actual baseline resolution.

The hardware trigger system of the CRESST experiment allows trigger to reliably on pulse heights which are 5 times bigger than $\sigma_{PD,b}$. Using $\sigma_{PD,b} = 0.241\,\text{keV}$ as value for the baseline noise, a theoretical detector threshold of $E_{thres} \approx 1.2\,\text{keV}$ can be assumed for the phonon channel of this prototype if operated in the main setup of the CRESST experiment.

The estimated threshold as well as the baseline resolution of the detector prototype do not show any negative influence introduced by the slit in the main absorber. The values

obtained for the performance of the phonon channel are aligned with the performance achieved in other CRESST-II detector modules with target crystals of the same size [71].

In summary, one can state that the creation of the slit in the target crystal for housing the light detector, does not affect the performance of the phonon channel on a relevant level. Furthermore, no negative effects are observed in the pulse development inside the target crystal or in the energy resolution of the phonon channel due the change of the surface-to-volume ratio of the target crystal.

6.3.3 Intrinsic Performance of the Light Detector

Significant changes were applied to the light detector setup. The absorber material is changed from SOS wafer to a mono-crystalline silicon wafer. The exchange of absorber material is not expected to affect the performance of the light detector to a large extend since, in terms of phonon propagation, SOS wafers and mono-crystalline silicon show similar behavior. The increase of the light detector's dimensions is expected to influence the performance as cryogenic detector negatively. The enlargement of the absorber volume by 25 % causes that a reduced phonon density is present in the absorber after a given energy deposition (compared to a detector featuring a smaller absorber volume, see discussion in chapter 3). Therefore, the temperature signal detected by the TES for a given energy is expected to be smaller in the light detector used within the slice detector design. In addition, the enlargement of the surface available for the light collection is expected to increase the influence of position dependencies in the detector response. However, in regard of the overall performance of the light channel, the reduction of the cryogenic performance is expected to be counterbalanced by the better light collection efficiency for scintillation signals.

Figure 6.6 shows the recorded spectrum of the ^{55}Fe-source which is used to calibrate the light detector. The identification of this event class is achieved by applying pulse shape cuts to the light channel. Direct energy depositions feature faster pulse shape than energy depositions caused by a scintillation events. In addition, the phonon signal is used as anti-coincidence veto to reject all events having an energy larger than 0 in the target crystal.

The spectrum shown in figure 6.6 can be fitted using the superposition of two Gaussians. Since the statistics for the k_β is small, the same σ is used to fit both peaks. The results of the fit are summarized in table 6.1

$E_{cal}[keV]$	*amplitude [V]*	*resolution [V]*
5.89	3.712 ± 0.006	0.082 ± 0.006
6.46	4.058 ± 0.022	0.082 ± 0.006

Tabelle 6.1: ^{55}Fe calibration of the light detector operated in the slice detector prototype.

For the ^{55}Mn K_α X-ray line (5.89 keV) a resolution of $1\sigma = (0.13 \pm 0.02)$ keV(2.2%) is determined. This value is in good agreement with other CRESST-II light detectors for which detector resolutions of ≈2% are common for mono-energetic X-ray lines. The

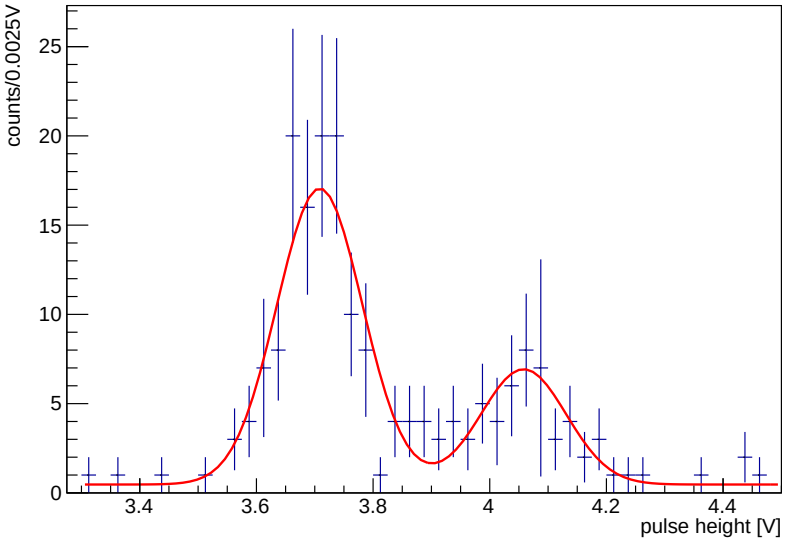

Abbildung 6.6: Isolated ^{55}Fe-source spectrum recorded with the light detector of the slice detector prototype. By fitting the two peaks with Gaussian functions, an energy resolution of $\sigma = (0.13 \pm 0.02)\,\mathrm{keV}$@$5.89\,\mathrm{keV}$ (2.2%) is determined.

relative position as well as the intensity ratio of the peaks is in agreement with the expected spectrum of a ^{55}Fe-source.

Due to the lack of empty baseline samples, the baseline resolution σ_b of the light detector cannot be derived with the standard method (see section 4.2). To give an upper limit on this quantity, the smallest triggered test pulse is used to evaluate the performance of the light detector (similar to the phonon channel, see section 6.3.2). The energy of the smallest triggered test pulse is $(0.162 \pm 0.002)\,\mathrm{keV}$ having a 1σ detector resolution of $(5.44 \pm 0.8)\,\mathrm{eV}$ (relative detector resolution 3.3 %). As discussed before (see section 4.2), the use of the detector resolution for an energy > 0 can be considered as conservative approach for determining the baseline resolution of a cryogenic detector. Thus, the actual baseline resolution of the light detector used in this setup is expected to be smaller than the derived value for the baseline resolution σ_b using the smallest triggered test pulse.

The upper limit on the baseline resolution of this light detector is in good agreement with the average values achieved for conventional CRESST-II light detectors for which $\sigma_b = 5 - 7\,\mathrm{eV}$. Thus, the increased volume of the light absorber by 25% is not reflected in the performance of the light detector as cryogenic device.

Since only a single detector of this type has been produced until now, a comparison between different light detectors of this kind is not possible. Nevertheless, the performance of the light detector as cryogenic detector is on the same level as other CRESST-II light detectors. Therefore, it can be assumed that the increase in light collection efficiency is directly translated in a better relative performance of the light channel and, hence, in a better discrimination power for backgrounds.

6.3.4 Energy Detected as Light

The fraction of energy detected as light (EDL) is derived for the slice detector design using the method described in section 4.5.2.

The energy scale for direct energy depositions in the light detector is defined using an ^{55}Fe source. For events taking place in the target crystal, the energy range is set using the ^{57}Co source. Since the ^{55}Fe source irradiates the main absorber as well, this source is also used for measuring the EDL at small energies. In table 6.1, the calibration values are listed for direct energy depositions in the light detector.

The integral ratio of the normalized standard events of direct light detector hits and scintillation events is determined to be 1.133 (derived by numerical integration). The calibration factor ζ_{cal} determined for this light detector is

$$\zeta_{cal} = \frac{5.891\,\mathrm{keV}}{3.714\,\mathrm{V}} \cdot 1.133 = 1.797\,\mathrm{keV/V}. \tag{6.1}$$

Using this calibration factor, the EDL is derived for the slice detector prototype. The results are summarized in table 6.2.

E_{cal} *[keV]*	*PD amplitude [V]*	*LD amplitude [V]*	*detected energy in LD [keV]*	*EDL [%]*
5.89	0.019 ± 0.002	0.10 ± 0.02	0.18 ± 0.03	3.10 ± 0.62
122.06	0.339 ± 0.007	2.18 ± 0.11	3.88 ± 0.24	3.18 ± 0.20
238.80	0.628 ± 0.011	3.90 ± 0.17	$7,01 \pm 0.41$	2.93 ± 0.17
			average	3.07±0.19

Tabelle 6.2: Combined results of the measured EDL of the slice detector design. By using three identified peaks in the energy spectrum, the EDL is determined for different energies.

The averaged result of the light collection efficiency using different peaks in the spectrum is $(3.07 \pm 0.19)\,\%$. This value exceeds the typical values for the EDL achieved with the conventional detector design by 50% [48] . This value is in agreement with the results for the light collection efficiency derived by the simulation where an improvement of the light collection efficiency is predicted to be $\approx 45\,\%$, too. The improvement of the measured EDL is large enough to rule out that the improvements are exclusively related to the change of target crystal material. $ZnWO_4$ is reported to have a $\approx 10\,\%$ higher scintillation yield than $CaWO_4$ [90] which is not sufficient to explain the observation. Therefore, the improvements in the EDL can be related by the changes applied to the detector design.

The results can be used to draw the following conclusions on the photon propagation in a detector module.

In the slice detector, the amount of light which is trapped within a cylindrically shaped crystal without the possibility to reach the light detector is able to significantly add to the detected light signal. By positioning the light detector ïnsidethe target crystal, this

is exploited. According to the simulation, the loss of photons due to reabsorption in the target crystal is reduced by a factor of ≈ 2. However, the fraction of photons which is lost in the target crystal of a conventional detector module is relatively small (11.5 %). Hence, the observed gains in the light collection efficiency are not sufficient to be solely related to this effect.

Therefore, the losses in the detector housing (i.e. the scintillating and reflective foil, TES, clamps) are confirmed to play significant role during the photon propagation. This conclusion is additionally supported by the simulation of the light collection efficiency. The number of necessary reflections on foil surfaces to guide a photon to the light detector is reduced from ≈ 11.2 to ≈ 4.6 in the slice detector design. Accordingly, losses due to absorption of light in the foil are reduced which is reflected in the strong improvement of the EDL.

6.3.5 Particle Identification

To illustrate the background discrimination capabilities of the phonon-light detectors, the recorded data is presented in the light yield vs. energy plane. Figure 6.7 shows the calibration data set recorded by the slice detector prototype module after the application of all cuts. Theses cuts aim to remove events from the data sets for which the precise determination of the pulse parameters is not guaranteed. Disturbances (e.g. SQUID artifacts) or pile up events are discarded from the analysis for this reason. Additionally, all event classes not solely related to interactions in the main absorber are identified and discarded, for example, all carrier related events.

In figure 6.7, the red lines indicate the interval which contains 90% of the events, the black line shows the median of the distribution.

Due to the improved EDL, it is expected that the width of the recoil bands is reduced (see section 6.1). To quantify the improvements in the detector response, the parameters of the electron recoil band are derived using the phenomenological model described in section 4.3. The parameters are derived by fitting the data using a binned likelihood method (1-D approach) and not by 2-D maximum likelihood fit (see equation 4.10). The reason for choosing this approach is related to the inhomogeneity of the light detector's response at energies between $\approx$ 80 and 90 keV. To extract the width of the electron recoil band, i.e. σ_{LY}, it is not necessary to describe the center of the electron recoil band (LY_c) in full detail. Thus, in order to avoid the complex adjustment of the 2-D maximum likelihood function to describe the center of the event distribution correctly, the following approach is used: The data is separated in energy bins with a defined width. For each of them, the projection in the light yield plane is fitted with a function describing the light yield distribution appropriately. By scanning the energy range using a moving interval approach, the width of the electron recoil band $\sigma_{LY}(E)$ as well as the center of the electron recoil band LY_c are extracted from the data as a function of the energy. The main advantage of this method is that it allows the extraction of $\sigma_{LY}(E)$, which is dominantly defined by the detector design and the performance of the light channel, with high precision without the necessity to adapt LY_c to the characteristics of the target crystal (i.e. intrinsic contamination, non-proportionality effect) and of the

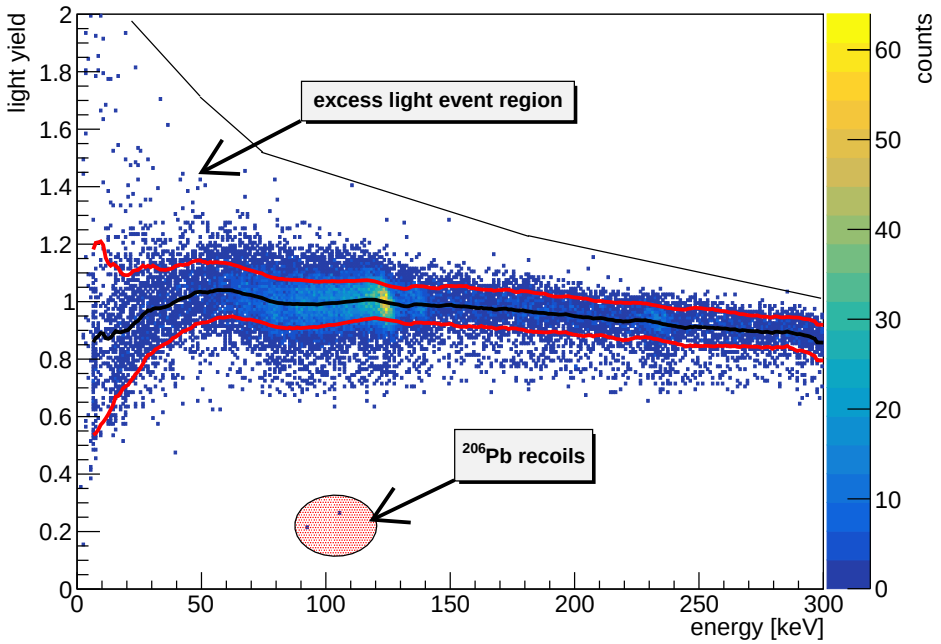

Abbildung 6.7: Light yield vs. energy scatter plot showing the calibration data set after all quality cuts. The β/γ-band is distorted by a inhomogeneity of the transition of the light detector between 80-90 keV. The center of the light yield band is indicated by the black solid line. Additionally, the interval in which 90% of the events are located in shown (red lines). At energies < 103 keV, events related the (surface) α-decay of ^{210}Po to ^{206}Pb are seen as population below the β/γ-band with a light yield of $\approx 0.2 - 0.3$. Additionally, towards smaller recoil energies, a population of excess light events which is located above the β/γ-band.

thermometers. For the evaluation of a detector design, which is the intention of this analysis, only σ_{LY} is needed.

For the data recorded with the prototype of the slice detector design, the bin size of the energy range fitted as single interval is set to 10 keV. For moving the interval, a step size of 1 keV is used. This step size was found to be the best compromise between having a sufficient number of events in an energy bin to allow the fit routine to converge and a fine energy resolution. In data sets with more events, the interval can be reduced to achieve a better energy resolution.

Like in other CRESST-II detector modules, the light yield distribution in an isolated energy range is initially assumed to be normal distributed and is, therefore, fitted with a single Gaussian. The band width σ_{LY} is fitted using equation 4.6. In addition, the parameters describing center of the light yield distribution LY_c are derived using equation 4.5. However, due to the fact that the function describing LY_c is not adapted to the target crystal in full detail, the results of the fit are only given for the sake of completeness.

parameter	*fit result*
$S_0(f)$	$0.153\,\mathrm{keV}^2$
S_1	$(0.75 \pm 0.01)\,\mathrm{keV}$
S_2	$(2.40 \pm 0.19) \cdot 10^{-4}$
p_0	1.04±0.03
p_1	$(-5.02 \pm 0.53) \cdot 10^{-5}\,\mathrm{keV}^{-1}$
p_2	0.18 ± 0.03
p_3	$(19.56 \pm 3.67)\,\mathrm{keV}$

Tabelle 6.3: Parameters derived for describing the electron recoil band of the slice detector prototype (background data set). The given uncertainties are fit errors.

The fit results for the parameters describing σ_{LY} and LY_c are summarized in table 6.3.

As mentioned before, the parameterization of the center of the light yield band using equation 4.5, $LY_c(E)$ is not adapted to the characteristics of the target crystal and the thermometer in full detail (i.e. inhomogeneity at 80-90 keV is not implemented). Therefore, the values derived for $LY_c(E)$ have a larger systematic uncertainty which is an increased reflected in the fit uncertainty. Nevertheless, the values derived for the paramtrization using equation 4.5 show the expected features. No significant deviation from other detectors is observed in comparison to the results presented in [23] [43] and [65]. Thus, the use of $ZnWO_4$ target crystal has no significant impact on the band description or on the expected leakage of background events into the ROI of dark matter searches.

In the following, the parameters for describing $\sigma_{LY}(E)$ in the slice detector measurement are compared with the average parameters obtained for the conventional module (see table 4.1).

The parameter S_0 is not determined by fitting but is calculated with equation 4.7 using the detector resolutions and the EDL determined in the previous sections. Therefore, the parameter S_0 is fixed during the fit routine (denoted in table 6.3 with (f)). The S_0 value obtained for this measurement is competitive with the best detector modules of CRESST-II. The main reason is the higher EDL which reduces the share the baseline resolution of the light detector contributes to S_0 significantly (see section 4.3). The S_1 parameter, which dominantly accounts for the uncertainty introduced by photon counting, is in agreement with the performance achieved with the conventional CRESST-II detector modules. However, the value of this parameter does not meet the expectations for the slice detector design. Since $S_1 \propto \mathrm{EDL}^{-1}$, one expects a strong improvement of the parameter based on the increased value of the EDL. The same behavior is observed for the S_2 parameter. Also this value is larger than it is observed in a conventional CRESST-II detector module with average performance which reflects the influence of the position dependencies on both parameters.

The following considerations are given to explain the observations. Over the full energy range, an asymmetry of the light yield distribution is observed which is, as mentioned before, a response to the position dependencies of the light collection efficiency in the

crystal. As shown by simulation (see section 6.1), the detector design of the slice module is expected to cause a light yield distribution which cannot be described with a Gaussian. This expectation is confirmed experimentally by the observed leakage of a small amount of events towards smaller light yields over the full energy range (see figure 6.7). Position dependencies are usually reflected in the S_2 parameter. Though, the strong correlation of the fit parameters causes that the S_1 parameter is influenced by the position dependent light collection efficiency, too. Especially at low energies, S_1 provides the only possibility to account for the increased width of the electron recoil band. Therefore, both parameters, S_1 and S_2 are fitted to be larger than usually observed.

The asymmetry of the light yield band renders the established method used for describing the light yield distribution in a given energy interval with a single Gaussian inadequate. Using the superposition of two Gaussians allows to describe the data in a better way. In addition, the parameterization of the excess light events in the low energy region improves the description of the light yield distribution.

Figure 6.8a shows the data fitted with a single Gaussian in the energy range 150 and 170 keV while figure 6.8b shows the same data set being described by a fit function composed of two Gaussians.

For recoil energies > 150 keV, no excess light events are observed above the electron recoil band. Reason for this is that the small amount of scintillation light which is additionally created by the foil is negligible compared to the total amount of scintillation light. Therefore, internal electron recoils cannot be disentangled from events with excess light character. In addition, the number of events with excess light character is negligible compared to the total background number being present in the electron recoil band. This allows to investigate the asymmetry of the light yield distribution caused by the position dependencies in the light collection efficiency in this energy range without the necessity to account for the excess light events specifically.

The position dependencies in the light collection efficiency are assumed to be energy independent which implies that the effect of events leaking to smaller light yields has to be observed over the full energy range. This behavior is confirmed by the event distribution shown in Figure 6.7.

By describing the position dependencies with a second Gaussian, an empirical approach is chosen. The simulation of the light propagation is able to reveal that the strength of the asymmetry in light yield strongly depends on the individual crystal parameters (i.e. scattering, absorption, reflectivities). This concludes in the requirement that the parameters and, in extreme cases, the model describing of the light yield distribution in a given energy interval has to be adjusted for each target crystal.

As mentioned before, the influence of position dependencies is best estimated in an energy range in which the effect excess light events is not observed. Therefore, the position dependence is investigated in the energy range between 150 and 170 keV. The parameters derived by fitting the data shown in figure 6.8b are given in table 6.4.

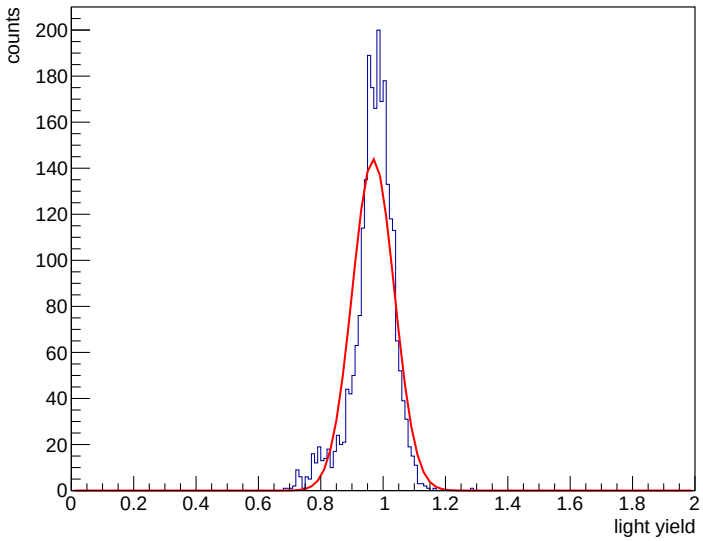

(a) Energy slice of in the light yield plane between 150 and 170 keV fitted by a single Gaussian (red line).

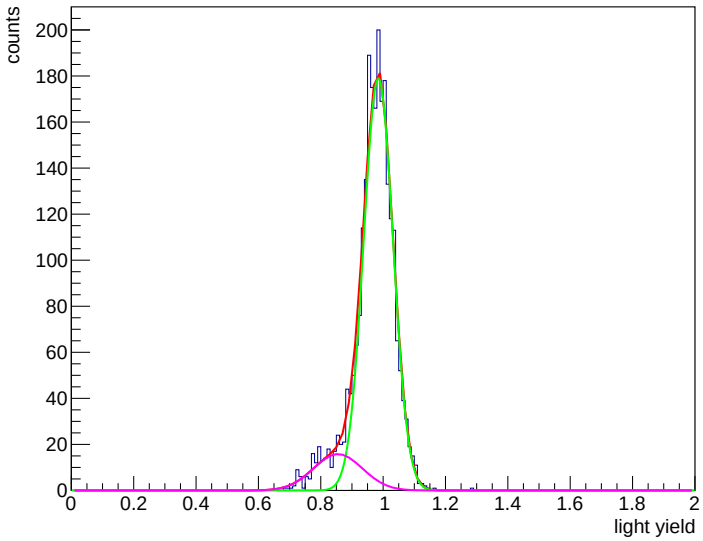

(b) Energy slice of in the light yield plane between 150 and 170 keV. To the data, a superposition of two Gaussians is fitted (red line). While one Gaussian describes the main event population (green line), the second accounts asymmetric shape caused by position dependencies (purple line).

Abbildung 6.8: Comparison between the different fit models to describe the observed light yield distribution in a limited energy interval.

fit parameter	*fit result*
$x_{c,1}$	$9.86 \cdot 10^{-1}$
σ_1	$4.48 \cdot 10^{-2}$
$x_{c,2}$	$0.89 \cdot 10^{-1}$
σ_2	$9.29 \cdot 10^{-2}$
A_1/A_2	3.89
σ_1/σ_2	0.48

Tabelle 6.4: Fit parameters derived by using the two Gaussian model to figure 6.8b.

Figure 6.8b illustrates that the superposition of two Gaussian allows to describe the data phenomenologically. By assuming that the position dependencies are energy independent, the high energy range can be used to estimate the widening because of this effect over the full energy range. To derive the parameters describing excess light event population in the low energy region with a reduced set of free fit parameters, the ratios of the amplitudes and the widths of the two Gaussians are fixed. This is done based on the assumption that the strength of the effect causing the leakage of events towards smaller light yields in energy independent and the width of the recoil band is dominantly defined by the performance of the light channel. Figure 6.9 shows the light yield distribution in the energy range between 0 and 20 keV including the fit.

The fit routine is highly sensitive to the start parameters, which indicates that the chosen model is over constrained and that the fit parameters are strongly correlated. The low statistics in the low energy region hinders the precise determination of the parameters further.

The comparison of the derived fit parameters using this method to the values obtained for an average conventional detector module using the standard method is not straight forward. Problematic is the fact that, in the conventional detector modules, position dependencies are usually sufficiently small that the light yield band is well described in the width derived using a single Gaussian for fitting. By adding a second Gaussian to account for the asymmetric shape of the light yield distribution in the slice detector module, the width of the parametrization cannot be related to the value derived by the standard approach.

Hence, in order to compare different detector modules in performance, one has to find quality parameters which are independent from the model used to describe the light yield distribution of the recorded events. Therefore, the following approach is used.

Independent of the light yield distribution, one can determine the median and the interval limits in which a certain percentage of the events are contained in for a given energy range (see figure 6.7). The general approach is to derive the median of the light yield distribution and to find an upper and lower limit based on the number of events which chosen to be in the interval. This means, that half of the accepted events are located above the median of the light yield distribution while the other half is located below the median of the light yield distribution. Consequently, the upper limit and the lower limit are able to have a different distance to the median of the event distribution

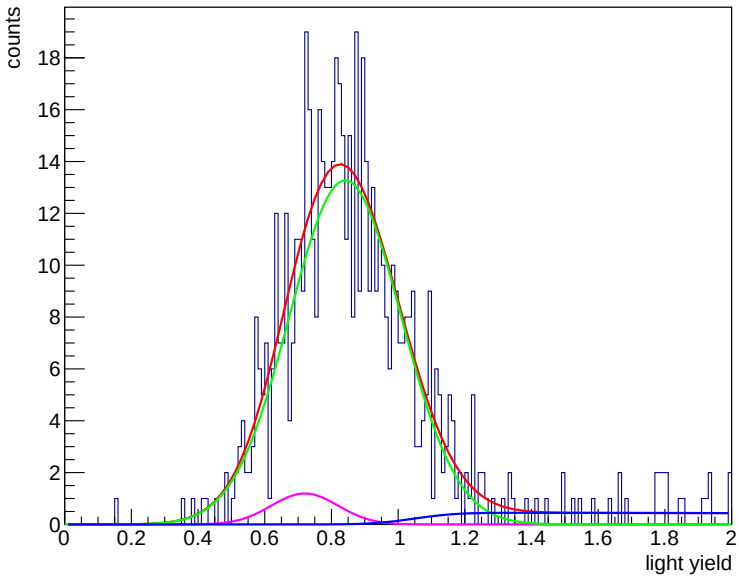

Abbildung 6.9: Light yield distribution in the energy range between 0 and 20 keV. To the data, a superposition of two Gaussian and equation 4.20 is fitted (red line). While the two Gaussian describe the main event population related to main absorber hits (green and purple line), the second accounts for excess light events (blue line).

in case the events are distributed asymmetrically.

In case of a normal distributed event distribution, the 90% interval is equal to $1.645 \cdot \sigma$. In addition, the median of a normal distributed light yield distribution is identical to its center value. Therefore, the method to derive the light yield parameters with the 2-D maximum likelihood fit and the integration method return the same results for the conventional detector module.

For the slice module, though, the light yield is not normal distributed but follows the model described in the previous paragraphs. However, the integral approach allows to derive the limits in which a certain event fraction is located. Since for the slice module the light yield distribution can be described analytically with the distribution function discussed before, the analytical solution of the cumulative distribution function is available. Hence, the median and the limits of the intervals can be calculated based on the fit results. Since due to the asymmetrically distributed event population the upper limit and lower limit are not equally far away from the median, the average value is used instead.

To compare the performance of the slice module with other detectors, the width of the electron recoil band σ_{LY} is determined using the median and integral method. By fitting the median and the average width in which the corresponding event number is contained with the equations 4.5 and 4.6, the parameters describing the width of electron recoil band are derived a second time (see table 6.5).

parameter	*fit result*
S_0(f)	$0.153\,\mathrm{keV}^2$ (f)
S_1	0.462±0.050
S_2	0.006±0.002
p_0	1.04±0.01
p_1	$-5.28 \cdot 10^{-4} \pm 5.27 \cdot 10^{-5}$ keV^{-1}
p_2	0.180 ± 0.022
p_3	19.56 ± 3.67 keV

Tabelle 6.5: Parameters derived using the integral method to describe the width of the electron recoil band.

The fit results derived with new parametrization of the light yield show a significant difference to the fit results assuming that the events is normal distributed in the light yield plane (see table 6.3). Since the model describes the data in better way than the initially used one, the fit parameters are not distorted. In comparison to an average CRESST-II detector (see table 4.1), the detector performance of the slice design is now confirmed to be positively influenced by the increased EDL.

The parameter S_1 scales according to $1/EDL$ as expected and confirms that the performance of the light channel is improved by the better light collection efficiency. Since the performance of the light detector as cryogenic device is not degraded by the large size of the light absorber (see section 6.3.3), the improvements can be solely related to detector design and the larger light collection efficiency. Additionally, the increased influence of position dependencies is reflected in the value of S_2.

To illustrate this observations, figure 6.10 depicts the light detector resolution $\sigma_{LD} = \sigma_{LY} \cdot E$ with the respective contributions for a conventional detector module with average performance and the slice prototype detector. In addition, the relative contribution of the respective terms to σ_{LD} are shown.

Figure 6.10 shows that the position dependencies in the light collection influence the detector resolution only at large energies to an extend that a relevant change in the light detector's performance is observed (see red curves). In the energy range relevant for dark matter searches, the improvements in light collection efficiency result in reduced contribution of the S_1 term (see green curves) while the increased position dependencies, reflected in S_2 term, are small. Consequently, the slice detector prototype is assumed to provide a better discrimination power for backgrounds in the ROI of dark matter searches than the average conventional detector module.

In section 4.3, two methods for quantifying the discrimination power of a detector module were introduced: Either by defining an analysis threshold based on the parameters describing the recoil bands or by estimating the expected background leakage in the ROI with a data driven simulation. Both methods can be applied for detector modules in which the event distribution can be modeled using a data driven simulation. In this case, a fair comparison between the the conventional detector design and the slice detector design is possible because the event distributions can be modeled according to

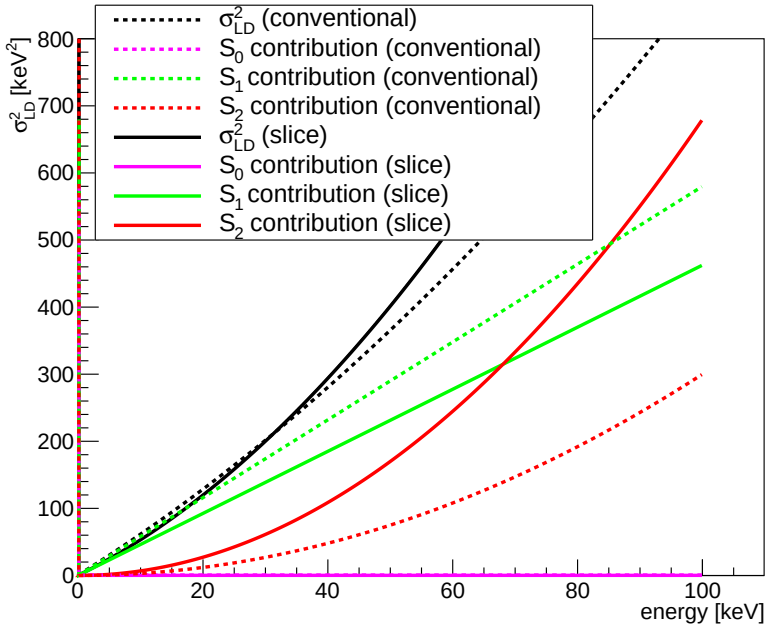

(a) σ^2_{LD} as function of the energy E. In addition, the contributions the terms containing S_0, S_1 and S_2 add to σ^2_{LD} are shown.

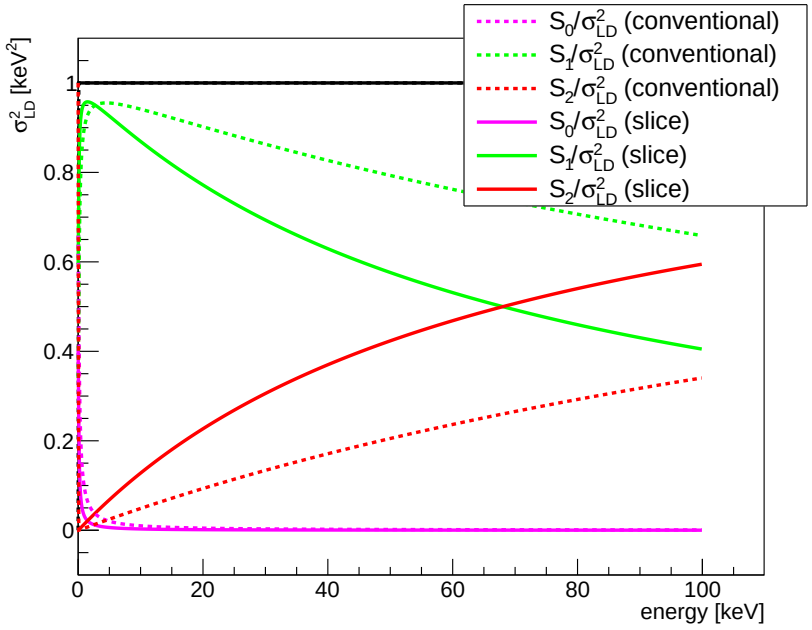

(b) The relative contribution to σ^2_{LD} of the terms containing S_0, S_1 and S_2.

Abbildung 6.10: Comparison of the light channel performance between conventional detector module (averaged performance, dashed lines) and the slice detector prototype (full lines).

the experimentally acquired parameterization. For the simulation, the assumed target crystal properties are identical for both detector geometries (i.e internal contamination, strength of the non-proportionality effect, scintillation efficiency). Additionally, it is assumed that the acquired exposure is the same.

The simulation proofs the strong influence of the EDL on discrimination power in the low energy region. Although the position dependencies in the slice module potentially increase the leakage of electron background into the ROI, the simulation predicts that the number of misidentified events in the ROI above a common energy threshold of 1 keV is reduced by (75.40 ± 1.72) % compared to an average conventional detector module. For the analysis threshold, a value (11.2 ± 1.5) keV is derived for a conventional detector module with average performance. For the slice detector, this value is lowered by a factor of ≈ 2 to (6.4 ± 1.2) keV. Both methods confirm that the improved light collection efficiency improves the background discrimination in the relevant energy range for dark matter searches. Additionally, it can be shown that the influence of the position dependencies in the light collection efficiency becomes negligible (see figures 6.9 and 6.10) because the asymmetric shape of the light yield distribution is washed out. As a consequence, the asymmetric shape of the light yield band becomes irrelevant in the low energy range while the overall discrimination power is improved by the better light collection efficiency.

6.4 Conclusive Comments on the Slice Design

The slice design proves that the performance of the light channel strongly depends on the geometric layout of the detector. By breaking the symmetry of the cylindrical target crystal and by putting the light absorber ïnsidethe main absorber, the light collection is significantly improved. The experimental test of this detector concept confirms that the measured EDL exceeds the average value of a conventional CRESST-II detector module (≈ 2 %) by a factor 1.5 reaching 3.07 %. Main reason for the improvement is that the average distance a photon travels before being collected by the light detector is shortened by a factor of 3 while the number of necessary reflections to guide a photon to the light detector reduced by a factor 2. Both effects lead to an improvement in the light collection efficiency in the detector module and, thus, in the measured EDL.

The observed asymmetry in the light yield distribution requires an adjustment of the standard method to derive the correct parameters for describing the recoil bands. Because of the geometric arrangement, the light collection efficiency is inhomogeneous for different regions of the crystal which is reflected in an asymmetric shape of the light yield distribution. By including the asymmetric shape of the light yield band in the analysis, the performance of the slice detector module can be described phenomenologically over the full energy range. For dark matter searches the asymmetric shape of the light yield has no negative impact. Compared to the other factors influencing the discrimination power of a detector, the position dependencies are negligible in the relevant energy range below 40 keV. More impact can be attributed to the gains achieved in the light collection efficiency which improves the resolution in the low energy range significantly covering the

increased position dependencies of the detector design. In direct comparison, the slice detector concept is able to provide a better discrimination power than a conventional detector module with average performance. The number of background events located in the ROI above a common phonon detector threshold of 1 keV can be reduced by (75.40 ± 1.72) % by the improved performance of the light detector. In case an analysis threshold is used to determine the discrimination power, the slice detector is able to provide a factor of 2 value lower analysis threshold. While the conventional detector modules are able to provide an analysis threshold of (11.2 ± 1.5) keV, the slice prototype provides an analysis threshold of (6.4 ± 1.2) keV). Thus, compared to the conventional detector design, the slice module is expected to exceed the sensitivity for dark matter of an average CRESST-II detector having the same performance of the cryogenic detectors used for phonon and light readout.

Never intended to be deployed in the CRESST main setup, the slice design does not provide a fully scintillating detector housing. Nevertheless, it is able to illustrate the influence of the detector design on the performance of a dark matter detector. Specifically, the positive influence of an improved light collection efficiency on discrimination power of a detector module is shown.

7 Beaker Detector Concept

In this chapter, the development and testing of the second newly developed detector design is covered: The beaker detector". Its development was started with the intention to overcome the limitations of the conventional CRESST-II detector design in regard of the identification of external background sources and the poor light collection efficiency for scintillation light (see section 4.8).

To achieve these goals, the commonly used detector layout of CRESST-II is changed drastically. Main feature is a large scale, beaker shaped light detector which surrounds the target crystal in almost every direction. Since the light detector covers a large solid angle, the light collection efficiency is drastically improved because the losses occurring during the propagation of the light are reduced. Additionally, this design establishes a complete and active 4π veto system for external background sources by adapting the composite design using a large TES carrier crystal [89].

A scheme of beaker detector design is given in figure 7.1.

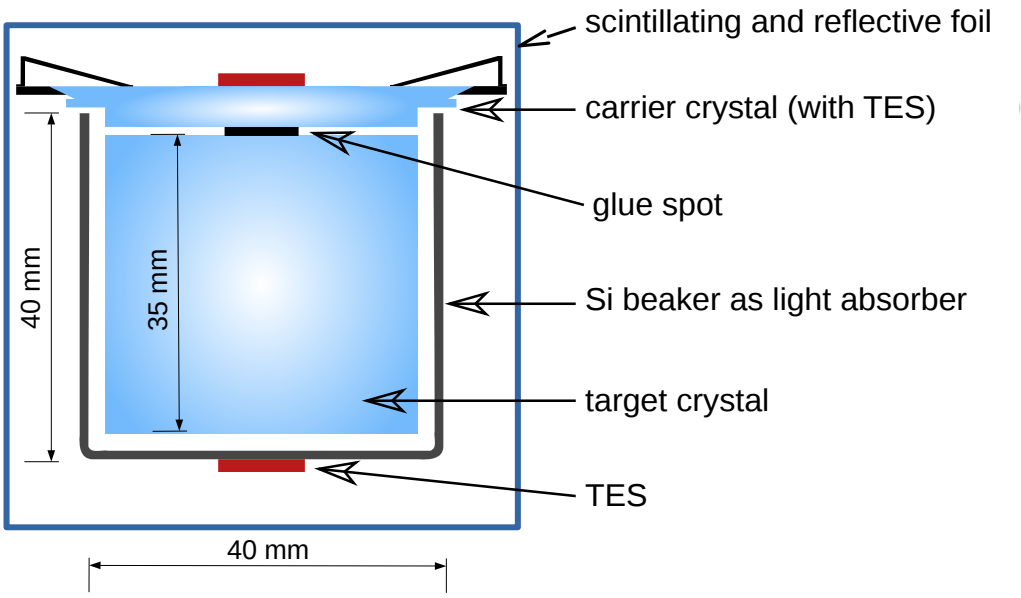

Abbildung 7.1: Scheme of a CRESST-II detector module featuring a large scale, beaker shaped light absorber.

Two detector prototypes of this design were operated for two years in the CRESST main setup at Gran Sasso. Based on this long term measurement, a detailed analysis of the system is performed in the following sections.

7.1 Design Goals

The development of the beaker module takes into consideration the disadvantages identified for conventional detector design and addresses all points mentioned in section 4.8. These are:

1. the poor light collection efficiency limiting the capability to discriminate β/γ-backgrounds from a possible signal. Especially towards detection threshold, the number of background events leaking in the region of interest can be reduced through an improved performance of the light channel.

2. the presence of ëxcess light events", namely events whose signals detected in the light channel exceed the normally observed light signal for electron recoils in the target crystal. The parametric band description of the recoil bands in the low energy region is complicated by their presence.

3. the presence of non-active surfacesïn line of sight to the target crystal. This introduces the possibility that degraded surface α-decays cause a background contribution in the region of interest for dark matter searches.

To overcome the first limitation, the geometry provided by a beaker shaped light absorber is ideal. By surrounding the target crystal in most directions with a light absorber, the solid angle covered by the light detector is massively increased compared to the detector layout of the conventional detector design. This minimizes the number of reflections that are necessary to guide a photon to the light detector and reduces the average distance a photon needs to travel inside the crystal before its detection. Therefore, the losses due to (re-)absorption either in the crystal or the detector housing are reduced.

To investigate the photon propagation inside the beaker detector design, the same simulation code is used as for the detector designs discussed in the previous chapters. The simulation estimates the light collection efficiency in the beaker design to be 80.6 %. In comparison, the simulation estimates the light collection efficiency in the conventional detector design to be 38.3 %. The main reason for the large gain in the light collection efficiency is the reduction of the average path a photon travels before its detection by a factor of 8 (compared to the conventional detector design) to 1.8 cm. Therefore, losses inside the main absorber are reduced by (75-85) % and due to absorption in the foil by (85-90) %, respectively. Due to the reduced propagation distance, position dependencies in the light collection efficiency are as well reduced. Therefore, the light yield distribution of the recoil bands is not expected to show any influence of position dependencies.

The larger amount of detected photons as well as the reduced influence of the initial starting position of the photons on the light collection efficiency is illustrated in figure 7.2 which shows the output of the simulation in the light yield vs. energy plane.

Compared to other detector designs presented in previous chapters, the width of the light yield band is reduced significantly. By applying the parametric band fit (see section 4.3) to fit the simulated data, the S_1 parameter is predicted to be improved by a factor

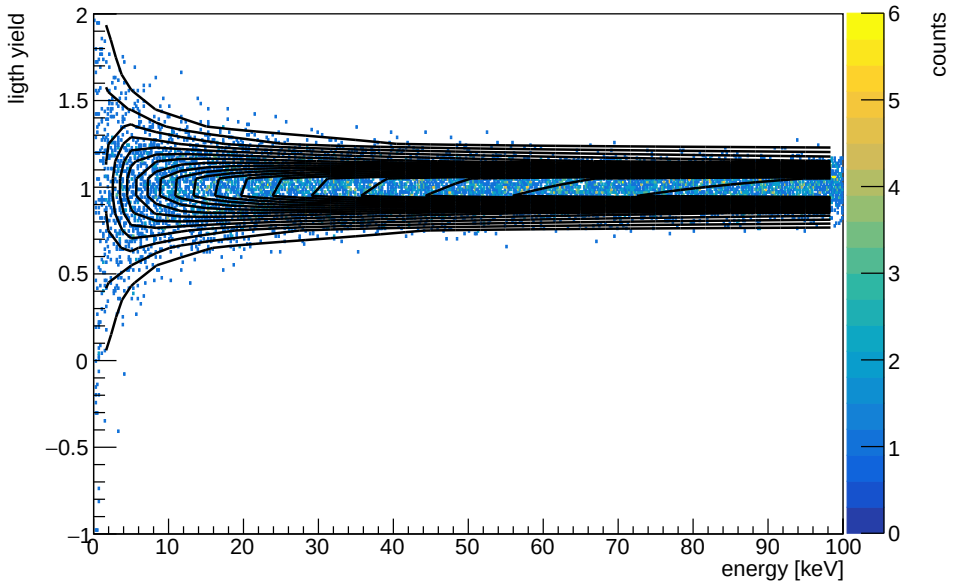

Abbildung 7.2: Simulated light yield vs. recoil energy plot for the beaker detector module. The black lines indicate the 2-D likelihood fit using equation 4.10 which is used to extract the parameters describing the electron recoil band. The light collection efficiency is strongly improved compared to the conventional module which yields in a smaller width if the electron recoil band and, hence, in a better particle identification power (i.e. reduced width of the event bands).

of 3 compared to a conventional detector module. The S_2 parameter, accounting for position dependencies, is massively reduced ($< 10^{-5}$) as position dependencies do not play a relevant role in the beaker detector.

The second and third disadvantages of the conventional detector module are tackled by replacing the indirectly read out detector parts of the detector housing by actively read out surfaces. Surface α-decays and external β-backgrounds are identified and discriminated by their unambiguous signal characteristics in the beaker or the carrier crystal. In the conventional detector design, the identification of these events relies on the scintillation mechanism of the detector housing (i.e. the foil) and the light collection efficiency of the detector design. Therefore, the additional light signal contribution, which is used for the identification of these event classes, is small (EDL for αs absorbed in VM2002 foil $\approx 0.8\,\%$ [74]) rendering the veto mechanism less reliable than the active system used within the beaker design.

In this chapter, it will be demonstrated how the beaker design addresses all aspects which are currently limiting the sensitivity of the conventional CRESST-II detector module. In combination with a better understanding for external backgrounds, the beaker detector module design promises a better sensitivity for dark matter searches.

7.2 Technical Description of the Detector Design

Designed to be deployed in the CRESST-II setup at Gran Sasso, the beaker module is developed to match the outer dimensions of the conventional CRESST-II detector modules (see section 2.3). The mass of the cylindrically shaped main absorber is reduced by 30 % from $\approx 300\,\mathrm{g}$ (standard absorber size of CRESST-II detectors) to $\approx 220\,\mathrm{g}$ (diameter 38 mm, height 35 mm). This allows to mount the target crystal inside a beaker shaped light absorber having the dimensions of target crystal of the conventional detector module (diameter 40 mm, height 40 mm, wall thickness 0.4 mm). In this configuration, the beaker provides an area of appropriately $60\,\mathrm{cm}^2$ for collecting light which increases the active area by a factor 5 compared to a standard light detector of CRESST-II.

To avoid any line of sight between the main absorber and non-active surfaces a cylindrical carrier crystal with increased dimensions (diameter 42 mm, height 5 mm, mass $\approx 38\,\mathrm{g}$) is glued onto the main absorber. In combination with beaker shaped light detector, a true 4π veto is achieved for the target crystal.

The composite detector design. i.e. the use a smaller crystal carrying the TES for the main target crystal is adapted from the conventional design for which this concept was tested intensively [89]. However, the dimensions of the carrier crystals are increased in the beaker detector to allow the establishment of the 4π veto. The carrier crystal is also used to hold the target crystal since the connection between the carrier crystal and the detector housing is established with silver coated bronze clamps (see figure 7.1).

The TES structure used in the beaker detector design is identical to the one used for the phonon channel readout in the conventional CRESST-II detectors (see section 2.3.2). The same sensor is used for measuring energy depositions in the main absorber as well as in the carrier crystal. A detailed discussion how events with different origin are identified is found in section 7.3.1.

The carrier and main crystal are machined from the same raw crystal to match the crystal orientation of the two absorbers. This reduces the appearance of thermal tensions/stress in the glue and the crystal during the cooling process for which the veto mechanism based on the light yield cannot be used. The glue spot connecting the two crystals is designed to be as small as possible while providing enough force to ensure a proper mechanical connection. Having a diameter of $\approx 6\,\mathrm{mm}$ and a thickness $\leq 10\,\mu\mathrm{m}$ (as derived from the number of Newton rings), the mass of the glue spot amounts to about $300\,\mu\mathrm{g}$. The thickness of the glue spot is mainly defined by the capillary forces between the crystal's polished surfaces.

As silicon provides good absorption efficiency at the wavelength of the scintillation light of $CaWO_4$ ($> 55\,\%$ [92]) and because it can be obtained as high quality crystal with low contaminations, the beaker is manufactured from mono-crystalline silicon (<100>, FZZ, undoped, 20 kOhm/cm). Despite the fragility of silicon, beakers can be manufactured with a wall thickness of only 0.4 mm. For the performance of the light detector as cryogenic calorimeter, a thinner wall is generally favored since the absorber volume can be reduced while area available for light collection is kept constant. However, the probability for a position dependent detector response is increased in thin absorbers due to the influence of the phonon scattering length on the signal evolution in the absorber.

Figure 7.3 shows the beaker shaped silicon light absorber during the TES production.

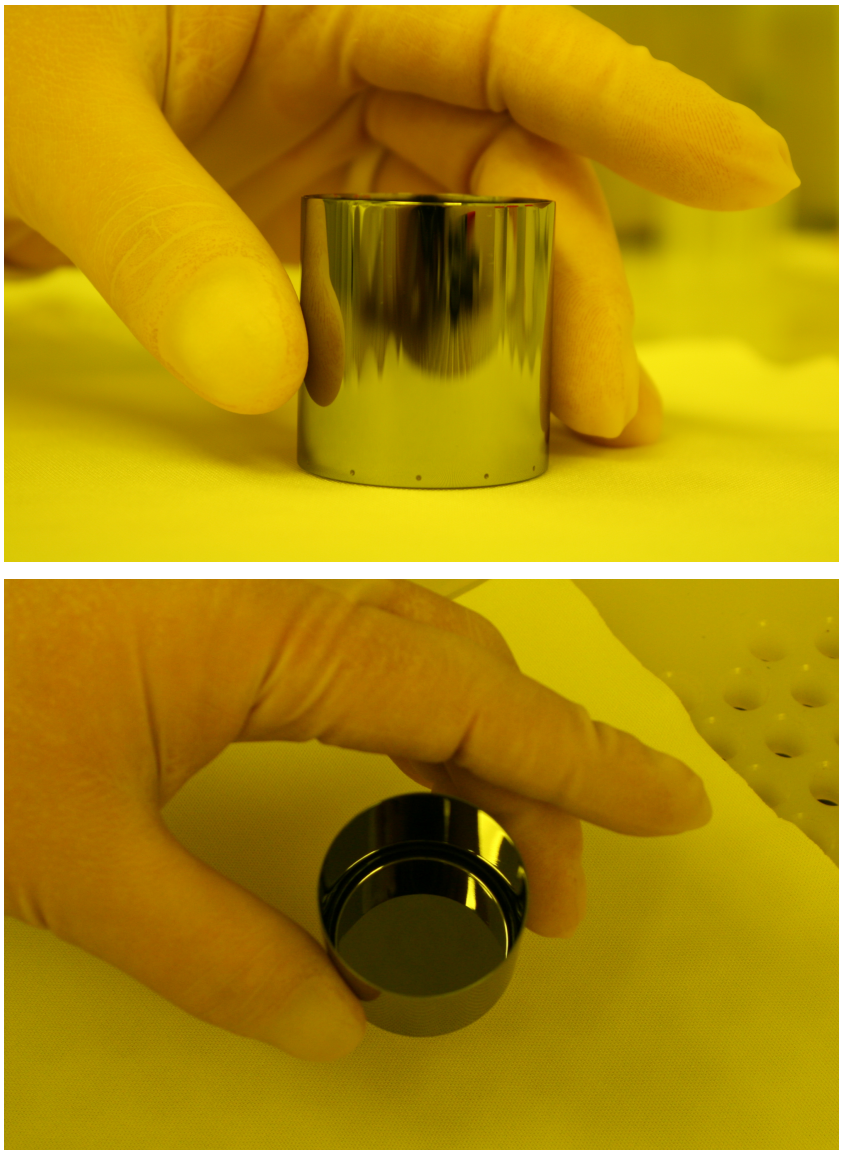

Abbildung 7.3: Photographs of a beaker shaped silicon light absorber during the TES production in the clean room.

The beaker is read out by a tungsten TES (thickness 80 nm) that is equipped by phonon collectors made of aluminum (thickness of 1 μm, (5 x 1) mm^2 (twice)). A further increase in sensitivity is intended to be gained by partially covering the thermometer by a thin Au layer at the area where the phonon collectors and the W-TES overlap. In this region of the thermometer, the electronic band gap of the phonon collector is reduced by normal conducting character of the gold film and the proximity effect. This adaptation of the thermometer structure intends to increase the thermalization efficiency

of quasiparticles reaching this part of the thermometer to enhance the sensitivity of the sensor (for more information see section 3.3).

Due to the increased dimensions the beaker, improvements of signal height achieved by the improved light collection compete with the larger volume of the absorber. Compared to the absorber used for standard CRESST-II light detector, the beaker's volume is increased by a factor of 5. A larger volume of an absorber causes reduced phonon density after a certain energy deposition and, consequently, a reduced energy entry into the TES. In order to account for this reduction, the collection area of the TES is increased by a factor of 10 compared to the thermometer structure used for the standard CRESST-II light detector to match the reduced energy flow in the thermometer. Based on the pulse model for the signal evolution in cryogenic detectors with TES readout (see section 3.3), the area of the TES has to scale linearly with absorber volume to maintain the same collection time for a the TES (τ_{film}, equation 3.8). Thus, a increase of the thermometer area by a factor of 5 is justified with this argumentation. The remaining enlargement is justified by the expected reduction of the life time of the non-thermal phonons in the beaker (τ_{crys}). Although the surface to volume ratio is identical for the beaker and a standard CRESST-II light detector, the geometry is expected to reduce τ_{crys} as more scattering processes are expected take place before a phonon is finally collected by the TES. In order to keep the ratio between phonons thermalizing in the TES and phonons thermalizing in the absorber on the same value (ϵ, equation 3.6), an additional reduction of τ_{film} is necessary which is achieved with the increased area the thermometer covers.

To complete the module, the detector housing surrounding the absorbers is completely lined by reflective and scintillating VM2002 foil (see figure 7.1). At the top of the module the foil enhances the light collection efficiency in the detector housing since this part of the main absorber is not covered by the light detector. The rest of the detector housing is lined with foil to prevent any direct line of sight between the beaker shaped light detector and the surrounding setup.

7.3 Testing and Results

In the following section, the performance of the beaker detector concept is evaluated. Two prototype modules with this design were deployed in CRESST-II (Phase 2). Next to calibration data sets (^{57}Co-calibration and AmBe neutron calibration), an extensive background data set was recorded. The data extends over ≈1.4 years (12.000 h) for each of the modules which corresponds to a raw exposure $\approx 115 - 120\,\mathrm{kg \cdot d}$ (per module). Due to the large size of the data sets, high statistics were achieved allowing a detailed analysis and evaluation of the detector concept.

7.3.1 Intrinsic Performance of the Phonon Detector

In this section, the performance of the phonon/heat channel as cryogenic detectors is evaluated. The methods applied for the evaluation were introduce in section 4.2

The threshold of CRESST-II detector channels is directly measured by injecting artificial heat pulses via an integrated TES heater. The value given as E_{thres} is defined as the energy level where (heater) pulses achieve a trigger efficiency of 50 %. The measured trigger efficiency is determined by fitting equation 4.1 in the relevant energy range to the recorded histogram of heater pulses. Using this procedure, the obtained values for E_{thres} and the baseline noise $\sigma_{PD,b}$ are given in table 7.1. The energy scale is set using the ^{57}Co calibration.

	E_{thres}	$\sigma_{PD,b}$
beaker module 1	11.223 keV	1.641 keV
beaker module 2	1.631 keV	0.325 keV

Tabelle 7.1: Energy of the threshold and baseline noise of the two beaker type detector modules operated during CRESST-II(Phase 2).

The baseline noise of the detectors, listed in the second column of table 7.1, are in agreement with the peak width (1σ) obtained for the smallest triggered test pulse amplitude for which no degradation in the trigger efficiency is observed. As mentioned before, the detector resolution of the smallest triggered test pulse amplitude can be considered as conservative upper limit for the baseline noise (see section 4.2.2). For module 1, the detector resolution of the smallest triggered test pulse is 1.400 keV. For module 2, a detector resolution 0.316 keV is determined using the same method.

The performance variations observed for phonon channels of different CRESST-II detectors are generally large. Values for E_{thres} between 0.3 and 5 keV are commonly reported for different CRESST-II detectors [69] [71]. For the baseline noise, values between 0.065 and 1 keV are reported [69] [71].

The performance of the phonon channel in detector module 1 is below the level usually observed for CRESST-II detectors. However, the poor performance of module 1 is most probably not related to the detector design but to a poorly performing thermometer. In this readout channel, an uncommon small signal-to-noise ratio is observed although the noise of the baseline (i.e. baseline RMS) is of the same size. Compared to the beaker module 2, the signal-to-noise ratio is one order of magnitude worse. A relation to the glue connection between the main absorber and the carrier crystal is ruled out because the performance level is poor for both event classes.

In beaker module 2, the detector threshold E_{thres} as well as the baseline resolution σ_b are able to compete with the best performing CRESST-II detectors. Thus, the general performance of the phonon channel in beaker detectors shows no general performance degradation, but with only two detector modules of this kind operated until now no reliable statement can be given.

In the beaker detector design, main absorber and carrier crystal are read out with the same temperature sensor. However, the TES is located on the carrier crystal. The two detector components are connected with a glue interface which establishes a mechanical connection and allows the signal propagation from one to the other detector part. The glue interface between the two crystals is expected to introduce losses which are reflected

in a reduced pulse height for events originating from the main absorber, therefore, in a worsening of the detection threshold.

Compared to other CRESST-II detector designs also using a carrier crystal for the TES, the mass of the carrier crystal used for the beaker detectors is increased. The increased mass of the carrier crystal allows to collect sufficient statistics for a spectral analysis of carrier events. Since main absorber and carrier crystal are machined from the same crystal, the intrinsic contamination with radioisotopes, thus, the spectral shape of the electron recoil band is identical. The spectral intensity scales according to the mass ratio of the two absorbers. By comparing the detected pulse height for a certain energy, performance differences are revealed (see figure 7.4).

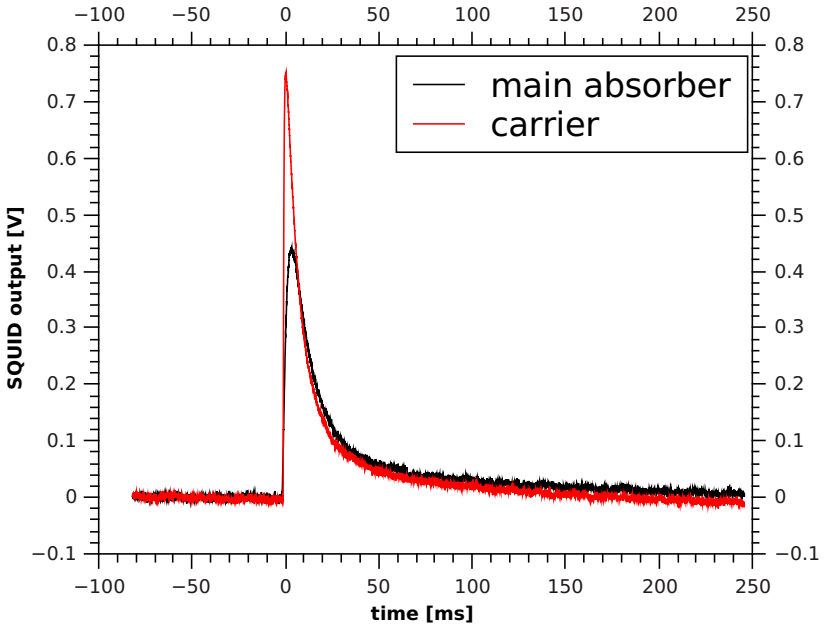

Abbildung 7.4: Illustration of the pulse shape and pulse height differences for a 46.5 keV energy deposition in the main absorber and in the carrier crystal recorded with the phonon channel of beaker module 2.

For module 1 and module 2, the pulse height of main absorber events is reduced by 51 % (module 1) and 48 % (module 2) compared to carrier events with the same energy. The loss of pulse height causes, that for main absorber events, the detection threshold is a factor 2 higher than for carrier events. Therefore, the use of a carrier system is confirmed to have an impact on the sensitivity of a detector module for dark matter. However, it is important to note, that the mass of the carrier is significantly smaller and, therefore, performance gains are expected for carrier events. Since in the beaker detector design a true 4π-veto is achieved using the carrier crystal to cover the surfaces the beaker is not able to cover, the worsening of the detection threshold in the phonon channel is accepted to achieve this design goal.

7.3.2 Intrinsic Performance of the Light Detector

The realization of the design goals of the beaker detector module, especially the improvement of the discrimination power for background events, relies dominantly on the performance of the light detector. Due to the increased dimensions of the light absorber, the performance of the light detector as cryogenic detectors is expected to be reduced. The mass as well as the surface area of the light absorber are increased by a factor 5 (from $12\,\mathrm{cm}^2$ to $60\,\mathrm{cm}^2$) compared to the SOS light absorber used for the conventional detector module. Thus, gains in signal height achieved by a larger light collection efficiency compete with a reduction in intrinsic detector sensitivity. To account for the increased absorber volume of the light detector, the thermometer structure of the beaker is adapted (see section 7.2).

Furthermore, the possibility for position dependencies in the detector response is increased for the beaker. Depending on the distance between the energy deposition and the thermometer, the detected signal can experience additional losses which cause an additional degradation of the detector resolution. Reason for this effect is reduced cross section of the beaker, which affects the phonon propagation in the absorber and, therefore, the signal evolution.

In the following paragraphs, the performance of the light channel as cryogenic detector is evaluated using the same methods as for the conventional modules (see section 4.2).

The energy scale for direct energy depositions in to the beaker is set using ^{55}Fe X-ray calibration sources which illuminate both beakers directly on the mantel area. The calibration with an ^{55}Fe X-ray calibration source produces two mono-energetic peaks at $5.89\,\mathrm{keV}(\mathrm{K}_\alpha)$ and $6.49\,\mathrm{keV}(\mathrm{K}_\beta$, intensity $\approx 11.7\,\%$ of K_α) [67]. Pulse shape analysis allows to identify direct light absorber hits and allows to separate the direct energy depositions unambiguously from scintillation events (more information will be given in section 7.3.4). In addition, the signal in the phonon channel is used as anti-coincidence veto to reject all events with an energy deposition in the main absorber.

The calibration spectra recorded with the two beaker shaped light detectors are are shown in figure 7.5.

In both spectra, a position dependent detector response is observed which masks the expected spectral shape of the calibration data. Since the recorded spectra differ strongly, they are discussed in the following individually.

For the beaker shaped light detector operated in detector module 1 (figure 7.5a), at least four distinct peaks can be identified in the spectrum of the ^{55}Fe calibration source. The relative position as well as the relative intensities of the peaks suggest that the spectrum of the source can be separated into two separate event populations. One that is related to K_α X-ray line and one that is related related to K_β X-ray line. By using a fit model based on two Fermi-function like cut-off functions which are combined two exponential rise/decay functions, each of the two event population can be described empirically. Both event populations show a similar behavior which can be explained with a position dependent detector response. Each event population consists of two peaks which are connected by an asymmetrically shaped valley. The number of events contributing to the K_α and K_β population corresponds to the literature value of the

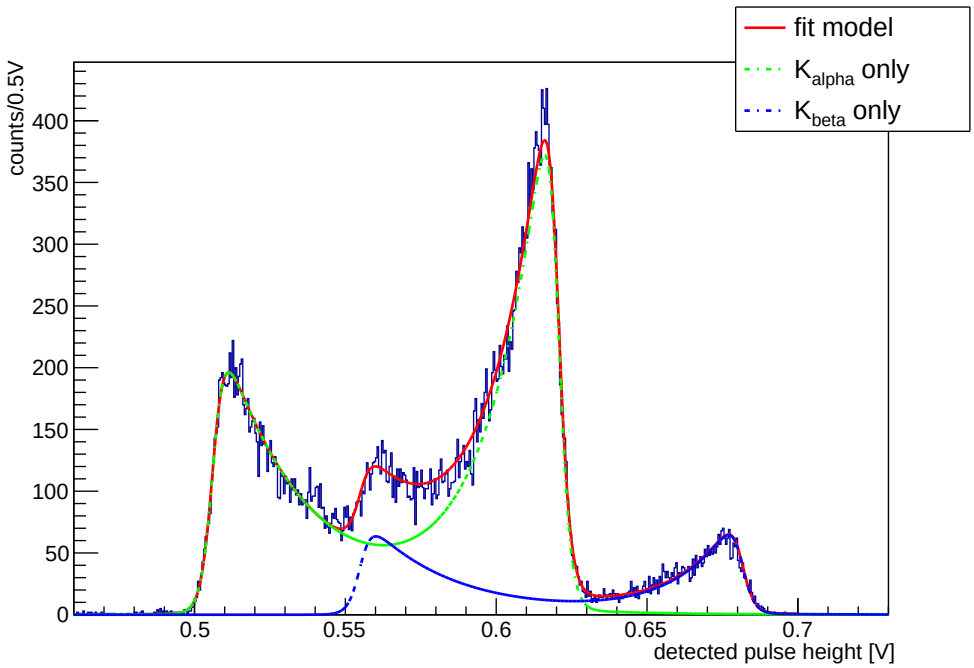

(a) Beaker light detector (module 1).

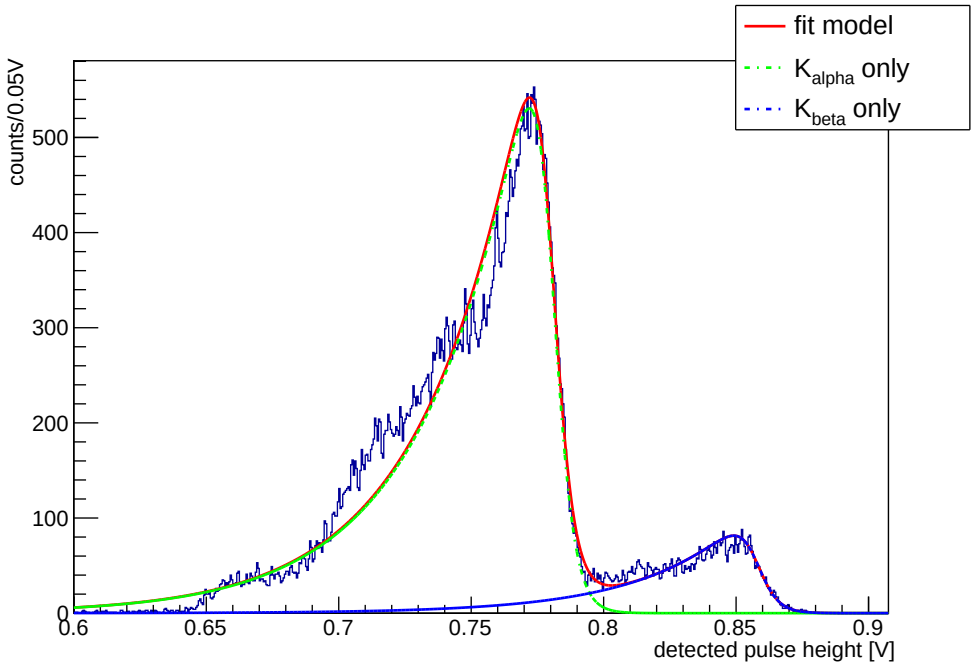

(b) Beaker light detector (module 2).

Abbildung 7.5: Spectrum of the ^{55}Fe calibration sources illuminating the beaker shaped light detectors. The recorded spectra are discussed in detail in the text.

decay. However, the peaks in the respective on the left and right side do not have the same height. The high energetic, falling edge as well as the low energetic, rising edge of the spectrum represent the maximal/minimal detector response for a given energy. The steep rise/decay of the local maxima at the edges indicate that the intrinsic detector resolution for a certain event class with a defined position of absorption is much better that the broad spectrum suggests. In between the minimum and the maximum of the spectrum, the event distribution is broadly smeared, creating an asymmetric shaped valley between the two peaks. This observation suggests that the spectral shape is related to the specific detector response for a certain location of absorption. As a consequence, a precise energy calibration of light detector in beaker module 1 cannot be performed without further, very specific assumptions.

The effect of a position dependent detector response is confirmed by the second calibration spectrum which is recorded by the beaker shaped light detector operated in detector module 2 (figure 7.5b). Here, the calibration spectrum shows two peaks with the expected ratio in peak positions (i.e. energy) and intensities. The position dependent detector response is less pronounced, but still visible as asymmetric broadening of the two peaks to smaller pulse heights. Also here, the spectrum can be separated in two event populations which are correlated to K_α X-ray line and the K_β X-ray line of the source. In this case, the model used for describing a single component of the spectrum is composed by a single Fermi-like function and an exponential rise. In contrast to the beaker shaped light detector operated in detector module 1, an energy calibration can be performed using the identified peaks since the spectrum is in agreement with the expectation.

For both beaker shaped light detectors, but especially for the beaker shaped light detector operated in detector module 1, a significant variation in the detector response is observed for X-ray interactions. Developed in the scope of the CRESST-II experiment, though, the light detectors are intended for measuring a scintillation light signal and not for measuring X-ray interactions.

In the following paragraphs, the influence of the position dependent detector response for mono-energetic X-rays on the capability to measure scintillation light signals is investigated. The main difference between scintillation signals and X-ray interaction is that an energy deposition is distributed over the full area the detector provides for light absorption instead of a single, localized energy deposition. Hence, one can assume that a scintillation based event sees the averaged effect of a position dependent detector response which depends on the distribution of the photons detected in the light detector.

The investigation of these effects is difficult because the majority of the input parameters necessary to describe the problem are generally unknown. Nevertheless, the X-ray calibration spectra can be used to model the influence of the effects on the detected pulse height for scintillation events using a simulation. The simulation has the following approach:

1. Creation of a photon with a random energy according to the emission spectrum of $CaWO_4$.

2. Photon propagation in the detector and collection in the light detector.

3. Response of the light detector for each photon as a function of the interaction process (i.e. position dependent detector response (DR)).

4. Sum over all generated photons to compare the detected energy with the energy of a X-ray absorbed at a certain position of the detector.

The emission spectrum of $CaWO_4$ is known [44]. Based on this knowledge, the energy distribution of the photons connected to a scintillation event can be modeled precisely. The photon propagation and collection in the light detector can be simulated realistically using the simulation code for estimating the light collection efficiency (see previous chapters). Hence, the distribution of the absorption locations on the photons can be modeled. The detector response for a given absorption point is usually not precisely measured. For this, the light detector has to be illuminated with a known energy at different locations of its surface which is usually not done during the detector characterization. Nevertheless, the second and third point can be estimated by using the spectra under the assumption that a single source illuminates the beaker homogeneously. In this case, the recorded spectra, shown in figure 7.5, can be understood as probability distribution for the detector response. This allows to estimates the detector response for a scintillation event in comparison to an X-ray interaction with the same energy at a specific detector position.

The last assumption for the simulation is a simplification of the detector response since it relates the recorded spectra solely to position dependent response while possible influence of geometric effects is neglected.

Using the simulation approach outlined before, the detector response for scintillation events is estimated. The procedure is explained in detail for the light detector operated in detector module 1. The detected energy of scintillation signal with an energy E_{det} is calculated with

$$E_{det} = \underbrace{\Sigma_{i=1}^{n}}_{\text{number of photons (Poisson distributed)}} \left(\underbrace{E_{photon,i}}_{\text{scintillation spectrum}} \cdot \underbrace{DR_i}_{\text{detector response}} \right). \tag{7.1}$$

The relative detector resolution $\Delta E_{det}/E_{det}$ is calculated with

$$\left(\frac{\Delta E_{det}}{E_{det}}\right)^2 = \left(\frac{\sqrt{n}}{n}\right)^2 + \left(\frac{\sigma_{photon}}{E_{photon}}\right)^2 + \left(\frac{\Delta DR}{DR}\right)^2. \tag{7.2}$$

In equations 7.1 and 7.2, n is used as the number of simulated photons, $E_{photon,(i)}$ as the individual photon energy, E_{photon} as the average photon energy according to the scintillation properties of the target crystal, σ_{photon} is the variance introduced to the photon energy E_{photon} due to the scintillation process, DR the detector response function and ΔDR the uncertainty of the detector response function DR.

To generate the same energy deposition in the light detector as for an X-ray with an energy of 5.89 keV an average number of 2031 photons is necessary. To account for the intrinsic uncertainty of photon counting, the number of photons in a single event is

Poisson distributed around this value. Each photon has an energy which is in agreement to the scintillation spectrum of $CaWO_4$. Using the fitted spectrum of the ^{55}Mn K_α event distribution as probability distribution for the detector response, each photon energy is multiplied with a random detector response according. For the detector response, it is assumed that the high energetic tail of the event distribution corresponds to a detector response of 1. The distribution of the detector response for the photons generated to simulate one event is shown in figure 7.6) in blue. In addition, the average detector response of a scintillation event is calculated. By repeating the calculation (i.e. 10000 events), a histogram of the average detector response is generated (figure 7.6), red line).

The result of the simulation shows that, for scintillation events with an energy of 5.89 keV, the effect of the position dependent detector response is averaged and results in a normal distributed event population for a large number of simulated events. Thus, inhomogeneities in the detector response are averaged by the homogeneous distribution of the events over the surface available for light collection. This finding is in agreement with measurements made with standard CRESST-II light detectors. The usually observed detector response for scintillation events is normal distributed which is reflected in the parametric band description (see section 4.3).

Nevertheless, the detector response for scintillation events is reduced compared to the maximal detector response for X-rays. The average detector response for this event class is 0.916 with a 1σ of 0.0221 (2.24 %) (beaker 1) and 0.975 with a 1σ of 0.0212 (2.17%) (beaker 2), respectively.

For smaller photon numbers, thus, for smaller energies, the effect of the position dependent detector response is investigated as well. In this case, the number of detected photons becomes smaller and the averaging effect of the position dependencies is reduced. This can be reflected in the relative detector resolution.

The investigated energies are 2 keV and 100 eV[1]. The simulation shows that the average detector response is invariant for different energies. In addition, the simulation shows no indication that the simulated light signals are not normal distributed around the average detector response. Though, the 1σ width of the simulated events increases towards smaller energies. The results of the simulation applied to the beaker shaped are summarized in table 7.2. Based on the simulation, one can state that the influence of the detector response on the final detector resolution for scintillation events is small compared to other effects. The broadening of the detector response is dominated by the uncertainty introduced by the photon counting statistics as this contribution is a factor 10 larger than the other uncertainties.

The energy calibration of the beaker shaped light detectors is determined using the average detector response DR of the the beaker detectors. This means, the energy calibration is corrected according to their detection efficiency for scintillation light which is determined using the simulation code explained in the previous paragraphs. For the light detector operated in detector module 1, the calibration factor $\zeta_{cal,1}$ is determined

[1] These energies correspond to the expected scintillation signal for electron recoil events in energy range of the ROI for dark matter searches (i.e. $E = 1 - 40$ keV).

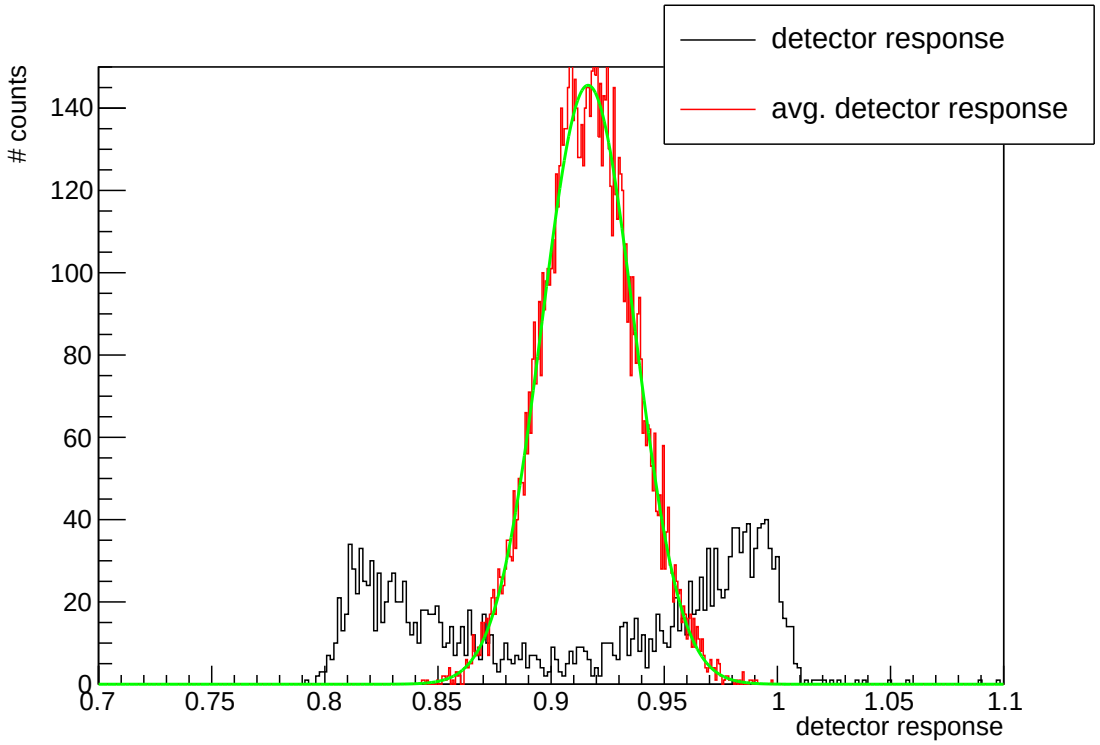

Abbildung 7.6: Simulated detector response of 10000 events (scintillation) with an energy of 5.89 keV. The recorded ^{55}Fe spectrum of the beaker light detector of module 1 is used as detector response function (black spectrum). The high energetic peak is normalized to detector response of 1. The red spectrum shows a histogram of the average detector response for a scintillation event with an energy of 5.89 keV. It can be shown that the influence of the position dependent detector response is averaged by the large number of detected photons per event. As a consequence of this averaging effect, the events are normal distributed around an average detector response (fit is indicated as green line). The average detector response for the beaker shaped light detector of module 1 for scintillation events is 91.6 % while the relative detector resolution is 2.2 % (1σ width).

to be

$$\zeta_{cal,1} = \frac{0.621\,\mathrm{V}}{5.89\,\mathrm{keV}} \cdot 0.916 = 0.097 \pm 0.0021 \frac{V}{keV} \tag{7.3}$$

and the calibration factor $\zeta_{cal,2}$ for the light detector operated in detector module 2

$$\zeta_{cal,2} = \frac{0.780\,\mathrm{V}}{5.89\,\mathrm{keV}} \cdot 0.975 = 0.129 \pm 0.029 \,\frac{\mathrm{V}}{\mathrm{keV}} \tag{7.4}$$

The intrinsic detector resolution cannot be determined based on the calibration data without further assumptions. Nevertheless, different options can be named to give an

E_{det}	*avg. DR*	$\Delta E_{det}/E_{det}$ *DR*	$\Delta E_{det}/E_{det}$ *DR+scin*	$\Delta E_{det}/E_{det}$ *DR+Poisson*	$\Delta E_{det}/E_{det}$ *DR+scin+Poisson*
beaker 1					
5.89 keV	0.916	0.0017	0.0017	0.0222	0.0223
2 keV	0.915	0.0029	0.0040	0.0371	0.0380
100 eV	0.907	0.0130	0.0178	0.1689	0.171
beaker 2					
5.89 keV	0.975	0.0006	0.0016	0.0216	0.0217
2 keV	0.978	0.001	0.0029	0.03671	0.0371
100 eV	0.961	0.0043	0.0129	0.1602	0.1609

Tabelle 7.2: Summary of the simulation results for the average detector response and the relative detector resolution $\Delta E_{det}/E_{det}$ for different energies E_{det} for the beaker shaped light detectors operated in detector module 1 and 2. The influence of the different uncertainties on the total uncertainty is given with the values listed in the different columns.

estimate on this detector parameter.

For scintillation events, the intrinsic detector resolution can be assumed to be identical to the total uncertainty the simulation derives. Thus, a $1\sigma/E$ resolution of 2.24% (beaker 1) and 2.17% (beaker 2) can be estimated.

A less conservative approach is used if one estimates the detector resolution for a limited area of the light detector. This eliminates the influence of the position dependence and allows to investigate the intrinsic resolution of the thermometer used for the light detector. The isolation of the events is achieved under the assumption that the steep rise and decay of the two event populations represent the minimal/maximal detector response to a given energy for the most distant and the closest absorption point. In this case, the width of the flanks on the left and right side of the spectrum are defined by the intrinsic resolution of the TES. By fitting the high energetic flanks with a Gaussian, one can determine a $\sigma_{LD} = 56.2 \pm 1.2\,\text{eV}$ (0.8%) for beaker 1 and a $\sigma_{LD} = 76.8 \pm 1.3\,\text{eV}$ (1.2%) for beaker 2. These values exceed the normally observed performance of standard CRESST-II light detectors for which a relative detector resolution of 1-2 % is common.

The baseline noise of the beakers $\sigma_{LD,b}$ is derived by fitting empty baseline samples with the standard event and applying the standard energy reconstruction (see section 4.2). The amplitudes returned are normal distributed around zero and allow the extract the baseline noise $\sigma_{LD,b}$. Table 7.3 summarizes the values obtained for the beaker shaped light detectors. The values for $\sigma_{LD,b}$ are in good agreement with other CRESST-II light detectors. No significant influence of the increased light absorber dimensions is observed in the baseline noise $\sigma_{LD,b}$.

In summary, one can state that the performance of the beaker shaped light detectors shows no major worsening due to the increased dimensions of the light absorber. Due to the increased dimensions of the light absorber, a position dependent detector response for X-ray interactions is observed. For scintillation light signals, theses position dependencies

detector	$\sigma_{LD,b}$
module 1	6.87 eV±0.06 eV
module 2	5.66 eV± 0.05 eV

Tabelle 7.3: Baseline resolution σ_b of the beaker type light detectors operated during CRESST-II (Phase 2).

are less relevant since the large number of detected photons help to cover this effect. Nevertheless, a reduction of the average detector response of up to 10 % is observed for scintillation signals detected in the beaker shaped light detectors. The relative detector resolution is only marginally influenced by the increased light absorber dimensions.

The detector performance of the beaker shaped light detectors as cryogenic light detectors is reduced in direct comparison to the standard light detectors of CRESST-II. Main reason for the reduction is the increased influence of position dependencies on the detected signal height. Nevertheless, the reduction in performance is on a moderate level which allows to assume that it can be counterbalanced by the increased light collection efficiency in the beaker detector design.

7.3.3 Energy Detected as Light

As stated in section 7.1, the beaker design aims to reduce the average distance scintillation photons travel before being absorbed in the light detector to reduce the number of photons lost during propagation. The simulation of the light collection efficiency estimates that for the beaker module the amount of energy detected as light can be improved by a factor 2-2.5 compared to the conventional detector module.

The fraction of energy detected as light is determined using the method described in section 4.5.2. It is based on comparing the detected energy for scintillation light with direct energy depositions in the light detector. To set the energy scale of the light detector for direct energy depositions, the ^{55}Mn K_α X-ray lines of the ^{55}Fe source directly illuminating the light detectors is used (see calibration spectra in figure 7.5). The energy scale for scintillation light events is determined using the ^{57}Co calibration data. Using the normalized standard events for direct light detector hits and scintillation events, the integral ratio is used to account for the pulse shape differences between the two event classes. Table 7.4 lists the calibration values used for the determination of the EDL.

	LD amplitude [V] @5.89 keV	*average det. response*	*integral ratio*	$\zeta_{cal,x}$ *[keV/V]*
beaker 1	0.620	0.914 ± 0.0221	1.218 ± 0.055	0.097 ± 0.0021
beaker 2	0.780	0.975 ± 0.0217	1.221 ± 0.063	0.129 ± 0.029

Tabelle 7.4: Summary of the parameters used for the calculation of the EDL.

Using these calibration parameters, the fraction of energy detected as light is derived. The parameters used and the results are summarized in table 7.5.

E_{cal}	*LD amplitude [V]*	*detected energy in LD [keV]*	*EDL [%]*
module 1			
122.06 keV	0.470±0.018	5.532±0.230	4.53±0.19
136.49 keV	0.535±0.018	6.236±0.235	4.55±0.17
module 2			
122.06 keV	0.676±0.027	6.297±0.277	5.15±0.23
136.49 keV	0.762±0.028	7.094±0.289	5.19±0.21
		average	4.86 ± 0.09

Tabelle 7.5: Combined results of the determination of the fraction of energy detected as light (EDL) in the beaker modules. The combined result is derived using the ^{57}Co calibration data set (γ-ray lines 122.06 keV and 136.49 keV). The average value of the share of energy detected as light is (4.86 ± 0.09) %.

The measured EDL exceeds in both beaker modules the average values achieved by conventional CRESST-II detector modules by a factor 2-2.5. The average value is (4.86 ± 0.09) % exceeding the EDL achieved in the conventional detector module ((1.9 ± 0.3) % [48]) and the slice detector design ((3.08 ± 0.21) %, section 6.3.4).

The systematic uncertainty of the EDL value is dominated by the light detector resolution for scintillation events. For direct energy depositions, the resolution of the light channel is mainly defined by its performance as cryogenic detector (see section 7.3.2). For events originating from the target crystal, i.e. scintillation signals, the performance of the light channel experiences a further reduction which is not directly correlated to the light detector. Local and intrinsic variations of the scintillation process in $CaWO_4$ [70] and position dependencies in light collection efficiency worsen the resolution for events originating from the main absorber. For the scintillation of the 122.08 keV γ-ray (^{57}Co source), a resolution of 3.9 % (module 1) and 4.1 % (module 2) is measured. In comparison with the resolution of the light channel for direct hits (see tables 7.3 and 7.4), a reduction of a factor 2 is observed. Other parameters (i.e. the intergral ratio) can be determined with high precision (uncertainty $< 1\%$) and influence the total uncertainty marginally.

The difference between the measured EDLs of the beaker modules is too large to be explained by the systematic uncertainty of the method used for its determination. Variations in the scintillation efficiency of the target crystals as well as their optical quality are able to explain the discrepancy of the results achieved in both detector modules. In reference [48], the scintillating efficiency is measured for different $CaWO_4$ crystals. There, variations in of $\mathcal{O}(10\,\%)$ are reported which is sufficient to explain the observed differences.

The combined result of (4.79 ± 0.09) % is consistent with expected improvements based on the simulation of the light collection efficiency. The measured values exceed the average results achieved by the conventional detector modules and indicate that the particle identification capabilities are improved for the beaker detector design. The position dependencies in the detector response for X-ray interactions, which result in a

reduction of the average detector response for scintillation light, are counterbalanced by the increased light collection efficiency of the beaker detector design which implies that the discrimination power for background can be improved according to the expectations. The influence of the EDL on the discrimination capabilities is discussed in the next section.

7.3.4 4π-Veto System

One of the major design weaknesses of the conventional detector design is that it does not provide fully vetoing detector housing. The beaker detector design overcomes this limitation using a true active 4π veto system. Main intention of the veto system is to reject all events which are not in agreement with the expected event signature of an interaction occurring solely in the main absorber.

In the following sections, the working principle of the 4π veto system is explained in detail using the better performing detector module (beaker module 2). In order to illustrate the discrimination power of this detector design in regard of external backgrounds the raw data will be cleared step by step. Figure 7.7 shows the data set of beaker module 2 before the 4π-veto is applied.

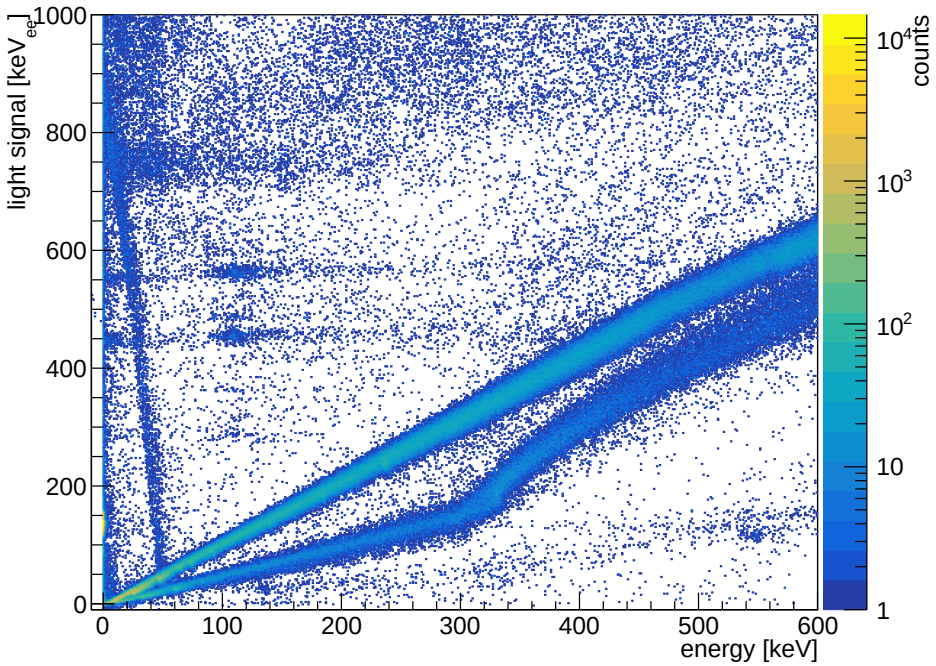

Abbildung 7.7: Initial data set of beaker module 2 before the external backgrounds are removed using the 4π-veto system.

7.3.4.1 Discrimination of Carrier Events

In order to achieve a 4π veto, the identification of events related to the carrier crystal has to be achieved with high efficiency down to the detection threshold of a detector module. Since the carrier crystal is in direct contact with non-scintillating surfaces (e.g. bronze clamps), the carrier itself experiences the same design flaws as the target crystal in the conventional design in regard of external backgrounds. To assure that carrier related backgrounds do not limit the sensitivity of the detector modules, all carrier events are rejected.

In figure 7.8, the different event populations are marked to facilitated their identification.

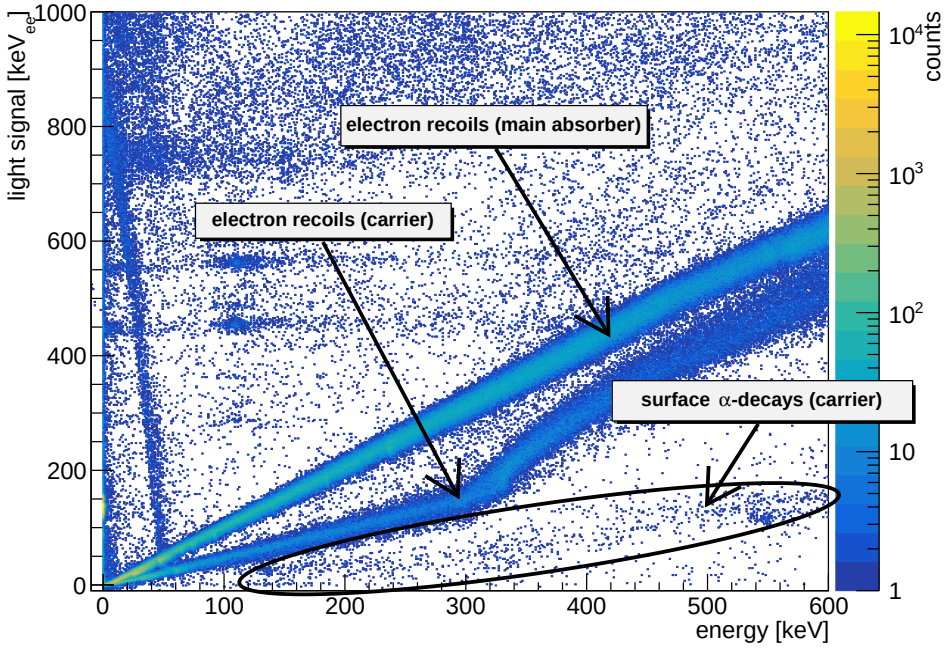

Abbildung 7.8: Identified electron recoil event population originating from the main absorber and the carrier crystal. In addition, the surface α-decays in the carrier are marked.

Next to the dominant event population related to the electron recoils occurring in the main absorber crystal, a second prominent event population can be identified as the election recoils taking place in the carrier crystal. In addition, the α band related to surface decays can be identified as event population below the electron recoil band. The reduced slope of the carrier related event population is related to the smaller light yield of carrier events because of the geometric layout of the beaker detectors and the incorrect pulse height determination of carrier events with the template fit.

The identification of events taking place in the carrier crystal is achieved by applying pulse shape analysis to the signals recorded in the phonon channel. As mentioned in

section 3.1.2, the pulse shape of an events is defined by the dimensions and geometry of the cryogenic detector. The phonon propagation and thermalization reflect these detector parameters and allows to disentangle events which occurred in the carrier from events which occurred in the main absorber. The possibility to use this method is introduced by the presence of the glue connection between the two detector parts. The glue interface between the main target crystal and the carrier crystal affects the phonon transmission in such a way that an absorber characteristic pulse shape can be developed.

A distinct pulse shape difference is observed between carrier and main absorber events in both beaker modules operated during CRESST-II (Phase 2) (see figure 7.9). Using the pulse model for describing the signal composition of an event (see section 3.1.2), the time constants of the carrier events are determined (see table 7.6).

pulse parameter	*carrier (B1)*	*main (B1)*	*carrier (B2)*	*main (B2)*
A_n	1.219	2.036	1.22	1.36
A_t	0.175	0.249	0.114	0.151
τ_{in}	0.79	3.74	0.44	1.06
τ_n	13.92	16.10	8.44	13.25
τ_t	80.11	89.40	98.15	130.91

Tabelle 7.6: Pulse parameters derived by fitting the normalized standard events for carrier and main absorber events of beaker 1 (B1) and beaker 2 (B2).

The rise time (τ_{in}) of carrier events is significantly faster than the rise time of main absorber events. The pulse shape parameters describing the decay of the pulses (τ_n, τ_t) show only a small difference between the two event classes. The time constant describing the decay of the non-thermal pulse component is reduced since it is related to the smaller dimensions of the carrier. The time constant describing the decay of the thermal pulse component is only affected on a small level as it is dominantly defined by the thermal link of the thermometer system.

Given the presence of pulse shape differences, the rejection of carrier events using pulse shape analysis is possible. The carrier cuts applied to the data are designed to achieve an effective and complete background rejection while the reduction of the exposure due to a reduced cut survival probability for main absorber events is intended to be as small as possible.

To identify carrier events as such, different pulse shape parameters can be used like, for example, the peak position of an event. In the analysis performed during this work, all pulse shape parameters are used to achieve the best results in terms of rejection power. In the following, the cut definition used for all pulse shape parameters is explained using the peak position parameter as example. Figure 7.10 shows the peak position vs. energy scatter plot using the data recorded with the phonon channel of beaker module 2 after all energy independent data quality cuts were applied. These include the cuts on the RMS of the baseline, the multiplicity, the left-right baseline value and an energy > 0. Thus, the events in the remaining data set can be assumed to be valid events while events showing artifacts are removed.

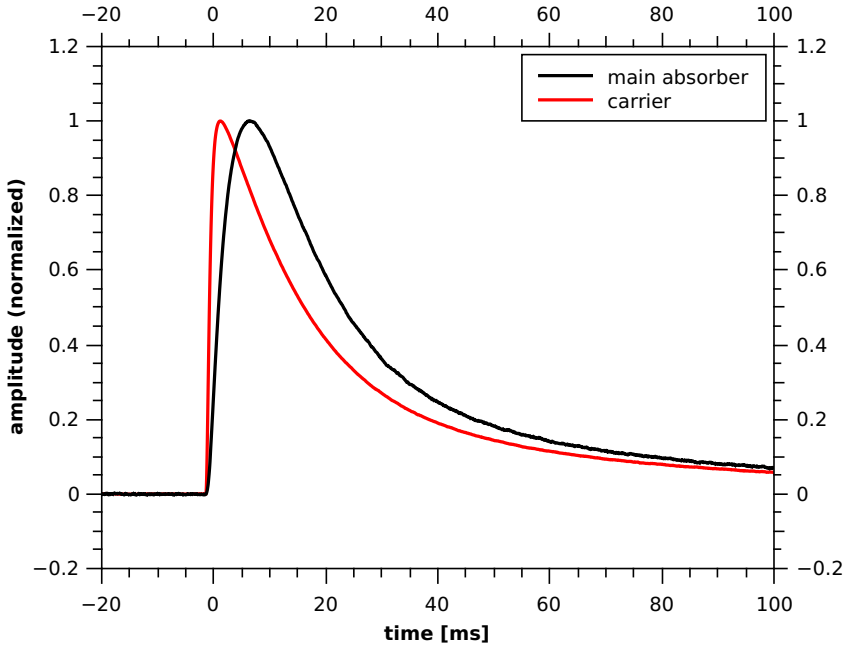

(a) Beaker module 1

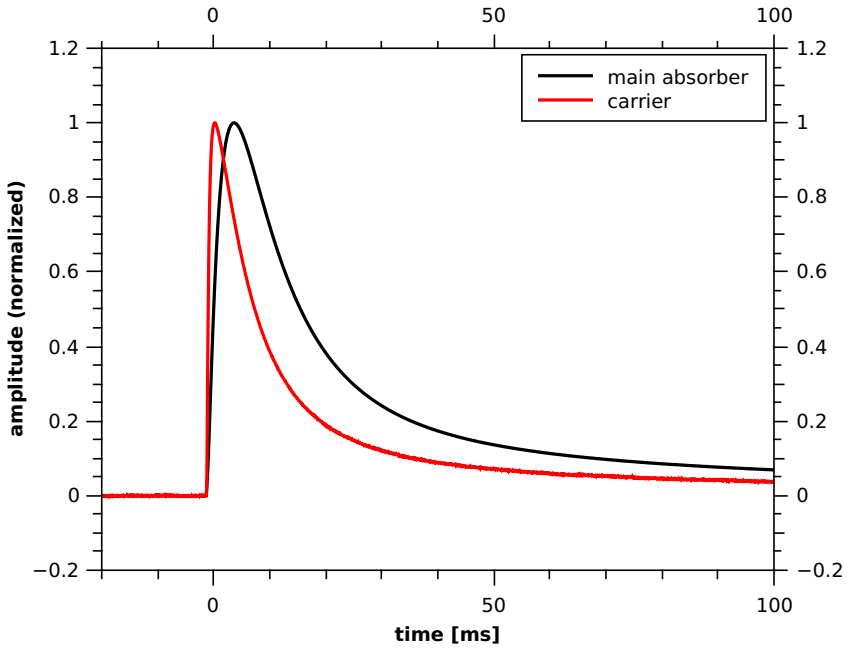

(b) Beaker module 2

Abbildung 7.9: Comparison of the normalized standard events of carrier and main absorber events in the two beaker modules. In both cases, the carrier events reach the peak of a pulse ≈ 5 times faster.

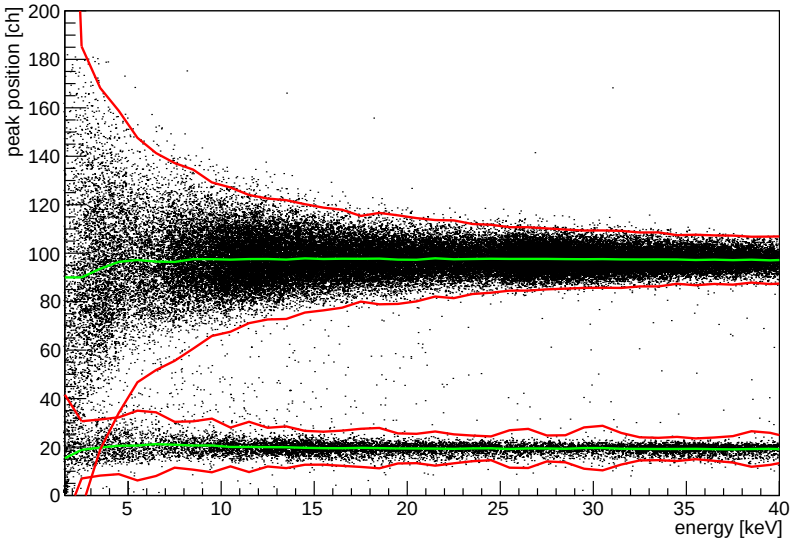

Abbildung 7.10: Scatter plot showing the peak position vs. energy plane (beaker module 2). Events with a peak position of ≈ 100 are identified as main absorber events while carrier events are centered around a peak position of ≈ 20. The boundary in which 90 % of the events with a certain origin are expected are indicated with red lines. The center of the respective event populations are shown as green line.

In the chosen presentation, the events form bands which can be correlated to a certain event class. Two major event populations are identified. Events with a peak position of ≈ 100 are identified as main absorber events while carrier events are identified with a peak position of ≈ 20. For each event class, the events are expected to be normal distributed around an average value as the widening is expected to be dominantly caused by the detector resolution. Thus, the interval in which the events from a certain event class are located can be derived for a limited energy interval by fitting a Gaussian to the respective population (90% interval is indicated by the red lines).

Towards smaller energies, the reduced signal-to-noise ratio causes the event populations to overlap because the pulse shape parameters become more and more influenced by the baseline noise. In figure 7.10, this behavior is observed as broadening of the respective event bands. For events with small energy, the pulse shape parameters cannot be used to disentangle main absorber events from other event classes. The pulse parameters are determined with an uncertainty too large to a assure an unambiguous assignment. In order to remove carrier events down to detector threshold, the cuts are made in such a way that an effective background removal is assured. To keep the contamination with carrier events at the desired level, two approaches are available to define the cut acceptance region at small energies.

1. The definition of an energy independent cut limit (shown in figure 7.11a as solid

purple line). The limit is defined by the total amount of expected leakage of carrier events in the cut acceptance region over the full energy range. In this case, the cut limit is set to allow less than one carrier event is expected to survive the carrier cut on the peak position. The accepted events are marked in purple as well. Since the highest probability for leakage is given by the first bin above detector threshold, the impact of the latter is large on the cut limit. In bins at higher energies, the amount of events leaking into the acceptance region is smaller.

2. The definition of an energy dependent cut limit (see figure 7.11b). The events located in the acceptance region are marked in in purple. Since distribution of events can be estimated for energy bin individually, it is also possible to set a cut limit for each bin based on this distribution. By integrating the estimated leakage over the full energy range one can achieve an energy dependent cut definition based on the data. In this case, less than one carrier event is expected to survive the carrier cut on the peak position. As long the band do not overlap, the acceptance region corresponds to the main absorber band with the chosen acceptance limits. At lower recoil energies, where main absorber and carrier bands start to overlap, the acceptance region is reduced by the area the carrier band and the main absorber band cover simultaneously. This method distributes the possibility for carrier events leaking into the cut acceptance region equally over the full energy range and minimizes the number of main absorber events falsely removed from the data.

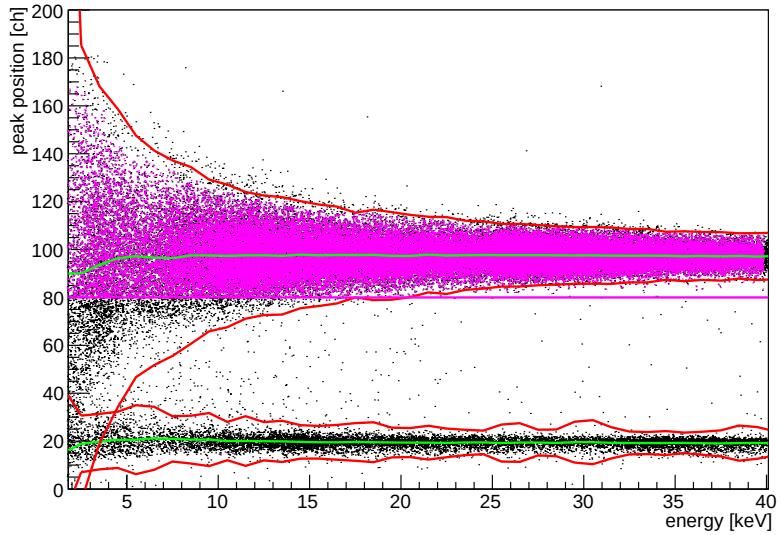

(a) Energy independent cut.

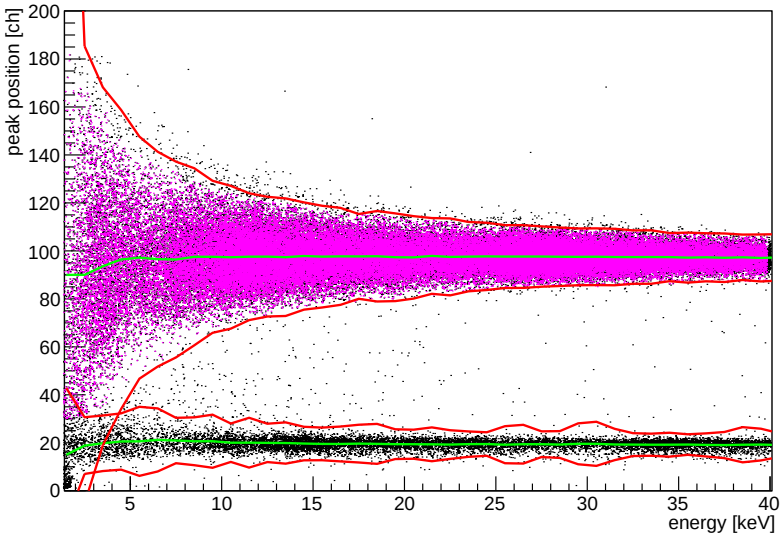

(b) Energy dependent cut definition.

Abbildung 7.11: Comparison of the different methods for the cut definition.

For the data set recorded for the two beaker modules, the energy independent cut definition was used. Although the cut survival probability is reduced at lower energies to a larger extend using this method, the amount of carrier events surviving the cuts is expected to be smaller. Therefore, this approach can be considered as more conservative.

To validate the efficiency of the applied cuts to the data a simulation is used. By superimposing standard events with randomly sampled baselines, it is possible to generate artificial events of a certain event class with the characteristic noise level of the respective

detector channel (method described in reference [69]). By scaling the amplitude of the superimposed standard event, the cut survival probability can be derived as a function of energy. The cut survival probabilities for the beaker modules 1 and 2 are given in figure 7.12.

The lines shown in figure 7.12 represent the final cut survival probability after all cuts are applied to the data. Thus, a general reduction of the survival probability by 10 % due to the stability cut and the removal of signal artifacts is introduced for main absorber events and carrier events.

For both modules, the final cut survival probability is derived down to the threshold of the phonon channel. For energies well above the threshold ($> 5 \cdot E_{thres}$), the cuts applied are highly effective to remove the carrier events. Above this energy, the survival probability for carrier events is negligible (i.e. no artificially generated events survives the applied cuts) while the cut survival probability for main absorber events is above 90%. However, for lower energies, the influence of the baseline noise is reflected in the cut survival probability for main absorber events and carrier events. In order to maintain a efficient veto mechanism, the decreasing signal quality requires to remove a larger fraction of main absorber events. This is reflected in the reduced cut survival probability for main absorber events. On the other hand, the probability that a carrier event survives the cuts increases towards smaller energies due to the choice of a energy independent cut definition. This is reflected in the increasing survival proportionality for carrier events towards small energies.

For beaker module 2 (figure 7.12b), the derived cut efficiency meets the expectation in regard of its shape and efficiency.

Due to the poor performance of the phonon channel of beaker module 1, which is also reflected in the bad detector threshold of this phonon channel (see section 7.3.1), a proper cut definition is impeded for this detector module. The baseline noise affects the observed pulse shape for events with an energy $< 50\,\mathrm{keV}$ to such a level that a complete removal of all events is would be necessary to achieve desired cut efficiency for carrier events. Consequently, the performance of beaker module 1 is not sufficient to allow a reliable statement on the performance carrier system in this energy range.

The efficiency of the carrier cuts can be illustrated with the data (see figure 7.13). After the application of all carrier cuts, the region below the electron recoil band of the main absorber is cleaned from electron recoils and α-interactions taking place inside or on the surface of the carrier crystal.

The removal of carrier events is not only necessary for the data recorded with detector modules of the beaker design. Establishing the appropriate cuts to remove them is also necessary in the data sets obtained with detector modules of the conventional design using the composite carrier concept [89]. The data of conventional detector modules has been analyzed in several works (see references [43] [65] [69]). The findings in these references confirm the behavior observed for the two beaker modules in regard of the carrier cut efficiency and the general cut survival probability. For energies five times larger than E_{thres}, the cuts designed to remove carrier events work highly efficient while the cut survival probability for main absorber events remains unaffected. Towards the threshold of the phonon detectors, the veto mechanism using pulse shape differences

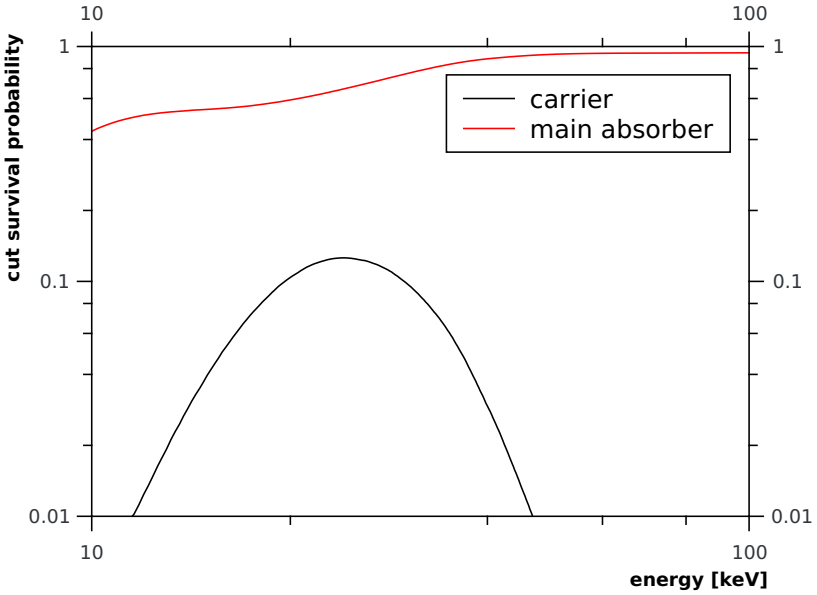

(a) Beaker module 1.

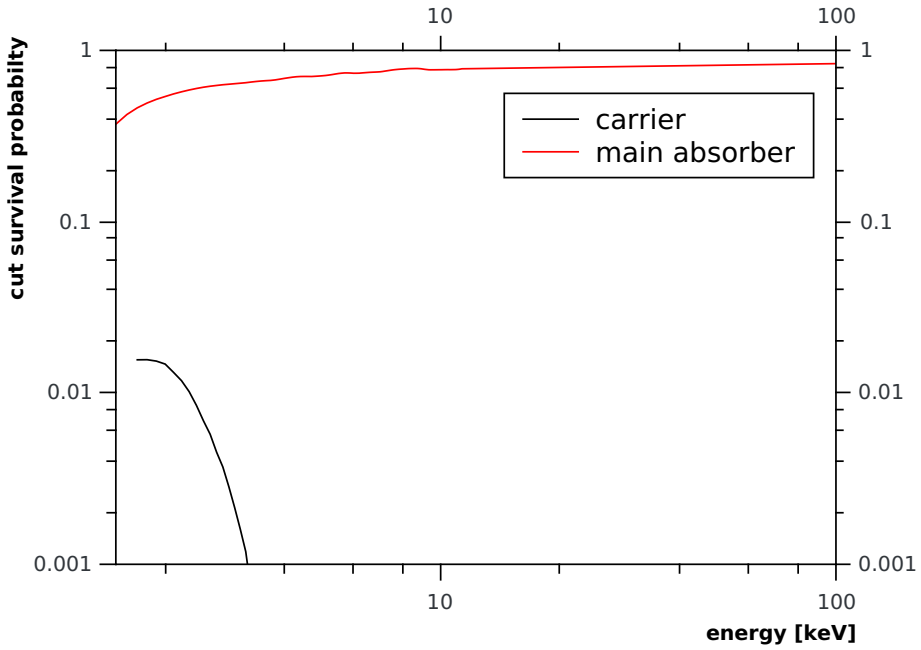

(b) Beaker module 2.

Abbildung 7.12: Cut survival probability for main absorber and carrier events. The shown energy scale is adapted to the individual performance of the phonon channels. For more information, see text.

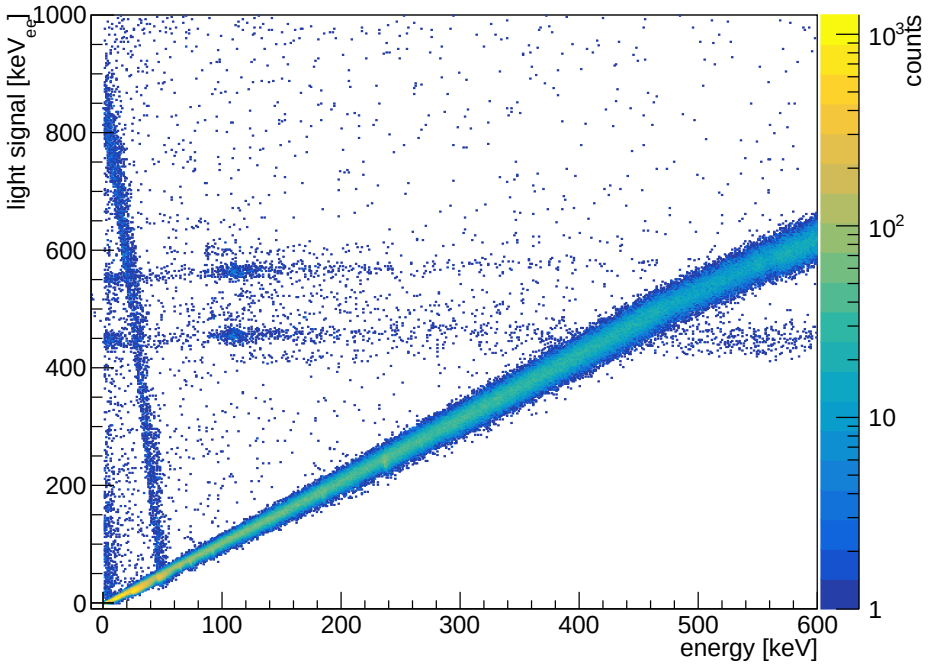

Abbildung 7.13: Remaining data set after the application of the carrier cuts

fails due to the fact that no differences can be extracted. The increased dimensions of the carrier used in the beaker detector design cause that the pulse shape differences are less pronounced and the veto of carrier events is more difficult. However, the pulse shape differences developed in the tested detector modules are sufficiently strong to achieve a discrimination power which is on the same level as the discrimination power achieved in other CRESST-II detector designs. Even in direct comparison with the best performing phonon channel of CRESST-II (Phase 2) equipped with a carrier crystal [69], the enlargement of the carrier crystal used for the beaker modules shows no negative impact on the final cut survival probability. Also in this module, the cut efficiency begins to be affected by the carrier cuts at energies below an energy which is 5 times larger than the reported detector threshold.

In summary, one can state that the rejection of carrier events is achieved with high efficiency if the performance of the phonon channel allows a pulse shape analysis with the usual accuracy obtained in CRESST-II phonon detectors. The identification of carrier events can be achieved down to the detection threshold of the detector module while the reduction of the exposure is not significantly increased in comparison with other detector designs using a carrier crystal for the TES readout. There is also no indication that the enlarged dimensions of the carrier crystal hinder the pulse shape analysis and affect the sensitivity of the beaker detector on an increased level because of surviving carrier events in the ROI.

7.3.4.2 Discrimination of Excess Light Events

The term ëxcess light eventrefers to all events whose light signals exceeds the normally observed scintillation signal of electron recoils in the main absorber crystal. In the conventional detectors, the reason for the events to have an increased light signal is the production of scintillation light in the detector housing (see section 2.3.4). In the beaker detectors, excess light events are dominantly caused by an additional, direct energy deposition in beaker (i.e. in the light channel).

Since this event class is considered as background, the 4π-veto system is intended to reject all events of this type. In figure 7.13 (i.e. after the application of the carrier cuts), the events with excess light character can be found as event population located above the event population which is related to electron recoils taking place in the main absorber.

Different kinds of particle interactions can lead to a light signal which exceeds the normally observed scintillation light signal of an electron recoil occurring in the target crystal. In CRESST-II detectors, excess light events are dominantly caused by external β backgrounds originating from the experimental setup (i.e. cryostat/shielding) or by α decays which take place on the surfaces of the target crystal or the detector housing. In the following, the mechanisms behind the excess light event signature is explained for external β-backgrounds and surface α-decays suing the schemes shown in figure 7.14.

Before being absorbed in the target crystal, a β-particle originating from the detector environment, is able to interact with the material surrounding the target crystal and deposit a part of its energy therein. Afterwards, these βs are absorbed in the main absorber in which they create a phonon and light signal corresponding to their energy and nature. In the conventional detector module, the scintillating foil lines the main absorber in almost every direction. Incoming β-particles are able deposit part of their energy to the foil which transforms this energy into scintillation light. Thus, the signal recorded by the light channel is the superposition of scintillation light created by the main absorber and a small amount scintillation light created by the surrounding foil (scintillation efficiency of the foil 0.8 % [93]). Compared to an event from the bulk of the target crystal, events with external origin have a larger light signal which shifts these events in the light vs. recoil energy scatter plots above the electron recoil band (see figure 7.13). This process is illustrated in figure 7.14a. In the beaker detector design, the detected event behind this background process is similar. Also here, part of the energy is not deposited in the target crystal but in the detector surrounding where additional light is created (see figure 7.14b). Intermediate, lossy processes like the scintillation process in the foil and the light propagation in the detector housing are avoided which results in larger additional light signal and facilitated identification of these events.

For α-decays that take place on a surface in direct line of sight to the target crystal or on the target crystal itself, the underlying physical interaction processes are different but the event signature in the detector channels is identical. During an α-decay, an α-particle and a daughter nucleus are created. One of two decay products is absorbed in the target crystal while the other one is absorbed in the detector surrounding (i.e. foil or light detector). Also here, the energy deposited in the detector surrounding causes

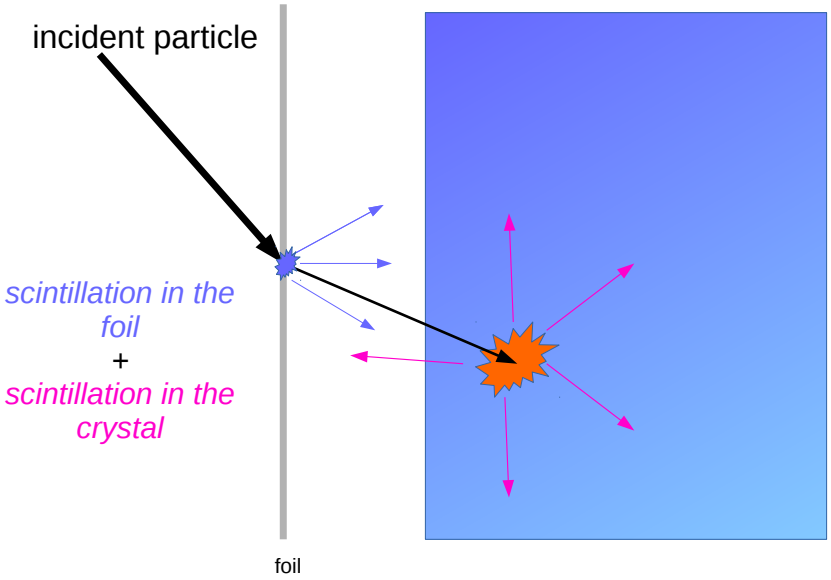

(a) Excess light events created in scintillating detector housings

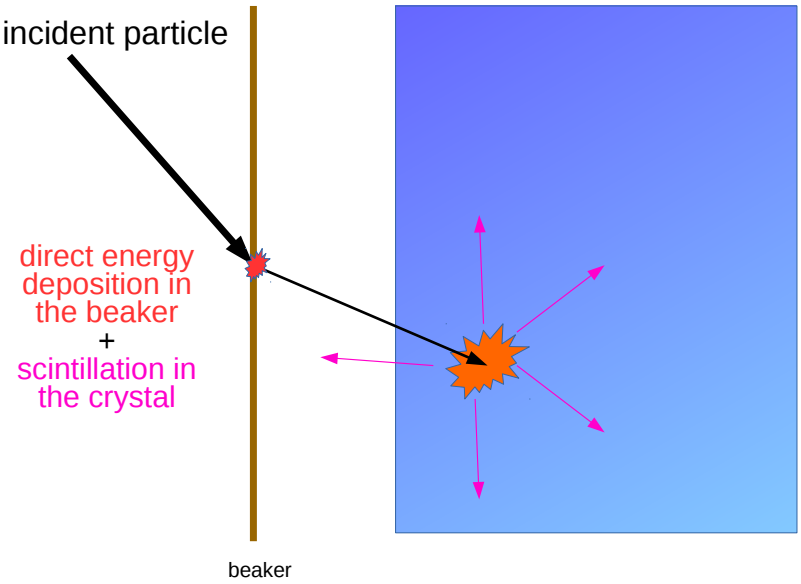

(b) Excess light events created in actively readout detector housings

Abbildung 7.14: Interaction mechanism behind the excess light events in different detector housings.

an additional signal in the light channel and allows to veto these events. In general, the α-particles and nuclear recoils are detected with an reduced light signal in phonon-light detectors. However, the additional light signal caused by absorption of the escaping particle in the beaker, causes that the event related to α-decays are located above the electron recoil band.

In detector designs which rely on a scintillating detector housing, excess light events cannot be disentangled from main absorber events by applying pulse shape analysis to the light channel. Although the scintillation mechanism of the foil VM2002 foil is significantly faster than the scintillation mechanism of $CaWO_4$, no significant pulse shape difference is observed for excess light events because the signal contribution of the foil to the total light signal is small.

For the beaker design, the situation changes. Since the beaker is actively read out, pulse shape differences between direct energy depositions in the beaker and scintillation light signals are more pronounced. Reason for this is the larger fraction the direct energy deposition contributes to the signal seen in the light detector and the fact that the energy is directly deposited in the light detector avoiding any intermediate process (i.e. scintillation process, photon propagation). To illustrate the pulse shape differences between scintillation signals and direct hits, the respective standard events of the light channel of beaker module 2 are shown in figure 7.15.

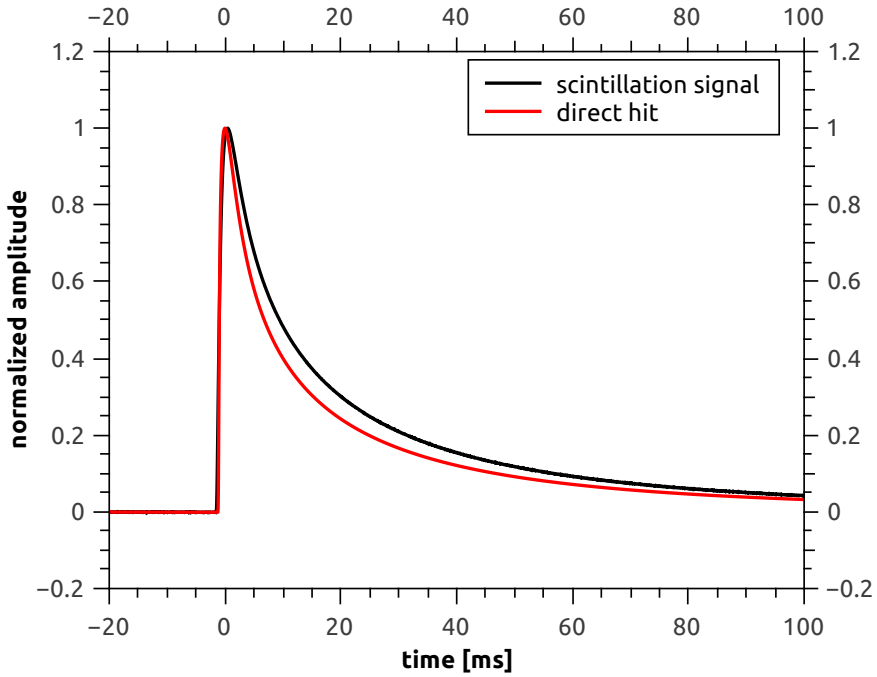

Abbildung 7.15: Comparison of the standard events derived for the beaker light detector. In black, the standard event for light signal of scintillation signal originating from the $CaWO_4$ crystal is shown, in red the standard event for direct light detector hits.

By applying pulse shape cuts on the light channel, the excess light events are removed from the data. Main goal of the cuts is to reject all events whose light signal differs from a scintillation signal originating from the target crystal.

Since the light signal of excess light events is significantly larger than the light signal of scintillation based events with same energy (i.e. in the phonon channel), their discrimination using pulse shape analysis is massively facilitated. The cut definition for removing the light excess events can be done without any energy dependence. The cut survival probability for main absorber events after the application of the pulse shape cuts on the light channel is already included in the final cut survival probability shown in figure 7.12 for both beaker modules. No significant reduction of the cut survival proportionality is introduced by the cuts designed to remove the excess light events (i.e. $< 1\,\%$).

In both detector modules, the number of events located in this excess light event region makes up $\approx 5\,\%$ of the total number of events in the shown energy range. Excess light events are found over the full energy range, nevertheless, there are clustered event populations which can be related to distinct background processes. Two of these backgrounds are discussed in detail in the following to illustrate that the 4π veto system allows a better understanding of the backgrounds seen in the detector module.

In figure 7.16, a cluster of events can be related to the β-decay of ^{210}Pb taking place on the surface of the beaker facing the target crystal or on the target crystal itself.

The discussed event population starts from the electron recoil band of the main absorber with a recoil energy of 46.5 keV and continues on the isoenergetic line[2] until the full energy is detected in the light detector. Consequently, the light signal is not only caused by scintillation but also by a direct energy deposition in the light absorber which allows its identification via pulse shape analysis.

The β-decay of ^{210}Pb has to branches (see figure 7.17) [67]. With a branching of 84%, the β carries an maximum energy of 17.0 keV. Additionally, the excited ^{210}Bi nucleus is created which emits a γ-ray with an energy of 46.5 keV. In the second branch (remaining 16%), the β is able to carry up to the full Q-value of the decay (63.5 keV).

The fact that the event population is located on the 46.5 keV isoenergetic line implies that the dominating branch is responsible for the observed event population. The event population is smeared towards larger energies by up to 17 keV indicating that the β is absorbed in the target crystal. This behavior is observed over the full range of the isoenergetic line. Both observations suggests that the γ-ray is responsible for the energy sharing between the phonon channel and the light channel.Therefore, one has to assume that the observed event signature is related to a secondary process in which the γ-ray creates a photo-electron on the surface of the target crystal. This electron is able to escape the main crystal and to distribute its energy between main crystal and light detector which allows to explain the observed event signature.

This event population is only observed in the beaker detectors. Therefore, the origin

[2] An isoenergetic line is observed if a process is able to distribute a defined energy freely between the phonon and light channel.

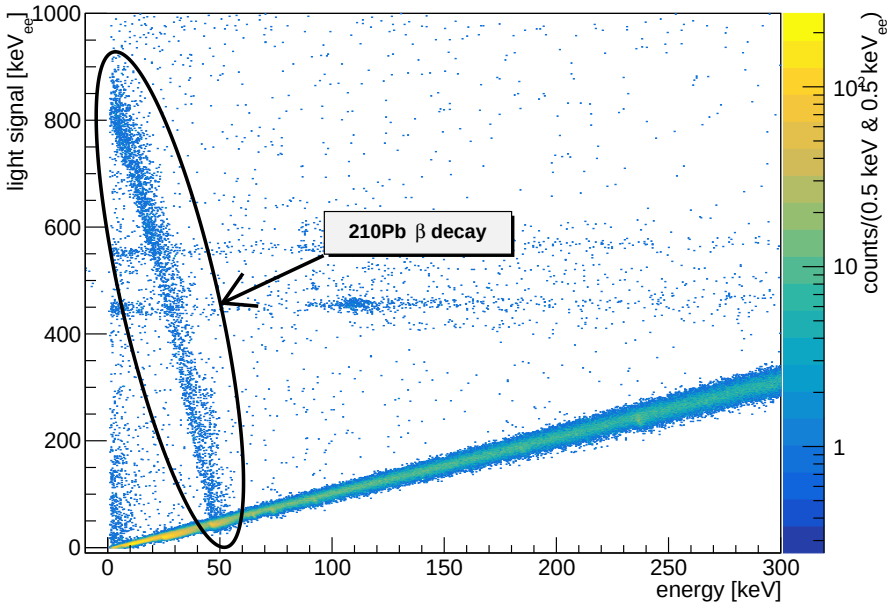

Abbildung 7.16: Light signal vs. energy scatter plot of beaker module 2, showing the event population related to the β-decay of ^{210}Pb taking place in the surrounding setup. The events are located on an isoenergetic line of 46.5 keV are smeared towards larger energies by the additional energy energy the β deposits in the main absorber.

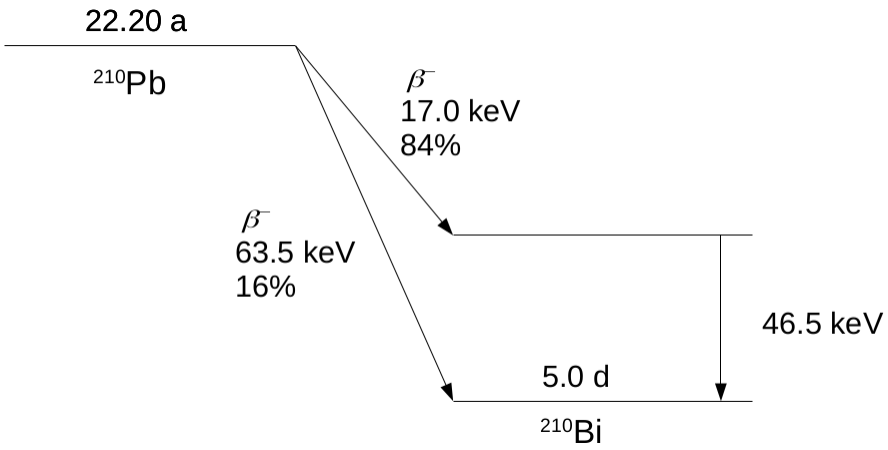

Abbildung 7.17: Decay scheme of ^{210}Pb.

of this event class is either related to the design of the beaker detectors or, more likely, the conventional module is not able to disentangle these events from the other β/γ-background observed in the target crystal.

The discussed event population allows to determine the EDL (see section 7.3.3) of the detectors using a second, completely independent approach. The energy calibration of

the light channel, which is given in keV_{ee}, is not correct for these events since the signal in the light detector is dominantly caused by the direct energy absorption. In case the light detector see the full energy of such an event, 46.5 keV are detected. According to the data shown in figure 7.13, this corresponds to an energy of $\approx 800 \pm 20\,keV_{ee}$ which can be translated to an EDL of $(46.5\,keV/800\,keV_{ee})$/integral ratio $\approx (5.14 \pm 0.15)\,\%$. In both detector modules, the measured EDL is confirmed using this second method.

Next to event population related to the β-decay of ^{210}Pb, several event cluster can be related in the data to the surface α-decay of ^{210}Po. This background is introduced by the contamination of the target crystal and the surrounding detector surfaces with ^{222}Rn during the production and mounting process of the modules. The following α-decay of ^{210}Po to ^{206}Pb is observed in all CRESST-II detectors [71] [69] [94]. In the following, the event signatures related to this decay process are explained.

In case an α-decay takes place on a surface, an α-particle and the daughter nucleus are produced from which only one is absorbed in the $CaWO_4$ target (see figure 7.18). Independent whether the α or daughter nucleus is detected in the main absorber, the scintillation signal from the main absorber is quenched compared to electron recoils (see table 2.1). For α-interactions, the scintillation light created in the target crystal is generally sufficient to allow the unambiguous assignment as background event. However, due to the reduced discrimination power of the detector modules in the low energy region, the background leakage of α-events into the ROI of dark matter searches is enhanced compared to electron recoils with the same energy. For nuclear recoils, the light yield veto fails to identify the event as background. Thus, the discrimination power for these events via the light yield veto is reduced or not possible if only the scintillation light signal created in the $CaWO_4$ target crystal is used for discrimination.

In general, the energy an α-decay deposits in the target crystal is well above the acceptance region for dark matter searches. Though, the full deposition of the energy into the phonon channel is not guaranteed. Due to surface scattering or in case the α emitters are embedded in the bulk of the surrounding materials, a degraded energy entry to the $CaWO_4$ crystal becomes possible which allows these events to appear in the region of interest for dark matter searches [73]. Therefore, the detection of the escaping particle via its absorption in a vetoed surface is crucial for the identification of surface α-decays.

In the following, the event signatures observed in the beaker module 2 related to the α-decay of $^{210}\text{Po} \rightarrow^{206}$ Pb(103 keV) + α(5304 keV) are explained. The contamination of the detector surfaces is high enough to assign some of the event populations visible in the data to this specific background source. In general, the following event signatures are expected for α-decays occuring on detector surfaces.

1. *Undegraded surface events (I):* α-particle is detected in the beaker light detector (5304 keV), ^{206}Pb-nucleus is detected in phonon channel (103 keV).
   Since the energy deposited in the phonon channel is well defined (103 keV), an identification of these events is achieved using this information. When the α-particle is absorbed in the beaker, the size of the energy entry exceeds the dynamic range of the light channels. In addition, the electronics of SQUID amplifier is too

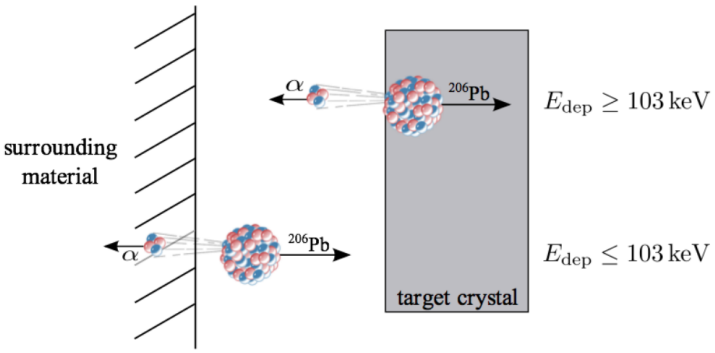

Abbildung 7.18: Illustration of surface α-decays showing the energy sharing between main absorber and detector housing.

slow to follow the signal. As a result, the recorded signal is flatend at top and the SQUID amplifier looses one or more flux-quanta, which is expressed in the to a new baseline. Both effects cause a strong deformation of the signal (see figure 7.19).

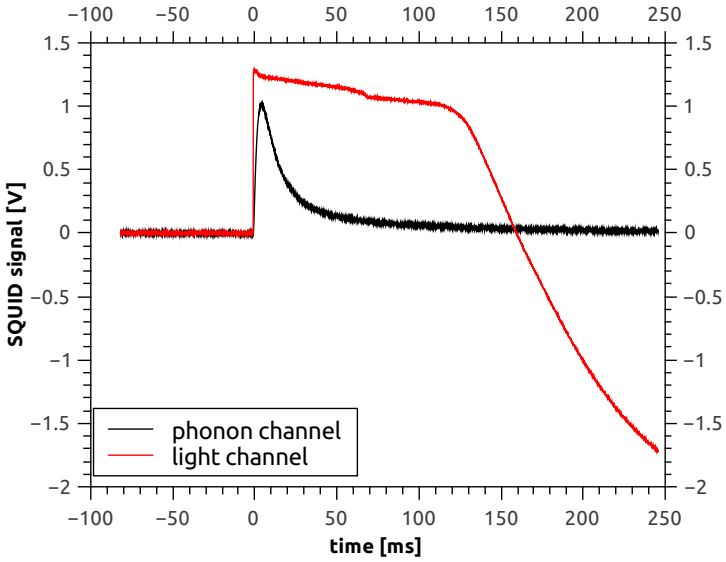

Abbildung 7.19: Typical event signature for a surface α-decay having the event signature of *Undegraded surface events (I)*.

For events having this pulse shape, the energy cannot be determined correctly using the template fit method. Though, the observed events show a characteristic and defined pulse height which is related to number flux-quantum losses the SQUID amplifier experiences. Depending on this number, the fitted pulse amplitudes have discrete values, meaning the derived pulse amplitudes are quantified. Therefore, these events are located at fixed positions in the light vs. energy scatter plots. In

figure 7.20, this behavior is used to identify this event population.

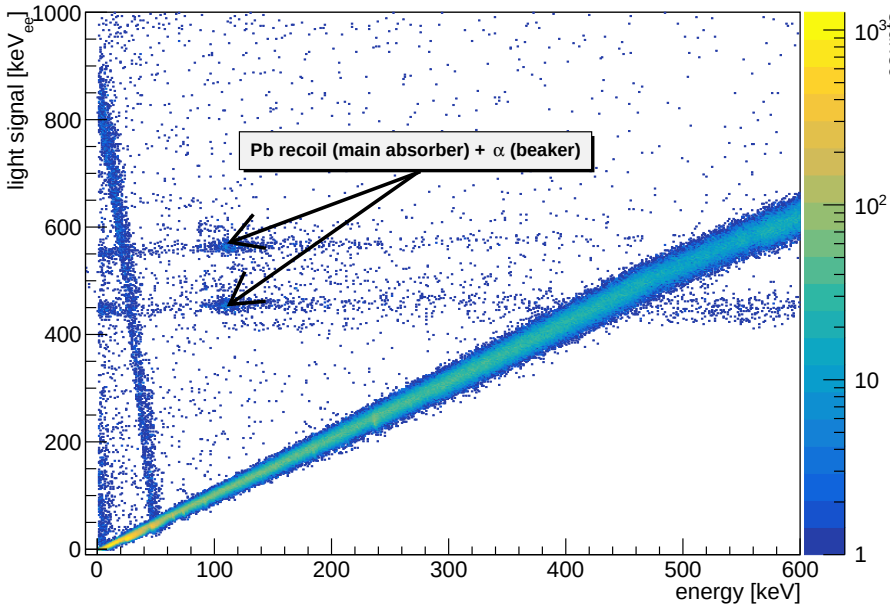

Abbildung 7.20: Event populations related to *Undegraded event signature (I)*.

In case the Pb-recoil deposits its energy in the carrier crystal, the α is able to deposit its energy in the beaker, in a scintillating part of the detector housing or in a non-scintillating clamp. These events are efficiently removed by the carrier cuts. In figure 7.7, thus, before the carrier cuts are applied, a clustering of these events is observed at an energy of 120 keV and a light signal of 40 keV$_{ee}$. These events are paired with a reduced light signal because the α is either absorbed in the foil or in a non-scintillating part of the detector housing. A clear separation between these two sub-classes is not possible.

2. *Undegraded surface events (II):* α-particle is detected in main absorber (5304 keV phonon signal+1000 keV$_{ee}$ light signal due to the quenched scintillation response of $CaWO_4$ to αs), ^{206}Pb-nucleus is detected in the beaker(103 keV as direct energy deposition which adds to the scintillation signal).
This event signature creates in both detector channels a signal which is well above the energy scale relevant for dark matter searches. Nevertheless, intrinsic and external α-decays can be identified in the high energy region which is shown in figure 7.21. Next to the intrinsic contamination of the main absorber and the carrier crystal[3] with α emitters, an event class related to surface α-decays is identified at 5304 keV. Due to the additional energy deposition in the beaker caused by the

[3]Due to the large size of energy entry to the phonon channel, the use of pulse shape analysis to discriminate carrier events is not applied.

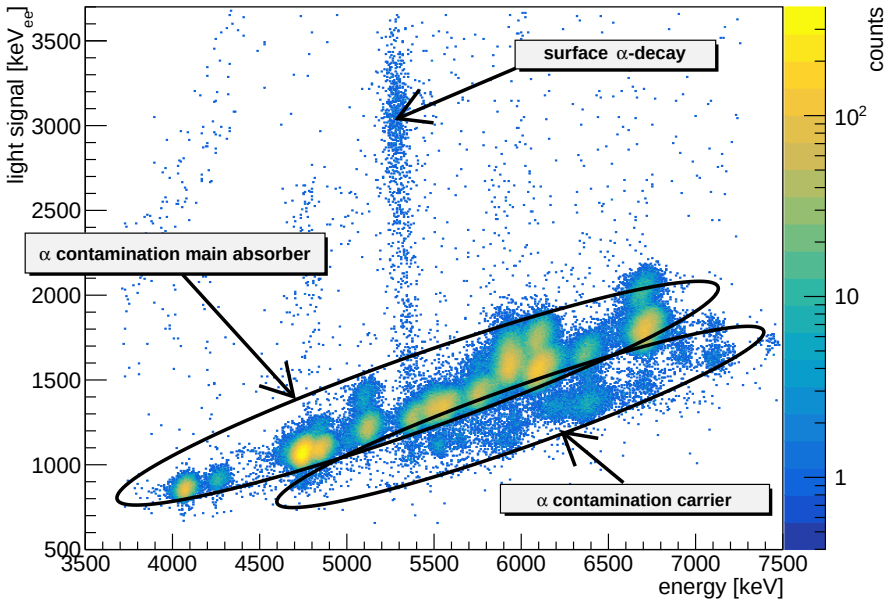

Abbildung 7.21: Light yield vs. energy scatter plot showing the energy range in which the intrinsic α contaminations of the main absorber and carrier crystal appear. In addition, the event signature of surface α-decays are identified.

absorption of the Pb-nucleus therein, the light signal of these events is shifted from the event band caused by intrinsic α contamination of the target crystal to larger values. The energy of Pb-nucleus (103 keV) is directly deposited in the beaker causing that the detected signal in the light channel is increased by a factor of 3 to $\approx$ 3250 keV$_{ee}$. The energy detected in the phonon channel is reduced by this amount of energy which is expressed by a shift of this event population from the Q-value of the decay (5407 keV) to the observed energy.

3. *Degraded surface events (I):* α-particle is detected in the phonon channel (5304 keV phonon signal+1000 keV$_{ee}$ light signal), the energy of the ^{206}Pb-nucleus is partially deposited in the beaker, the remaining energy is deposited in the phonon channel. Between the event population assigned to *Undegraded surface events (II)* and the intrinsic α-contamination of the main absorber, a connecting event band is observed (see figure 7.21). Due to elastic scattering on the surface the Pb-nucleus distributes its energy between phonon and light channel freely. Depending on the ratio of this energy sharing, the signal in the phonon and light channel is located on the isoenergetic line of the Q-value of the decay.

4. *Degraded surface events (II):* The energy of α is partially detected in the beaker (=> saturated light signal) or in the detector housing (i.e. carrier surface), ^{206}Pb-nucleus is detected in the main absorber(103 keV phonon signal)+ remai-

ning energy of the α-particle (0-5203 keV).
This event signature is not unambiguously identified for surface α-decays taking place on the main absorber or the inner beaker surface. Though, before the application of the cuts to remove all carrier related events, an event population related to this signature is observed in figure 7.7. The event population located below the electron recoil band of the carrier starting from an energy of $\approx 120\,\mathrm{keV}$[4] and extending from this energy in parallel to larger energies is related to αs depositing part of their energy in the carrier before escaping to the detector housing.

5. *Degraded surface events (III):* α-particle is detected in the beaker (=> saturated light signal), the energy of the ^{206}Pb-nucleus is partially detected in the main absorber (<103 keV phonon signal), the remaining energy is detected in the beaker but remains unnoticed (saturated light signal).
This event signature is not unambiguously identified in the data but is vetoed based on the signal in the light detector.

The identification of the event signatures 1-3 is achieved using the characteristic energy deposition of the decay process to the phonon channel. Therefore, the missing information on the total energy detected in the light channel is irrelevant. Nevertheless, these events are vetoed based on the deformed light signal. Since the other event signatures (4-5) have neither in the phonon channel nor in the light channel a defined energy entry, these cannot be identified unambiguously in the data. However, both event signatures are paired with a large energy entry to the light channel causing a deformed and undefined signal trace therein which allows their discrimination.

Surface decays related to α-decay of ^{210}Po are not the only background process which is paired with an undefined, deformed light signal. However, it is the only background which provides sufficient statistics to allow the unambiguous assignment of event populations to a specific decay process. Nevertheless, any other high-energetic interaction in the beaker is able to cause a reset of the SQUID amplifier, too. All events with this characteristics are located on the horizontal event clusters with an light signal of $450\,\mathrm{keV}_{ee}$ and $560\,\mathrm{kev}_{ee}$ (see figure 7.13) are rejected as background based on their pulse shape in the light detector.

7.3.4.3 Data Set after the Use of the 4π-Veto System

The 4π-veto system relies on the pulse shape analysis of phonon and light channel. Carrier events as well as all events not having pure scintillation light signal are removed from the data using this method. After the application of the pulse shape cuts, the remaining events are assumed to be related to interactions solely taking place in the target crystal. The final data set, used in the following sections for further analysis, is shown in figure 7.22.

[4] The energy is shifted from 103 keV to a larger energy because of the incapacity of the standard event fit to account for pulse shape differences.

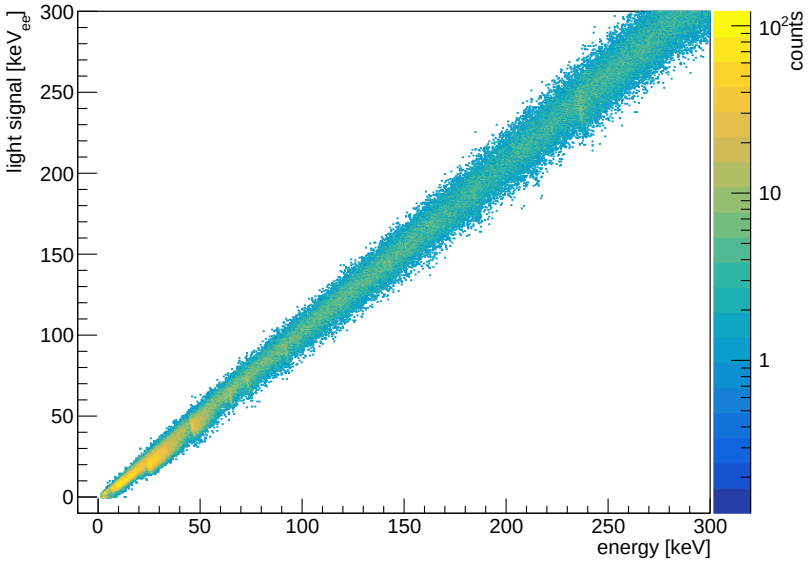

Abbildung 7.22: Final data set after the removal of the external backgrounds using the active 4π-veto system of the beaker module 2.

7.3.5 Particle Identification

To determine the particle discrimination capabilities of the beaker modules operated during CRESST-II (Phase 2), the data is analyzed in the light yield vs. energy plane. Using the 122 keV γ-rays of a ^{57}Co-source, the light yield of the electron recoil band is calibrated to unity. According to their quenching factors, the nuclear recoil bands are expected to arise at 11.2% (oxygen), 5.9%(calcium) and 1.7% (tungsten) [51].

The data sets of the beaker modules 1 and 2 are shown in the light yield vs. energy plane in the figures 7.23a and 7.23b after all cuts described before are applied. The red lines indicate the interval in which 90 % of the electron recoils are observed while the black line indicates the center of the electron recoil band.

In both detector modules, no indication is seen that external events survived the cuts. Neither excess light events nor surface α-decays are present in the data as it is expected after the use of the 4π-veto system.

Towards smaller recoil energies, the light detectors resolution decreases which is observed as a widening of the electron recoil bands. To quantify the width of the recoil band and the capability of the beaker modules to discriminate β/γ-background from nuclear recoils, the parametric band fit discussed in section 4.3 is applied to the data.

The data is fitted using the same approach like for the slice detector prototype. Instead of a 2-D likelihood fit, binned 1-D approach is chosen to fit the data. This method was already used for the analysis of the slice detector prototype (see section 6.3.5 for a detailed explanation).

In case of detectors using $CaWO_4$ target crystal, the model describing LY_c has to account for the material's particle dependent scintillation response for β and γ radiation.

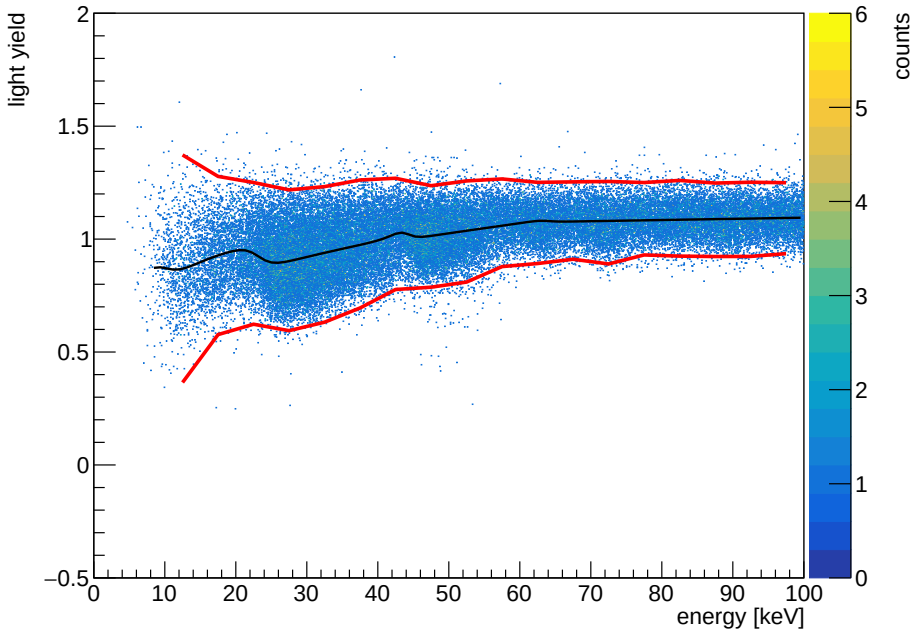

(a) Beaker module 1.

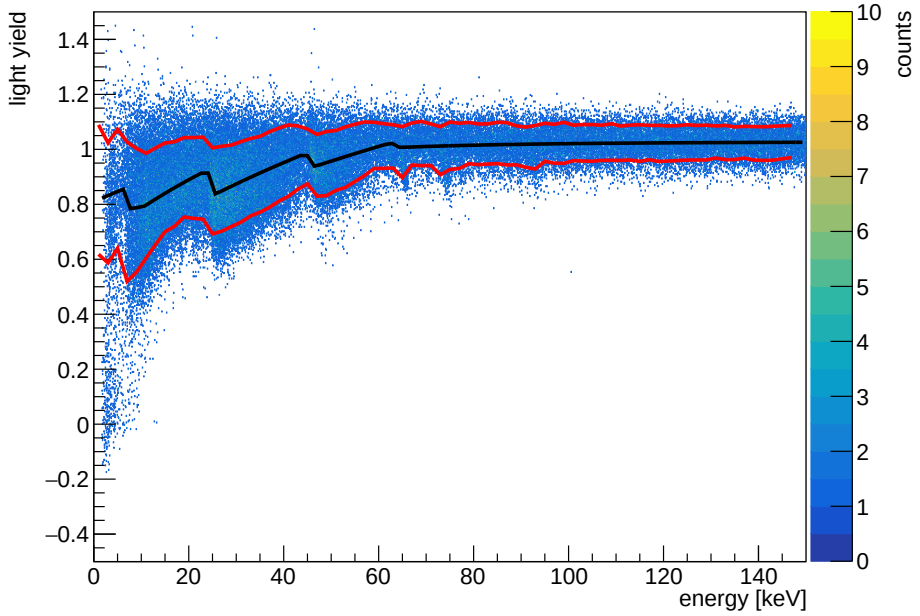

(b) Beaker module 2.

Abbildung 7.23: Light yield vs. energy scatter plot of the final data sets obtained with the beaker modules.

This is reflected in the bending of the electron recoil band, at certain energies, to smaller light yields (see figures 7.23a and 7.23b). The reason for this behavior is the different interaction mechanisms behind the respective particle events which cause that β spectra have a reduced light yield. For more information on the particle dependent scintillation response and the related non-proportionality effect see reference [95].

The spectral features in the electron recoil band can be related to intrinsic contamination of the target crystals. In the energy spectra of the phonon channels (see figure 7.24), the β-decay spectra of ^{228}Ra (start energy 6.7 keV), ^{227}Ac (start energy 9.3 keV and 24.6 keV) and ^{210}Pb (start energy 46.5 keV) can be identified [67]. The contributions of the respective backgrounds are also visible in the figures 7.23a and 7.23a as tear off edges where the bending of events towards smaller light yields stops abruptly and the electron recoil band returns to a center value of ≈ 1.

Using 1 keV intervals, the width of the light yield distribution of electron recoils is determined by fitting a single Gaussian to the electron recoil population. The derived width is fitted using equation 4.6 to extract the parameters S_0, S_1 and S_2 which allow a direct comparison to other detector modules. In case a second event population arises (i.e. nuclear recoils), an additional Gaussian is added to the fit function to describe the light yield distribution. In order to limit the number of free fit parameters, the width of the second Gaussian is defined by the width of the electron recoil band and respective quenching factor QF_x of the additional event population (equation 4.9).

In beaker module 2, an additional event population with a reduced light yield is visible for energies below 14 keV (see figure 7.23b), growing exponentially towards smaller energies (contribution indicated in figure 7.24b as red line). In beaker module 1, no statement can be given concerning this event population since the the poor performance of the phonon channel prevents the investigation of the energy range below 10 keV. However, a discussion on the possible origin of this event population will be given later in a dedicated section 7.3.6.

If this event population is not considered in the likelihood analysis, the description of the electron recoil band is influenced and the width as well as the center of the population is not determined correctly. Therefore, a second event population is added to the likelihood function describing the data of beaker module 2 meaning the low energy region is fitted using two Gaussian which are centered around a light yield of 0 and 0.8[5]. The small amount of events in the low energy range limits the possibility to precisely determine the fit parameters. Additionally, a strong correlation between the model parameters is observed.

To parameterize the center (LY_c) and the width of the electron recoil band (σ_{LY}) as function of the energy, the equations 4.5 and 4.6 are used. In table 7.7, the results of the fit are given. For comparison, the average values of detectors with the conventional design are given.

The description of the center of the electron recoil band $LY_c(E_r)$ does not show any significant differences compared to other detector modules. This is expected since these

[5]Due to the non-proportionality effect, the center of the electron recoil band is located below the calibration value of 1.

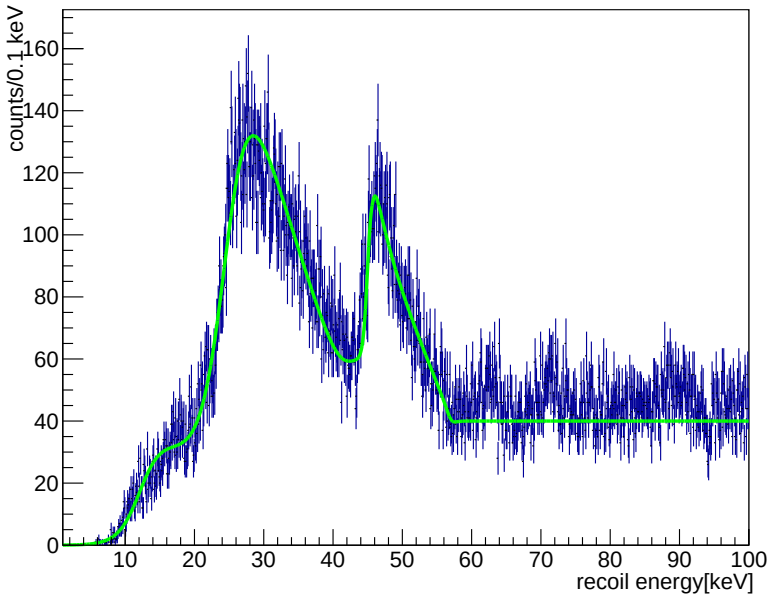

(a) Beaker module 1.

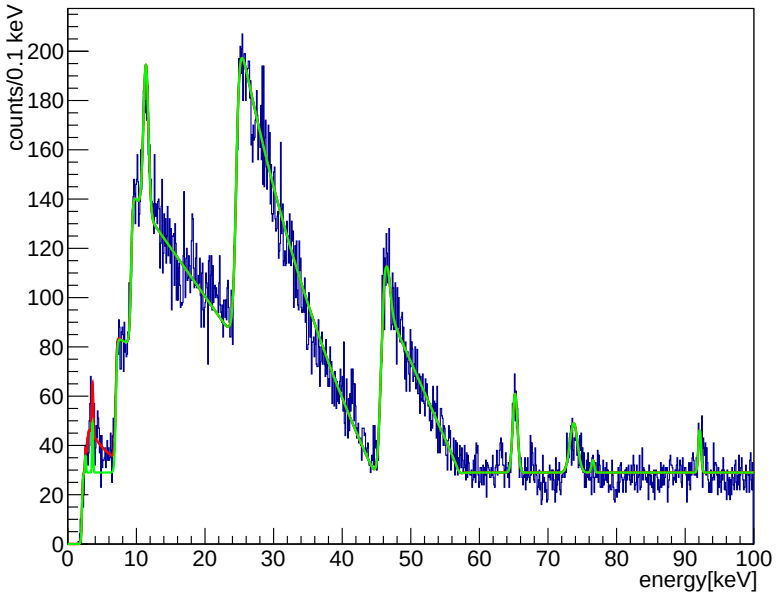

(b) Beaker module 2.

Abbildung 7.24: Spectra of the phonon channels recorded by the the beaker modules. The final data sets are shown. In addition, the fit of the spectrum is given (green line). For module 2, the event contribution caused by the events with light yield zero is shown (red line).

parameter	*module 1*	*module 2*	*avg. CRESST-II*
p_0	1.04	1.02	
p_1	$5.182 \cdot 10^{-4}$	$8.088 \cdot 10^{-6}$	
p_2	0.439	0.213	
p_3	7.997	23.661	
S_0	$2.675\,\mathrm{kev}_{ee}^2$(fixed)	$0.103\,\mathrm{kev}_{ee}^2$ (fixed)	$0.612\pm0.210\,\mathrm{kev}_{ee}^2$
S_1	$0.328 \pm 0.014\,\mathrm{keV}$	$0.256 \pm 0.010\,\mathrm{keV}$	$0.580\pm0.025\,\mathrm{keV}$
S_2	$< 1 \cdot 10^{-5}$	$< 1 \cdot 10^{-5}$	0.0003 ± 0.0002

Tabelle 7.7: Results of the parametric band fit to describe the electron recoil bands in the beaker module 1 and 2. The given uncertainties are fit errors (beaker modules) or statistical uncertainties (avg. CRESST-II module). For the discussion of the results see text.

parameters are defined by the intrinsic crystal properties of the target and not dependent on the detector design. In both beaker modules, the shape of the electron recoil band is similar to the observations made with other detectors, including the strength of the non-proportionality effect. For a comparison with other CRESST-II detectors, see references [43], [93] or [22].

The resolution σ_{LY} obtained for the beaker modules reflects the impact of the EDL. Based on the gains acheived for the EDL by the improved light collection, S_0 and S_1 are expected to show a smaller value. This is especially the case, since the performance of the beaker shaped light detectors as cryogenic devices show no degradation in comparison to other CRESST-II light detectors.

As discussed before, S_0 accounts for the baseline noise (i.e. the detector resolution for zero energy) of the two readout channels and is calculated using equation 4.7. During the fit of the data S_0 is fixed as it can be calculated with the independently derived detector resolutions for the respective readout channels and the measured EDL. Depending on the baseline resolution of phonon and light detector the influence of the EDL on S_0 varies. In case of the beaker modules, the light detector's contribution to S_0 becomes negligible since $\sigma_{b,LD}$/EDL becomes small compared to the phonon detector's baseline resolution $\sigma_{b,PD}$. This is especially the case for beaker module 1, given that the performance of the phonon channel is extremely poor. The baseline resolution $\sigma_{b,PD}$ of module 1 is eight times larger than the baseline resolution $\sigma_{b,PD}$ of module 2 (see section 7.3.1). Therefore, the impact of the good performance of the light channel on S_0 is insignificant in beaker module 1.

The fit parameter S_1 accounts for the energy dependence in the detector resolution of the light detector. Two main aspects influence this parameter. First, S_1 accounts for the intrinsic increase of the relative resolution of the light detector as cryogenic detector (see section 4.2.2). Second, and more dominantly, S_1 reflects the uncertainties which are introduced per detected photon. Therefore, the S_1 scales according to the Poisson statistics ($\sqrt{\text{number of detected photons}}$) and is proportional to (1/EDL). The performance of the phonon detector has no influence on S_1. Therefore, S_1 can be considered

as the best quantity to evaluate the influence of the light channel's performance on the discrimination power. Since S_1 contributes dominantly to the total σ_{LY} in the ROI, it is the defining quantity for the discrimination power in this energy range.

In both beaker modules analyzed in this work, the value obtained for S_1 fulfills the expectation of being significantly smaller than the S_1 values derived for the average CRESST-II detector (see table 7.7). The measured values align with the values obtained with simulation which was carried out to investigate the light collection efficiency in the beaker detector.

The S_2 parameter behaves for the beaker modules in a similar way as it is observed in other detector modules. The values for S_2 are $< 1 \cdot 10^{-5}$. Thus, S_2 does not contribute significantly to σ_{LY} in the relevant energy range for dark matter searches. The parameter is fitted smaller than in other detectors indicating that position dependencies are reduced for the beaker detector design. This observation is in agreement with the improved EDL and the simulation which relates the better light collection efficiency to a shorter traveled distance of photons inside the detector housing. At same time, losses related to reabsorption in the crystal and, consequently, the uncertainties introduced by these losses are reduced.

Based on the improved EDL achieved in the beaker detector design, the rejection efficiency for electron recoils is expected to be significantly improved compared to other detector designs. As mentioned before, two methods are available for evaluating the discrimination efficiency of a detector (see section 4.4): The definition of an analysis threshold, thus, the energy above which no electron recoil event is observed in the ROI with a probability of 5σ or the number of expected background in the ROI for a certain amount of contamination in the target crystal. Both methods are used to compare the performance of beaker module 2 with the average performance of a standard CRESST-II detector. Using the values of the parametric band fit derived for module 2 and the same assumption set as used in section 6.3.5 (i.e. analysis threshold: $E_{thres} = 1.5\,\text{keV}$, background contamination: 100 events/(0.1keV)) the data driven simulation is repeated 20 times for each detector geometry. According to the simulation, the expected number of electron recoil events leaking into the ROI for dark matter searches is expected to be reduced by $(85.69 \pm 0.64)\,\%$ compared to an average conventional detector module with the same amount of contamination. Also the average analysis threshold is reduced from a value of $(11.15 \pm 1.51)\,\text{keV}$ (conventional detector design) to $(4.41 \pm 0.92)\,\text{keV}$ (beaker detector design). Both numbers show, that the discrimination efficiency of detectors with the beaker detector design is improved compared to other CRESST-II detector designs. Main reason for this is the improved EDL due to the changed detector geometry, which is reflected in a significantly smaller value of S_1.

7.3.6 Event Population with Reduced Light Yield

In beaker module 2, an unexpected event population with light yield of approximately zero can be identified (see figure 7.23b). This event population is not in agreement with known backgrounds. This population has an upper boundary at an energy of 14 keV and increases exponentially in intensity towards smaller energies. In the ROI, 160 events are

observed. The light yield of this event population is centered at a value of 0.12. Figure 7.25 shows a projection into the light yield plane of detector module 2 for recoil energies 0-15 keV, thus, into the energy range in which the excess event population is observed.

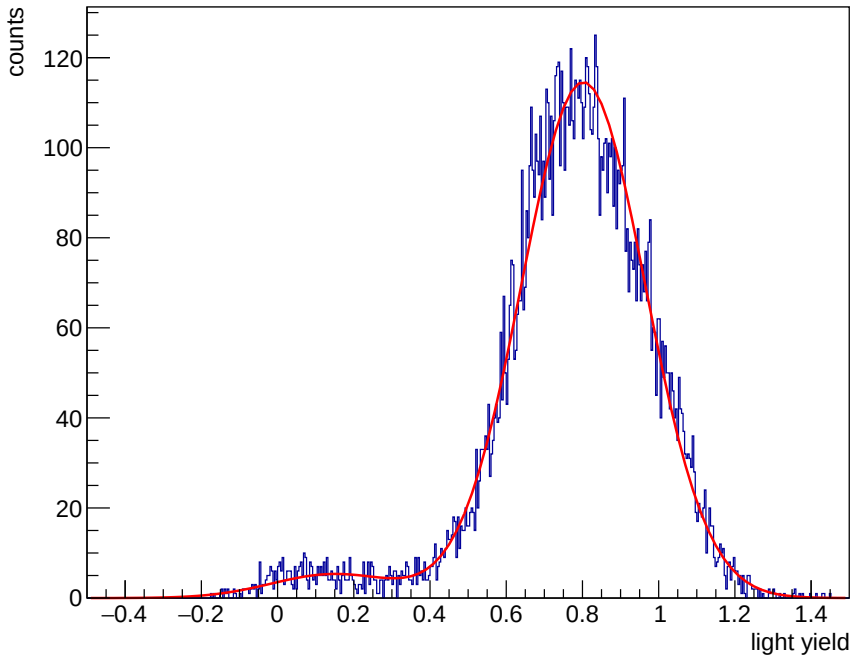

Abbildung 7.25: Light yield distribution of the energy range < 15 keV of the data recorded with module 2. Next to the expected electron recoil population with a light yield of 0.9 and second population with reduced light yields is observed. Additional to the data, the best fit using two Gaussian is given (red line).

The observed number of events is too large to be explained by carrier events surviving the pulse shape cuts (see section 7.3.4). Based on the simulation performed to test the discrimination power of the cuts for carrier events, less than 1 carrier event is expected to survive the carrier cuts. Since these events with light yield zero survive the carrier cuts, no significant pulse shape difference to main absorber events exists. This suggests that their origin is in the main absorber or closely related to this absorber. In addition, no time variation of the rate of these events is observed.

Unfortunately, the performance of beaker module 1 is insufficient to observe this event population in this detector. Therefore, it is not possible to relate the detector design to these event class. Still, as the excess of events is only observed in a single module which is of new design, a relation to the detector design is the most conservative approach to explain this phenomenon.

In the following, two possible explanations are discussed:

- One possible explanation relates the excess to the non-scintillation glue spot used to establish the connection between main absorber and carrier crystal. Despite the fact that the amount of glue is small ($< 40\,\mu$l), energy depositions in the glue spot (contamination of the glue, interaction of external backgrounds with the glue) are able to induce a phonon signal. Since the glue is not scintillating, these events generally create no light signal which can be used to identify these events as background. Additionally, thermal stress relaxation at the interface between the glue and crystal (main absorber and carrier) can cause zero light events.

  In case the discrimination via the light yield of an events is not possible, pulse shape analysis of the phonon channel could be used alternatively. Nevertheless, depending where inside the glue the signal is created and in which absorber most of the energy/phonons are transmitted, the pulse shape of an events changes from (pure) carrier like to (pure) main absorber like. Hence, pulse shape analysis might not be able to identify all of these events which can be the reason why a small number of glue related events are able to survive the cuts designed to remove carrier events.

  In case of the beaker module, the probability that stress related events are created is enhanced due to the geometry of the glue connection. The connection between the main absorber and the carrier crystal is designed as depicted in figure 7.26.

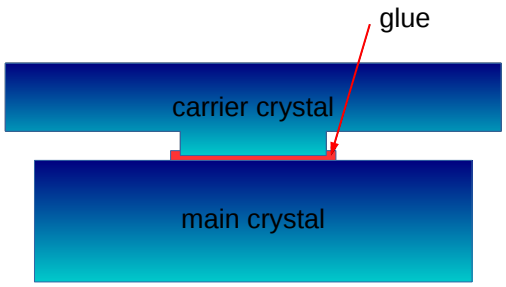

Abbildung 7.26: Illustration of the design of the glue interface connecting main absorber and carrier crystal

  The carrier crystal is machined with a nose which is used to define the area and shape of the glue interface. While the amount of glue is small between the flat crystal interfaces, this setup causes that a belt of glue is created where the indent ends. At this location, thermal stress may play an increased role due to the tensions the glue introduces to this location.

- The second explanation aims to relate the events with light yield zero to the remaining non-scintillating part within the detector housing which is the TES

(including its thermal links) of the phonon channel. For events depositing energy in the TES or its thermal link no light is produced. Additionally, the pulse shape of these events is unknown. In case direct TES hits or energy depositions in the thermal link are able to mimic the pulse shape of events originating from the main absorber, they are able to survive the cuts intended to reject these events. However, an intrinsic contamination of the metals used for the thermometer is unlikely because the level of radioactivity has to be high to explain the observed number events with the small amount of material contained in the thermometer.

A clear confirmation that the excess of events observed in the ROI for dark matter searches is related to the detector design is not possible due to the fact that only one of the two beaker modules is sensitive in the relevant energy range. Nevertheless, it is most probable that this event population is related to the detector design (i.e. the carrier system) because no other detector module ever operated within CRESST-II observes this excess.

7.4 Conclusive Comments on the Beaker Design

An analysis was performed on the two beaker modules operated during CRESST-II (Phase 2). The detectors collected a raw exposure of 120.3 kg·d (module 1) and 114.3 kg·d (module 2) which provides enough statistics for a detailed analysis of the detector performance. Through this analysis, it is possible to obtain a reliable characterization of the general performance of this detector design. Unfortunately, the performance of one detector module was degraded due to problems in the phonon channel which were not related to the detector design. Therefore, the in-depth evaluation of the detector performance in the relevant energy range of dark matter searches (i.e. < 40 keV) was only possible using one detector module.

The first major design goal of the beaker detector design is the improvement of the light channel's performance by increasing the light collection efficiency in the detector module. This is achieved by the large area light detector surrounding the target crystal in most directions.

The investigation of the performance of the beaker shaped light detectors as cryogenic light detectors reveals that, due to the larger dimensions of the light absorber, a increased influence of position dependencies is observed for the detector response. This is reflected in an unexpected spectral shape of the ^{55}Fe calibration data (see figure 7.5). While for X-ray interactions the effect of the position dependent detector response causes a signal variation of to $\pm 20\,\%$, the effect is averaged for scintillation light signals. Nevertheless, a reduction of the average detector response of up to 10 % is observed for scintillation signals. In terms of detector resolution, the increased influence of the position dependencies is covered by other, significantly larger effects (e.g. photon counting statistics).

Due to the improved geometry of the detector design, the light collection efficiency is increased by a factor 2.5 compared to the conventional detector design. The share of energy detected as light (EDL) is increased from an average value of $\approx (2 \pm 0.4)\,\%$ [48]

to $(4.79 \pm 0.09)\,\%$. The improvements can be completely related to the design changes applied to the detector module and are able to counterbalance the performance reduction due to the larger dimensions of the light detector.

As a consequence of the improved EDL, the discrimination power for β/γ-backgrounds is significantly improved. The expected leakage of internal β/γ-contaminations into the acceptance region for dark matter above an energy of 1 keV is reduced by $(85.69 \pm 0.64)\,\%$ if the same crystal is operated in a beaker detector module instead of a conventional detector module. In case an analysis threshold is defined, the beaker module is expected to achieve a threshold value of $(4.41 \pm 0.92)\,\mathrm{keV}$) exceeding clearly the values achieved with the conventional modules operated in the CRESST-II measurement campaigns which vary between (9.2-19.8) keV [71]. Thus, a better sensitivity for dark matter is expected solely based on the design related improvement of the light collection efficiency.

The second major design goal of the beaker detectors is the establishment of a true 4π veto system. The removal of external backgrounds of any kind is achieved with high efficiency. In the final data set all excess light events, as well as all surface α decays are removed. Accordingly, the sensitivity limitations of the conventional modules due to degraded surface α-decays are resolved.

The use of an actively read out detector surrounding proves to be an effective tool for the understanding of the detector modules in regard of backgrounds and event classes with unknown origin. Since the beaker as well as the carrier are able to identify events not originating from the solely bulk of the main absorber, event classes which are considered as background are identified unambiguously as such.

The identification of these events can be generally achieved using a fully scintillating housing, too. Especially for energies well above threshold, the veto of external backgrounds with the help of a fully scintillating detector housing is achieved with high efficiency rendering the beaker concept too complicated for the task. [74] Though, in the scope of the current generation of detectors aiming at lowest thresholds, the rejection of external backgrounds becomes more and more challenging. Since the energy conversion into photons via the scintillation process is usually inefficient, the veto signal is small which hinders the unambiguous identification of background events. In case the veto is achieved without relying on the scintillation mechanism of the foil, the background identification can be achieved with better precision in the low energy region. Thus, the leakage of background events into the ROI is expected to be reduced which results in a higher sensitivity of the detector module.

The establishment of a fully vetoing detector housing can be also applied for non-scintillating targets. There, the identification of particles interacting within the target cannot be granted by the light yield mechanism. Though, in case these materials are available with very small amounts of internal contaminations (e.g. silicon, germanium), the dominant background seen by the detectors is usually of external origin. If the beaker concept is used, these remaining backgrounds are identified by their interaction with the surrounding veto which allows to isolate the events which solely originate from the target crystal. Thus, the beaker concepts provides the possibility to operate any target crystal in a fully vetoing detector environment.

7.5 Second Generation of Beaker Modules

To overcome the limitations of the concept in regard of the dark counts arising in the region of interest different approaches can be followed. Assuming that these events are correlated with the carrier system and the glue interface establishing the connection between main absorber and carrier, changes to this part of the detectors are necessary.

A way to overcome this problem is to use two carrier crystals. If each carrier crystal is read out with a separate thermometer, the ratio of the signals in the two phonon channels can be used to identify events not originating from the main absorber. The new carrier system is depicted in figure 7.27.

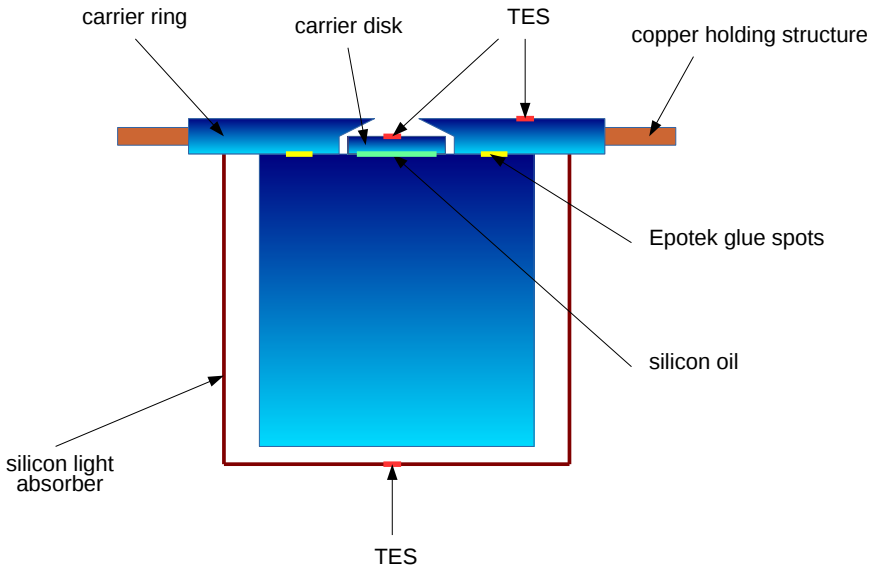

Abbildung 7.27: Scheme of the second generation of beaker detector modules. Two phonon readouts are used. The ratio between both readout channels is expected to reveal events not originating solely from the main absorber.

The thermal coupling between the main absorber and the carrier crystals, is intended to be weak for the ring and strong for the disk. By using tiny glue spots for the ring and a large silicon oil spot for the disk, the energy sharing is intended to be shifted to the TES readout of the disk. Nevertheless, both phonon channels have to provide a convincing threshold to allow the identification of events with ambiguous character in the low energy region since otherwise a rejection of pulses solely based on pulse shape analysis becomes ineffective in the relevant energy range.

Three beaker detector modules of this type are currently operated in the CRESST main setup at the LNGS taking data since mid of 2016 (CRESST-III (Phase 1)).

8 Summary and Discussion

In the field of direct dark matter searches, the CRESST-II experiment is the only remaining experiment using detectors based on the "phonon-light"-technique. Detectors of this type consist of scintillating $CaWO_4$ target crystal which energy depositions are quantified as temperature rise using a highly sensitive thermometer. Particle discrimination is achieved via the measurement of the simultaneously created scintillation light using a spatially separated light detector. This detector technology allows the CRESST-II experiment to have the detectors with the lowest energy threshold in the field, however, a perfect background discrimination in combination with large target masses is not achieved. Since the competing experiments using liquid noble gas detectors are able collect larger amounts of exposure in combination with very low background rates in the same measurement time, they set currently the best exclusion limits above a dark matter mass of $m_\chi > 5\,\mathrm{GeV/c^2}$.

In this work, the development of new detector concepts for the CRESST-II experiment is presented. These are intended to succeed the detector modules used during CRESST-II (Phase 1&2) (i.e. conventional design") while providing a better sensitivity in the mass range currently dominated by the liquid noble gas experiments. Main limitation of the conventional CRESST-II detector modules is their incapability to distinguish between electron recoils and nuclear recoils in the low energy range ($E < 10\,\mathrm{keV}$), hence, the limited discrimination power for intrinsic background interactions. Additionally, the detectors are subject to accept external backgrounds as valid events due to design related detector features.

The discrimination power of "phonon-light"-detector module relies dominantly on the relative performance of the light channel. In the low energy range, the signal-to-noise ratio of the light detector degrades which impedes the unambiguous assignment of an interaction as background or valid event event. Main reason for this is the small amount of energy that is detected in the light detector after an interaction in the target crystal. In order to improve the discrimination power of these detectors, the performance of the light channel has to be improved. Two approaches are followed during this work to achieve this goal.

First, the efficiency of the superconducting phonon collectors is investigated in order to evaluate, if the the performance of the low temperature thermometers can be further improved by optimizing the dimensions of the phonon collector films. Phonon collectors are superconducting thin films which replace parts of the existing thermometer structure to reduce the heat capacity of the structure while keeping the collection area for photons constant. A positive signal contribution is generated by this system if the generated quasiparticles have a diffusion length that allows them to diffuse in the phonon collector over a distance that an interaction in the tungsten TES becomes likely.

Using a dedicated setup, the diffusion of quasiparticles is investigated in thin film systems that are identical to the phonon collectors used in current thermometer structures. The measurement campaign revealed, that created quasiparticle are able to achieve diffusion lengths of $\mathcal{O}(2\,\mathrm{mm})$ while the life time of the quasiparticles is sufficently long to guarantee a complete collection in the TES ($\tau_{qp} \propto \mathcal{O}(0.5\,\mathrm{ms})$). Based on these findings, the dimensions of the phonon collectors are chosen too conservatively in the currently used thermometer structures of the light detectors. Additionally, the testing of the large area phonon collectors indicates the diffusion is currently limited by the film thickness of the phonon collectors, meaning that an increase of this film parameter enhances the efficiency of the system further. For future thermometer designs, larger and thicker phonon collectors are able to increase the sensitivity of the thermometer by up to 30 % if the dimensions are adapted accordingly to the measured diffusion length.

The second approach intends to increase the light collection efficiency in the detector modules by reducing the losses of the scintillation light experience after creation. Using a Monte-Carlo simulation, the propagation of photons in the conventional CRESST-II detector design is investigated. The simulation reveals, that the average path a photon travels inside the detector housing before being absorbed in the light detector is long enough to loose a significant fraction of the photons during the propagation process ($\approx$ 75 %). Based on the simulation, two new detector concepts were developed with intention to reduce the light losses inside the detectors.

The first detector design aims to investigate the influence of light trapping inside the target crystal on the light collection efficiency of a detector module. In the so called slice detector design, the light detector is place in narrow opening ïnsidethe target crystal. Based on the ray tracing simulation of the detector design, the light collection efficiency is predicted to improve by 50 % as light trapping is used positively to detect more photons in the light detector. This expectation is confirmed by measurement. The amount of energy detected as light is increased from $\approx 2\,\%$ (average value achieved by the conventional detector design) to 3.07 %. The increased light collection efficiency affects the discrimination capability for internal contaminations significantly. In case the same crystal is operated in the slice detector instead of the a conventional detector, the lower energy boundary of a background free acceptance region for dark matter interactions is lowered by a factor of 2 from 11.15 keV to 6.40 keV.

The second detector design uses a large scale, beaker shaped light detector to shorten the average distance the scintillation light travels inside the detector housing before being detected in the light detector. This reduces the losses the scintillation light experiences after creation and enhances the ratio of detected photons in the light detector. The ray tracing simulation of this detector design predicts an increase in light collection efficiency by a factor of 2-2.5. This expectation is confirmed experimentally by two prototype detector modules. The fraction of energy which is detected as light by the light detector is measured in this detector design with 4.79 %. Therefore, the background discrimination is significantly improved as the energy range in which particle discrimination can be achieved unambiguously is lowered to 4.42 keV.

Next to an improved light collection, the beaker detector design is the first CRESST-II detector ever to provide a active and true 4π-veto system for external backgrounds.

Since all surfaces with direct line of sight to target crystal are instrumented, external backgrounds are unambiguously identified by their unique event signature. In contrast to previous realizations of surface veto systems, the beaker detector concept is able to provide an veto system that identifies external backgrounds efficiently over the full energy range. Based on a detailed background analysis, the 4π-veto system is confirmed to provide a unprecedented understanding for different background sources and, therefore, to be a powerful tool to veto backgrounds.

The findings of this work show, that the detector design has a significant influence on the performance of the light channel and, hence, on the background discrimination power of a "phonon-light"detector. Based on the insights gained with the prototype measurements carried out for this work, the design of future CRESST detectors can be adapted. This is especially important in the scope of the CRESST-III dark matter search. Aiming at the lowest energy thresholds possible, particle discrimination in the low energy range becomes a crucial aspect for the sensitivity of the experiment. Compared to previous CRESST detector modules, the beaker detector concept is proved to provide the best rejection power for backgrounds with intrinsic and external origin.

Lastly, it is worth mentioning that the beaker detector concept, hence, the establishment of an active and true 4π-veto system, can be applied in numerous experiments in the field of astroparticle physics and rare event searches (i.e. coherent neutrino scattering, $0\nu\beta\beta$). Since the beaker detector concept can be applied to scintillating and non-scintillating targets, a 4π-veto system can be implemented in different experiments that are subject of being limited by external backgrounds.

Literaturverzeichnis

[1] F. Zwicky. Die Rotverschiebung von extragalaktische Nebeln. *Helvetica Physica Acta*, 2(6), 1933.

[2] V. C. Rubin and Jr. W. K. Ford. Rotation of the Andromeda Nebula from a Spectroscopic Survey of Emission Regions. *Applied Physics Journal*, 159:379, February 1970.

[3] P. J. Mohr, B. N. Taylor, and D. B. Newell. CODATA Recommended Values of the Fundamental Physical Constants. *Reviews of Modern Physics*, pages 63–66, 1998.

[4] V. C. Rubin, Jr. W. K. Ford, and N. Thonnard. Rotational properties of 21 SC galaxies with a large range of luminosities and radii, from NGC 4605 /R = 4kpc/ to UGC 2885 /R = 122 kpc/. *Astron. J.*, 238:471–487, June 1980.

[5] Shaaban Khalil and Carlos Munoz. The Enigma of the Dark Matter. *Contemporary Physics*, 43:51–62, 2002.

[6] Edvige Corbelli and Paolo Salucci. The Extended Rotation Curve and the Dark Matter Halo of M33. *Mon. Not. Roy. Astron. Soc.*, 311:441–447, 2000.

[7] C. Alcock et al. The MACHO Project: Microlensing Results from 5.7 Years of LMC Observations. *The Astrophysical Journal*, 542:281–307, 2000.

[8] M. Markevitch, A. H. Gonzalez, D. Clowe, A. Vikhlinin, W. Forman, C. Jones, S. Murray, and W. Tucker. Direct Constraints on the Dark Matter Self-Interaction Cross Section from the Merging Galaxy Cluster 1E0657-56. *The Astrophysical Journal*, 606(2):819, 2004.

[9] D. Clowe, M. Bradac, A. H. Gonzalez, M. Markevitch, S. W. Randall, et al. A Direct Empirical Proof of the Existence of Dark Matter. *The Astrophysical Journal*, 648:L109–L113, 2006.

[10] G. W. Angus, B. Famaey, and H. Zhao. Can MOND take a Bullet? Analytical Comparisons of Three Versions of MOND Beyond Spherical Symmetry. *Monthly Notices of the Royal Astronomical Society*, 371:138, 2006.

[11] Maruša Bradač, Steven W. Allen, Tommaso Treu, Harald Ebeling, Richard Massey, R. Glenn Morris, Anja von der Linden, and Douglas Applegate. Revealing the Properties of Dark Matter in the Merging Cluster MACS J0025.4–1222. *The Astrophysical Journal*, 687(2):959, 2008.

[12] A. A. Penzias and R. W. Wilson. A Measurement of Excess Antenna Temperature at 4080 Mc/s. *The Astrophysical Journal*, 142:419–421, 1965.

[13] C. Patrignani et al. Review of Particle Physics. *Chin. Phys.*, C40(10):100001, 2016.

[14] D. J. Fixsen, E. S. Cheng, J. M. Gales, John C. Mather, R.A. Shafer, et al. The Cosmic Microwave Background Spectrum from the Full COBE FIRAS Data Set. *The Astrophysical Journal*, 473:576, 1996.

[15] C. L. Bennett, D. Larson, J. L. Weiland, N. Jarosik, G. Hinshaw, N. Odegard, K. M. Smith, R. S. Hill, B. Gold, M. Halpern, E. Komatsu, M. R. Nolta, L. Page, D. N. Spergel, E. Wollack, J. Dunkley, A. Kogut, M. Limon, S. S. Meyer, G. S. Tucker, and E. L. Wright. Nine-year Wilkinson Microwave Anisotropy Probe (WMAP) Observations: Final Maps and Results. *APJS*, 208:20, October 2013.

[16] P.A.R. Ade et al. Planck 2013 Results: I. Overview of Products and Scientific Results. *A&A*, 594(A1), 2016.

[17] E. Hubble. A Relation between Distance and Radial Velocity among Extra-Galactic Nebulae. *Proceedings of the National Academy of Science*, 15:168–173, 1929.

[18] G. Lemaître. Un Univers homogène de masse constante et de rayon croissant rendant compte de la vitesse radiale des nébuleuses extra-galactiques . *Annales de la Société Scientifique de Bruxelles*, 47:49–59, 1927.

[19] P.A.R. Ade et al. Planck 2013 Results. XVI. Cosmological Pparameters. *A&A*, 594(A16), 2016.

[20] Adam G. Riess, Alexei V. Filippenko, Peter Challis, Alejandro Clocchiatti, Alan Diercks, Peter M. Garnavich, Ron L. Gilliland, Craig J. Hogan, Saurabh Jha, Robert P. Kirshner, B. Leibundgut, M. M. Phillips, David Reiss, Brian P. Schmidt, Robert A. Schommer, R. Chris Smith, J. Spyromilio, Christopher Stubbs, Nicholas B. Suntzeff, and John Tonry. Observational Evidence from Supernovae for an Accelerating Universe and a Cosmological Constant. *Astron. J.*, 116(3):1009, 1998.

[21] Franco Pavese. The New SI and the CODATA recommended values of the fundamental constants 2014 (arXiv:1507.07956), after the CCU 2016 draft of the 9th SI Brochure and its 22th meeting, September 2016.

[22] Michael Kiefer. *Improving the Light Channel of the CRESST-II Dark Matter Detectors*. PhD thesis, TU München, 2012.

[23] Jens Michael Schmaler. *The CRESST Dark Matter Search - New Analysis Methods and Recent Results*. Phd thesis, TU München, 2010.

[24] R. Overzier, G. Lemson, R. E. Angulo, E. Bertin, J. Blaizot, B. M. B. Henriques, G.-D. Marleau, and S. D. M. White. The Millennium Run Observatory: first light. *Monthly Notices of the Royal Astronomical Society*, 428(1):778–803, 2013.

[25] G. Jungman, M. Kamionkowski, and K. Griest. Supersymmetric Dark Matter. *Phys.Rept.*, 267:195–373, June 1996.

[26] Bergström L. Dark Matter Candidates. *New Journal of Physics*, 11(10):105006, 2009.

[27] R. D. Peccei and Helen R. Quinn. CP Conservation in the Presence of Pseudoparticles. *Phys. Rev. Lett.*, 38:1440–1443, Jun 1977.

[28] A. Browman, J. DeWire, B. Gittelman, K. M. Hanson, D. Larson, E. Loh, and R. Lewis. Decay Width of the Neutral π Meson. *Phys. Rev. Lett.*, 33(1400):1400–1403, 1974.

[29] Kalliopi Petraki and Raymond R. Volkas. Review of asymmetric dark matter. *Int. J. Mod. Phys. A*, 28:1330028, August 2013.

[30] Kathryn M. Zurek. Asymmetric Dark Matter: Theories, Signatures, and Constraints, November 2013.

[31] J. I. Read. The Local Dark Matter Density. *J. Phys.*, G41:063101, 2014.

[32] Martin C. Smith et al. The RAVE Survey: Constraining the Local Galactic Escape Speed. *Mon. Not. Roy. Astron. Soc.*, 379:755–772, 2007.

[33] Chris Kouvaris and Niklas Grønlund Nielsen. Daily modulation and gravitational focusing in direct dark matter search experiments. *Phys. Rev.*, D92(7):075016, 2015.

[34] Gianfranco Bertone, Dan Hooper, and Joseph Silk. Particle Dark Matter: Evidence, Candidates and Constraints. *Phys.Rept.*, 405:279–390, August 2005.

[35] G. Duda, A. Kemper, and P. Gondolo. Model Independent Form Factors for Spin Independent Neutralino-Nucleon Scattering from Elastic Electron Scattering Data. *JCAP*, 0704:012, 2007.

[36] J. H. Hubbell, Wm. J. Veigele, E. A. Briggs, R. T. Brown, D. T. Cromer, and R. J. Howerton. Atomic form factors, incoherent scattering functions, and photon scattering cross sections. *Journal of Physical and Chemical Reference Data*, 4(3):471–538, 1975.

[37] F. Donato, N. Fornengo, and S. Scopel. Effects of galactic dark halo rotation on WIMP direct detection. *Astropart.Phys.*, 9:247–260, March 1998.

[38] C. Enss. *Cryogenic Particle Detection*. Springer Berlin Heidelberg, 2005.

[39] P. Grieder. *Cosmic Rays at Earth*. Elsevier Science, 2001.

[40] G. Bellini et al. Cosmic-muon flux and annual modulation in Borexino at 3800 m water-equivalent depth. *Journal of Cosmology and Astroparticle Physics*, 2012(05):015, 2012.

[41] M.Kimmerle. *Data Analysis in the Direct Dark Matter Search Experiment CRESST and Calculation of the corresponding Limit on the Cross Section of Dark Matter*. PhD thesis, Universität Tübingen, 2010.

[42] Dariusz Malczewski, Jan Kisiel, and Jerzy Dorda. Gamma background measurements in the Gran Sasso National Laboratory. *Journal of Radioanalytical and Nuclear Chemistry*, 295(1):749–754, Jan 2013.

[43] F. Reindl. *Exploring Light Dark Matter With CRESST-II Low-Threshold Detectors*. PhD thesis, TU München, 2016.

[44] Moritz von Sivers. *Scintillating CaWO 4 crystals for the direct dark matter search experiments CRESST and EURECA*. PhD thesis, TU München, 2014.

[45] A. Münster, M. v. Sivers, G. Angloher, A. Bento, C. Bucci, L. Canonica, A. Erb, F. v. Feilitzsch, P. Gorla, A. Gütlein, D. Hauff, J. Jochum, H. Kraus, J.-C. Lanfranchi, M. Laubenstein, J. Loebell, Y. Ortigoza, F. Petricca, W. Potzel, F. Pröbst, J. Puimedon, F. Reindl, S. Roth, K. Rottler, C. Sailer, K. Schäffner, J. Schieck, S. Scholl, S. Schönert, W. Seidel, L. Stodolsky, C. Strandhagen, R. Strauss, A. Tanzke, M. Uffinger, A. Ulrich, I. Usherov, S. Wawoczny, M. Willers, M. Wüstrich, and A. Zöller. Radiopurity of CaWO 4 crystals for direct dark matter search with CRESST and EURECA. *Journal of Cosmology and Astroparticle Physics*, 2014(05):018, 2014.

[46] Sabine Roth. *The Potential of Neganov-Luke Amplified Cryogenic Light Detectors and the Scintillation Light Quenching Mechanism in $CaWO_4$ Single Crystals in the Context of the Dark Matter Search Experiment CRESST-II*. Phd thesis, TU München, September 2013.

[47] V. B. Mikhailik, H. Kraus, S. Henry, and A. J. B. Tolhurst. Scintillation studies of $CaWO_4$ in the millikelvin temperature range. *Phys. Rev. B*, 75(18):184308, May 2007.

[48] M. Kiefer, G. Angloher, A. Bento, C. Bucci, L. Canonica, A. Erb, F. v. Feilitzsch, N. Ferreiro Iachellini, P. Gorla, A. Gütlein, D. Hauff, J. Jochum, H. Kluck, H. Kraus, J.-C. Lanfranchi, J. Loebell, A. Münster, F. Petricca, W. Potzel, F. Pröbst, F. Reindl, S. Roth, K. Rottler, C. Sailer, K. Schäffner, J. Schieck, S. Schönert, W. Seidel, M. v. Sivers, L. Stodolsky, C. Strandhagen, R. Strauss, A. Tanzke, C. Türkoğlu, M. Uffinger, A. Ulrich, I. Usherov, S. Wawoczny, M. Willers, M. Wüstrich, and A. Zöller. In-situ study of light production and transport in phonon/light detector modules for dark matter search. *Nuclear Instruments and Methods in Physics Research A*, 821:116–121, June 2016.

[49] M. v. Sivers, M. Clark, P. C. F. Di Stefano, A. Erb, A. Gütlein, J.-C. Lanfranchi, A. Münster, P. Nadeau, M. Piquemal, W. Potzel, S. Roth, K. Schreiner, R. Strauss, S. Wawoczny, M. Willers, and A. Zöller. Low-temperature scintillation properties

of CaWO4 crystals for rare-event searches. *Journal of Applied Physics*, 118(16), 2015.

[50] S. Roth, C. Ciemniak, C. Coppi, F. v. Feilitzsch, A. Gütlein, C. Isaila, J. C. Lanfranchi, S. Pfister, W. Potzel, and W. Westphal. Cryogenic Composite Detectors for the Dark Matter Experiments CRESST and EURECA. *Opt. Mater.*, 31:1415–1420, 2009.

[51] R. Strauss, G. Angloher, A. Bento, C. Bucci, L. Canonica, W. Carli, A. Erb, F. von Feilitzsch, P. Gorla, A. Gütlein, D. Hauff, D. Hellgartner, J. Jochum, H. Kraus, J.-C. Lanfranchi, J. Loebell, A. Münster, F. Petricca, W. Potzel, F. Pröbst, F. Reindl, S. Roth, K. Rottler, C. Sailer, K. Schäffner, J. Schieck, S. Scholl, S. Schönert, W. Seidel, M. von Sivers, L. Stodolsky, C. Strandhagen, A. Tanzke, M. Uffinger, A. Ulrich, I. Usherov, S. Wawoczny, M. Willers, M. Wüstrich, and A. Zöller. Energy-dependent light quenching in CaWO $$_4$$ 4 crystals at mK temperatures. *The European Physical Journal C*, 74(7):2957, 2014.

[52] Patrick Huff. *The detector parameters determining the sensitivity of the CRESST-II experiment*. PhD thesis, TU München, 2010.

[53] Karoline Julia Schäffner. *Study of Backgrounds in the CRESST Dark Matter Search*. Dissertation, Technische Universität München, München, 2013.

[54] M. Janecek and W. W. Moses. Optical Reflectance Measurements for Commonly Used Reflectors. *IEEE Transactions on Nuclear Science*, 55(4):2432–2437, Aug 2008.

[55] Rafael Florian Lang. *Search for dark matter with the CRESST experiment*. PhD thesis, TU München, 2008.

[56] J. Clarke and A.I. Braginski. *The SQUID Handbook: Fundamentals and technology of SQUIDS and SQUID systems*. Wiley-VCH, 2004.

[57] A.Bento. *Aspects of the performance of alow temperature calorimeters fro x-ray spectroscopy with high detection efficiency*. PhD thesis, University of Oxford, 2004.

[58] F. Pröbst, M. Frank, S. Cooper, P. Colling, D. Dummer, P. Ferger, G. Forster, A. Nucciotti, W. Seidel, and L. Stodolsky. Model for cryogenic particle detectors with superconducting phase transition thermometers. *Journal of Low Temperature Physics*, 100(1-2):69–104, 1995.

[59] A. Senyshyn, H. Kraus, V. B. Mikhailik, and V. Yakovyna. Lattice dynamics and thermal properties of $CaWO_4$. *Phys. Rev. B*, 70:214306, Dec 2004.

[60] R. Strauss, J. Rothe, G. Angloher, A. Bento, A. Gütlein, D. Hauff, H. Kluck, M. Mancuso, L. Oberauer, F. Petricca, F. Pröbst, J. Schieck, S. Schönert, W. Seidel,

and L. Stodolsky. The ν -cleus experiment: a gram-scale fiducial-volume cryogenic detector for the first detection of coherent neutrino–nucleus scattering. *The European Physical Journal C*, 77(8):506, Jul 2017.

[61] A. Tanzke. *Low-Threshold Detectors for Low-Mass Direct Dark Matter Search with CRESST-III*. PhD thesis, Technische Universität München, München, 2017.

[62] M.Loidl. *Diffusion und Einfang von Quasiteilchen*. PhD thesis, Ludwig-Maximilians-Universität München, 1999.

[63] M. Kurakado. Possibility of high resolution detectors using superconducting tunnel junctions. *Nuclear Instruments and Methods in Physics Research*, 196:275–277, May 1982.

[64] C. Chi and J. Clarke. Enhancement of the energy gap in superconducting aluminum by tunneling extraction of quasiparticles. *Phys. Rev. B*, 20(11):4465–4473, Dec 1979.

[65] Andreas Josef Zöller. *Artificial Neural Network Based Pulse-Shape Analysis for Cryogenic Detectors Operated in CRESST-II*. Phd thesis, TU München, 2016.

[66] G. Angloher, A. Bento, C. Bucci, L. Canonica, A. Erb, F. von Feilitzsch, N.Ferreiro Iachellini, P. Gorla, A. Gütlein, D. Hauff, P. Huff, J. Jochum, M. Kiefer, C. Kister, H. Kluck, H. Kraus, J.-C. Lanfranchi, J. Loebell, A. Münster, F. Petricca, W. Potzel, F. Pröbst, F. Reindl, S. Roth, K. Rottler, C. Sailer, K. Schäffner, J. Schieck, J. Schmaler, S. Scholl, S. Schönert, W. Seidel, M. von Sivers, L. Stodolsky, C. Strandhagen, R. Strauss, A. Tanzke, M. Uffinger, A. Ulrich, I. Usherov, S. Wawoczny, M. Willers, M. Wüstrich, and A. Zöller. Results on low mass WIMPs using an upgraded CRESST-II detector. *The European Physical Journal C*, 74(12), 2014.

[67] R.B Firestone et al. *The 8th edition of the Table of Isotopes*. Springer., 1997.

[68] M. Sisti, O. Meier, M. Bühler, S. Cooper, V. Jörgens, M. Loidl, U. Nagel, F. Pröbst, W. Seidel, A. Stolovits, L. Stodolsky, S. Uchaikin, and L. Zerle. Massive cryogenic particle detectors with low energy threshold. *Nuclear Instruments and Methods in Physics Research Section A: Accelerators, Spectrometers, Detectors and Associated Equipment*, 466(3):499–508, 2001.

[69] G. Angloher, A. Bento, C. Bucci, L. Canonica, X. Defay, A. Erb, F. von Feilitzsch, N. Ferreiro Iachellini, P. Gorla, A. Gütlein, D. Hauff, J. Jochum, M. Kiefer, H. Kluck, H. Kraus, J. C. Lanfranchi, J. Loebell, A. Münster, C. Pagliarone, F. Petricca, W. Potzel, F. Pröbst, F. Reindl, K. Schäffner, J. Schieck, S. Schönert, W. Seidel, L. Stodolsky, C. Strandhagen, R. Strauss, A. Tanzke, H. H. Trinh Thi, C. Türkoğlu, M. Uffinger, A. Ulrich, I. Usherov, S. Wawoczny, M. Willers, M. Wüstrich, and A. Zöller. Results on light dark matter particles with a low-threshold CRESST-II detector. *The European Physical Journal C*, 76(1):25, 2016.

[70] M. Moszyński, M. Balcerzyk, W. Czarnacki, A. Nassalski, T. Szczęśniak, H. Kraus, V. B. Mikhailik, and I. M. Solskii. Characterization of CaWO $_4$ scintillator at room and liquid nitrogen temperatures. *Nuclear Instruments and Methods in Physics Research A*, 553:578–591, November 2005.

[71] G. Angloher, M. Bauer, I. Bavykina, A. Bento, C. Bucci, C. Ciemniak, G. Deuter, F. Feilitzsch, D. Hauff, P. Huff, C. Isaila, J. Jochum, M. Kiefer, M. Kimmerle, J.-C. Lanfranchi, F. Petricca, S. Pfister, W. Potzel, F. Pröbst, F. Reindl, S. Roth, K. Rottler, C. Sailer, K. Schäffner, J. Schmaler, S. Scholl, W. Seidel, M.v. Sivers, L. Stodolsky, C. Strandhagen, R. Strauß, A. Tanzke, I. Usherov, S. Wawoczny, M. Willers, and A. Zöller. Results from 730 kg/days of the CRESST-II Dark Matter Search. *The European Physical Journal C*, 72(4):1–22, 2012.

[72] K. H. Hellwege and O. Madelung, editors. *Landolt-Börnstein: Numerical Data and Functional Relationships in Science and Technology*, volume III/17a. Springer, Berlin, Heidelberg, New York, 1982.

[73] M. Kuźniak, M.G. Boulay, and T. Pollmann. Surface roughness interpretation of 730 kg days CRESST-II results. *Astroparticle Physics*, 36(1):77–82, 2012.

[74] R. Strauss, G. Angloher, A. Bento, C. Bucci, L. Canonica, A. Erb, F. von Feilitzsch, N. Ferreiro, P. Gorla, A. Gütlein, D. Hauff, J. Jochum, M. Kiefer, H. Kluck, H. Kraus, J.-C. Lanfranchi, J. Loebell, A. Münster, F. Petricca, W. Potzel, F. Pröbst, F. Reindl, S. Roth, K. Rottler, C. Sailer, K. Schäffner, J. Schieck, S. Scholl, S. Schönert, W. Seidel, M. von Sivers, M. Stanger, L. Stodolsky, C. Strandhagen, A. Tanzke, M. Uffinger, A. Ulrich, I. Usherov, S. Wawoczny, M. Willers, M. Wüstrich, and A. Zöller. A detector module with highly efficient surface-alpha event rejection operated in CRESST-II Phase 2. *The European Physical Journal C*, 75(8), 2015.

[75] W. L. Bond. Measurement of the Refractive Indices of Several Crystals. *Journal of Applied Physics*, 36(5):1674–1677, 1965.

[76] P. Huff. *The Detector Parameters Determining the Sensitivity of the CRESST-II Experiment*. Phd thesis, Technische Universität München, 2012.

[77] Michael Bass, Casimer DeCusatis, Jay Enoch, Vasudevan Lakshminarayanan, Guifang Li, Carolyn Macdonald, Virendra Mahajan, and Eric Van Stryland. *Handbook of Optics, Third Edition Volume I: Geometrical and Physical Optics, Polarized Light, Components and Instruments(Set)*. McGraw-Hill, Inc., New York, NY, USA, 3 edition, 2010.

[78] F. Petricca. *Dark Matter Search with Cryogenic Phonon-Light Detectors*. PhD thesis, Ludwig-Maximilians-Universität München, 2005.

[79] H. Kluck, G. Angloher, P. Bauer, A. Bento, C. Bucci, L. Canonica, X. Defay, A. Erb, F. v. Feilitzsch, N. Ferreiro Iachellini, P. Gorla, A. Gütlein, D. Hauff, J. Jochum,

M. Kiefer, H. Kraus, J. C. Lanfranchi, A. Langenkämper, J. Loebell, M. Mancuso, E. Mondragon, A. Münster, C. Pagliarone, F. Petricca, W. Potzel, F. Pröbst, R. Puig, F. Reindl, J. Rothe, K. Schäffner, J. Schieck, S. Schönert, W. Seidel, M. Stahlberg, L. Stodolsky, C. Strandhagen, R. Strauss, A. Tanzke, H. H. Trinh Thi, C. Türkoğlu, A. Ulrich, I. Usherov, S. Wawoczny, M. Willers, and M. Wüstrich. Search for low-mass Dark Matter with the CRESST Experiment, November 2017.

[80] R Strauss, G Angloher, A Bento, C Bucci, L Canonica, X Defay, A Erb, F von Feilitzsch, N Ferreiro Iachellini, P Gorla, A Gütlein, D Hauff, J Jochum, M Kiefer, H Kluck, H Kraus, J C Lanfranchi, J Loebell, A Münster, C Pagliarone, F Petricca, W Potzel, F Pröbst, F Reindl, K Schäffner, J Schieck, S Schönert, W Seidel, L Stodolsky, C Strandhagen, A Tanzke, H H Trinh Thi, C Türkoglu, M Ufflnger, A Ulrich, I Usherov, S Wawoczny, M Willers, M Wüstrich, and A Zöller. The CRESST-III low-mass WIMP detector. volume 718, pages 042–048, 2016.

[81] M. Loidl, S. Cooper, O. Meier, F. Pröbst, G. Sáfrán, W. Seidel, M. Sisti, L. Stodolsky, and S. Uchaikin. Quasiparticle diffusion over several mm in cryogenic detectors. *Nuclear Instruments and Methods in Physics Research Section A: Accelerators, Spectrometers, Detectors and Associated Equipment*, 465(2):440–446, 2001.

[82] W. Westphal. *Development and Characterization of Cryogenic Detectors for the CRESST Experiment*. PhD thesis, (not finished), 2008.

[83] J.Jochum. *Supraleitenden Tunneldioden als Detektoren in der Neutrino- und Astrophysik*. PhD thesis, Technische Universität München, 1994.

[84] R. C. Dynes, V. Narayanamurti, and J. P. Garno. Direct Measurement of Quasiparticle-Lifetime Broadening in a Strong-Coupled Superconductor. *Phys. Rev. Lett.*, 41(21):1509–1512, November 1978.

[85] K. Fuchs. The conductivity of thin metallic films according to the electron theory of metals. *Mathematical Proceedings of the Cambridge Philosophical Society*, 34(1):100–108, 1938.

[86] J. J. Yen, B. Shank, B. A. Young, B. Cabrera, P. L. Brink, M. Cherry, J. M Kreikebaum, R. Moffatt, P. Redl, A. Tomada, and E. C. Tortorici. Measurement Of Quasiparticle Transport In Aluminum Films Using Tungsten Transition-Edge Sensors, June 2014.

[87] J J. Yen, J M. Kreikebaum, Betty Young, Blas Cabrera, R Moffatt, P Redl, B Shank, P L. Brink, M Cherry, and Astrid Tomada. Quasiparticle Transport in Thick Aluminum Films Coupled to Tungsten Transition Edge Sensors. *Journal of Low Temperature Physics*, 12 2015.

[88] W. L. Bond. Measurement of the Refractive Indices of Several Crystals. *Journal of Applied Physics*, 36(5):1674–1677, 1965.

[89] M. Kiefer, G. Angloher, M. Bauer, I. Bavykina, A. Bento, A. Brown, C. Bucci, C. Ciemniak, C. Coppi, G. Deuter, F. von Feilitzsch, D. Hauff, S. Henry, P. Huff, J. Imber, S. Ingleby, C. Isaila, J. Jochum, M. Kimmerle, H. Kraus, J. C. Lanfranchi, R. F. Lang, M. Malek, R. McGowan, V. B. Mikhailik, E. Pantic, F. Petricca, S. Pfister, W. Potzel, F. Proebst, S. Roth, K. Rottler, C. Sailer, K. SchÃ¤ffner, J. Schmaler, S. Scholl, W. Seidel, L. Stodolsky, A. J. B. Tolhurst, I. Usherov, and W. Westphal. Composite CaWO4 Detectors for the CRESST-II Experiment. *AIP Conf. Proc. 1185, 651 (2009)*, December 2009.

[90] H. Kraus, V.B. Mikhailik, Y. Ramachers, D. Day, K.B. Hutton, and J. Telfer. Feasibility study of a ZnWO4 scintillator for exploiting materials signature in cryogenic {WIMP} dark matter searches. *Physics Letters B*, 610(1–2):37–44, 2005.

[91] Z. Kowalski, S.M. Kaczmarek, M. Berkowski, M. Głowacki, Y.A. Zhydachevskii, and A. Suchocki. Growth and optical properties of ZnWO4 single crystals pure and doped with Ca and Eu. *Journal of Crystal Growth*, 457(Supplement C):117–121, 2017. SI: CRYS_ECCG5.

[92] D. E. Aspnes and A. A. Studna. Dielectric functions and optical parameters of Si, Ge, GaP, GaAs, GaSb, InP, InAs, and InSb from 1.5 to 6.0 eV. *Phys. Rev. B*, 27:985–1009, Jan 1983.

[93] Raimund Johann Strauß. *Energy-dependent quenching factor measurements of CaWo4 crystals at mK temperatures and detector prototypes for direct dark matter search with CRESST*. PhD thesis, TU München, 2013.

[94] R. Strauss et al. A detector module with highly efficient surface-alpha event rejection operated in CRESST-II Phase 2. *Eur. Phys. J. C (2015) 75:352*, January 2016.

[95] S. Roth. *The Potential of Neganov-Luke Amplified Cryogenic Light Detectors and the Scintillation-Light Quenching Mechanism in $CaWO_4$ Single Crystals in the Context of the Dark Matter Search Experiment CRESST-II*. Phd thesis, Technische Universität München, 2012.

Abbildungsverzeichnis

Tabellenverzeichnis

Acknowledgments

The writing of this thesis was hard work for me. Nevertheless, the results achieved in this thesis are an effort which relies on the work of the many that are part of the CRESST collaboration. Without the team effort to keep the experiment running, this thesis would not have been possible. However, there are numerous persons I want to thank individually because they were there for me at times I needed advice and support.

First, I want to thank my first supervisor Prof. Dr. Stefan Schönert (TUM) for giving my the opportunity to write this thesis, for supervising it and for giving me the necessary support in the last years. Equal thanks go to my second referee Dr. Hubert Kroha (MPP).

Many thanks go to my daily supervisors Dr. Franz Pröbst (MPP) and Dr. Federica Petricca (MPP). Although very busy with leading the MPP group and the CRESST experiment, you always found the time for fruitful discussions and constructive advice guiding me to the best way to achieve my goals.

Special thanks deserve the two people proof reading my thesis. Without the seemingly endless efforts of Dr. Federica Petricca and Prof. Dr. Antonio Bento (MPP) to improve my writings, this thesis would not be ready at this point of time.

During my time at the Max-Planck-Institute, I had the pleasure work with a group of people which share my dedication and fascination to explore the unkown nature of dark matter. The collaborative efforts to achieve this vision is the glue of the group and assures the success of the project. All the people in the CRESST group, I consider as good collegues and many of them became good friends to me. Thanks a lot to all of you!

In this scope, I want to thank specifically Dieter Hauff. While the production of the detectors of CRESST-III, he was the most important person and always helped me when I had problems with a cryostat, a PVC or in the clean room.

Special thanks deserve Godehard Angloher which is the source of numerous innovations inside the CRESST experiment. Additionally, he is also the father of the beaker detectors. Without his endless commitment to realize the measurement of the beaker detectors in the CRESST setup at Gran Sasso, many of the result I presented in this work would not have been realized.

Outside the MPP group, I found many friends during my time at the MPP. The number of relations and people worth mentioning is to large to list. However, I want to highlight two people which became close friends to me and which helped in all circumstances: Dr. Florian Reindl and Dr. Karoline Schäffner. Late night discussions and numerous Skype meetings, were quite common in the last years and I am very grateful for all the help and advice you provided me in the field of science and for life.

Finally, I want to thank my family and friends for supporting me all the time, for grounding me when I was loosing contact to the real world and for showing me the joy

life offers apart from work. Many times, you helped me to focus and to give me the strength to master the exhausting challenges I had to face during my PhD.

Thank you!